8-8-2014

Performance and Durability of Electrodes with Platinum Catalysts in Polymer Electrolyte Cells Prepared by Ultrasonic Spray Deposition

William A. Rigdon
University of South Carolina - Columbia

PERFORMANCE AND DURABILITY OF ELECTRODES WITH PLATINUM CATALYSTS IN POLYMER ELECTROLYTE CELLS PREPARED BY ULTRASONIC SPRAY DEPOSITION

by

William A. Rigdon

Bachelor of Arts
West Virginia University, 2007

Master of Science
University of Central Florida, 2009

Submitted in Partial Fulfillment of the Requirements

For the Degree of Doctor of Philosophy in

Mechanical Engineering

College of Engineering and Computing

University of South Carolina

2014

Accepted by:

Xinyu Huang, Major Professor

Kenneth L. Reifsnider, Committee Member

Kyle S. Brinkman, Committee Member

Kevin Huang, Committee Member

Lacy Ford, Vice Provost and Dean of Graduate Studies

Dedication

To the *f*uture

Acknowledgements

For all that supported and motivated me,

including my family, friends, colleagues, teachers,

and especially my graduate advisor, Professor Xinyu Huang.

Resources, facilities, and other opportunities were provided by the

University of South Carolina

Abstract

Catalysts in the electrodes of polymer electrolyte cells serve a critical function in reactions which can be used to either generate electrical energy from chemical fuels or convert electrical energy into chemicals. For low temperature electrochemical fuel cells, platinum is often utilized for its exceptional catalytic activities towards hydrogen oxidation and oxygen reduction reactions of the anode and cathode, respectively. However, the limited supply of platinum and high demand result in prohibitive costs plaguing commercialization of this technology. Therefore, minimal amounts of the catalyst should be used to achieve the maximum output to reduce expenses. Electrochemical behavior is governed by the available reactive surfaces of the catalyst. A conductive material with high surface areas can be used in a composite approach to maximize nanostructured electrocatalyst sites. The state-of-the-art makes use of carbonaceous materials as the support. However, parasitic corrosion reactions of these materials in the electrode cause irreversible loss of activity that limits the useful lifetime of the cell, ultimately leading to its failure. Unfortunately, the supported platinum also can promote the catalytic oxidation of the carbon support where it is connected. Design of more resilient platinum catalysts could provide significant cost savings. An engineering challenge arises from their design and integration into the electrode.

Electron conductive paths in the support, proton channels in the electrolyte, and porous space are required in joint formation of active catalyst sites in the electrode. Phase boundaries and interfaces with the catalyst are critical to the design of this composite structure. Acidic ionomers, known as Nafion®, were chosen in this study for their facile proton conductivity, thermo-mechanical properties, and commercial availability. An automated process for depositing thin uniform electrodes directly on the polymer electrolyte membrane by ultrasonic spray deposition was developed. The material processing and deposition methods were refined for a variation of electrodes built with both supported and unsupported platinum catalysts. Characterizations of electrochemical performance were conducted to evaluate catalyst behaviors in working membrane electrode assemblies.

The catalyst should lower the activation energy of the reaction without being consumed. Preservation of electrocatalyst activity is critical to the durability of the electrochemical cell. Better platinum supports are needed for more reliable long-term performance. In proton exchange membranes, the electrocatalyst can experience high potential and low pH, limiting the selection of stable catalyst support materials. Platinum is a noble metal which has good intrinsic stability, but carbon is not in a thermodynamic equilibrium under these conditions. It is particularly problematic, as are many platinum alloys with less-noble metals which tend to be sacrificed to protect platinum during passivation. Ideally, the performance of catalysts should come without sacrifices to its stability. The nature and bonding of carbon atoms used in the support framework are an important determination factor of its corrosion resistance. Surfaces of carbon supports can also be functionalized to enhance their interactions with the catalyst. When stable

metal oxide phases are combined with carbon, useful junctions within electrocatalyst composites can be formed.

An alternative catalyst support construction to the conventional carbon black with high surface area and conductivity is viewed as an important goal in the development of performance and durability of electrodes. Carbon nanotubes offer some advantages in their material structure and properties. Multi-walled carbon nanotubes were selected for exceptional mechanical and transport behavior in the electrode, and relatively low production cost. A long range graphitic order can reduce the carbon corrosion kinetics. However, even graphitized carbon is still susceptible to corrosion and it bonds relatively weakly with platinum catalysts. This can lead to loss of active surface area through diffusion and detachment of the catalysts. To prevent this, a second phase was included into composite supports. Titania, a common name for titanium oxides, was first chemically bonded to the surfaces of carbon nanotubes to help anchor the catalysts through strong metal-support interactions. Advantages from the carbon nanotube and titania supports toward performance and durability were contrasted against a set of control samples and demonstrated in the cathode and anode.

A thorough literature review on the role of titania interfaces with the catalyst suggested application for the anode could provide further insight to its role in stability and activity. In this electrode, platinum catalyzed hydrogen oxidation suffers from contamination by trace amount of impurities that adsorb strongly on its surfaces. Carbon monoxide (CO) is one of the most persistent contaminants from reformation reactions and CO is also an intermediate in oxidation of other hydrocarbons, but despite its source, its adsorption onto reactive surfaces causes severe catalyst poisoning, limiting reactive

sites. In order to restore activity, potential, temperature, and/or oxygen pressure are applied to remove adsorbed contaminants. Electrochemical stripping requires oxidizing conditions that can also corrode electrocatalysts. Strong interactions between platinum and titania can potentially limit this oxidative process while also opening active sites near their interface through a bifunctional mechanism. These interfaces can be characterized as Schottky junctions that result in a synergistic relationship between activity and stability. In order to enhance charge separation across the Schottky barrier formed with n-type semiconductors, a doped form of titania was synthesized from niobium substitution in the transition metal oxide phase. Niobium was selected for its coordination, ionic radius, passivation behavior, and ability to form shallow donors. Advanced diagnostics were used to study titania supports in an electrochemical hydrogen pump to evaluate advantages for CO tolerance. Material characterizations of electrocatalysts were used to correlate the effects of support construction on resilient performance. Enhancements to the bifunctional reaction for CO oxidation as well as stability are proposed from the metal-metal oxide junction formed between catalyst and support. Performance and durability of electrochemical cells is improved by applying the science of materials and interfaces to the construction of catalyst supports for platinum in working electrodes, serving as an example for further progress and optimization.

Table of Contents

List of Tables

List of Figures

List of Abbreviations

A.....Amp

ADT .....Accelerated Degradation (Durability) Test

C.....Carbon

°C .....Celsius

CCM.....Catalyst Coated Membrane

CNT..... Carbon Nanotube

CO ..... Carbon Monoxide

CO_2.....Carbon Dioxide

CV .....Cyclic Voltammetry

D..... Diffusion Coefficient

DFT ..... Density Functional Theory

DOE .....Department of Energy

ECSA .....Electrochemical Surface Area

EDX .....Energy Dispersive X-ray Spectroscopy

EIS..... Electrochemical Impedance Spectroscopy

E_A .....Energy of Activation

E_F..... Fermi Energy

E_G ..... Energy (Band) Gap

eV ..... Electron Volts

F ..... Faraday Constant (96,485 C/mole)

G° ..... Gibbs Standard Free Energy

GDL ..... Gas Diffusion Layer

H+ ..... Proton

H_2 ..... Molecular Hydrogen (Diatomic)

H_2O ..... Water

HOR ..... Hydrogen Oxidation Reaction

I ..... Current

i ..... Current Density

K ..... Equilibrium Constant

M ..... Molar

MEA ..... Membrane Electrode Assembly

MO_x ..... Metal Oxide

MWCNT ..... Multi-Wall Carbon Nanotubes

n ..... Electron

NASA ..... National Aeronautics and Space Administration

Nb ..... Niobium

NbO_x ..... Niobia

NIST ..... National Institute of Standards and Technology

O ..... Oxygen

O_2 ..... Oxygen (Diatomic)

OCV ..... Open Circuit Voltage

ORR ..... Oxygen Reduction Reaction

P ..... Pressure

p..... Electron Hole

PEM ..... Polymer Electrolyte Membrane

PEMFC ..... Polymer Electrolyte (or Proton Exchange) Membrane Fuel Cell

Pt ..... Platinum

R..... Avogadro's Constant

R..... Resistance (Ω)

RDE..... Rotating Disk Electrode

sccm ..... Standard Cubic Centimeters per Minute

SEM ..... Scanning Electron Microscopy

SMSI ..... Strong Metal-Support Interaction

STEM..... Scanning Transmission Electron Microscopy

STP..... Standard Temperature and Pressure

T ..... Temperature

TEM ..... Transmission Electron Microscopy

Ti ..... Titanium

TiO_x..... Titania (reduced from TiO_2)

$TiNbO_x$..... Titania doped with Nb (10%)

V..... Electrical Potential (Volts)

XPS ..... X-ray Photoelectron Spectroscopy

XRD ..... X-ray Diffraction

XRF ..... X-ray Fluorescence

Chapter 1. Introduction and Background

Polymer electrolyte fuel cells are one application which could benefit from an improved catalyst support design. Cost has been a major barrier to the commercial success of this technology despite its potential in efficient generation of electricity. Fuel cells directly convert chemical energy into electrical current with low emissions and high efficiency, which is not subjected to the Carnot limit as in heat engines. They are proposed for transportation, stationary and portable power applications, but have seen only limited terrestrial applications so far. Introduction of the technical concepts can be related back to scientists Sir Humphry Davy, Christian Frederick Schönbein, and Sir William Grove with the first laboratory demonstrations coming before the commercial success of internal combustion engines, for instance. The technology has since been progressed by many other important historical contributions like the demonstration of the first practical hydrogen-oxygen fuel cell by Francis Thomas Bacon. Invention of the first polymer electrolyte membrane fuel cell (PEMFC) was by Willard Thomas Grubb and Leonard Niedrach at General Electric in the late 1950's. Success sparked NASA funding and use for Gemini missions in space exploration missions in the 1960's was a primary driving force behind more modern developments. Demonstration in terrestrial

transportation applications by Jeffrey Ballard and his company in 1980's promoted the adoption of the PEMFC as a potential replacement for internal combustion engines. Now, most of the major car corporations have active research and development programs in zero emission vehicles powered by PEMFC. As global concerns turn toward to our environment, this technology can lend itself to the use of sustainable fuels to reduce human dependence on the limited fossil fuel supply while helping to close the carbon cycle. Electrolysis and other electrochemical cells are also an established technology, but their widespread employment could also be assisted by more stable and active electrocatalysts. It is hopeful that better catalyst supports can improve not only fuel cells, but many related applications that are afflicted by similar problems.

One critical factor in the material design of fuel cell electrodes is reliance on precious metal catalysts like platinum and its alloys. To reduce the cost of the device, the minimal amount of platinum should have the greatest possible activity maintained over its useful lifetime. The catalyst is typically supported on another conductive high surface area material to form a composite electrocatalyst structure. Platinum group metals serve as the most active known catalysts for the oxygen reduction reaction (ORR) in the cathode of the PEMFC. This half of the net reaction is the rate limiting step of the fuel cell and determines the power output. Therefore, the cathode is the most important component of a PEMFC when operated with high purity hydrogen fuel. Hydrogen produced by reforming other hydrocarbon fuels either directly or indirectly can present daunting contamination challenges to the anode. Extensive efforts have been devoted to improve electrode properties for maximizing stable performance. The support for the catalyst serves to connect the catalyst with the electronic circuit. The fuel cell is also a

hostile environment in terms of the corrosive conditions the catalyst and its support can be subject to. Electrons are conducted through the support to participate in the ORR at the noble metal catalyst surfaces of the cathode. Ideally, these electrons should be supplied from the oxidation reaction occurring in the anode; however, they may be supplied from parasitic corrosion reactions, especially under aggressive conditions. Corroded regions of the electrocatalyst will no longer be able to contribute to the intended reaction due to irreversible losses. This ultimately contributes to its performance degradation and initiates its eventual failure. To this end, the stability offered by the support is vital to maintain the composite electrocatalyst performance.

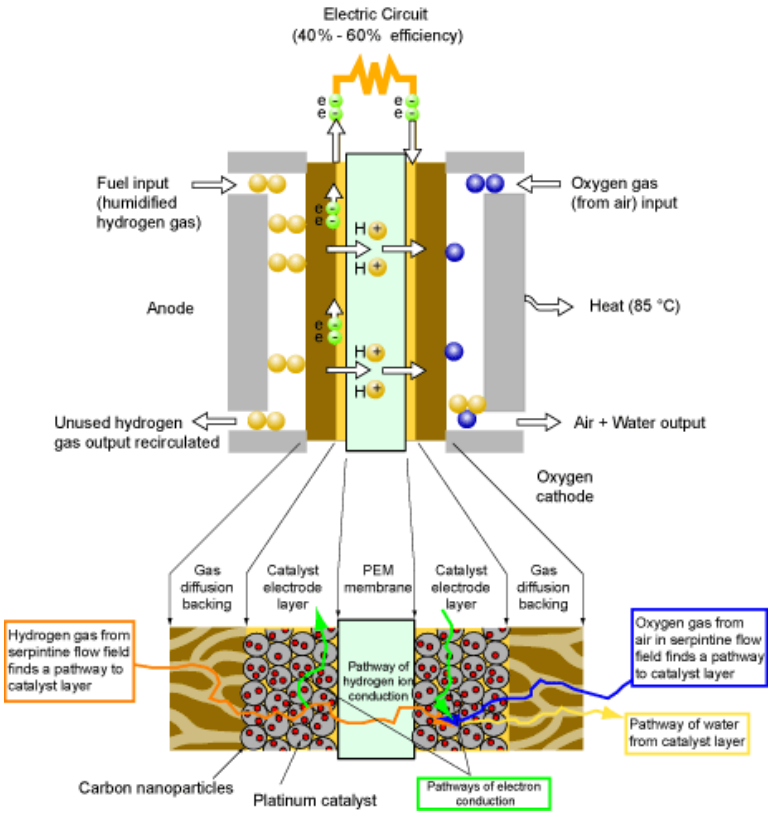

Figure 1.1 Proton exchange membrane fuel cell schematic
Source: http://physics.nist.gov/MajResFac/NIF/pemFuelCells.html

The catalyst support can significantly reduce the mass of precious metal catalyst required and maintain its performance. If ideally designed, the support can help promote the electrocatalytic reaction by facilitating charge transfer, mass transport of reactant fuels, and removal of products, for example. In this respect, inexpensive carbon has served effectively to distribute and connect platinum nanoparticles on its extensive surfaces. Carbonaceous materials are still considered the state-of-the-art and the most commercially successful catalyst support. However, carbon is known to be thermodynamically unstable in the cathode. Although, the oxidation kinetics are relatively slow until conditions become more severe at higher potentials, particularly. The oxidation of carbon prefers to start at defect sites on its disordered edges where carbon bonds are more easily cleaved. The properties of carbon depend on its chemical structure, but it is also well known that its instability is accelerated in the areas where it has bonded to platinum. Some specifics of the problem will be discussed in the literature review before possible solutions are investigated in the following chapters.

Platinum is an excellent electrocatalyst because of its high current exchange density in half-reactions of both electrodes. It is a noble metal with a high standard potential for oxidation. Platinum is much more thermodynamically stable than carbon, but it is not immune to corrosion. Under high potentials, which frequently occur during dynamic operation cycles, platinum also can be oxidized to a cation species. Mobile metal cations then diffuse into less desirable configurations with detached particles or lower active surface area that all result in eventual loss of performance. Unavoidably, the platinum cations diffuse into the electrolyte membrane and some will plate out (reduced by cross over hydrogen) as particles inside the membrane electrolyte. When molecular

hydrogen and oxygen are present, free radicals can be generated around these particles inside the membrane and the radicals locally attack the polymer chain, resulting in chemical and mechanical degradation. Consequently, specific advantages can be realized by materials which limit the corrosion and relocation of platinum. The degradation mechanism will be reviewed and experimental evidence is provided elsewhere, but the focus of the work will be on the development of new alternatives to traditional platinum on carbon.

Metal oxides can form stronger interactions with catalyst. When metal oxide is used in catalyst supports, these interactions may provide several benefits to the electrocatalyst. However, metal oxides are not great electronic conductors. Their properties can be tailored by changing the defect chemistry of the structure to increase the concentration of mobile charge carriers, including the use of dopants. Non-equilibrium states can be used if careful consideration is given to balancing charges in the operating environment. A strontium titanate perovskite was considered as catalyst support in an early study by modifying its defect chemistry and conductivity. Valuable lessons regarding the corrosion and thermodynamic stability were learned with regard to use of alternative catalyst supports in the PEMFC cathode. Later, titanium oxides (i.e. titania) was coated on carbon supports to form a composite. This approach proved more practicable in both the anode and cathode. Advantages from the strong interaction of platinum with titania were studied in the electrochemical cell and additional materials characterization helped to elucidate the specific roles they played in improving performance and durability.

A composite structure adopted in this study was inspired by the combination of benefits that could be realized from a dual phase support. Platinum is known to be more stable on the metal oxide surface because the strong metal-support interaction with titania and preferential bond location there. However, these materials offer poor conductivity and more conductive phases typically have very low surface area. A composite electrocatalyst was built from a carbon nanotube (CNT) framework covered with relatively small amounts of titania before decoration with platinum nanoparticles to form triple junctions. This composite material can still offer interconnected electronic pathways to platinum while enhancing corrosion resistance and sustaining performance over long durations.

Carbon nanotubes were chosen for several important reasons. The high aspect ratios of these materials help form and maintain an open support structure that can enhance transport of products and reactants. They also offer a long range graphitic order with less defects and improved corrosion resistance. Surface functionalization of carbon nanotubes is a key to realizing its useful properties. Composite phases were chemically bonded to the nanotube walls through surface functionality. Simplified material synthesis strategies were chosen for their ease of implementation and proof of concept in this work. Corrosion resistance over standard carbon black is another vital reason to choose a representative form of highly graphitized and ordered carbon precursor.

Validation of a dual phase catalyst support is an important goal of this research. Each material phase offers a unique advantage that can only be recognized by the preparation of a composite electrocatalyst. The carbon is functionalized with acid groups that react with the base titanium metal alkoxide from a sol-gel that is then calcined to

form a passive semi-crystalline surface. This is followed by a microwave-assisted polyol reduction process to deposit the nanostructured platinum catalysts. The catalyst composites are dispersed in an ink suspension with the other conductive phases to deposit electrodes on polymer electrolyte membranes in order to fabricate a MEA which can be tested in real fuel cell hardware. Accelerated durability testing conditions were then applied to these MEAs to monitor the changes in their performance over time.

Utilizing electrocatalysts that offer added durability for polymer electrolyte cells, the lifetime cost of the materials will be reduced. Greater longevity in especially aggressive conditions can extend the operating envelope of electrochemical cells. This problem has plagued the development of fuel cell technology for transportation and other applications where dynamic loading is required and commonly encountered, for example. This composite engineering approach serves to justify the design of more durable electrocatalysts that can be evidenced through implementation of materials selection and design that will contribute to further improvements in research and development.

1.1. Catalyst and Support Stability

1.1.1. Platinum and Pt Alloys

Platinum is one of the most noble and corrosion resistant metals known. However, no metal is immune to corrosion. At equilibrium in standard state, a very thin protective oxide film covers its surface which helps to make it so corrosion resistant. Regardless, the extreme conditions found in the PEMFC are enough to oxidize platinum

and destabilize it. Platinum has the $4f^{14}$ $5d^{9}$ $6s^{1}$ electron configuration, it is a Group VIIIB noble metal, and can exist in several positively charged oxidation states.

The Pt catalysts can become oxidized by the corresponding reactions [1]:

(1) $Pt + H_2O \rightleftharpoons PtO + 2H^+ + 2e^-$ $E^o = 0.980 - 0.0591\ pH$

(2) $PtO + H_2O \rightleftharpoons PtO_2 + 2H^+ + 2e^-$ $E^o = 1.045 - 0.0591\ pH$

(3) $PtO_2 + H_2O \rightleftharpoons PtO_3 + 2H^+ + 2e^-$ $E^o = 2.000 - 0.0591\ pH$

(4) $Pt^{2+} + H_2O \rightleftharpoons PtO + 2H^+$ $\log (Pt^{2+}) = -7.06 - pH$

(5) $Pt \rightleftharpoons Pt^{2+} + 2e^-$ $E^o = 1.188 + 0.0295 \log(Pt^{2+})$

(6) $Pt^{2+} + 2H_2O \rightleftharpoons PtO_2 + 4H^+ + 2e^-$ $E^o = 0.837 - 0.1182\ pH - 0.02955 \log (Pt^{2+})$

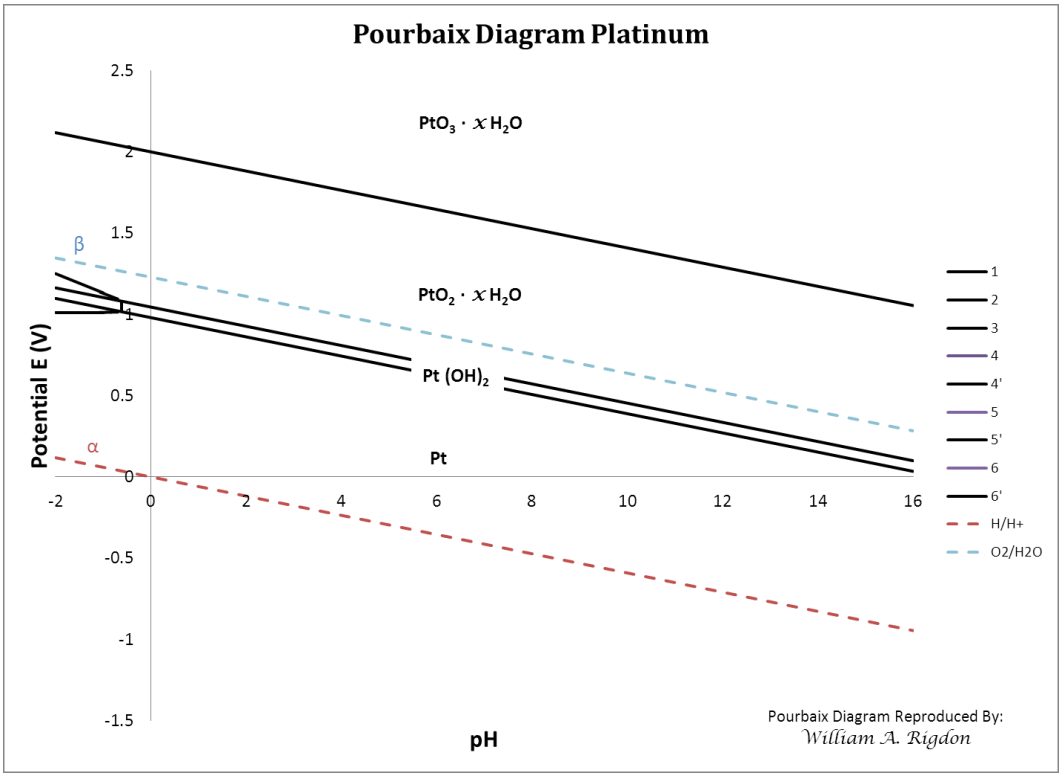

Figure 1.2 Pourbaix diagram of Pt at standard temperature and pressure

The electrochemical equations for the Pt water system were adopted from values of the thermodynamic equilibrium state of the metal provided by M. Pourbaix first published circa 1966 [1]. The original Pourbaix diagram does not take into account some modern updates which explain minor differences in the formation of free energy leading to a larger Pt^{2+} region [2]. Despite these differences, a general agreement exists that Pt with surface oxide species is the equilibrium phase in acidic solution at the cathode of a hydrogen-oxygen cell at open circuit condition.

The Pt ion dissolution and solubility in the electrolyte determine the diffusive capability of the Pt particles. This includes the dissolution of Pt cations, diffusion through the electrolyte, and the growth of crystallites. These induce adverse effects on fuel cell performance and should be mitigated. Pt cation solubility increases with potential, temperature, and pOH. Platinum nanoparticles used for the catalyst are also less stable as a result of their size and increased surface energy [3].

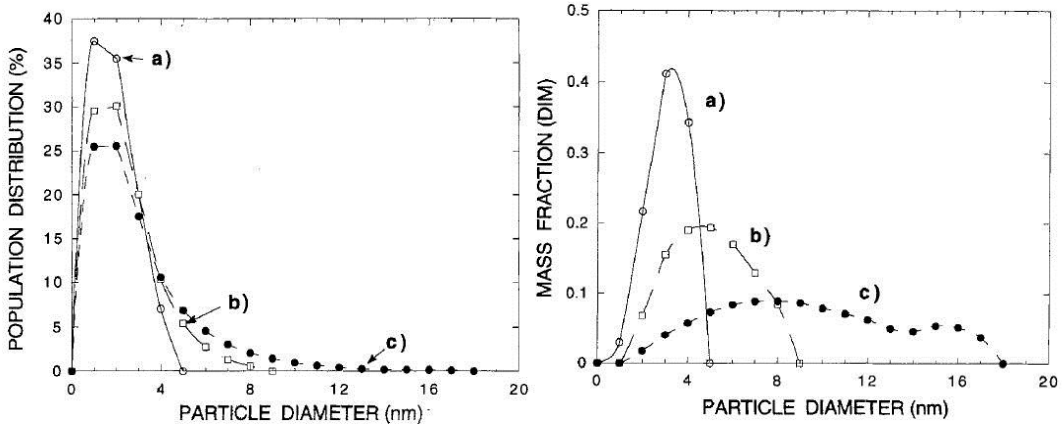

Figure 1.3 Platinum particle ripening in the cathode
(a) fresh (b) 1320 hours (c) 2200 hours [4]

Mahlon Wilson was one of the first to design electrodes with the use of carbon supported platinum mixed in with the ionomer binder, though he also recognized the problem of platinum particle stability from long duration experiments operated at 80 °C and 0.5 V hold as seen in Figure 1.3 [4, 5]. When Pt dissolves in the electrolyte, it can then diffuse and grow into larger crystals which offer lower surface tension and minimizes their electronically strained lattice configurations and reactive surface sites. This causes a loss of ECSA and platinum deposition in the polymer electrolyte, contributing to its degradation. The effect of potential on Pt dissolution was compared experimentally by Ferreira et al. and showed the following relationship compared to those measured and predicted values by Pourbaix; an experiment by Bindra was also plotted in Figure 1.4 following the predicted trend, although electrode tests show some deviations from his equation in a simulation similar to fuel cell conditions [6].

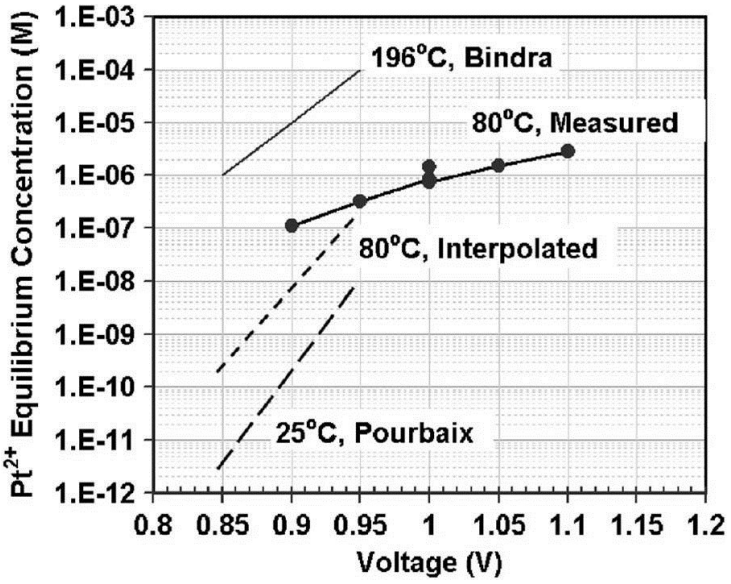

Figure 1.4 Platinum solubility equilibrium vs. potential [6]

The effect of temperature and humidity on the loss of Pt surface area during a potential cycling test measured by size approximations applied to XRD results and illustrated in Figure 1.5. The temperature and humidity affect the hydration of the membrane which can limit solubility and diffusivity of the ions electrolyte. Although, potential and pH are electrochemical driving forces for corrosion reactions.

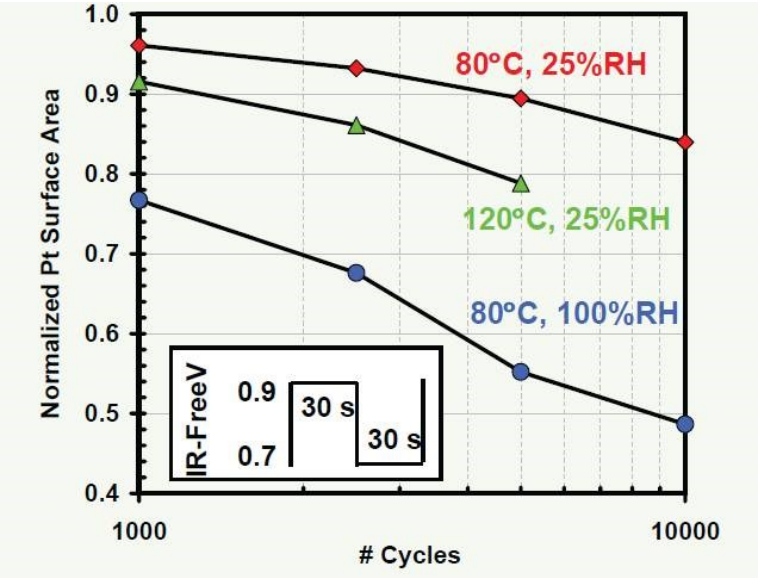

Figure 1.5 Pt surface area losses from RH and temperature effects [7]

Pt cation diffusion rates in PFSAs are not well publicized, but it is observed that Pt^{2+} mobility in this electrolyte is reduced by about an order of magnitude when the humidity is decreased from 100% to 25% at 80 °C [7]. At higher temperatures above the boiling point of water, the membrane hydration is lower despite the same relative humidity due to the phase change. Metal cation diffusion in the electrolyte plays a major role in the surface area loss. A schematic of some different Pt dissolution and diffusion methods are presented in Figure 1.6. There is often a combination of these events occurring during corrosion.

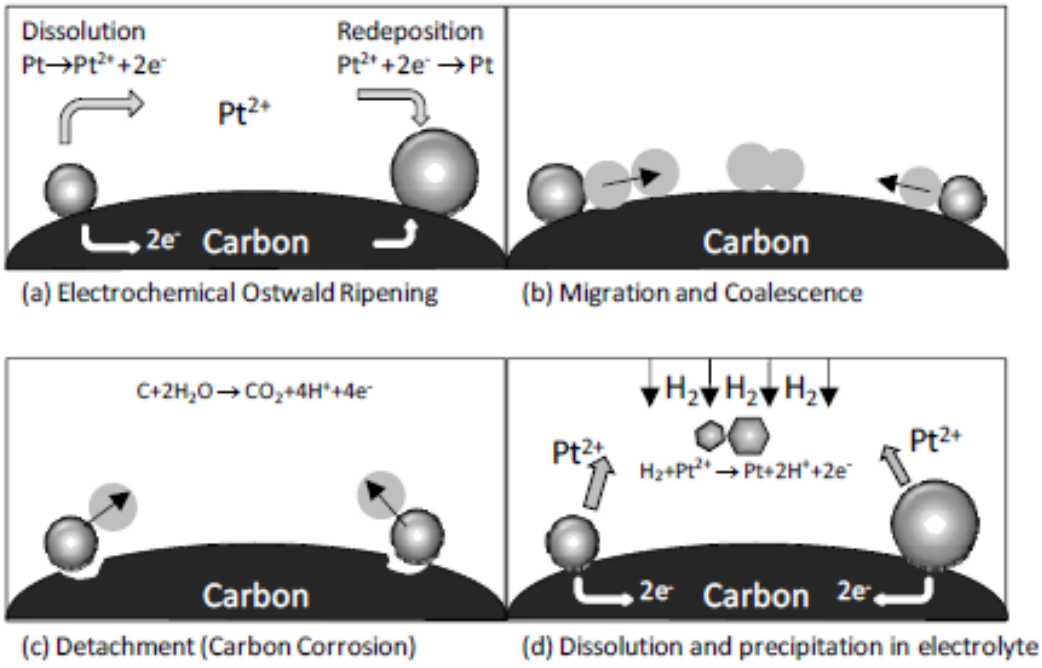

Figure 1.6 Possible Pt diffusion and degradation mechanisms [8]

At constant potential, the Pt dissolution rate has been studied and follows a rate dependent on the circumstance. Mathias et al. reported their results based on two separate regimes. Despite a similar decay rate in potential of 20 and 25 μV/hour, the surface area loss is much more pronounced at OCV conditions as seen in Figure 1.7. However, many electrochemical cells are operated under dynamic conditions which can be even more aggressive. In variable conditions, the surface states of the electrocatalyst are constantly undergoing changes to adopt more stable configurations.

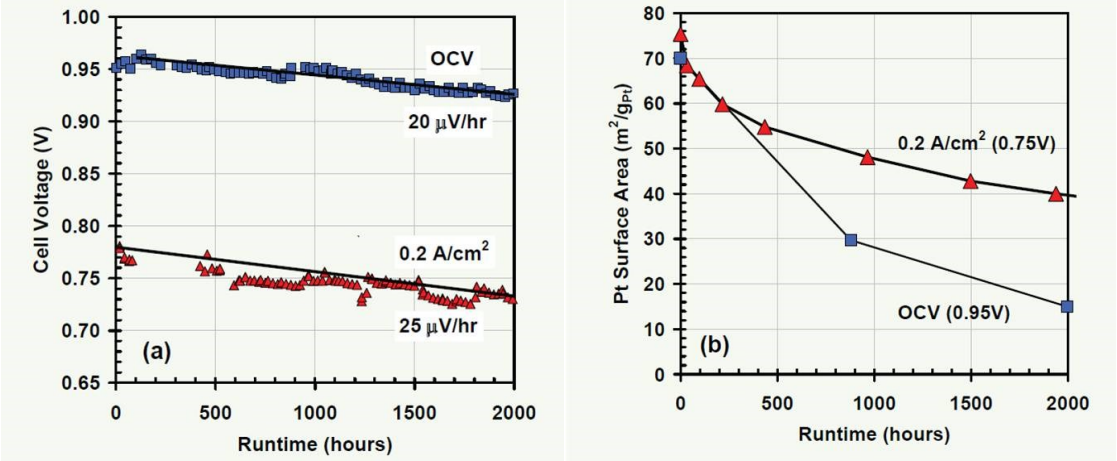

Figure 1.7 (a) Voltage decay and (b) surface area loss under constant potential [7]

In a study of Pt/C and Pt electrodes in acidic solution, the concentration of dissolved Pt cations increased from 0.65 to 1.1 V, but decreases at potentials > 1.1 V under room temperature conditions [7]. This has been attributed to the formation of a protective oxide surface film in the passivation region. The equilibrium concentration of dissolved Pt cation and the Pt dissolution rates at 0.9 V hold were comparable for high surface area carbon supported platinum and polycrystalline wires [9]. In another similar study of Pt on gold electrodes, the oxide film was determined to reach a saturation point at 1.15 V_{RHE} at 80 °C [10]. The dissolution rate was strongly dependent on temperature and potential. The measurements made by a quartz crystalline microbalance allow for in-situ determination of mass dynamics and the data are relevant for measuring Pt dissolution which typically operates at a similar temperature in the PEMFC.

Many publications have observed the effect of operational parameters in PEMFC on this behavior. Several models have been developed to predict and quantify the experimental evidence. Most notably, Darling and Meyers created a model which includes a potential dependent dissolution of Pt, platinum oxide formation, chemical

dissolution of Pt oxide ($PtO + 2H^+ \rightarrow Pt^{2+} + H_2O$), and a surface tension driven growth of platinum nanoparticles [11]. This model reasonably correlates to experimental work with the inclusion of a cathodic term to predict equilibrium oxide coverage on Pt surfaces [12]. They later adapted the model to fit the transient behavior of a fuel cell cycled between hydrogen/air and air/air at OCV and to more accurately predict Pt dissolution and diffusion [13]. However, Gasteiger and co-workers at GM contested the model because they did not take into account the effect of crossover hydrogen and Pt reduction by ($Pt^{2+} + H_2 \rightarrow Pt + 2\ H^+$). Their results found that only about half of the platinum surface area loss was attributed to the Pt ripening and the other half was deposited as reduced Pt in the ionomer phase of the cathode, near the electrode-membrane interface where hydrogen concentration was highest from crossover [6]. Gasteiger and colleagues would later go on to produce a model which tried to account for the degradation of the whole MEA [14]. A physics-based model which considered dissolution of Pt and deposition on Pt nanoparticles, diffusion of Pt ions in the MEA, and Pt cation reduction by permeating hydrogen was developed by Bi and Fuller [15]. The group led by T. Fuller later updated the simulation with the role of particle size distribution on dissolution and prediction of inter-particle interactions between Pt oxides [16]. A multi-scale model by Franco and Gerard of corrosion in a PEMFC was coupled with electrocatalysis mechanisms to explain performance degradation [17]. The simulations suggest some interesting features such as the existence of an "optimal" external current inducing a maximal durability. However, holding cells at constant optimal conditions is impractical in most applications which require cyclical current loading.

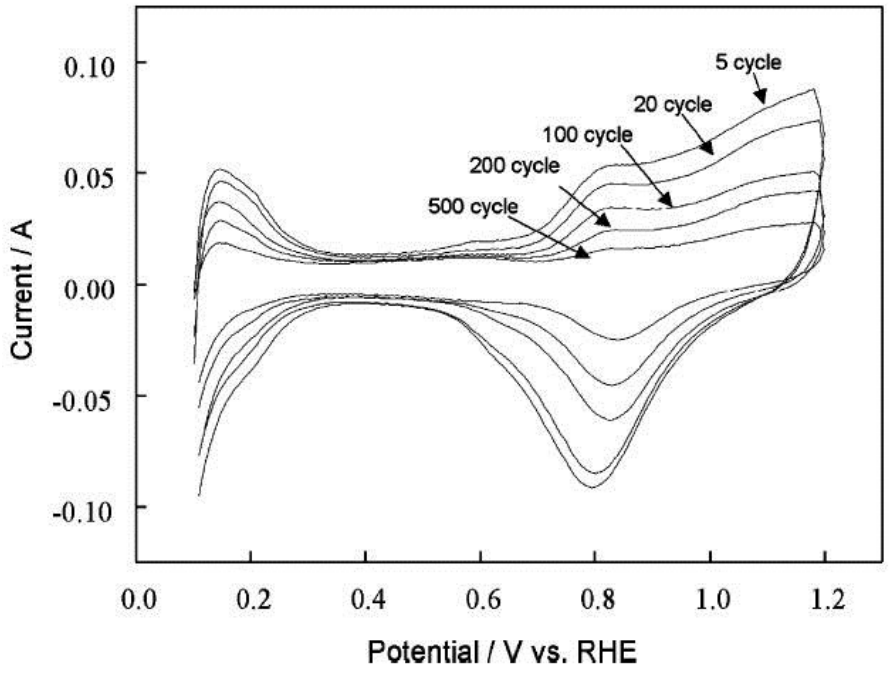

Figure 1.8 Potential cycling reduces the active electrochemical area [18]

Cycling operations with extreme maxima and minima have an accelerated effect on not only support corrosion, but also Pt dissolution. It is believed that cycling can remove the protective oxide and hydroxide surfaces which form on Pt and speeds up the corrosion during return to high potential which can dissolve some surface atoms before it is passivated again. This data for PEMFC was presented by Patterson in 2002 in an ECS *Transaction* [12]. Potential cycling had historically been known to increase corrosion processes in phosphoric acid fuel cells where carbon corrosion is also a significant problem and was highlighted in a classic paper by Kinoshita, Lunquist, and Stonehart; the paper showed how the cycling profile could accelerate corrosion rates [19]. They varied cycling parameters and ran profiles of square and triangular waves of the supported Pt electrodes. Yasuda et al. showed the effect of cycle number and upper potential limit by varying cell conditions that also resulted in Pt deposition in the membrane as shown by

Figure 1.8 [18]. A thorough TEM analysis investigated the distribution of Pt in the polymer electrolyte [20]. Another comparison of unsupported crystallites to those supported on graphite was investigated along with an observation of morphology changes, surface area, and corrosion rates. A comprehensive study by Mitushima et al. compared the potential cycling by several wave profiles and frequencies on consumption rate of Pt in PEMFCs [21]. The frequency of reaching the upper limit was found to be more critical than the hold time at this condition because a surface passivation on platinum can prevent further consumption when held at constant potential.

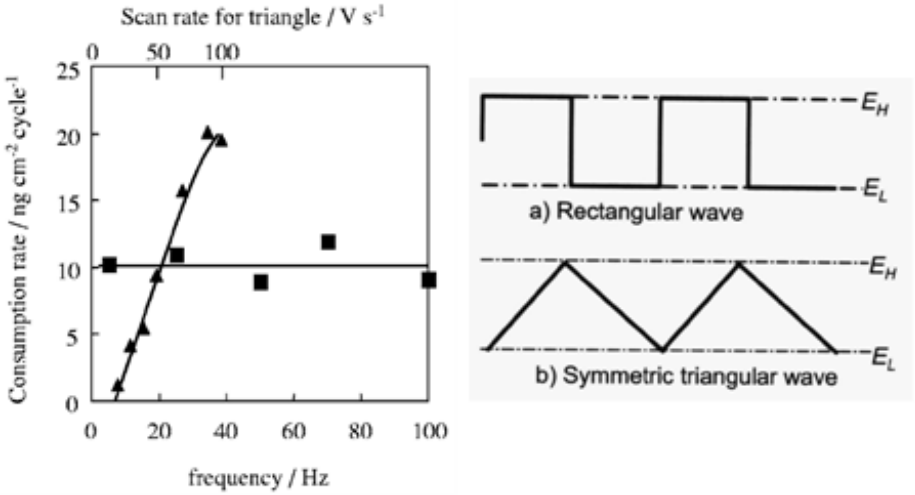

Figure 1.9 Consumption of Pt vs. frequency for triangular and rectangular wave profiles from 0.5-1.8 V at 40 °C with patterns represented by their shape [21]

Detached Pt particles (from carbon support) are ineffective in the fuel cell reaction. Pt cations diffusing into the membrane can reduce proton conductivity and lead to more degrading mechanisms of the ionomer. Pt reduction in the ionomer poses a major risk to the material. The rate and location of Pt^{2+} reduction and nucleation in the ionomer was found to depend on partial pressure of both hydrogen and oxygen [22]. From experimental evidence, a model was developed to predict the Pt dissolution and

deposition in Nafion electrolyte. A concentrated band of reduced Pt formed across the in-plane direction which corresponded to the rates of crossover for hydrogen and oxygen gases in the MEA. Experimental evidence of the localized Pt band region was found by several research groups and depicted in Figure 1.11 [[6], [20]]. The Pt catalyzed the crossover gases to form water at these sites, but undesired oxidative free radical reaction intermediates like HO· and HOO· were found to rapidly degrade the polymer chains of perfluorosulfonic acid ionomer. Other metals such as iron (II) can be even worse for this degradation as studied by the Fenton reaction [[23]]. The evidence for formation of these products; HF, CO_2, SO_x and H_2O_2 were found in the exhaust gas by mass spectrometry [[24]]. The polymer membrane defines the mechanical properties of the MEA and when degraded by this mechanism, they become thin and brittle. Loss of compliance can lead to leaking and cracking that allows gases to crossover and they react directly without producing useful current. Yoon and Huang demonstrated the loss of mechanical strength which was initiated from corrosion of the cathode in the MEA by performing a tensile test on the cathode side of the MEA that was separable due to the unique bi-layer fabrication design.

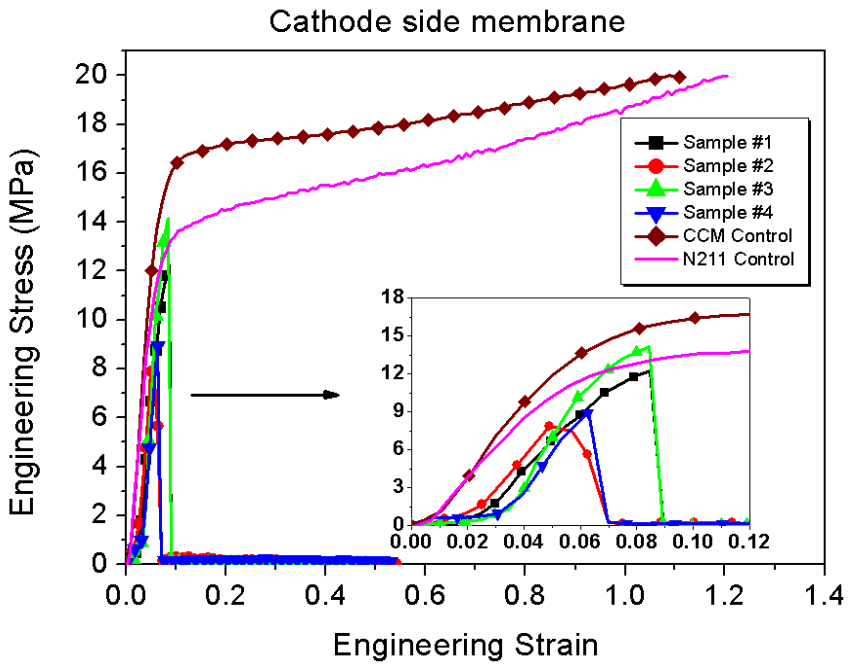

Figure 1.10 Stress-strain curves of MEAs before and after accelerated degradation [25]

As anticipated, the chemical and mechanical degradation are very closely related. The N211 sample is an untreated piece of Nafion® polymer and the CCM control sample is a fresh catalyst coated membrane. Samples 1-4 have been subjected to various accelerated degradation test conditions. Designing a more corrosion resistant cathode will be an important step to building a more durable PEMFC and its eventual commercialization. A schematic is offered here to further understand the dissolution and re-deposition of the Pt in the electrolyte. A precipitation band particularly weakens the polymer that yields plastically under stress. The devastating circumstances and ultimate failure caused by metal dissolution and re-deposition is just suggested in this review, but can be summarized in other publications [26].

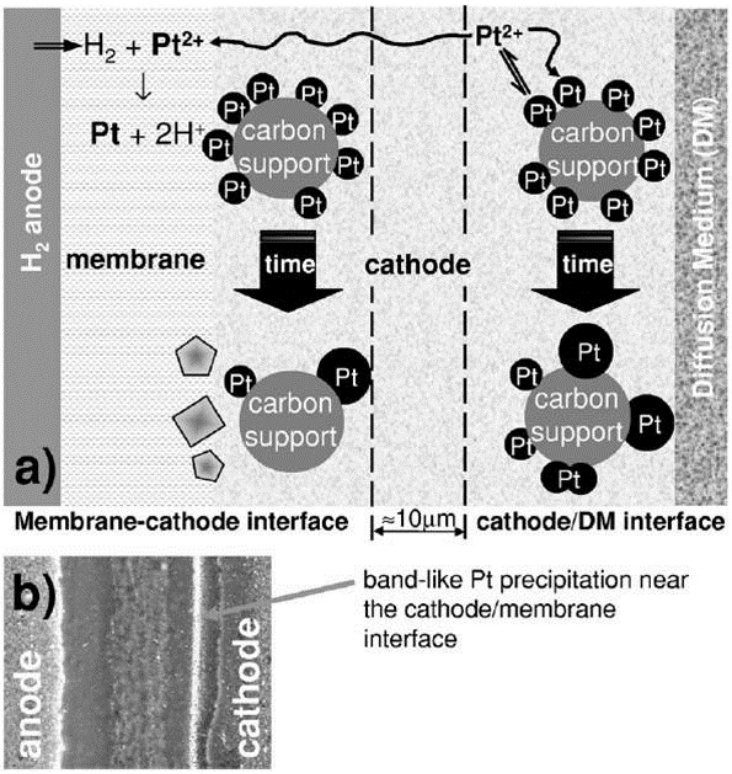

Figure 1.11 (a) Schematic of Pt dissolution and band formation (b) in MEA [6]

1.1.2. Carbon Supports

Carbon is a popular electrode support material in part because of its good conductivity and slow corrosion reaction kinetics, but the corrosion still proceeds even at low potentials. When the fuel cell electrodes are subjected to high potentials of OCV or even higher from the starvation of hydrogen gas, irreversible damage will occur to the electrode structure. The frequency, duration, and pattern of these potential variations can drastically alter the reaction kinetics [27]. Understanding these mechanisms can lead to effective mitigation methods.

These accelerated events happen under transient conditions of fuel cell operation and are especially damaging during conditions like start up, shut down, and anode flooding. Flooding is more likely to occur in the cathode where water is generated and

also diffuses through the membrane due to electro-osmotic drag of diffusing protons. However, anode flooding caused by low current densities, back-diffusion of water, and general water mismanagement can also transgress. It is harder to remove anode flooding with low hydrogen flow rates and it directly leads to corrosion [28]. During flooding, the H_2 diffusion becomes significantly reduced through the liquid water phase [29]. This condition in the fuel cell leads to reactant starvation, back diffusion of air (oxygen), and local cathode overpotentials even higher than OCV. This effect is similar to that when reactants are depleted during start-up and shut down. A fuel concentration gradient forms across the MEA from inlet to outlet during start-up and the opposite during shut down. Air or oxygen gas can replace these volumes which supply the necessary condition for corrosion to occur [2, 30]. This condition can be described by a hydrogen/air front.

The carbon corrosion reaction is accelerated as a result of the hydrogen/air front phenomena leading to reverse-current decay [31]. When this happens, ORR actually takes place in the anode. The electrons can be conducted from another region of the anode, and the oxygen (permeated through MEA and other seals after long-term idling) forcing protons diffusion from the cathode to the anode. The reverse-current of protons comes from two reaction sources at the cathode. The oxidation of water also known as the oxygen evolution reaction (OER) or water electrolysis is one source of the protons. The other source is the carbon oxidation reaction (COR) also known as carbon corrosion. These reactions are also competing under normal operation, but become considerably faster when the hydrogen/air boundary is formed. Region B is starved of H_2 and has a higher oxygen concentration from air that has crossed into the electrode during idle. When hydrogen fuel is re-introduced into the anode, a hydrogen/air boundary is formed.

Region A would arise during this time, starting near the H_2 near inlet, while Region B would more prevalent closer to the outlet. The mechanism can be further understood by Figure 1.12.

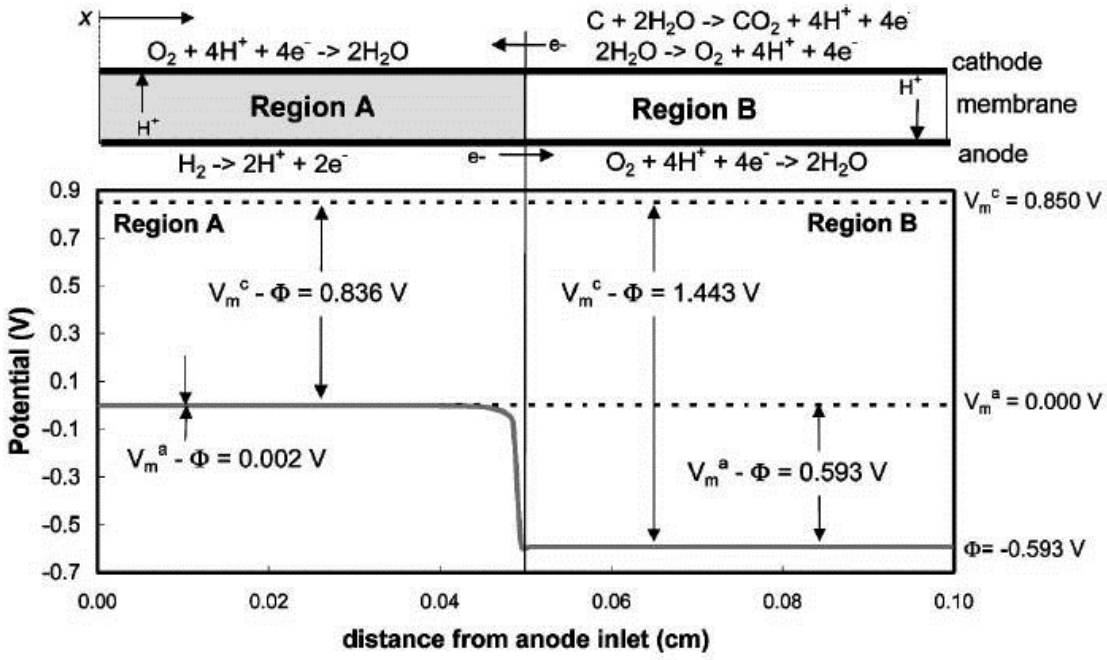

Figure 1.12 Reverse-current decay mechanism from a H_2/air boundary in anode [31]

A potential drop in the starved anode region accelerates carbon corrosion by raising the potential difference at the cathode to extreme values up to ~1.44 V. Carbon corrosion causes many adverse effects in the cathode which directly affect the demise of performance and operational lifetime of the fuel cell. The structure of the electrode is altered and permanently degraded. This leads to a change in material properties of carbon, surface bonding characteristics, decrease in surface area, and an increase in electronic resistivity [3, 32, 33, 34]. The cathode layer thins and also becomes more compact which limits mass transport. In addition, the surface oxidation makes the carbon

more hydrophilic and more susceptible to flooding. First, the performance will decline and ultimately it will lead to the death of the fuel cell.

Carbon corrosion can occur in both cathode and anode of a PEM fuel cell. Anode carbon corrosion can also happen when there is a complete fuel starvation of one or more cells in a working stack [35]. The starved cells are driven into a reversed operation with the anode potential becoming higher than the cathode potential. The corrosion mechanism is similar to that of the cathode. This state triggers water electrolysis and carbon oxidation on the fuel cell anode in order to provide the required protons and electrons for the reduction of oxygen at the cathode. The oxidation of the anode carbon is also possible when applied potentials are great enough to drive the reaction. This review will focus on cathode corrosion, primarily. The gas diffusion layer (GDL) can also be considered as part of the MEA, although its behavior is not included in great detail in this review. There have been only a few reports about GDL degradation and those primarily include an electrode preparation process directly on the diffusion media [36]. Because the GDL does not contain an ion conductive phase and it is also protected by a hydrophobic fluoropolymer, the corrosion of this material is typically slower in relative comparison to the oxidation of carbon catalyst supports in the cathode. In addition, the gas flow (bi-polar) plates are often made of exfoliated graphite with epoxy binders derived of carbon. These materials are all exposed to the atmosphere and potential of the cell, and thus can be corroded as well. Though, carbon oxidation is accelerated by catalysts and is of significantly greater concern.

Carbon becomes electrochemically oxidized to form a surface oxide and then by subsequent evolution of carbon dioxide. The mechanism for carbon corrosion has been

suggested to follow an electron transfer step by hydrolysis of the C^+ on the surface, eventually yielding CO_2 (g). Evidence for the mechanism has been offered by IR spectroscopy, ellipsometry, XPS, and electrochemical methods [37]. The intermediate reaction steps are listed here [38].

(A) $C \rightleftharpoons C^+ + e^-$

(B) $C^+ + H_2O \rightleftharpoons CO_{ads} + 2\ H^+ + e^-$

(C) $CO_{ads} + H_2O \rightleftharpoons CO_2 + 2\ H^+ + 2\ e^-$

Surface oxides are regarded as reaction intermediates of the corrosion mechanism which can be simplified by the above equations and understood as the formation of surface functional groups at active potentials. The literature has identified carboxyl, carbonyl, phenol, quinone, and lactone groups by NMR [39]. Carbon oxidation starts at defects and boundaries primarily where valence σ electron orbitals are exposed. The adsorption of surface species containing oxygen and/or hydrogen is chemically possible due to electron availability. In the presence of water, they are oxidized to carbon dioxide at potentials greater than 0.207 V_{RHE} [27].

(1) $C + 2\ H_2O \rightarrow CO_2 + 4\ H^+ + 4\ e^-$ $\quad E^o = 0.207$ V

(2) $C + H_2O \rightarrow CO + 2\ H^+ + 2\ e^-$ $\quad E^o = 0.518$ V

(3) $CO + H_2O \rightarrow CO_2 + 2\ H^+ + 2\ e^-$ $\quad E^o = -0.103$ V

Carbon is thermodynamically unstable at most fuel cell operating conditions. However, corrosion does not proceed at significantly measurable rates until higher potentials, as seen Figure 1.13. The corrosion of solid carbon directly to CO_2 is the

energetically preferred reaction [35]. This is generally accepted as the predominant corrosion pathway in the fuel cell environment. Carbon corrosion reactions are determined by the electron transfer step to the adsorbed oxide and the rate increases with potential, temperature, water activity, and pOH [7, 35]. The surface roughness, defect concentration, porosity and texture of carbon all factor into the reaction kinetics because they enhance the adsorption of the oxide [37]. The defect-free crystalline lattice, such as the basal plane of graphene, has significantly lower corrosion rates than the contribution from plane edges [40]. The corrosion current decays with time and obeys the following dependence: $I(t) = kt^{-n}$, where n is about ½. It was found by Stonehart that corrosion currents stabilizes near equilibrium values after 1000 minutes at constant potentials > 1.0 V. He attributed this to the preliminary oxidation of disordered carbon and defect sites [19]. The presence of oxygen in the air front at the anode also enhances corrosion compared to pure nitrogen and is illustrated in Figure 1.13 [35].

The presence of aqueous electrolyte is also essential, but several studies have found the highest corrosion rates at lower humidity levels [41]. This discrepancy may be related to competition between carbon corrosion and water electrolysis. The Nernst potential is directly dependent on water activity and temperature. The corrosion shows a linear relationship with molar water concentration while the temperature relationship follows an Arrhenius type behavior [35]. This approximation for corrosion current from 100 % RH was offered by Gasteiger and co-workers. $i_{CO_2} \propto 10^{E/TS} e^{-E_0/RT} t^{-m}$, where the Tafel slope, TS = b = 150 mV/decade; activation energy, E_A = 67 kJ/mole; and time decay exponent m = 0.30 which is independent of temperature and potential [7, 27].

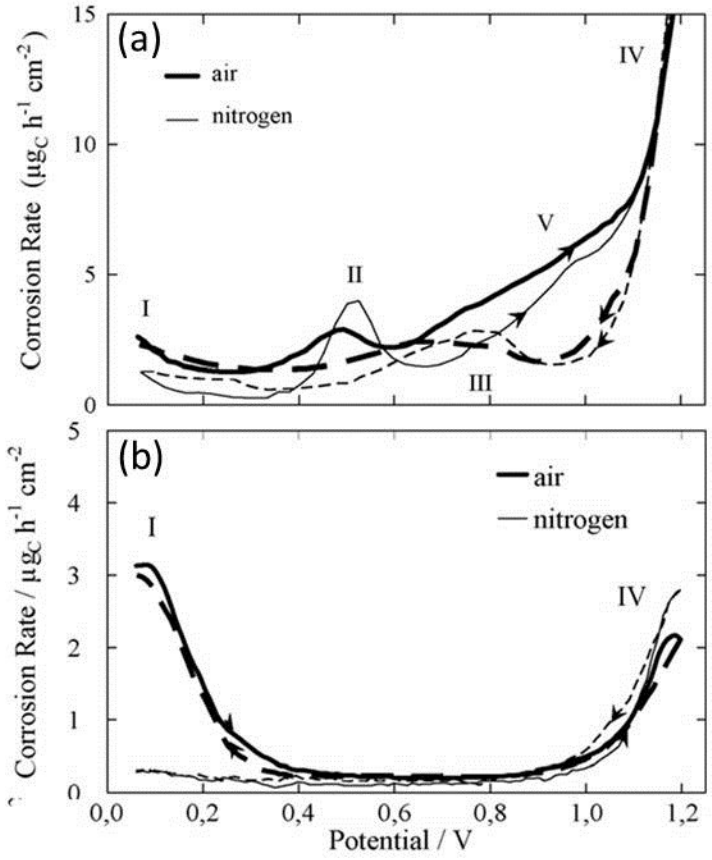

Figure 1.13 Effects of air vs. N_2 in corrosion of (a) Pt/C and (b) C electrodes where solid lines represent anodic sweeps and dashed show cathodic sweeps [35].

Carbon corrosion kinetics in presence of platinum catalysts has been modeled by several research groups. There is some variability in the models as result of complicated interplay of factors as well as the prior history of the electrodes. Darling and Meyers also modeled the carbon corrosion by the reverse-current mechanism during the mal-distribution of hydrogen across the anode [42]. Takeuchi and Fuller produced a model based on important membrane electrode assembly design parameters, such as the oxygen reduction exchange current density on the negative electrode and the permeability of the membrane [43]. One of the most comprehensive analyses proposed by the General Motors Fuel Cell Research and Development group includes a model of electrode

kinetics, H_2 starvation, and start-stop; coupled kinetic and transport; and pseudo-capacitance which accounts for the reactions that supply or consume electrons in transient start-stop events and are normally neglected [14]. However, the authors admittedly suggest needed improvement for carbon corrosion kinetics associated with voltage cycling.

Potential cycling has been shown to have a significant enhancement of corrosion acceleration which occurs by a different mechanism than start-stop cycling. There is no actual air-hydrogen front formed in this scenario. Simulated accelerations typically apply potential to the working cathode under inert gas and vary it with reference to the hydrogen anode. Reduction and oxidation occur as cycles repeat. Chemical oxidation of carbon by hydrogen peroxide can actually occur at low potentials below the standard state potential as evidenced by peak I in Figure 1.13. Hydroxyl surface groups on platinum are destabilized at lower potentials [44]. Typically they react to form water, but peroxide species like hydrogen peroxide can be formed and were measured in nitrogen atmosphere at low concentrations [45]. In contrast, the oxygen reduction on carbon alone mainly forms the hydrogen peroxide species which reacts with carbon supports by [46]:

(4) $C + H_2O_2 \rightarrow C\text{-}O_{ad} + H_2O$

(5) $C\text{-}O_{ad} + H_2O_2 \rightarrow CO_2 + H_2O$

On Peak II, a reaction from adsorbed CO species near Pt can become oxidized at lower potentials by the bifunctional mechanism in reaction (6) when the acidic oxygen functional groups in the vicinity are adsorbed on Pt.

(6) $Pt\text{–}CO_{ad} + Pt\text{–}OH_{ad} \rightarrow Pt_2 + CO_2 + H^+ + e^-$

Peak III coincides with the reduction of oxygen groups on Pt that oxidize carbon by reactions (4 and 5) with hydrogen peroxide. When potentials are increased, the effect of Pt on corrosion becomes more noticeable. The onset of peak IV is noticeable at 0.3 V on Pt/C compared to that of C electrode at 0.9 V. The contribution from the catalytic effect of platinum oxide groups which reduces the overvoltage of bridging carbon-oxygen bonds by enabling reaction (7) [35].

(7) $C\text{-}O_{ad} + Pt\text{–}OH_{ad} \rightarrow Pt + CO_2 + H^+ + e^-$

As platinum is aged and grows and the surface is covered in acidic oxygen functional groups, the ability to reduce hydrogen peroxide is lowered. Peak V becomes more pronounced on aged electrodes as surface oxygen forms on carbon and follows reaction step similar to (3) which follows (2) below 0.9 V. The consequence is dynamic corrosion rates which are increased in distinct potential ranges during cycling. The range and pattern of cycling is also important and have been shown to increase corrosion rate as well. A wider range of upper and lower limits drastically increases electro-oxidation at high overvoltage before surfaces get restructured when the oxide is reduced at lower potential regime. Current cycling accelerated stress test resulted in similar findings to those from potential cycling. A comparison between minimum current steps at 120 and 20 $\frac{mA}{cm^2}$ showed much faster degradation at the lower extrema [47]. The corrosion behavior at constant current and/or potential makes it possible study one predominant reaction mechanism and the effects of the other variables.

At constant potential, one mechanism dominates and carbon corrosion becomes easier to model. Also, a protective oxide layer which is stable at corresponding potential creates a limiting situation and eventual linear decay. During transient operations, the

time scale is not long enough to build up these stable oxide layers. Holding potentials at high values near OCV builds up an oxide layer which creates a greater concentration of unreacted fuel [35]. Carbon support degradation opens new initiation sites for continued carbon oxidation by a positive feedback. Despite the generally accepted and intuitive surface defect initiation of oxidation, it is not unambiguously accepted. Liu et al. proposed an inside out carbon corrosion mechanism based on their electron microscopy investigation which revealed a collapse of the porous electrode structure, causing the loss of mass transport in the electrode [48]. A decline in the corrosion rate over time described by Stonehart and several others is shown to proceed at initiation sites are attacked initially [19].

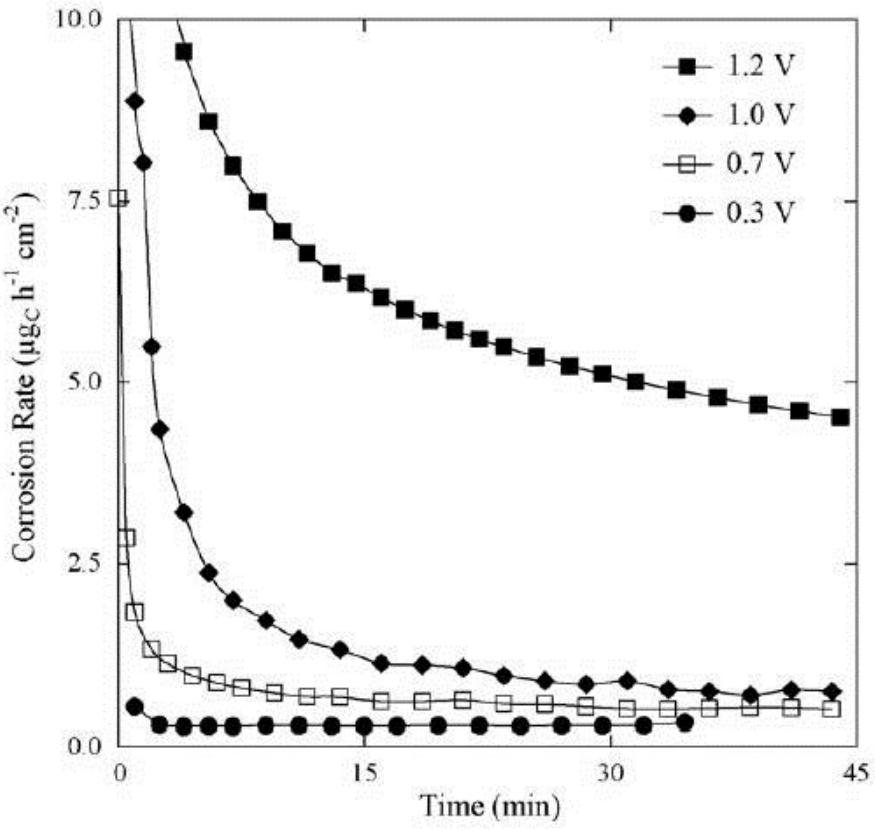

Figure 1.14 Decline of corrosion rate at constant potentials [35].

As platinum diffuses and separates from the carbon support, the area is reduced; this may also account for a diminished corrosion rate at constant V [35]. When the two materials are no longer coupled, the synergistic effect no longer exists. It is known that the low pH also leads to enhanced corrosion although this effect has not been well studied other than the use of half-cell simulations with acid electrolyte at fixed concentration. In the PEM fuel cell, dissociated protons diffusing through the polymer electrolyte create this added acidity. However, as carbon oxides are formed, they can complex protons in the electrolyte and can contribute to the corrosion by altering pH:

(8) $CO_2 + H_2O \rightarrow 2\ H^+ + CO_3^{2-}$

where $pH = pK_{a_1} + \log\frac{[HCO_3^-]}{[CO_2]}$ and pK_{a_1}= 6.35 at STP [49]

Carbon has a [He] $2s^2\ 2p^2$ electron configuration and the inorganic carbons formed by overlapping π bonds or hybridized sp^2 carbons are those applicable to electrode supports. The covalent bonding patterns and degree of order determine the structure. The structure of the carbon will establish its properties. The desirable properties of carbon which make it attractive to this purpose are varied. Carbon materials can offer high surface-to-volume ratio which enhances reactant diffusion and adsorption. It also offers good electron conductivity, chemical stability, weight, and cost [37]. Recent developments in long range ordering have provided new advantages for graphitic carbons. Specifically, nanostructured materials have presented several important benefits over activated carbons and carbon black. The long-range graphitic behavior of graphene

and carbon nanotubes has shown the most promise in regard to corrosion resistance of viable carbon supports.

The structure and properties of the carbon play a significant role in these reactions. Amorphous carbons with only short range ordering show poor corrosion resistance in comparison. Electrochemical degradation is slowed significantly by carbon graphitization. Graphite is composed of sp^2 carbon atoms bonded with three neighboring carbons in planar hexagonal rings also referred to as graphene sheets. These graphitized carbons show greater hydrophobicity and lower oxygen adsorption which also correlates with corrosion resistance. Corrosion is preferred at surface defects and disorder in the carbon lattice [37]. The process can also start at edges and corners of basal planes where free electrons are present [35]. These sites offer lower activation energy of electron transfer and surface oxide formation. This hydrophilic nature of the catalyst layer is more susceptible to corrosion for these reasons and can also create transport problems if it causes water to accumulate in the electrode.

One of the best ways to enhance fuel cell performance is through maximizing the utilization of Pt catalyst. This requires homogeneous dispersion of small well bonded Pt nanoparticles. The effect of oxidative pre-treatment of carbon has been shown to greatly improve this requirement. The benefit of this procedure was explained by an increase in Pt dispersion with an increase in oxygen surface groups. The oxygen anion groups increased the electronic interaction strength with Pt cations during reduction. The more stable oxygen groups were able to anchor Pt during the sintering treatment and prevent agglomeration [50]. There may be some advantages to these defects in catalyst utilization

by deposition of small well dispersed particles at these negatively charged sites, but this review will focus on factors influencing corrosion.

Recently, carbon nanotubes and graphitic ordered porous carbons have gained enormous popularity as support materials for electrocatalysts because of their surfaces and stability. Experimental evidence has demonstrated improved corrosion resistance in graphitized supports. For example, it was shown that when Vulcan XC-72 was graphitized in reducing furnace at 2973 K an oxidative test showed a one third reduction in normalized surface area [38]. A comparison between XC-72 and multi-walled carbon nanotube supports was completed by Y. Shao et al revealed about twice the resistance to electrochemical oxidation at 1.2 V over 192 hours in 0.5 M H_2SO_4 [51]. The improved results were hypothesized from specific interaction between the carbon and platinum. Carbon nanotubes are essentially rolled-up sheets of graphene so the corrosion resistance is described by a similar mechanism, but the nanotubes may enhance Pt-C bonding. It is supposed that the π electron orbital has greater exposure based on the tube curvature. Ordered porous carbons can have tailored diffusive properties with reports showing high utilization of nanoparticle surfaces and high mass activities [52]. Those with layered orientations of their graphene planes formed conductivities higher than some metals. The carbon nanotubes have varying degrees of conductivity based upon their conformation. The transport of reactants through carbon structured supports is critical to their application. A further discussion on carbon microstructure and property is not included, but can be inferred from the allotropes of carbon in the graphic below.

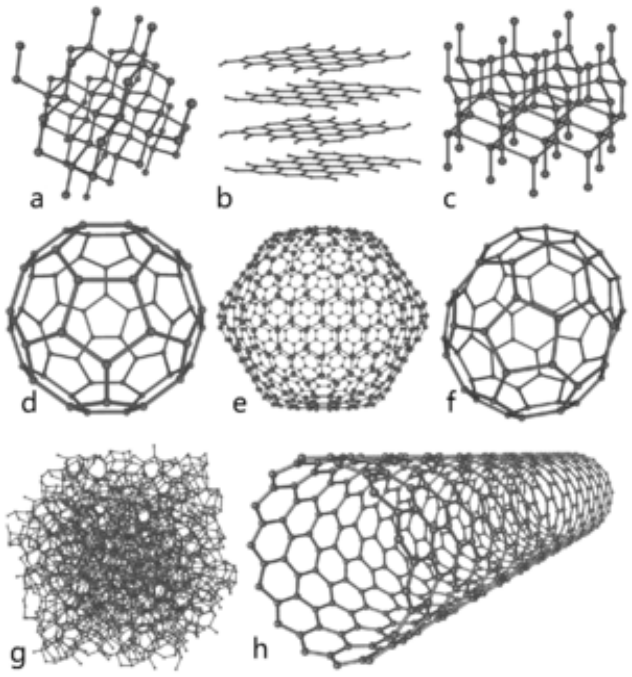

Figure 1.15 C allotropes (a) diamond (b) graphite (d) C_{60} (g) carbon black (h) CNT
Source: http://en.wikipedia.org/wiki/carbon

The corrosion of Pt/C in PEMFC must first be understood by the individual nature of the materials, but it is the presence of Pt catalysts on carbon which actually accelerate the corrosion reaction. The synergistic effect of the two materials is critical to comprehension of the overall corrosion mechanism. Pt nanoparticles can be deposited on to carbon by a variety of techniques from the gas or liquid phase and form very effective electrodes. The most prevalent methods for fuel cell electrocatalyst synthesis are from the liquid phase and include impregnation, colloidal synthesis, and electrodeposition. The optimal preparation of nanometer sized (~ 3 nm) Pt crystallites has been found for ORR [39]. Ideally, a small mass of Pt with high surface area and electrochemical utilization will be achieved. The Pt nanoparticles have been shown to catalyze the oxidation of carbon materials in many studies as indicated previously by reactions 6 and

7. Lower energy intermediate states in the carbon oxidation pathway facilitate the corrosion of the support by the catalyst presence.

The regions of chemical interactions in the vicinity of the metal and support exhibit the greatest corrosion due to the formation of reactive oxygen radical species on the Pt surface. In a simulated study of carbon corrosions, a pure glassy carbon electrode can be compared to one decorated with catalysts similar to model structures prepared by Goeke et al. [53]. Monitoring CO_x reaction products by non-dispersive infrared (NDIR) spectroscopy, revealed no CO evolution in the Pt/C electrode. The results indicated that CO adsorbed strongly onto the Pt surface, and was oxidized at 0.55 V to CO_2 above this potential at typical operating temperature [35]. A similar experiment was performed by measurement of CO_x products with mass spectrometry under cycling of electrodes with varied Pt loadings. A relationship with higher Pt loading and CO_2 peak intensity confirmed more rapid generation and an Arrhenius plot of E_A was significantly lowered by this junction [54]. The interaction between Pt and carbon supports is of great importance when studying their corrosion.

Metal-support interfaces are best described by Pt bonding to carbon by different Fermi energy levels and electron donation from the carbon support to Pt [55]. This bonding nature has been revealed by ESR and XPS [56]. Electronic modifications of the metal by electron donating supports like graphite have been identified by a technique coupling infrared spectroscopy with carbon monoxide sorption calorimetry measurement. It also permitted an identification of the type, number, strength, and energy distribution of the surface sites on the catalyst as a function of the metallic interaction with the catalyst support [57]. Enhancing the interaction through strong anchoring sites improves the

catalytic properties by bond disorder in the adsorbed metal clusters. The presence of acidic oxygen containing groups on carbon is believed to hinder electrocatalytic activity for reduction while basic nitrogen functionalized carbons helped the cathode performance [58]. The carbon support also can have a beneficial effect on shifting the d-band energy center for platinum [59, 60]. However, the bond interaction between Pt and carbon is weak despite increased strength by carbon surface oxidation and other functionalization techniques. This ultimately contributes in large part to the enhanced dissolution between the two materials.

As discussed, there are many factors which accelerate the oxidation of platinum and the corrosion of carbon catalyst supports. The presence of Pt on carbon alone is enough to accelerate the reaction. Corrosion testing has been exemplified in the laboratory by a number of different experimental setups.

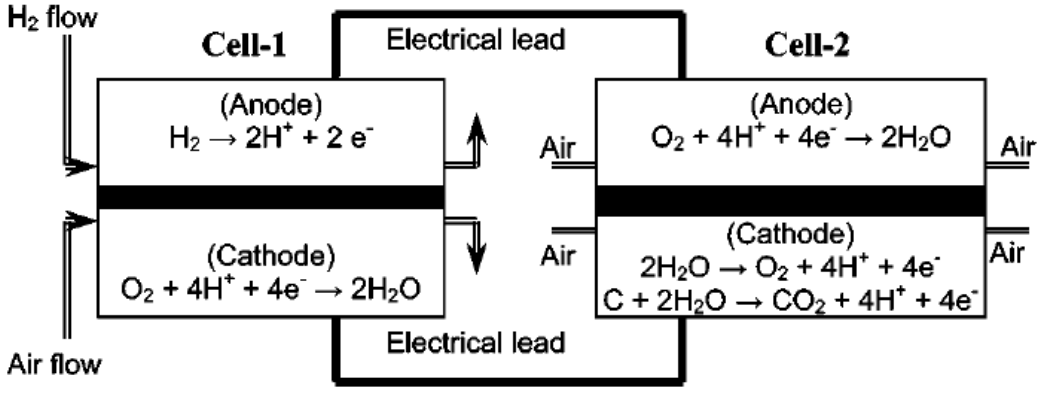

Figure 1.16 Dual cell setup simulates reversal and H_2/air front [31]

The locally starved H_2 condition is the most widely accepted culprit of rapid carbon corrosion. Jarvi and co-workers were able to simulate cell-reversal conditions in controlled manner by using two separate cells with controlled atmospheric conditions

[31]. Similar experimental setups were also completed by other groups which measured potentials about twice as high as OCV from the air/fuel boundary [61]. A cell reversal set-up to simulate stack operation and low fuel stoichiometry was tested to gain insight into fuel supply problems. Measurements showed severe cathode corrosion and reduction of Pt surface area with local effects also observed by a segmented cathode while coupled EIS was used to observe changes in electrode resistance [34]. In another simulation, a region of the anode was blocked with a hot pressed pieced of polyethylene film on to the electrode active area [12]. This "blocked" condition persists under many different real circumstances when the anode is not completely filled with H_2 like start-stop cycles, flooding, gas crossover, improper thawing after freeze, and other methods causing the reverse-current phenomena to proceed [32].

Other accelerated tests at constant potential did show some interesting corrosion phenomena. A constant potential hold test at 1.2 V compared low surface area to high surface area carbon black (BP 2000 vs. Vulcan XC-72) at the same platinum loading and their relative corrosion rates. The XC-72 corroded faster which was thought to be a result of the higher degree of platinum coverage per unit mass of carbon despite a lower physical surface area. The test was completed in the presence of dry and humidified air. In the presence of humidity, the corrosion increased substantially in both types of carbon as measured by mass loss [62]. When the Black Pearls 2000 was graphitized at 3000 °C, it still had larger surface area than XC-72, but the thermal stability was greatly enhanced. Another study on the XC-72 support, which is often used as an industry benchmark and baseline for comparison, measured the formation of various oxygen functional groups on carbon and the change in wettability by sessile drop method; the transformation towards a

more hydrophilic nature with oxidation is known to change water transport and lead to unstable performance [63]. Surface attraction and repulsion to water is a condition which is not easy to model because it is an electronic scale phenomenon, but it has been determined empirically to relate with corrosion rate. Expedited degradation has also been known to happen around the edges of the electrocatalyst. An experiment to study regions of cathode overlap was performed and modeled to show degradation by a similar mechanism to that of a constant high potential at OCV. This experiment also showed slightly enhanced carbon corrosion at low RH which the model couldn't account for [64]. The relative humidity is necessary to facilitate charge transfer in the ionomer, but it also serves as a factor in corrosion and mass transport and its effects are difficult to simplify.

There have only been a limited number of studies on the effect of humidified gases on carbon corrosion. A water activity dependent carbon corrosion mechanism was proposed to account for the RH effect and was verified experimentally in a cell reversal experiment by Du et al [65]. When an air/air cell was held at open circuit in a dry condition, the active area of the cathode was gone in 3 hours and microscopy showed complete disintegration of the cathode and even damage to the backing layer. In the first 15 minutes, the cell potential climbed to 1 V when current density was held at 0.002 A/cm^2, then as all the water was consumed, the OER overpotential increased. The relative contribution of the COR increases as the activity or concentration of water is reduced. In summary, the presence of MEAs exposed to low RH for an extensive period of time, as in the case of a hot stop, were found to experience unusually high cell voltage decay as a result of accelerated cathode carbon corrosion. This work shows a reverse-current mechanism could be sustained for a finite time at higher humidity without

suffering unrecoverable damage to the cathode. Dry starts and stops have been inferred as especially detrimental.

Besides changing operational conditions of the fuel cell, the effect of carbon microstructure has shown promise for its corrosion resistance. It was noted that graphitic carbon held some important advantages over more disordered carbon and a report by Cherstiouk et al. was published to validate the quantification of this effect and further elucidate this connection [40]. It was found that corrosion currents scale with specific carbon surface area so current densities normalized to surface area were used to compare filamentous carbon, Sibunit carbons, and carbon blacks. The carbon filament structures showed the lowest corrosion rates. They also verified the use of a substructural parameter that was calculated from the proportion of 3-D to 2-D ordering and the number of graphene layers in a crystal. Thus, the value was an approximation of the carbon fraction at layer boundaries. The experimental results proved that corrosion propagates from these boundaries and they reaffirmed the $t^{-0.5}$ dependence on corrosion rate. Their work also promoted the motivation for more work on ordered porous carbons of the Sibunit family which possesses high crystallinity. Another report made a similar comparison between multi-walled carbon nanotubes with variable diameters and the XC-72 supports. They found the diameter of tubes had little measurable effect, but compared to XC-72, a major improvement could be confirmed [66]. The nanotubes were also hydrogen annealed to remove surface defects and further improve corrosion resistance. Another recent study showed that carbon nanotubes grown directly on a gas diffusion media with sputter coated Pt layer could offer effective fuel cell performance, but also showed improved durability in comparison to the XC-72 supports [67]. A systematic

study revealed a similar result for multi-wall carbon nanotubes when compared to the commercial Vulcan carbon black as shown in Figure 1.17 [68]. Pt deposited on to graphitic carbons, especially carbon nanotubes have shown as much promise as any combination of carbon and Pt.

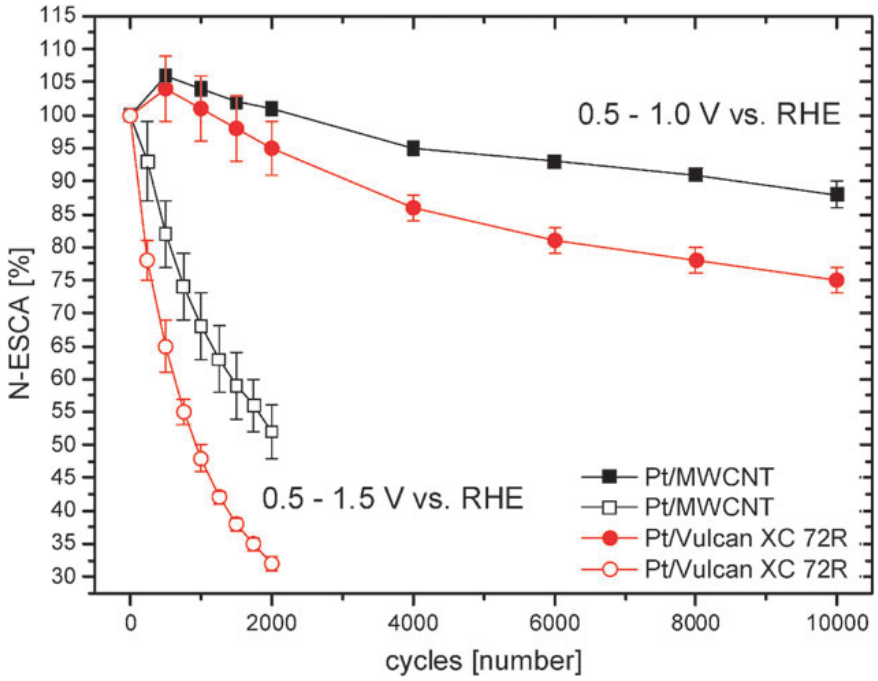

Figure 1.17 Comparison CV Plots from Pt/C (red) and Pt/CNT (black) [68]

Most studies have found a strong relationship between the loss of Pt surface area and the corrosion current. The catalytic activity of Pt is also affected by the particle size in non-linear relationship because it is well known that nano-sized Pt has higher activity than larger Pt particles [69]. In electrocatalysts, the Pt was observed to grow to a critical size before carbon oxidation became the primary corrosion mechanism [68]. For example, Pt foil is very stable, but Pt-catalyst nanoparticles can promote spontaneous combustion of fuel at room temperature. Although not discussed in this report, it is well documented that Pt-alloys can have many benefits over Pt that includes higher tolerance to impurities

and higher catalytic activities, but their corrosion resistance may also be another benefit. In the latter case, the alloyed metal will serve as the sacrificial anodic metal. PtCo alloy catalysts which demonstrated better bonding to the carbon support also resisted agglomeration and diffusion into the ionomer under real operating conditions at constant current [16].

Smaller catalysts particles are more active because they have a higher concentration of surface active sites and greater specific activity although there stability is a greater concern. An X-ray absorption spectroscopy technique was employed to understand the difference in catalytic activity of Pt nanoparticle versus bulk platinum. The authors were able to study the variation of the electronic and local structures of nanometer Pt during a potential cycling test. A decrease in the bonding distance between Pt-Pt bonds of the nanometer Pt catalysts, especially those under 3 nm was found. However, catalysts under about ~4 nm diameter are generally characterized as too unstable for the cathode environment as evaluated by *in-situ* small angle X-ray spectroscopy [70, 71]. Many studies of electrocatalyst degradation have also used an XRD technique to measure the change in Pt crystal size like those shown in Figure 1.18. Ferreira et al. used this material characterization tool to study the Pt growth during potential cycling as seen below.

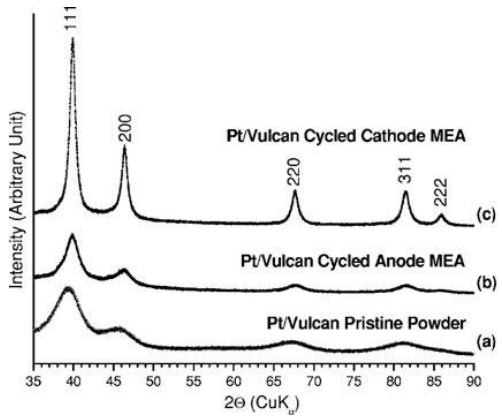

Table I. The average size of platinum crystals in pristine and cycled Pt/Vulcan samples estimated from the $\{111\}_{Pt}$, $\{200\}_{Pt}$, and the $\{220\}_{Pt}$ peaks using the Scherrer equation.

Sample description	Pt crystal size (nm) $\{111\}_{Pt}$	Pt crystal size (nm) $\{200\}_{Pt}$	Pt crystal size (nm) $\{220\}_{Pt}$	Average Pt crystal size (nm)
Pt/Vulcan pristine powder	2.3	2.3	2.3	2.3
Pt/Vulcan cycled anode MEA	4.2	3.6	4.0	3.9
Pt/Vulcan cycled cathode MEA	10.5	10.6	10.3	10.5

Figure 1.18 XRD analysis of catalysts and Pt crystal size

ECSA loss is typically measured by electrochemical methods like cyclic voltammetry and the integration of the H_2 sorption peaks. The specific surface area decreased from 63 to 27 $\frac{m^2}{g_{Pt}}$ after 1000 hours of cycling [6].

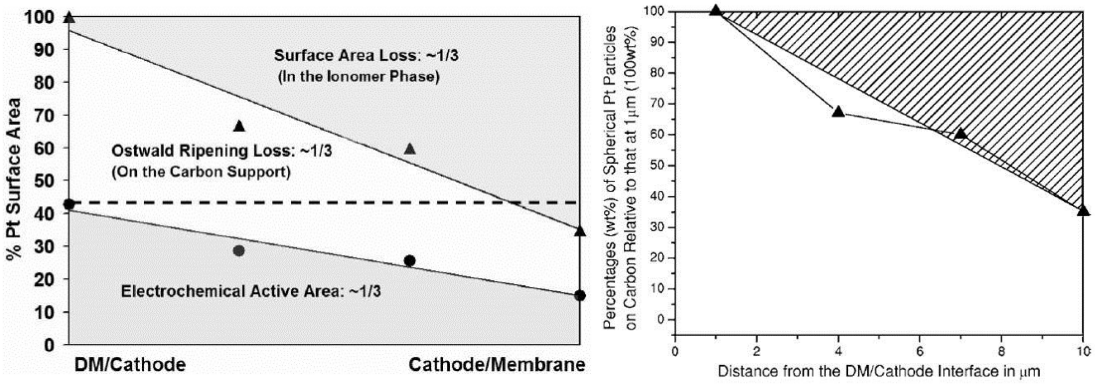

Figure 1.19 Loss of Pt profile from diffusion media electrolyte interface [6]

The platinum surface area loss near to the diffusion media (DM) interface is primarily due to Ostwald ripening, while the loss at the other electrolyte side has greater contribution from crossover hydrogen that precipitates the Pt^{2+} cation in the ionomer. This ultimately leads to a chemical attack of the polymer and the loss of mechanical properties. This problem originates from the corrosion of the catalysts and is a major

cause of fuel cell performance and failure. Preventing corrosion of the cathode in PEMFC has been a high priority in current fuel cell research and development efforts.

It has been suggested throughout this review that there are effective strategies to mitigate electrocatalyst corrosion by improving the material properties and operational conditions of the PEMFC. Optimal operating currents and stable electrical loads could be drawn to prevent the cell from reaching extreme potentials where corrosion reactions can be accelerated. Electrically shorting the fuel/air boundary to prevent the reverse current mechanism is also effective. Another approach could use hydrogen cathode inundation to prevent corrosion by converting the fuel cell to a hydrogen pump or simply using a thorough inert gas purge before start-up would also be useful [65].

Some of the corrosion effects could also be limited by the material properties of the electrocatalyst. It was shown that Pt catalysts reduce the E_A of the OER. This energy is greater when the Pt becomes disbanded from the carbon support. Some Pt-alloys can enhance this metal-support interaction with carbon. However, this review focused primarily on the state-of-the-art pure Pt only catalysts. Their bonding to carbon is affected by the carbon surface functional groups and the carbon microstructure. Carbon can take a wide variety of structures and properties. Carbon with a higher degree of ordering and lower defect concentration at exposed boundaries provides better corrosion resistance. This is typically indicative of carbon with higher hydrophobicity. However, carbon must have defects where the platinum can bond and transfer charge through the support. Carbon has been the focus of this review because it is the leading commercial choice, but the carbon corrosion in presence of Pt is well documented despite the improvements to carbon microstructure. Finding methods to lower Pt loading by using

better dispersions and increasing mass activity will reduce the effect of Pt-C interaction. Although not previously referenced, there is much new and promising work on the development of alternatives to carbon.

In conclusion, cathode electrocatalyst corrosion in the MEA of PEMFCs is a critical issue to their viability and valuable application. There are methods to inhibit the corrosion and these need to researched and developed further for future progress. Creative ideas are needed for new materials with the desired support properties. Possible composite materials with multiple functionalities may be required. These need to be developed before a true breakthrough can be made.

1.1.3. Metal Oxides

Metal oxides are simply an oxidized form of the metal that results from their electrons becoming shared with oxygen orbitals. Transition metals can range in oxidation state between discrete energy levels that are related to the number of available electrons in the metal valence. Delocalized electrons from the conduction band become occupied by oxygen anions, typically with a -2 oxidation state. Due to its electronegativity, oxygen forms stable chemical bonds with positive metals. A primary advantage of using metal oxides in the catalyst support is from the stability they can provide. However, the electrons localized in oxygen bonds are not capable of carrying charge through the material. Lightly oxidized metals can still conduct some charge, but as the oxidation state of the metal is increased, they become more resistive. The surface of metals becomes oxidized first because it is always exposed to a higher oxygen pressure. Once all available electrons become occupied, the metal is said to be

passivated. Passivated metals can develop a surface oxide boundary that prevents them from further corrosion reactions. Metal oxides can be directly prepared and assume a crystalline arrangement with coordinated oxygen anions around metal cations. Essentially, there is a trade-off between metal conductivity and its oxidation state. This is particularly true at the temperatures used to operate polymer electrolyte cells. In fact, there are only a few metal oxides which can exhibit passivation behavior in the PEMFC environment as represented by the elements in red of the periodic table in Figure 1.20 when predicted for equilibrium behavior at 80 °C and low pH [72]. In this case, metal oxides will be employed for corrosion resistance in addition the strong bond they can form with catalysts.

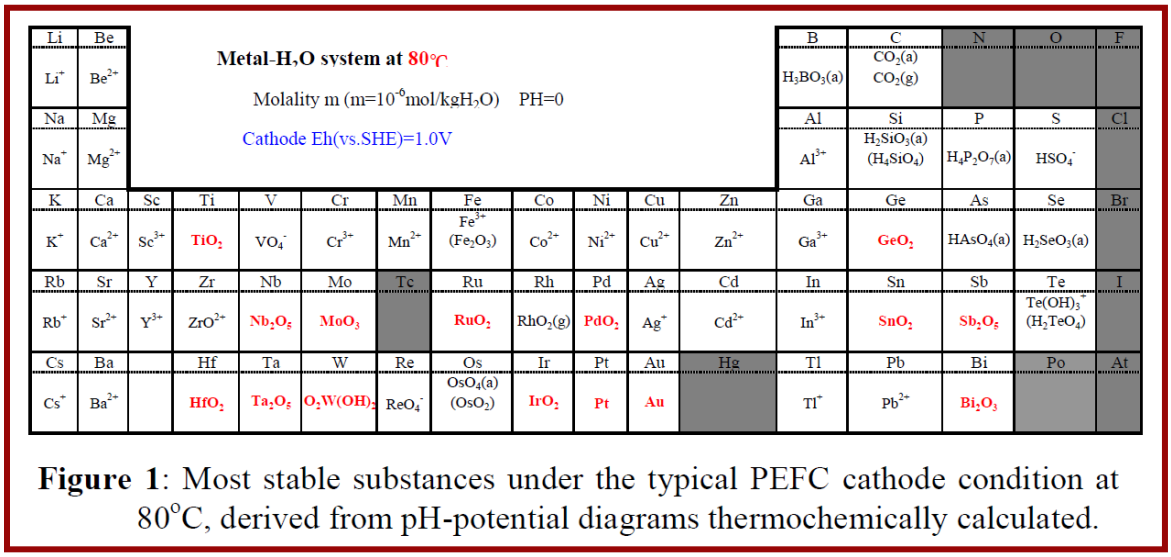

Figure 1.20 Periodic table of stable metal oxide elements [72]

1.1. Metal Oxide and Carbon Composite Supports

Metal oxide materials have garnered a lot of interest from the PEMFC research community. Stability advantages over carbon make these materials more resistant to oxidation when oxygen anion forms stable bonds with the metal. However, oxides alone have had limited success in commercial materials because they are too resistive and typically larger crystals are required for bulk conductivity. Rendering the support properties through a composite approach with more stable phases covering carbon should allow for the synthesis of an effective catalyst support. This is a challenge which lacks validation in working fuel cells, but the number of publications on metal oxide supported catalysts has seen exponential growth. These have primarily been conducted in half-cell and RDE tests which don't necessitate highly connected electrodes or an ionomer phase. A bottom-up strategy to build nanostructured metal oxides on carbon framework could provide desired conductive properties and high surface area support for the catalyst.

Titanium dioxide (TiO_2) is the most thermodynamically stable compound of the two atoms in the fuel cell. It exists naturally in three common crystal structures: anatase, brookite, and rutile. The rutile structure has lowest heat of formation -944 kJ [73]. However, evidence suggests that at the nanoscale, the anatase form may actually be more stable [74]. All crystal structures of titanium dioxide are semiconductors with a wide band gap (E_g) ~ 3 eV, though it is dependent on the phase. Titanium is most commonly found in its +4 valence state at STP because of its [Ar] $4s^2 3d^2$ electron configuration. Oxygen has a [He] $2s^2 2p^2$ and a -2 valence electron concentration. Altering the Ti:O stoichiometry can be an effective way to increase the electron carrier concentration and

improve the conductivity. There is a fine balance between adding conductivity and its corrosion resistance.

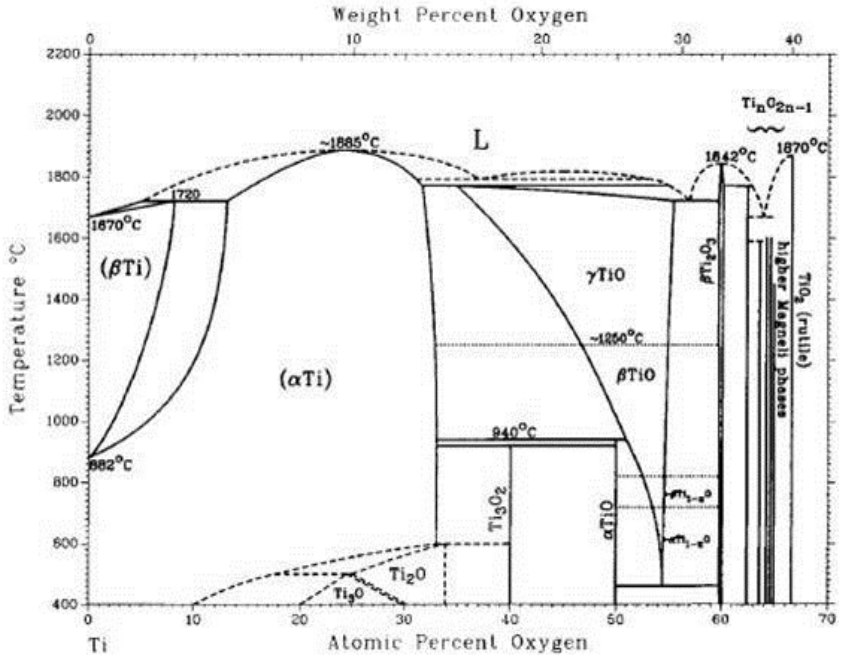

Figure 1.21 Titania phase diagram based on oxygen content and temperature [75]

Titania has exhibited electrical properties from an insulator to a conductor. Titanium dioxide is often classified as a semiconductor despite its wide gap between the valence and conduction bands. The outermost filled orbitals of elemental titanium are $4s^2$ and $3d^2$ and that of oxygen are $2s^2$ and $2p^4$. In TiO_2, the Ti ions are in a distorted octahedral environment and formally have a Ti^{4+} ($3d^0$) electronic configuration. The valence band of TiO_2 is composed primarily of oxygen 2p orbitals hybridized with Ti 3d states, while the conduction band is made up of 3d orbital around titanium. The electrical conduction mechanism is typically n-type and results from excess electrons. Anatase titanium dioxide has the highest insulation capacities and dielectric strength. The band gap value, E_g, for the anatase type is 3.2 eV, for the rutile type is 3.02 eV and for the

brookite type 2.96 eV. Other stoichiometric ratios like TiO, Ti_2O_3, Ti_3O_5, and Ti_4O_7 have resulted in lower band gaps and higher electrical conductivities. Some of the best combinations for stability and conductivity values have been measured in Ti_4O_7. This material is sold commercially by the Atraverda Corporation and known as Ebonex® with resistivity as low as 10^{-3} Ω·cm at 298 K [75]. More generally, these are known as Magnéli phases with chemical formula T_nO_{2n-1} (where n is between 4 and 10) [76]. They are formed at high temperatures under low oxygen atmosphere. Magnéli phases and other sub-stoichiometric ratios are stable, have good corrosion resistance, and are often used in acidic environments, including electrode applications in the literature dating back to 1990 and even earlier.

TABLE I. Crystal structure data of TiO_2.

	Rutile[a]	Anatase[a]	Brookite[b]
Crystal structure	tetragonal	tetragonal	orthorhombic
Lattice constants (Å)	a=4.5936	a=3.784	a=9.184
	c=2.9587	c=9.515	b=5.447
			c=5.145
Space group	$P4_2/mnm$	$I4_1/amd$	$Pbca$
Molecule/cell	2	4	8
Volume/molecule (Å^3)	31.2160	34.061	32.172
Density (g/cm^3)	4.13	3.79	3.99
Ti—O bond length	1.949(4)	1.937(4)	1.87～2.04
(Å)	1.980(2)	1.965(2)	
O—Ti—O bond angle	81.2°	77.7°	77.0°～105°
	90.0°	92.6°	

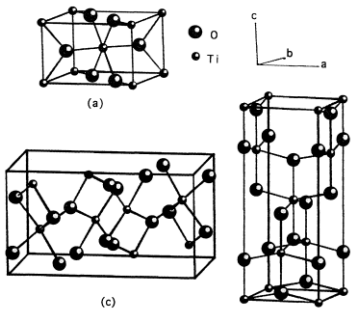

FIG. 1. Crystal structures of TiO_2. (a) Rutile. (b) Anatase. (c) Brookite.

Figure 1.22 Crystal structures of titanium dioxide [77]

The resistivity of TiO_2 is as high as high as $10^{12\text{-}13}$ Ω·cm at 298 K [77, 78]. Reduced Magnéli phases with low resistivity have been prepared and tested as catalyst supports [79-81]. However, they had several detractive properties which make them unsuitable for application to PEMFC. They have some corrosion resistance in acidic environments, but could be further oxidized to TiO_2 at higher potentials [82]. Also, the high temperature required for synthesis of Magnéli phases give them very low surface

areas ~1 m^2/g. Other preparation techniques to form composites will likely be necessary to construct suitable conductive supports that can be applied effectively in electrodes.

The electronic configuration of a material is closely related to its thermal and optical properties. Titanium dioxide, like other ceramics, has relatively low thermal conductivity because of the lack of free electrons. The rutile crystal demonstrated an average thermal conductivity of 11 W/(°C·m) between the 100 °C to 800 °C range. The conductivity for anatase was 17 W/(°C·m) for the same range. The rutile form has a thermal coefficient of expansion of approximately 8 x 10^{-6}/°C in the temperature range 0 to 1000 °C while anatase is slightly higher at 9 x 10^{-6} [83]. Rutile has the specific heat capacity of 418 J/mole °C at 20 °C where $c_p = 75.19 + 1.17T + -18.20T^{-2}$ J/mole·K [73]. The Debye temperature was found to be 187 °C, where below this value the temperature dependence can be related to the specific heat capacity [77]. The values for anatase are similar, but the specific heat would be slightly lower because of the lattice structure and greater atomic spacing between Ti atoms. It should be noted that the thermal properties are greatly affected by defects in the structure and the resultant free electrons will also change the electrical properties as well. The refractive index of a material, $n = (\varepsilon_r \times \mu_r)^{0.5}$, can be quantified by its dielectric strength.

TABLE V. Calculated static dielectric constants of TiO_2.

	Rutile			Anatase	Brookite
Static dielectric constant $\varepsilon(0)$					
Calc. (present)	6.62			6.04	7.89
Experiment	6.33[a]			5.62[a]	
Components:					
$\varepsilon_x(0)$					8.34
$\varepsilon_y(0)$					7.21
$\varepsilon_{x-y}(0)$	6.46,	6.4,[b]	5.80[c]	5.99	
$\varepsilon_z(0)$	6.95,	7.3,[b]	7.07[c]	6.13	8.13

Figure 1.23 Dielectric constants of TiO_2 crystals and orientations [77]

It is observed that the static dielectric strength, or the permittivity at 0 K, varies with lattice direction and is highest in the z direction for rutile and anatase which is parallel to the c lattice parameter. Relative permittivity, ε_r, can be calculated from static permittivity, ε_s, divided by the permittivity of a vacuum, ε_o. Refractive index is also based upon the relative permeability of the material which is found $1.1 < \mu_r < 1.2$ [77, 84]. This gives titanium dioxide a refractive index of 2.5 - 2.9. This is one of the highest known indices for all materials and its brightest white comes from ability to refract visible light when particle size is optimized to about half its wavelength (200~350 nm). The bright white material is commonly used as a pigment in make-up, paint, food coloring, dyes, textiles, and many other purposes requiring an opaque dispersion of the visible electromagnetic spectrum. However, its optical properties vary depending on the nature of crystal and defects found within it.

The high dielectric constant of titania gives result to its widespread use in capacitive devices and other related technical applications. In fact, titanium dioxide was used in capacitors in some of the original televisions and radios because it was critical to

store high charges in small volumes in these devices [85]. In modern applications, they have found uses in gate insulators in MOSFETs where it is critical to maintain high oxide capacitance while making thinner layers that can prevent leakage current from electron tunneling [86]. In wavelengths shorter than visible, the material exhibits strong absorbance. Photons with energy greater than the band gap, $E_{h\upsilon} > E_g$, can excite an electron from valence band to the conduction band. This phenomenon is of primary importance for applications in photocatalysis and photovoltaics. Free electrons on the surface bond with H_2O and can electrolyze the splitting of water molecules. This process can also form reactive intermediates like ·OH radicals which have very high oxidative potential. This field of research has produced the greatest number of journal articles on the material in recent times. Below are some schematics of how titania is used in photocatalysis and photovoltaics.

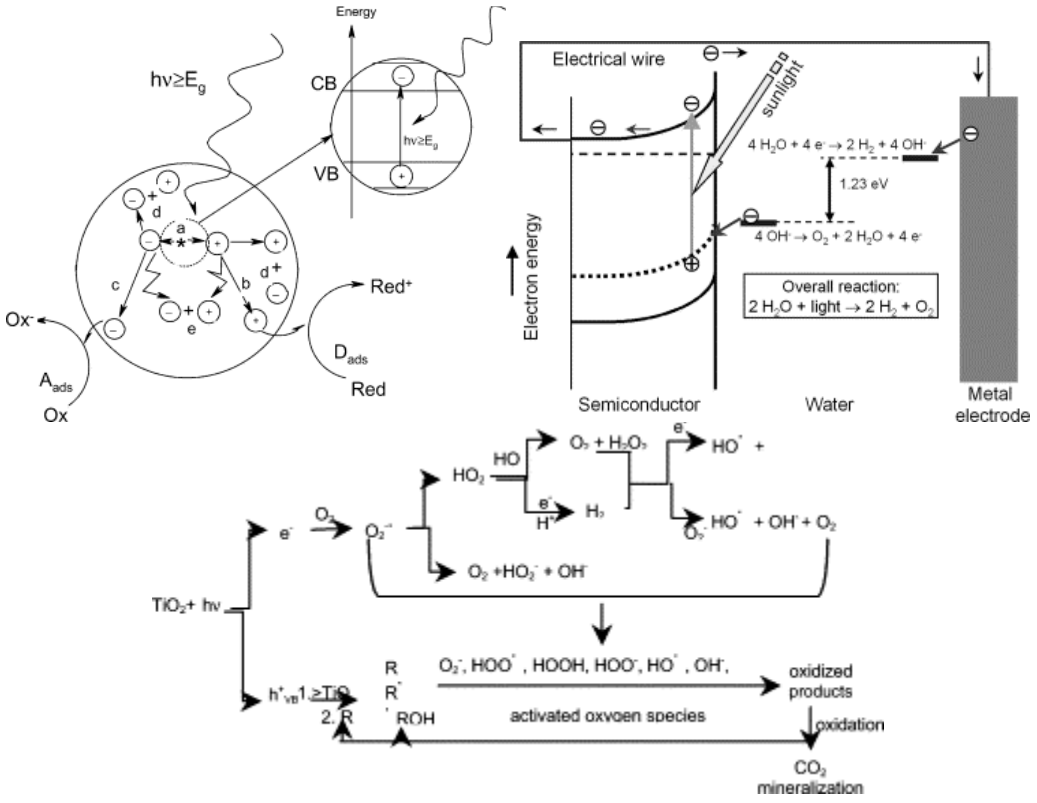

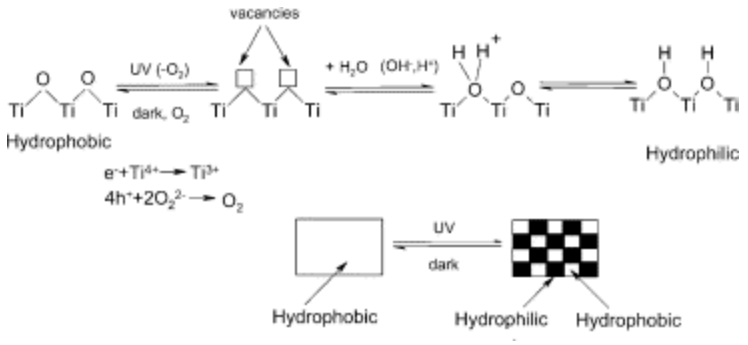

Figure 1.24 Schematic of reactions utilizing titania photocatalysts [87]

Many efforts have been made to alter the electrical properties of titania by doping it with transition metals and anions, coating it with quantum dots, introducing defects, and formation of titania composites. Most of the pioneering work was done to enhance photoresponse to perform more efficient redox reactions when excited by photons of lower energy in the visible region, for example. The new materials have demonstrated many different effects and properties of charge transfer, electron-hole recombination rates, lower band gap(s), adsorption capacity, morphology, phase stability, intermetallic and interionic bonding, and more. It is out of the scope of this review to discuss in detail all these effects. Some interesting results from the metal coating of titania with Group VIIIB metals like platinum, the doping of titania with some Group V transition metals like niobium, and carbon modified titania as well as carbon-titania supports will be investigated. When platinum is reduced on n-type titania semiconductors, a Schottky junction can be formed. This results from the energy band bending and alignment of Fermi levels. Metals with low work functions like platinum can cause electrons to accumulate at the interface of titania due to a barrier formed between the two materials. When electrons are excited in the oxide and they can cross the barrier into conductive metal, recombination is prevented with a reactive electron hole left behind. The

separation of charge may be influential in the role of metal oxide supported catalysts used in the electrode. In fact, the electrochemical potential can control its reactivity by a similar way to stimulation of photochemical reactions as was famously reported by Honda and Fujishima [88].

Quite possibly, the most attractive advantage of titania based supports is the strong bond they form with Pt catalyst nanocrystals. Some surface cations in oxides can be reduced to lower states which facilitate a strong metal-support interaction (SMSI) with group VIII noble metals like Pt when supported on TiO_2, a term notoriously dubbed by S. J. Tauster [89]. Pt particles on the surface of oxides formed a strong bond and appeared as flattened "raft-like particles" to Tauster. An intermetallic interaction exists between reduced Ti atoms and the noble metals on their surface. Later, it was discovered that actually the Ti cations from the oxide had diffused around its surfaces and physically encapsulated catalysts. A scanning tunneling microscopy observation of encapsulated SMSI catalysts was compared with those heat treated in air and their morphology was compared; the oxidation state of titania in the support plays a critical role in CO oxidation [90, 91]. Bonnani et al. also realized the encapsulation was at least semi-reversible and dependent upon preparation conditions. In any case, it may be comprehensive to study SMSI from the perspective of electron band diagrams and the resulting junctions formed, such as the Schottky type which has also been used in other supported heterogeneous catalysts [92]. The study of these junctions has been very important to the development of engineering of almost all electronic circuits, for example. It would be a remarkable achievement if this depth of understanding in electrochemical potential could advance

electrocatalyst design for fuel cells and related technology to new levels that generate widespread success in its commercial adoption.

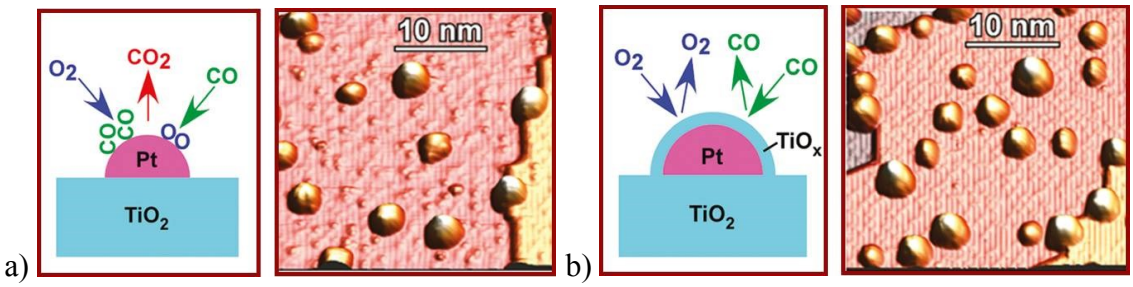

Figure 1.25 Pt-TiO_2 supported catalysts a) ideal CO oxidation b) encapsulated Pt [90]

Tauster first published his findings in 1978, but added the electron micrograph of Figure 1.26 in afterwards in a later publication which extended these phenomena to other oxides from the left side of the transition metal series. A molecular orbital study by his colleague at Exxon followed in 1978 to explain how reduced transition metal oxides could transfer an electron from metallic Pt with a nearly full d-orbital [93]. The intermetallic bonding theories and correlations of Brewer, Friedel, and Miedema also predict a thermodynamic relationship between metals having half-filled vacant d-orbitals bonded to metal atoms having full or nearly full d-orbitals [94]. A lot of literature on this topic exists with varying descriptions about the interaction; however, a simplified understanding was offered by John Robertson in 2010 when he related the mechanism of electronic charge compensation, metal induced gap states, and defect reactions on semiconductors by his description of electronegative transition metals from the right side of the series deposited on electropositive metal oxides from the left side [95]. In any case, these intermetallic interactions are much stronger than those directly between carbon and platinum and could serve to anchor the catalyst and prevent dissolution.

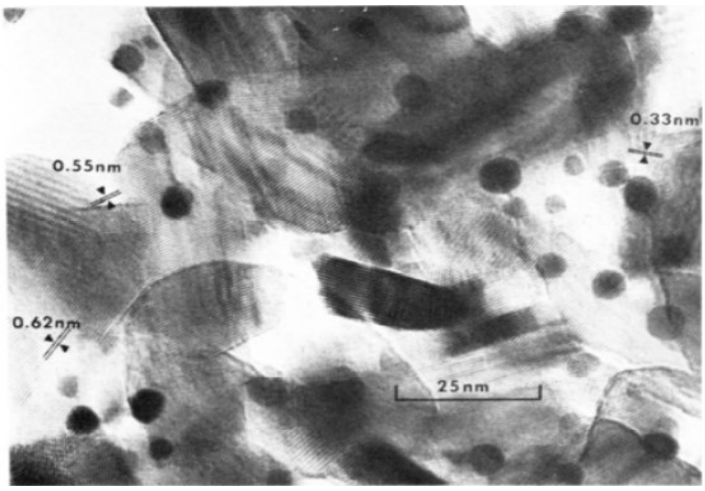

Figure 1.26 Electron micrograph of SMSI from Pt on titania [96]

Titanium oxides, or titania, are a promising electrocatalyst support candidate for several reasons. One benefit of this material is it can offer high surface areas through the creation of porous microstructures. Titanium dioxide has a high melting point near 1870 °C and this provides a large undercooling window to form smaller critical radii (r*) where $r^* \alpha 1/\Delta T$ [97, 98]. This property also allows for titania to form many interesting nanostructures with large available surfaces. Titanium precursors are typically dissolved in a complexing solution before being bonded to carbon in order to control the material nanostructure over larger scales and other substrates. Many interesting designs can result from titania composites which are often applied to maximize their surfaces. Some common synthesis procedures use a colloidal suspension or sol-gel preparation combined with a templating agent like an organic surfactant, polysterene spheres, or silica opal particles. These are then evaporated during calcination or etched away with a strong acid and become a sacrificial template. This leaves behind highly ordered pores with

controlled dimensions. Many interesting nanostructures have been prepared for a wide range of applications.

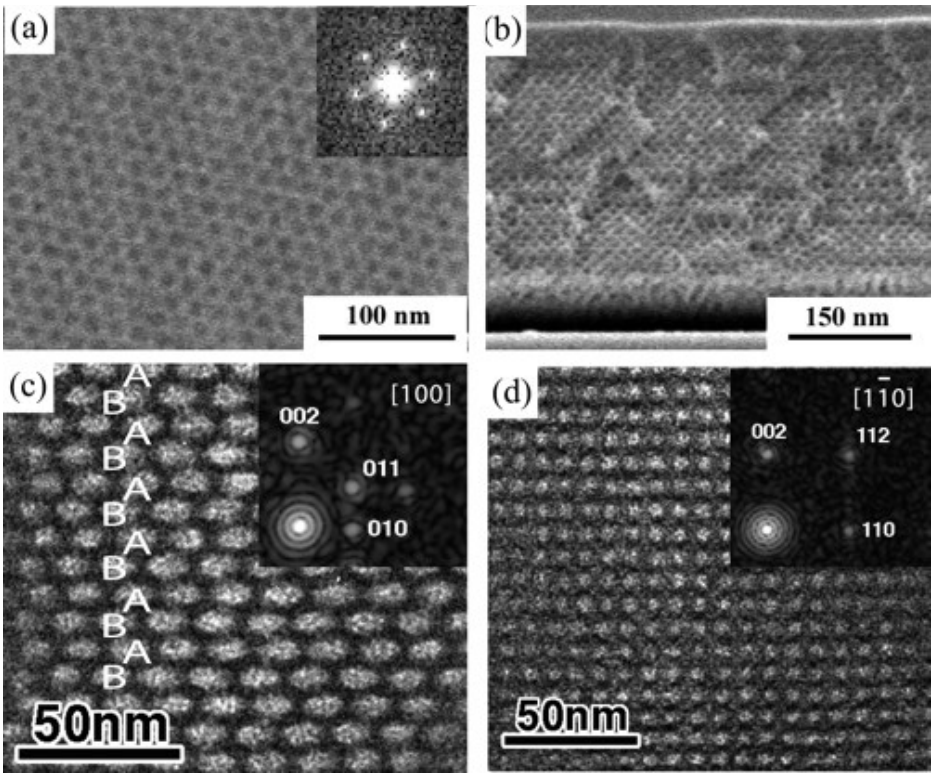

Figure 1.27 Preparation effects from templating agents on pore distribution [99]

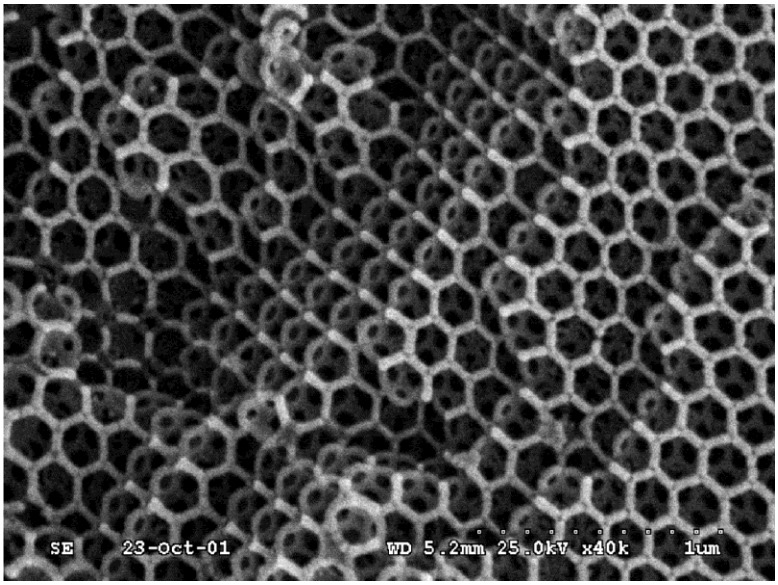

Figure 1.28 Skeletal inverse opal structure after removal of pore former [100]

Titania supported Pt catalysts have been investigated as early as 1986 for phosphoric acid fuel cells and other oxide supports have also been used as electrodes in solid oxide fuel cells, but this review will focus on their application to PEMFCs and their benefit to low temperature electrocatalysis [59, 101]. Most titania catalyst supports with stoichiometric values near TiO_2 have negligible catalytic activity for ORR without addition of Pt or Pt/C to electrodes when studied by several half-cell reactions [102, 103]. However, these tests do not necessarily require highly conductive catalyst supports and resistive values, including oxide capacitance, are often corrected from activity calculations. Some of these compositions have also tested actual Pt/TiO_2 electrocatalysts in real fuel cell conditions and achieved results which are nearing those of commercially available Pt/C products [104]. In 2009, some of the best published results to date demonstrate that Pt/TiO_2 performance may rival that of Pt/C electrocatalysts while also possessing markedly better durability in accelerated testing conditions [105].

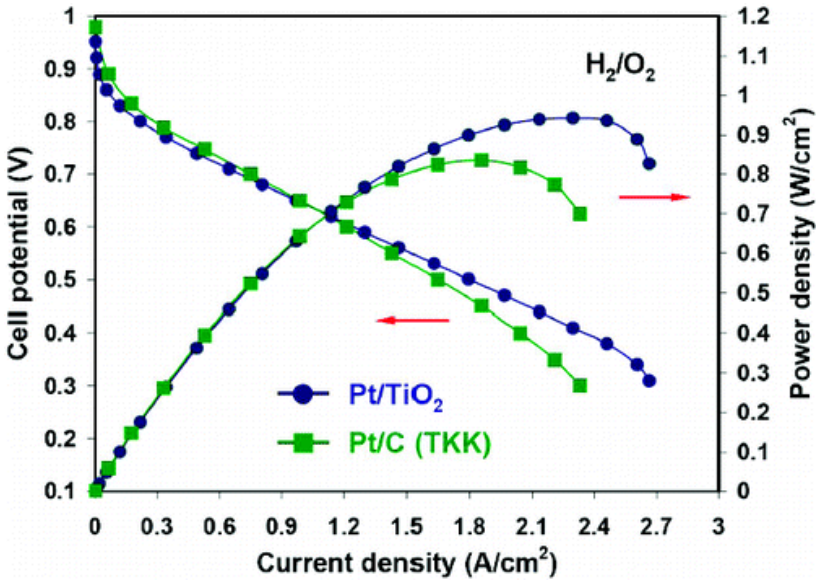

Figure 1.29 A Pt catalyst supported on TiO_2 shows stability benefits in fuel cell [105]

This electrocatalyst used a very high Pt mass fraction and used added conductive filler materials in the electrode. These electrodes are known to have transport and flooding issues. Very little processing detail was revealed in this communication, however. Nevertheless, the most obvious benefit of Pt/TiO_2 electrocatalysts is the improved resistance to corrosion as seen in Figure 1.30.

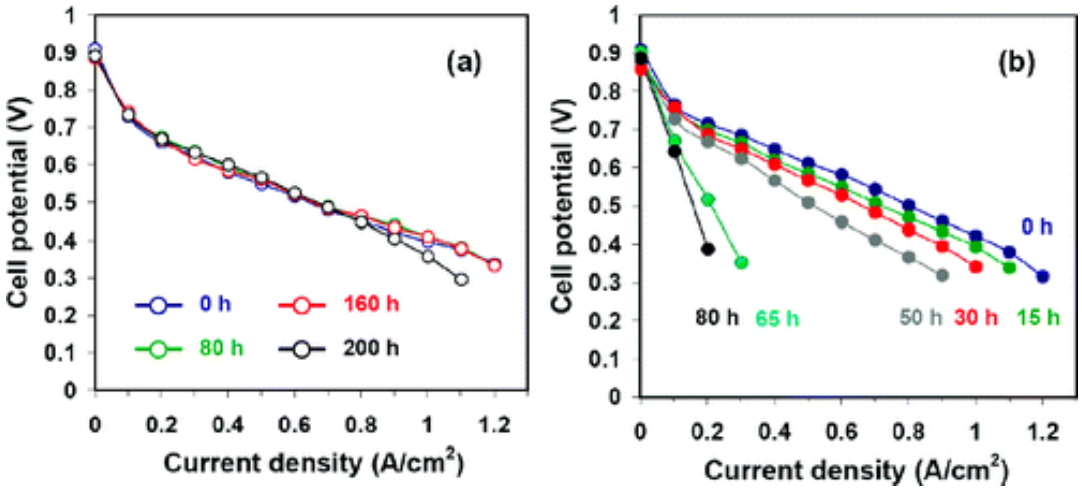

Figure 1.30 (a) Pt/TiO_2 electrocatalysts show very stable performance in 1.2 V hold and (b) Pt/C is quickly degraded in comparison to Pt/TiO_2 [105]

Some research groups have attempted to simply mix titania with carbon to form a more conductive composite support with limited success. $Pt/C+TiO_2$ materials were investigated for fuel cell performance and Pt was deposited on carbon black then titania was added by hydrolysis and its durability rivaled the commercial Pt/C in a real PEMFC during cyclic voltammetry degradation tests, but did not improve cell performance or catalyst activity [106]. A TiO_2 and carbon black slurry mixture were used as support and impregnated with Pt which showed good resistance to Pt migration and agglomeration in ORR [107]. S. von Kraemer published a similar concept from Pt deposition on

commercially purchased titania mixed ultrasonically with carbon black that also yielded a similar result [108]. However, the mixture of carbon and TiO_2 has likely not offered the optimum performance improvement due to the lack of material synthesis control and the structural ordering required for the dual benefit. Engineering the interface between the metal and metal oxide should not be overlooked in the use of titania for electrocatalyst composites. This interface could be an important source of the synergy between activity and stability.

The concept of altering the band gap in titania by doping the material to shift the Fermi level E_F may provide one mechanism to improve its conductivity in addition to its role in catalysis. Doping can introduce additional electron energy levels into the band gap that may be populated by electrons which cause the E_F to shift up or down. Similar transition metal dopants have offered conductivity increases in titania and altered its electronic properties, specifically the addition of niobium. Niobium has the closest ionic radius to titanium for a +5 valence state with same coordination number and it also forms a strong metal-support interaction with Pt [96]. The enhanced conduction mechanism seems to be a result of Ti^{4+} partially substituted with Nb^{5+} and this leaves some oxygen vacancies in the crystal structure that form shallow electron donor sites. These vacancies allow electrons localized at metallic interfaces to become charge carriers. Resistivity values of some titania thin films were measured as low as 10^{-3} and even 10^{-4} $\Omega \cdot cm$ in one report with increasing niobium concentration up to ~8 atomic percent which is near the substitutional saturation limit in rutile phase [109-111]. However, in a nanoparticle synthesis of mesoporous films (190 m^2/g and 43% porosity) with 20% Nb content, 0.25 S/cm conductivity was measured [112]. Doping Nb in titania can form solid solutions up

to even higher concentrations in the more relaxed anatase structure [113, 114]. Addition of Nb also results in greater phase stability of the anatase by increasing the rutile phase transformation temperature and retarding grain growth [114]. There is an extensive collection of literature on Nb doped titania and its defect chemistry, but the addition of metals like Pt can also have a significant contribution to its defect properties.

There is some contradicting evidence in a few reports over the phase necessary to achieve acceptable conductivity. Some have suggested that a rutile phase is necessary to develop a suitable electrocatalyst while others report the anatase phase can also exhibit sufficient conductivity [115, 116]. The discrepancy may come as a result of the preparation technique used and the reducing condition. When the metal oxides are prepared by a direct phase transition path, then kinetics are often faster than reducing an already stabilized crystalline phase. Huang et al. used a sol-gel procedure to prepare the conductive rutile phase by reducing the oxide at higher temperature [117]. The transformation temperature for the densely packed rutile phase with (~ 550 °C) is higher than that of the metastable anatase phase. The greater temperatures required for the rutile transformation also limits the porosity of titania and decreases the surface area substantially. A long range crystalline order is needed to maintain the conductivity over greater distances and prevent recombination at grain boundary defects. The niobium doped titania would also result in a reduced oxidation state (non-equilibrium) of transition metals in the oxide which would be subject to further oxidation and not as stable as the non-conductive TiO_2 (see Pourbaix diagram), for example. However, defects at the interface are considerably more stable when resulting from strong metal-support interactions. Quite possibly, there is a way to utilize a stable form of titania by

depositing on carbon framework from a simple sol-gel process to fabricate a high surface area support with sufficient conductivity before depositing the Pt catalyst to form unique interfaces and heterojunctions.

Demonstration of a new approach which could offer the benefits of stability and improved catalytic activity without sacrificing valuable surface area is an important objective of this study. Growing titania onto a substrate like graphitized forms of mesoporous carbon or carbon nanotubes from a solution deposition process offers an ideal support that can withstand transformation temperatures needed for composite preparation which can be scaled up well due to its simplicity. Titania has been coated on to similar carbon substrates for other applications (i.e. photocatalysis and photonic crystals) without losing the integrity of carbon substrate structure to support. In these applications, the carbon is typically used as an electron sink that is ideal for separating reactive holes in the functionalized surface with titanium oxide [118].

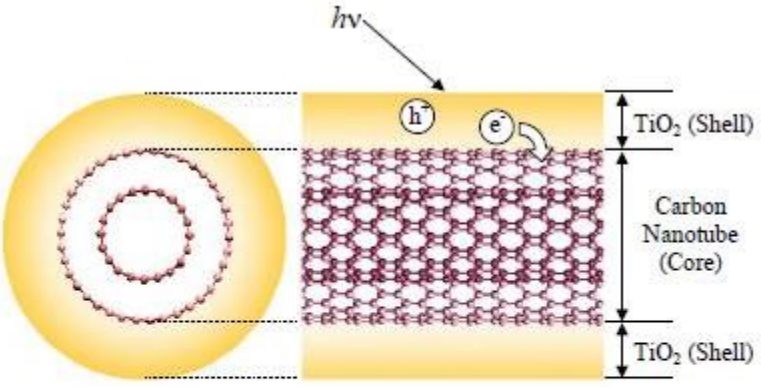

$$TiO_2/CNT \xrightarrow{h\nu} TiO_2(h_{VB}\cdots e_{CB})/CNT \quad (1\text{-}4)$$

$$TiO_2(h_{VB}\cdots e_{CB})/CNT \rightarrow TiO_2(h_{VB})/CNT(e_t) \quad (1\text{-}5)$$

$$TiO_2(h_{VB})/CNT(e_t) + OH^-_{TiO_2\,surface} \rightarrow TiO_2/CNT(e_t) + OH^{\bullet}_{TiO_2\,surface} \quad (1\text{-}6)$$

Figure 1.31 CNT-TiO_2 composite for photocatalyst application [118]

Ordered mesoporous carbon materials have been defined as having pore sizes from 2-50 nm and they have been tested as supports for Pt catalysts. Chang et al reviewed mesoporous carbon for fuel cells, but stated that the application is still in its infancy [119]. Others have prepared the mesoporous carbons with high conductivity for direct methanol oxidation in the anode. Mesoporous carbon is typically prepared by forming a silica template than etching it away with strong acid or patterning carbon with polymer spheres then evaporating them. These materials have exemplified surface areas as high as 500 m^2/g. Titanium carbides used for supercapacitors can have even higher surface areas [120]. A characterization of 3-D ordered porous carbon coated with titania nanoparticle composites was done by Zhiyong Wang for a possible gas sensor application [121]. If mesoporous carbon could be coated with titania and hold its porous structure, it could offer many advantages as a composite electrocatalyst support.

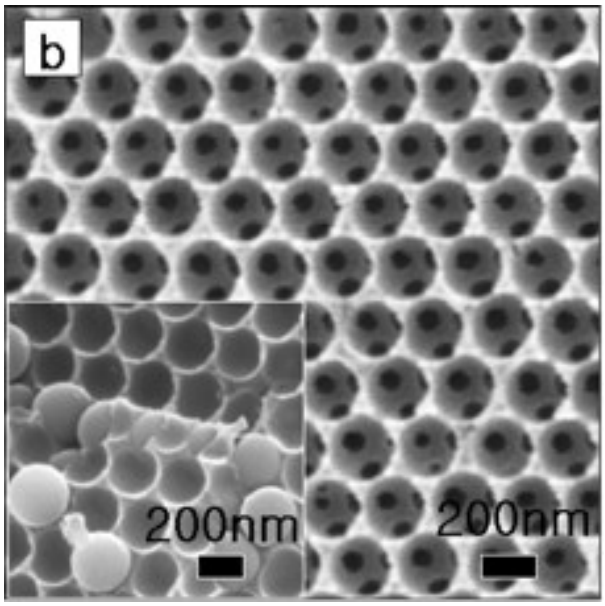

Figure 1.32 3-D ordered macroporous carbon with high surface area [119]

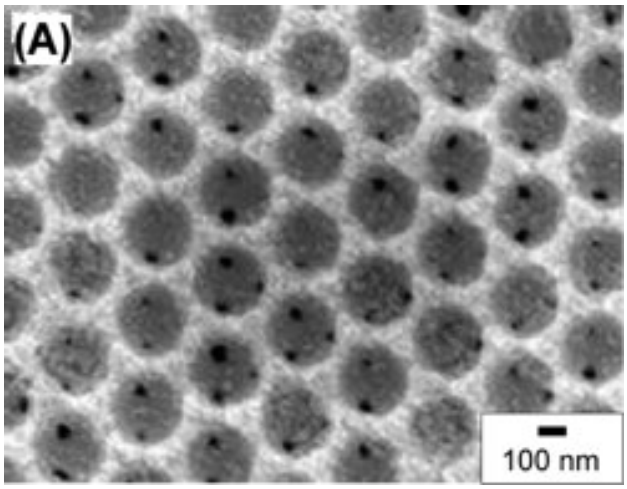

Figure 1.33 3-D ordered carbon has been coated with thin coverage of titania [121]

Carbon nanotubes are one carbonaceous material which can withstand high annealing temperatures in air up to about 450 °C which is also sufficient for the anatase phase transition [122]. CNT supported titania composites can be prepared with high aspect ratios and suitable conductivity. Titania has been coated on to the surface of CNT by a few different methods and several reports have now investigated their use for fuel cells. P. Vincent first published results of composites from CNTs dispersed in a titania sol-gel [123]. Others groups have since studied a CNT coated TiO_2 deposition procedure using ultrasound irradiation in aqueous solution [124, 125]. Varying preparations of multiwall carbon nanotubes (MWCNTs) have successfully grown titania crystals on them by a sol-gel method as shown in Figure 1.34 by Jitianu et al [126-128]. Carbon nanotubes were first oxidized to create carboxylic acid groups and oxygen defects on the surface. These anionic sites serve as attachment points for the titanium cations. This is effective for preparing a uniform and thin film of titania particles to the surface. The loading of titania on carbon will have an effect on its crystallinity and also its electronic properties. Carbon-titania composites were the then filtered and calcined to achieve a high surface

area photocatalyst. Bin Liu et al. used a similar chemical approach to prepare mesocrystals of anatase TiO_2 onto multi-walled CNTs with controllable surface coverage, surface area, crystal orientation, and TiO_2/CNTs ratio shown in Figure 1.35 [129]. Other efforts have also focused on the composite structure for enhanced photocatalysis, but their work found optimum results from only a small concentration of CNT which are not nearly as dependent on the formation of a conductive network. More uniform crystalline coatings were grown on single-wall CNT arrays using a metal-organic chemical vapor deposition process, but this is not as friendly for loose powders or scaling up synthesis [130].

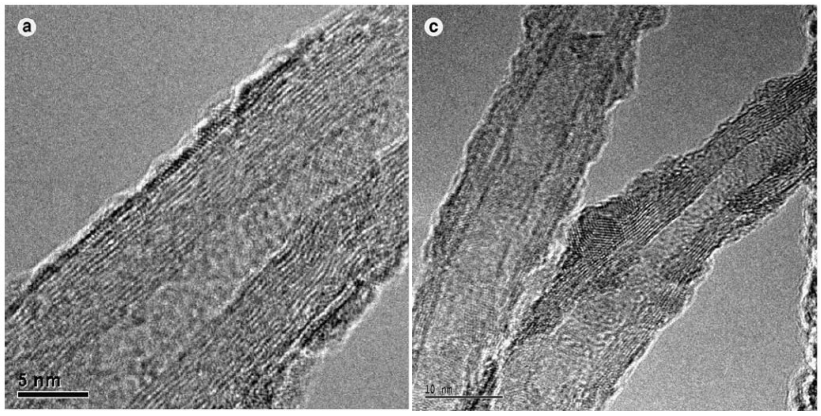

Figure 1.34 Sol-gel synthesis of thinly covered titania on CNT [128]

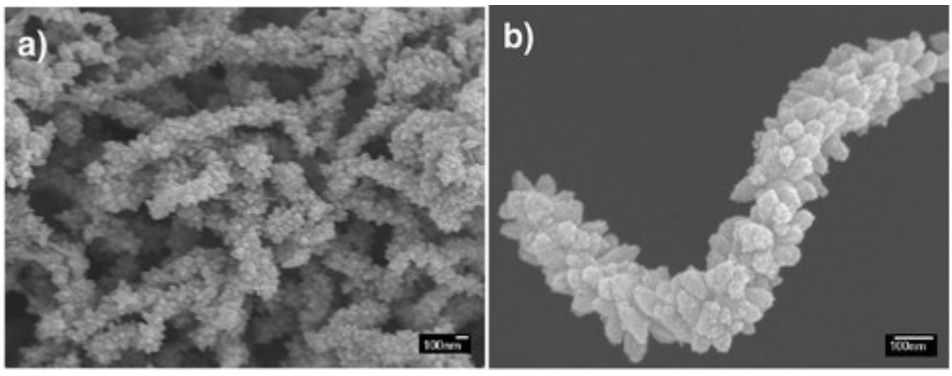

Figure 1.35 High resolution SEM of CNT covered with large titania nanocrystals (a) a film of nanotube composites and (b) an individual composite [129]

A composite material made from both CNT and TiO_x may be an excellent alternative to pure carbon and could be a platform to demonstrate a proof of concept for further understanding and development. If crystalline titania nanostructures were well connected and bonded to carbon nanotubes, they should offer composite support that limits carbon oxidation effects from exposure to a corrosive environment. Platinum catalysts would then be anchored to the titania where a stronger bond with the metal oxide would be more likely to prevent dissolution of the catalyst while electronic contact with CNT can still percolate an interconnected network. In all cases of Pt reduction on composite supports, it seems that the metal tends to deposit on or in contact with the metal oxide. When this idea was originally conceived, there had been very little published electrochemical results, but there have since been quite a few studies using very similar composite structures. However, guiding principles for their design lack a depth of understanding required to build better electrocatalysts. Furthermore, validation in working electrodes still remains a question of concern.

The number of publications on this metal oxide catalyst support for electrocatalyst has seen an enormous surge in recent years. Some of the most promising results from the work in this field have included a composite based structure. In 2010, a $Pt/TiO_2/C$ electrocatalyst was used for a test in ORR behavior of a working fuel cell and revealed improved performance after aging [[104]]. This cathode showed improvement over Pt/C in accelerated aging test when potential was cycled 0.6-1.2 V for 3000 repetitions. In this case, the carbon was a Vulcan XC-72 carbon black and although the initial performance was not as good, the durability was markedly better. However, it is suspected that a

better control of over interfacial formation and improvements in elemental proportions will improve the understanding of fundamental mechanisms which can guide further advancements for this combination of materials.

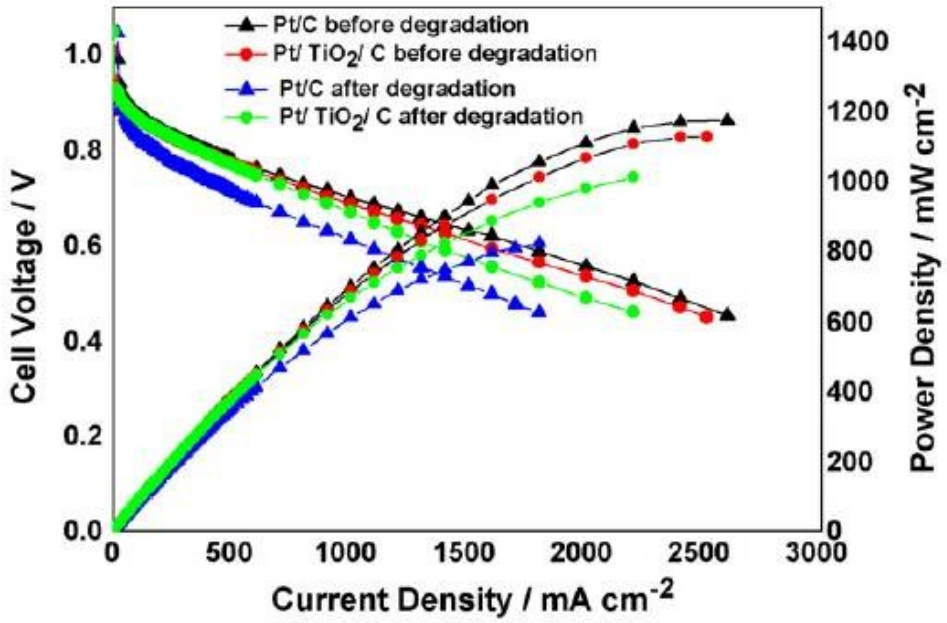

Fig. 4. Performances of PEMFC single cells. $P_{H_2} = P_{O_2} = 0.2$ MPa; $T_{cell} = 80\,^{\circ}C$; $T_{a,humi} = 90\,^{\circ}C$; $T_{c,humi} = 85\,^{\circ}C$.

Figure 1.36 Comparison of a Pt-TiO_2-Carbon electrode to Pt-Carbon [104]

A recent report from PNNL has studied the benefit of the triple phase junction formed when Pt is bound at the interface of the carbon and metal oxide. It is believed this triple phase junction is what may help realize both the benefit of stability and performance. A thorough investigation of this was published on a graphene functionalized with indium tin oxide (ITO) and later tin oxide nanostructured surfaces [131, 132]. The activity and stability limits for ITO have also been explored for ORR [133]. Although a different material from titania, some of the same chemical principles can be applied because of similarities at the interface of materials, especially the junction

between metal-metal oxides. This publication included both experimental findings from electrochemical cells and a DFT model to predict the favorable arrangements of electrocatalysts at the carbon-metal oxide junctions as seen in Figure 1.38.

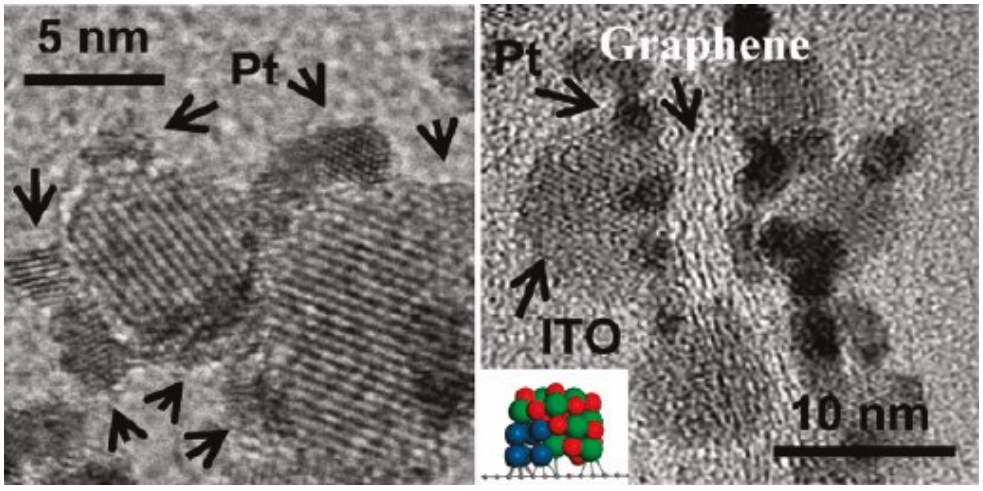

Figure 1.37 TEM image of triple junction between metal-metal oxide-graphene [131]

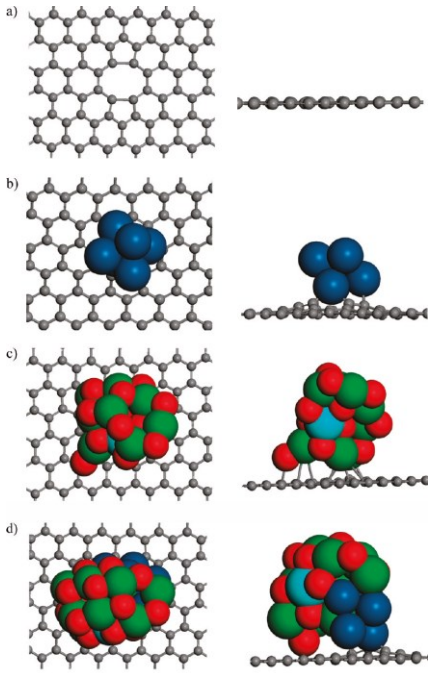

Figure 1.38 (a) Defects in graphene serve as binding site for b) Pt, c) ITO, and d) ITO-Pt when sequentially reduced on the surface to form the electrocatalyst composite [131]

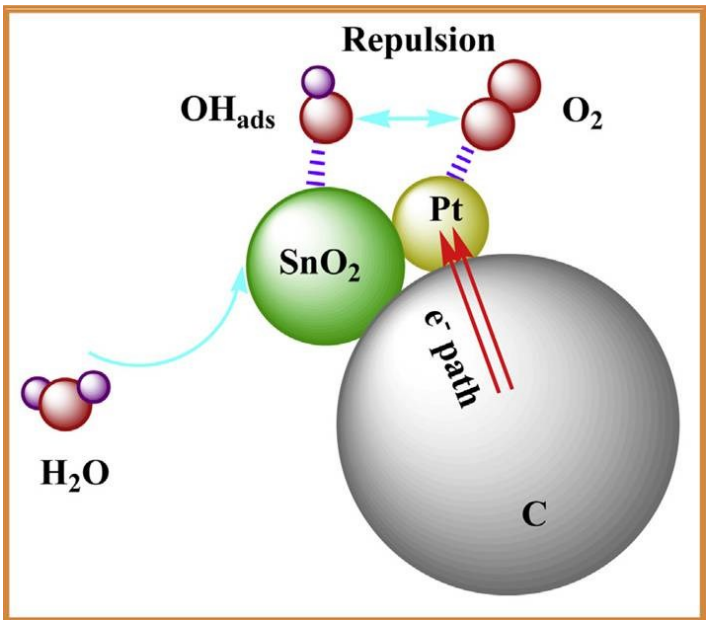

Figure 1.39 Pt-SnO_2-C schematic of ORR enhancement [132]

A group from Harbin Institute of Technology reported a carbon riveting process of metal oxides to enhance the electronic contact of a Pt/TiO_2/C system. This requires the utilization of a post-processing step to mix an organic carbonaceous material such as glucose; when cooked, a connecting carbon skeleton remained [134]. A working electrode showed an improvement of stability in a 0.5 M H_2SO_4 when subjected to potential cycling that could be measured by the change in electrochemical area and the change in particle size distribution. This same group went on to demonstrate a similar processing strategy and aging test for a multi-wall CNT that encapsulated a 20 nm titanium dioxide powder inside its hollow center then followed with microwave-assisted polyol reduction and carbon encapsulation [135]. The authors present an even more stable electrocatalyst material that only grew an average of 3% in particle diameter in comparison to 23.4% in the previous publication, an approximate 7.5 times improvement. This inspiring work published from 2011 was based on RDE study, but effectiveness in a real fuel cell

cathode is still uncertain. A report from 2012, demonstrated a hierarchically structured Pt/CNT@TiO_2 for stability purpose that showed a similar starting active area for a similar loading of Pt/CNT, but had 78% surface area remaining after potential cycling compared to 57% for the latter [136]. Although many of the details are left out of this communication, the schematic for material synthesis is provided in Figure 1.40.

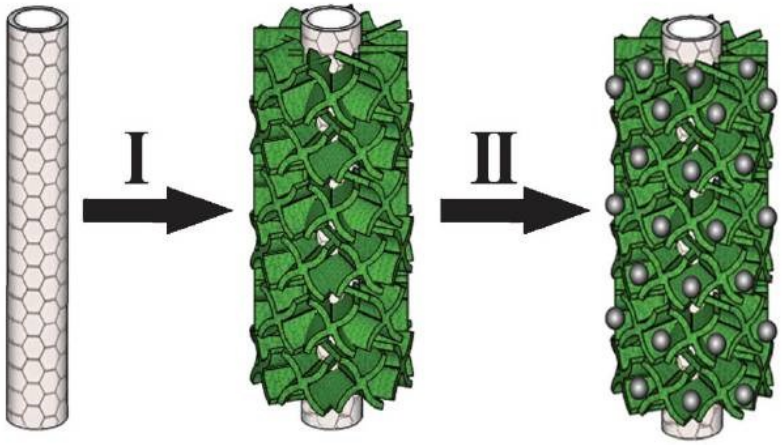

Figure 1.40 Templated synthesis of TiO_2 (green) followed by Pt (gray) deposition [136]

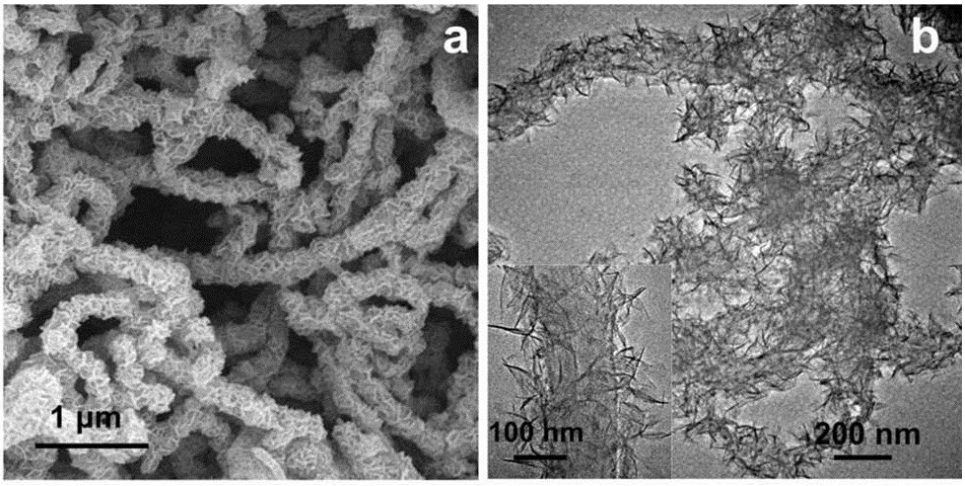

Figure 1.41 (a) SEM and (b) TEM electrocatalyst composites (Pt-TiO_x-CNT) [136]

Ultrathin titania on CNT supports for platinum was published in a comprehensive study for the first time in August 2012 [137]. Multi-wall CNTs were covered with a titanium alkoxide precursor from a sol-gel and the procedure is summarized in Figure 1.42. After 1000 potential cycles, the Pt-MWCNT@UT-TiO_2 had 62% of active Pt area remaining compared to only 35% for Pt-MWCNT and less than 44% for Pt-C. Smaller Pt nanoparticles ~1.6 nm were prepared on the composite support which offered a remarkably high 285.5 m^2/g active catalyst area. Surprisingly, the conductivity was also higher for a solid made from the composite with titania. Extensive materials characterization including XPS attempts to explain the effects and the role of SMSI in benefits to activity and stability. The lead author, N. G. Akalework included this work in his dissertation as well as a Mo doped titania used for the anode. Since 2012, several other groups have also published new results of this materials system and are included in the introduction to later chapters. Notably, some of the most recent publications from Professor Kan Huang's group at University of Missouri have also included studies in the cathode and for anode oxidation reactions with CO and alcohols [138, 139].

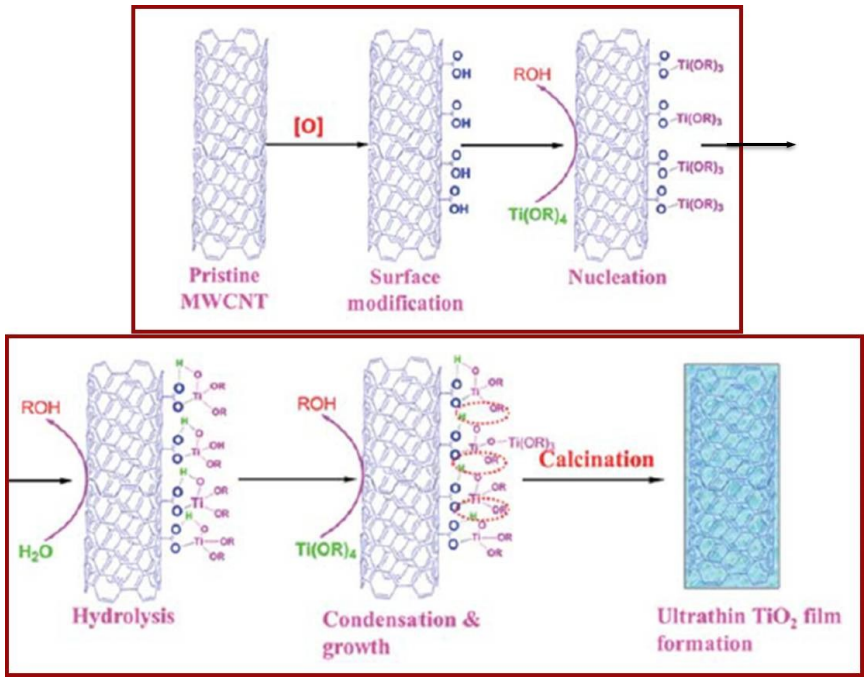

Figure 1.42 Ultrathin titanium oxide film covered on multi-wall CNT

Another study published in 2012 utilized a carbon nanotube array grown on Inconel and RF sputtered with niobium oxide films of 2 or 10 nm [140]. This was followed by platinum sputtering for mass loadings of 0.03, 0.09, and 0.15 mg/cm^2). A half-cell study in 0.1 M $HClO_4$ from 0.5 to 1.4 V for 10,000 cycles showed significant durability improvements over the control sample without the NbO_2 under layer. This slightly reduced form of Nb^{+4} was able to provide effective conductivity while also providing exceptional stability that claimed to completely preserve ORR activity when cycled in the range from 0.6 to 1.1 V. An investigation of amorphous niobium oxide on carbon has been reported for benefits as a Pt support in both electrodes [139, 141]. There is some concern whether NbO_2 phase or +4 state of the metal would be maintainable since it is not in the preferred +5 oxidation state found at equilibrium. However, oxidation kinetics may be relatively slow and worth a closer investigation.

Although the kinetics for metal oxidation may be very slow, it will eventually assume the thermodynamically stable oxidation state associated with its environment. The surface atoms are most susceptible to the change because of their contact to the environment. The environment of the fuel cell is dependent upon the operation conditions, but specifically the cathode is an acidic state at high potential. Titania based electrocatalysts were first investigated for their use in electrodes with use of Magnéli phases sold as commercially available product known as Ebonex and reported in classic literature [76]. There have been several reports which have attempted to realize the benefits of the material because of its electronic conductivity that arises from the oxygen defect concentration, electron compensation, and the reduced form of the metal that provide for its conductivity. However, a nice review in 1998 warned of the issues related to its stability and low surface area [80]. The material has been demonstrated benefits in both electrodes and was also more stable when compared to XC-72 carbon in simulated cathode condition of the fuel cell [79, 142, 143]. However, the average charge of the titanium ion is between +3.5-3.8, which is less than ideal +4 Ti cation. The Pourbaix diagram shown in Figure 1.43 indicates that titanium would prefer the TiO_2 passivation state in typical regions of operation for the cathode of the hydrogen fuel cell, although some surface hydroxide may also be encountered at pH near 0 which is not indicated here on this simplified version of stability regimes.

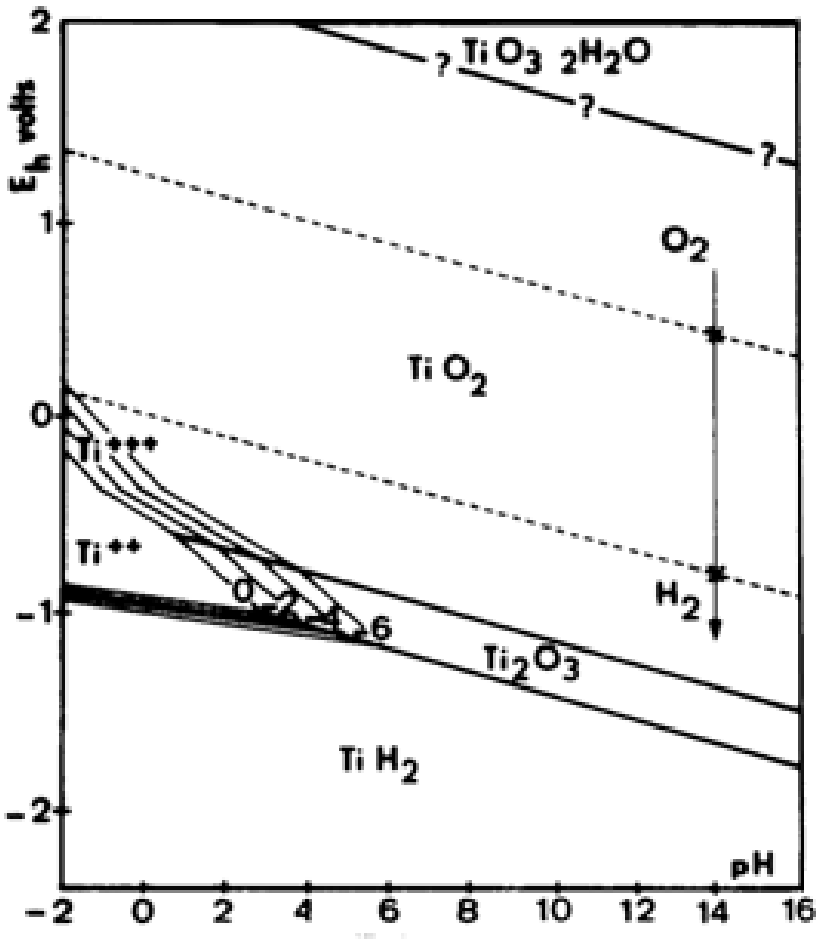

Figure 1.43 Pourbaix diagram for titania in aqueous system at STP

In fact, a recent report from the National Research Council of Canada and the Institute for Fuel Cell Innovation has synthesized nanofibers of NbO_2 and Ti_4O_7 as Pt supports with some conductivity that showed a surface passivation film [[144]]. Material characterization through XPS and XRD showed how the surface film adopted an equilibrium conformation over time. Both supports were subject to ECSA and ORR losses after 1000 cycles that were attributed to the formation of this insulating surface oxide. Niobium is a very suitable dopant in titania and it is another metal which can exist in a state of passivation as seen in

Figure 1.44 [[145]]. A better result was claimed for a microsphere catalyst support from Nb-doped TiO_2 with a high specific surface area which was cycled in 0.5 M sulfuric acid from 0.05-1.2 V in RDE study and lost just 15% of starting Pt area after 1000 cycles [[146, 147]]. A partnership between NRCC and AFCC tested the efficiency of Pt deposited on carbon composite coated with the Nb-doped of titania that had a support surface area of 176 m^2/g in the rutile phase [[148]]. This electrocatalyst was cycled between 0.6-1.2 V in 0.1 M perchloric acid and lost 35% of its mass activity after 1000 cycles, although it had better stability than a Pt/C control.

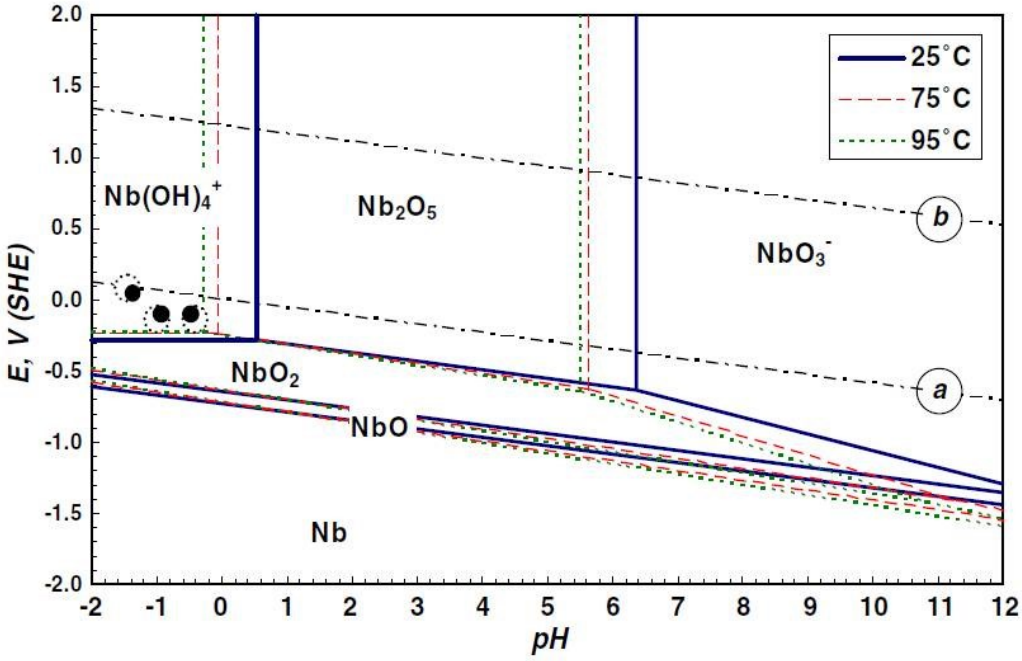

Figure 1.44 Pourbaix diagram for the aqueous Nb system at 25, 75, and 95 °C

The passivation layer on metallic surfaces is a thin layer of oxide that forms on its surface. This is based in part on the magnitude of standard free energy of formation for the metal oxide. The oxide layer can serve to greatly reduce the transport of corrosive

species to the underlying or supporting metal structure below the surface. Some values for the enthalpy of formation from metal oxides are presented in the graph in Figure 1.45. An Ellingham diagram is presented in Figure 1.46 to depict the standard Gibbs free energy of Ti-Nb-O system from the DoITPoMS website interactive feature. The tenacity of the oxide layer is a function of its bond strength; more stable oxides are less likely to undergo further oxidation or corrosion in the case of electrochemical reactions addressed in this review. As seen in Figure 1.45, noble metals have less stable oxides and are unfavorable to form in case of platinum at standard conditions.

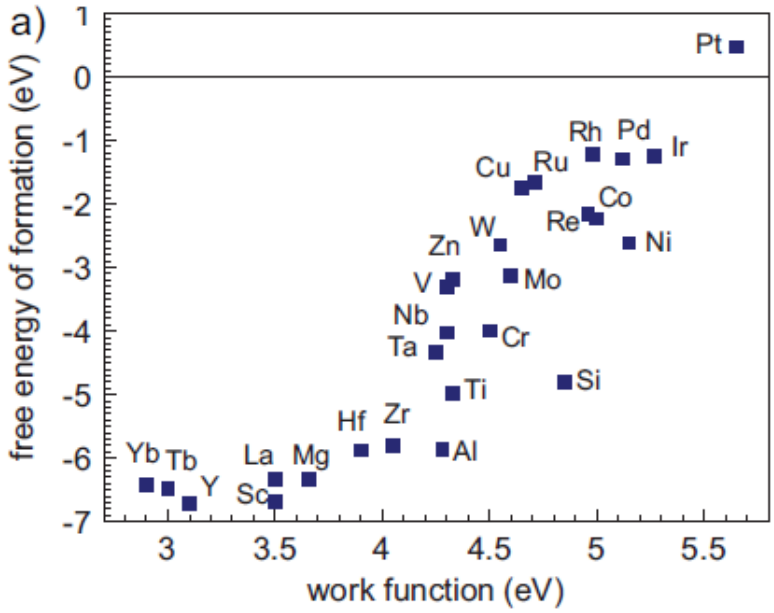

Figure 1.45 Heat of formation of metal oxides vs. work function [95]

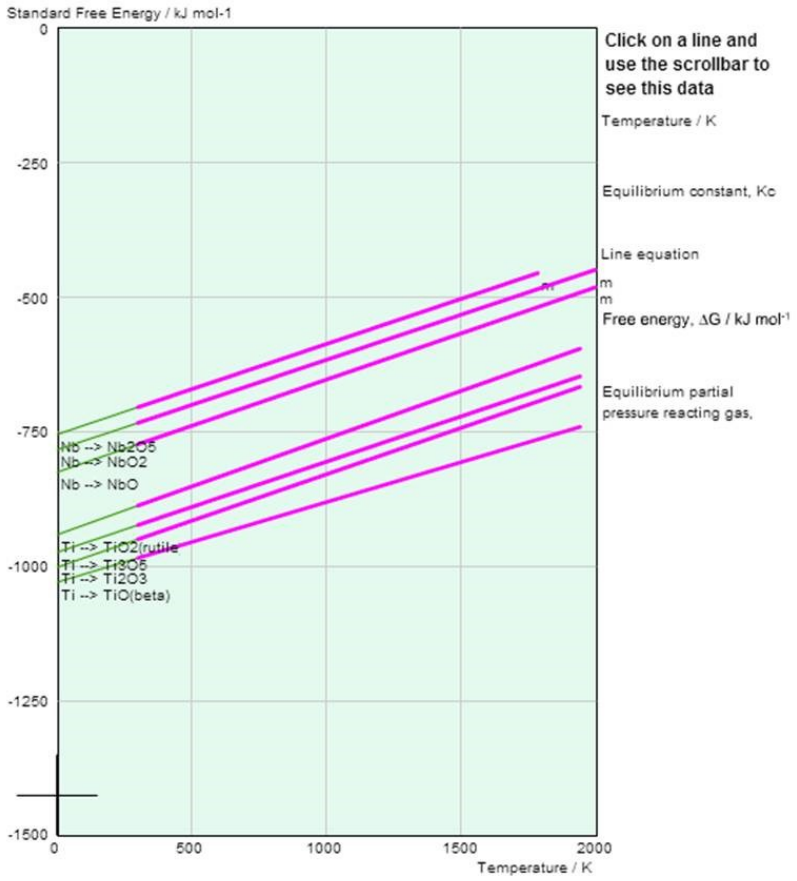

Figure 1.46 Ellingham diagram of Ti-Nb-O system

Several reports attempted to use the heavily reduced metal oxide phases and claimed some success, but when tested over many potential cycles this far from equilibrium state material is not really viable, it become irreversibly oxidized after cycling. The use of reduced cations like Ti^{+3}, in TiN have been tested for their efficacy as Pt supports [149]. However, the same authors published two subsequent papers detailing the oxidation kinetics and the material's time dependent corrosion to TiO_2 at its surfaces [150, 151]. Recent findings have been presented on the electrocatalytic behavior of reduced transition metals from Group IV-VI in RDE tests with materials such as TiO which have revealed high activity for non-Pt alternatives. However, little evidence

suggests that these metals oxides could maintain a stable performance over any extended test condition. It seems more success has been seen by balancing charge differences using acceptor or donor dopants in titania. The full extent of these publications cannot be adequately covered in this review so it will suffice to say that by only slight deviation of the equilibrium state of metal oxides, a more active and stable initial state can be prepared with regard to the electrochemical cell environment.

Niobium donor dopants in titanium oxides have been most thoroughly investigated because of similar ionic radii and coordination numbers to titanium. The donor states a more positively charged atom which must be balanced by introduction of a negative compensation. Extra oxygen can either be integrated into the lattice or a vacancy will leave a non-bonding electron [[152]]. Although there may be the possibility of adding conductive states into the material, these are not intrinsically as stable as the fully oxidized form. This is why it is desirable to form very thin nanostructures of the equilibrium metal oxide on the carbon surface which can serve as strong anchoring sites and while dopants can also help resist encapsulation from SMSI [[153]]. Niobium, tantalum, tungsten, and vanadium oxides are other example materials which are also stable in the cathode region and can additionally offer SMSI as well as good corrosion resistance thanks to a very stable passivation film.

Doped titania has since garnered much attention from the fuel cell community based on several successful results. Alex Bauer et al. used an electrospinning technique to obtain high aspect ratio fibers of polyvinyl pyrrolidone polymer containing ceramic precursor of titania and the resultant composite fibers were heat treated at 850 °C [[146]]. This heat treatment served to crystallize the ceramic precursor and also to form

carburized electronic contact between the phases. The cell performance and surface area was less than a Vulcan XC-72 supported Pt in comparison; however, the stability of normalized surface area showed a marked improvement. An ORR ring-disk electrode showed improvements in both activity and stability. A similar result was also found by Do et al. for a polystyrene latex templated high surface area Nb doped TiO_2 with mass activity compared traditional carbons [[154]]. Though, these works all highlighted the need for further electrode development and better MEA testing.

Carbon doping has been one popular method to lower the E_g for titania and has been proven an effective application for many photocatalysts which can red-shift the band gap from the UV to the visible region of the electromagnetic spectrum. The motivation for this work has been the more efficient use of longer wavelength photons that are more intense in natural environments. The results from a well-executed experiment show that carbon doping of titania enhances the solar absorption [[155]]. The theory of carbon doping of titanium dioxide was the title of a paper by Di Valentin who discussed these experimental results and applied DFT calculations to predict the state of energy bands in the structure [[156]]. The results for carbon C^{+4} substituted titanium Ti^{+4} centers shows a reduction in E_g for anatase crystals by 0.1 eV. This is also the most stable position for the carbon dopant, but it can also found in other positions including interstitial sites and even in oxygen vacancies. These situations are in part dependent on the dopant concentration and six occupied 2p states which lay 0.3-1.3 eV above the valence band and the gap is reduced to 2.46 eV when both defects are included. The anatase phase is the predominant crystalline structure found for maintaining semi-crystalline high surface area supports. A publication from carbon doped titania with CNT

composite support for Pt electrocatalyst was recently found to improve ORR activity over Pt/C [[138]].

A systematic study to understand the role of crystallite size in the catalyst stability was conducted for titania in several phases. The degree of crystallinity is often measured by XRD and the diffraction pattern can give an estimation of the crystalline structure and distribution. Jiang et al. used a microwave assisted polyol process for Pt deposition on commercially available and uniform titania crystallites; the catalyst particle size change from before and after an accelerated cycling potential cycling protocol was measure [[157]]. The report shows an improved stability for 20 nm titania particles. The titania mass fraction was varied from 30-90% and the optimum value found was 40% of the total for the smallest decrease in ECSA. The anatase phase undergoes a transformation above 300 °C, but the uniform rutile phase is only obtained under higher temperatures > 550 °C which can be seen in Figure 1.47.

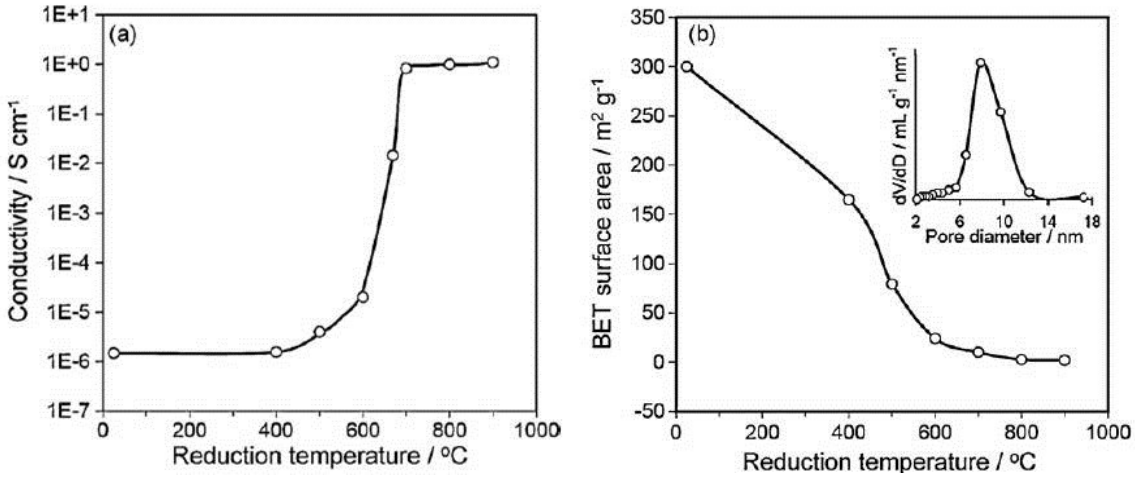

Figure 1.47 Increased reduction temperature improves conductivity, but decreases surface area [[117]].

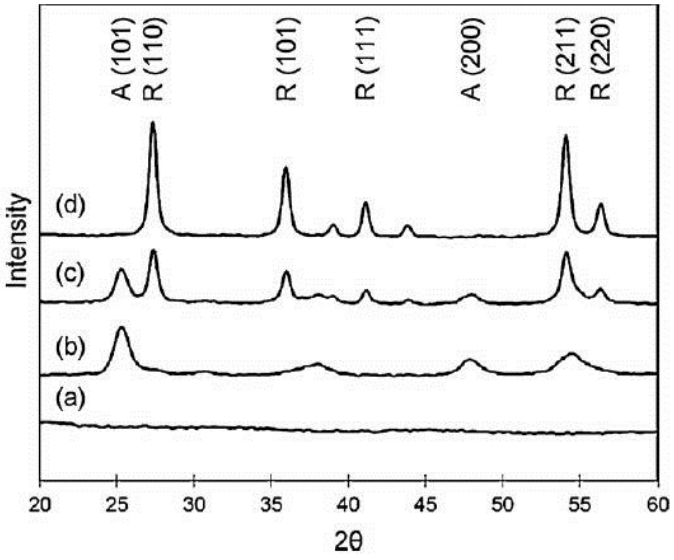

Figure 1.48 XRD pattern shows phase change for 25% Nb doped crystal with increase in temperature from (a) 25, (b) 500, (c) 600, and (d) 900 °C [117]

The rutile structure actually has a narrower band gap than anatase and the material is more conductive when the structure is doped as seen above. This is likely a result of greater bulk conductivity and decrease in surface area that this phase transformation imparts. Grain boundaries can also become charge recombination centers that limit long range conduction. Another USC group reported a doped titania with conductivity of 1.11 S/cm after reduction [117]. This value is higher than proton conductivity of the electrolyte, but less than electronic conductivities of carbon. The area change from this material cycled up to 1.4 V shows significant improvement relative to a conventional carbon, but the electrocatalyst is not immune to surface area loss as seen from RDE test. It is believed the metastable anatase structure will hold the most promise for the fuel cell based strictly on available area and stability benefits only.

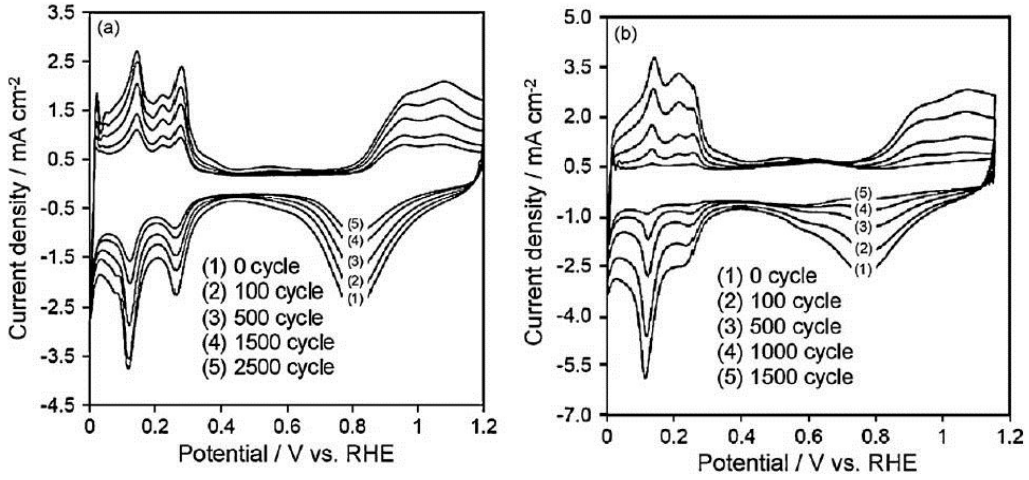

Figure 1.49 Pt cycling stability of a) Nb doped TiO_2 rutile contrasted with a conventional b) carbon black [117]

It is not the objective to enhance the conductivity of the oxide in supports. The role of the oxide in composite support is primarily for stability, though possible activity enhancements to the noble catalyst may also be possible. It is hypothesized that great improvement on catalyst performance and stability can potentially be realized from a composite metal oxide and conductive carbon hybrid.

There have been several interesting discussions in this review related to the electronic conductivity of titania, but some have also considered its proton transport in the hydrated state when hydroxyl group forms on its surfaces [158-160]. The equilibrium diagram suggests that an orthotitanic acid $Ti(OH)_4$ or the dehydrated complex $TiO_2 \bullet 2 H_2O$ or metatitanic and the TiO^{++} which can perform the anionic hydroxyl exchange with surface water. Although the literature found on this topic is scarce, there are a few reports suggesting that it can contribute to proton conduction by functionalization with sulfonic acid groups [158]. A space charge induced hydrogen ion insertion in nanoscale anatase TiO_2 was evidenced through neutron diffraction by measuring deuteron density in

the crystal structure [161]. This sample was immersed in a concentrated sulfuric acid solution to simulate the electrolyte of the fuel cell. A space charge layer from deuterium insertion depended in part on the crystal size, but the diffusion in this material at 300 K and 20% RH was only three times lower than that of Nafion and increased with temperature which shows promise for fuel cell electrolyte materials. Related, but earlier works by Ekström and Gustavsson have shown a benefit in ORR by depositing thin Pt films ~ 3 nm on to Nafion membranes with and without titania layer ~20 nm [162]. The substrate is not credited for enhancing specific activity, but there was an added benefit from the increase in surface area and it was also hypothesized that the titania actually contributed to the proton conduction. It seems that the proton conduction over tens of nanometers length scales is sufficient to reach the catalyst surfaces which are not in direct contact with the Nafion. In fact, many reports have included titania phases in the polymer for added improvements that included ionic conductivity in low humidification after a report by Watanabe, Uchida, and Stonehart [163]. Other metal oxides including zirconium, tungsten, and tantalum have provided similar benefits. When sulfate and phosphate groups were attached to Zr or Ta, they were able to provide some of these functions including proton conduction to catalyst sites [164, 165]. Ionic surface conduction from hydrated surface functional groups can extend the electrolyte contact as seen in Figure 1.50.

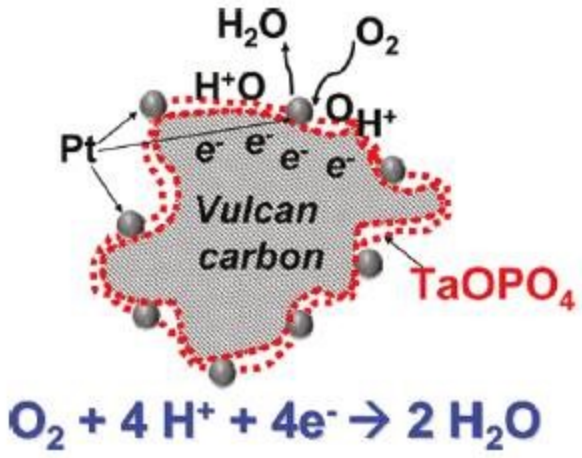

Figure 1.50 Metal oxide (TaO_x) with surface acidity for proton conduction

A specific goal for material synthesis in this research project is to enhance catalyst support system stability by taking advantage of the strong metal-support interaction between platinum and titania. The proximity and electronic contact of the deposited catalysts will form a triple phase boundary in this composite. The carbon nanotubes serve as the conductive foundation, with better stability than carbon black as evidenced by the results from Appendix A. The recent progress shown in the experimental work has aimed to realize these benefits in PEM cells through easily implementable synthesis routes. Further understanding and optimization are necessary and will be discussed in the future approach with regard to following chapters. The fundamental design concept of CNT/titania support is to use one material (CNT) to provide a conductive network and use another material (titania) to provide stability enhancement. A CNT network provides for a high surface area titania support. The composite support concept could offer synergistic function which cannot be realized by its individual constituents. Junctions formed with the model platinum catalyst will create

useful interfaces. When understood from fundamental principles, design is possible from sub-atomic level up to the scale of electrochemical cells.

1.2. Electrode Preparation by Ultrasonic Spray Deposition

The design of the electrode is very closely related to the materials used to prepare it, though the fabrication process is equally important. The electrode is simply comprised of three phases; electrocatalyst, electrolyte, and open space. These domains must be intricately connected by methods which are difficult to control. This is in part due to the very fine length scales over which the arrangement must take place. Electrode microstructure has a critical effect on cell performance and can also play a role in durability. Furthermore, it is not trivial to explain the contribution of processing because it is difficult to visualize what is happening on these scales and the effects are often convoluted. The mass transport of reactants and products is a complicated by two-phase flow (gas and liquid) and partially dependent on the transfer of charge in the electrode. For example, flooding in the electrode can present a problem that is related to obstruction of mass transport processes. This will limit performance, but also can lead to durability problems. A comprehensive review of electrode fabrication procedure would be out of context for discussing the catalyst and support stability. However, it should suffice to say that a highly automated and reproducible process for fabricating electrodes can benefit this research by providing a consistent and uniform MEA that is suitable for cross comparisons between different material platforms for platinum electrocatalysts.

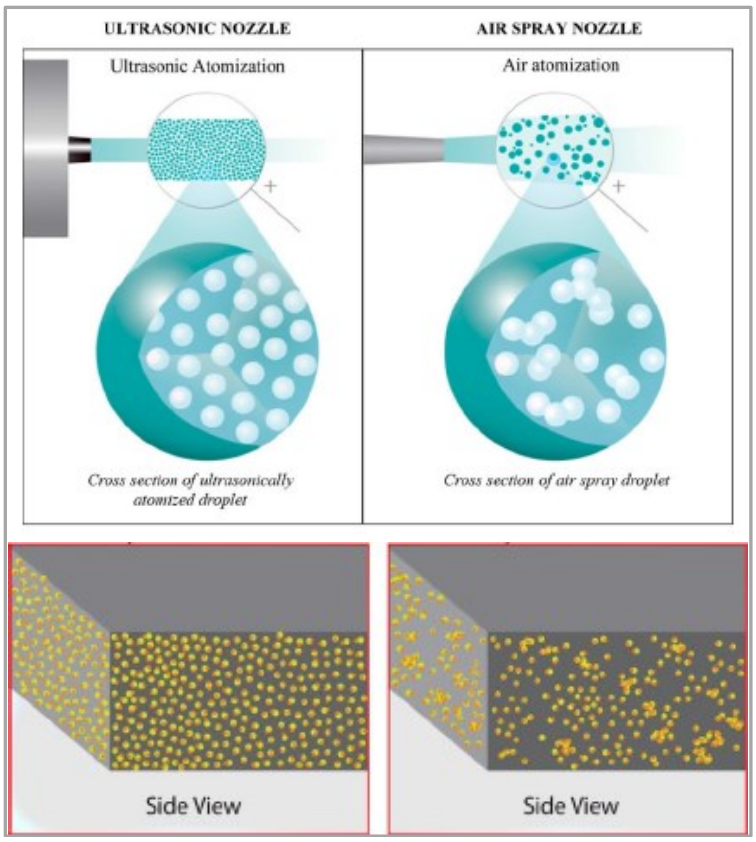

Figure 1.51 Ultrasonic spray (left) and air spray electrode (right)

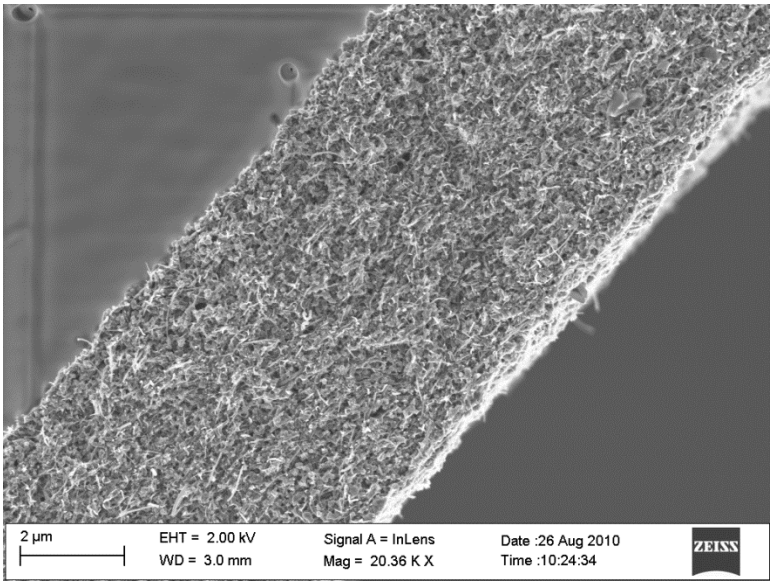

Figure 1.52 Field emission SEM of electrode side profile

Chapter 2. High Performance Supported Platinum Catalyst Fuel Cell Electrodes by Ultrasonic Spray Deposition

2.1. Abstract

The core of a polymer electrolyte membrane fuel cell is the membrane electrode assembly (MEA). Manufacturing processes for MEA have significant impact on their performance and durability. The authors report an ultrasonic atomization and spraying technique to deposit catalyst layers directly on to the membrane was developed for the construction of membrane electrode assemblies. Electrochemical test of as-fabricated MEAs indicated very good performance and reasonable stability. The platinum yield of the fabrication process was found to be ~ 90% for this electrode geometry.

2.2. Introduction and Background

Ultrasonic vibration of a liquid surface attached to substrate causes the formation of surface capillary waves. As the amplitude increases, the rupture of capillary surface waves occurs; liquid droplets are subsequently ejected from the surface [166, 167]. To realize the ultrasonic spray process, the atomized droplets using ultrasonic atomizer can

be shaped and moved around with low velocity air or other carrier gas. Applications of ultrasonic spray technology range from ordinary liquids to molten metal for air conditioning, drug delivery, powder production, combustion, textile coating, solar cell manufacturing, and lately fuel cell manufacturing [168, 169]. The major advantages of ultrasonic spray include uniform spray with narrow distribution of droplet sizes, controllable mean droplet size diameter by ultrasonic forcing frequency, low droplet velocity (soft spray) that minimize splashing and material waste, quiet operation, low energy consumption for atomization and spray shaping. The ultrasonic spray technique also allows for multiple syringe pumps and mixing at the atomization surface. Many customizable features on the equipment can be adjusted to improve the deposition and electrode performance.

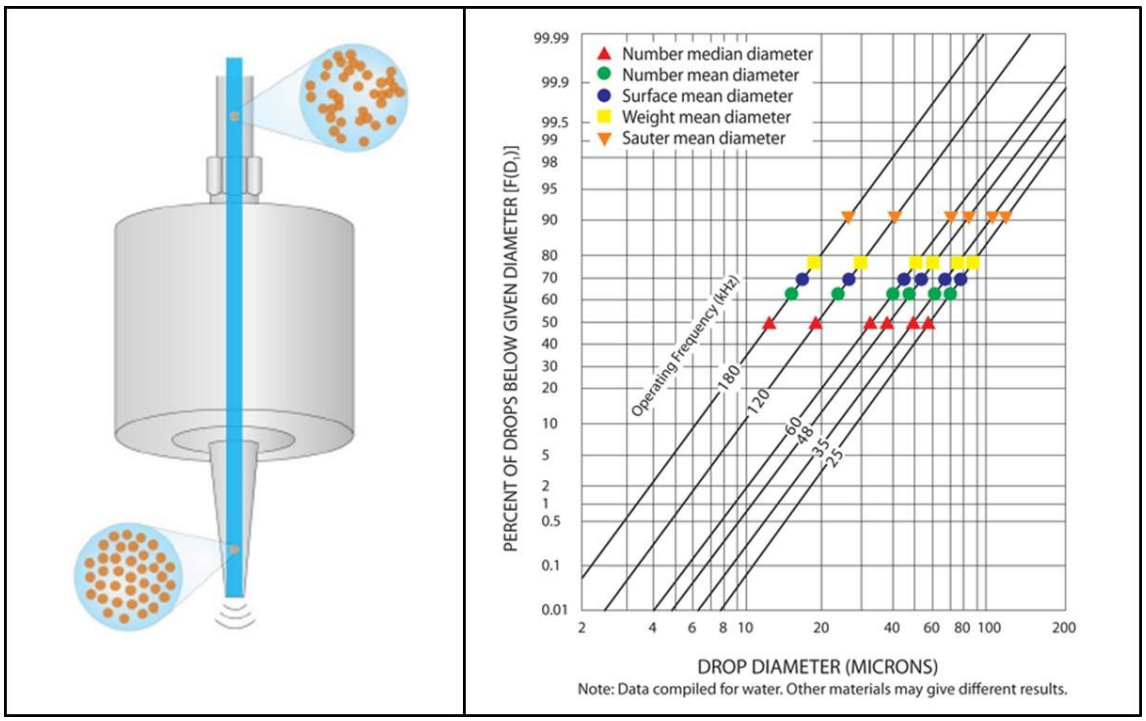

Figure 2.1 Ultrasonic nozzle (left) and droplet size distribution vs. frequency (right)

An ultrasonic spray process to fabricate membrane electrode assemblies has been applied for fuel cell testing. A commercial Sono-Tek® Exactacoat was used for this purpose. The spray parameters, such as generator frequency, ink feed rates, heater temperature, nozzle speed and height, et cetera were investigated for the production of membrane electrode assembly with Pt/C catalysts and Nafion membrane. The electrochemical performance of the ultrasonic sprayed MEAs was characterized by fuel cell testing. By optimizing the spray parameters, MEAs with high performance were successfully fabricated. The current density of the MEA reached over 1000 mA/cm^2 and 2000 mA/cm^2 at 0.6 V when operated on hydrogen/air and hydrogen/oxygen (no back pressure), respectively. The ultrasonic spray technique was found to be a versatile and promising technique for producing membrane electrode assemblies with high electrochemical performance. A thin homogeneous layer with uniform catalyst dispersion is the result of this highly automated process that provides for consistent and reproducible MEA performance. Estimations of catalyst yield and utilization are important in scaling up ultrasonic spray deposition in order to spray larger areas at faster rates. Spraying catalyst inks directly on the polymer includes causes wrinkling by solvent uptake, but heating the substrate can accelerate its evaporation and reduce this problem. By direct deposition, the electrode interface with the membrane can be intimately bonded by the procedure applied. Interfacial resistance between the electrode and electrolyte can be minimized by this process. A consistent and uniform electrode provides for better characterizations and comparisons between different fabrications.

2.3. Experimental Procedures

2.3.1. Ink Preparation and Deposition

The ink was formulated using carbon, platinum, DI water, isopropyl alcohol, and Nafion® solution (DE-521 from DuPont). The catalytic active ingredient of the ink is carbon supported platinum (HiSpec™ 9100) from Johnson Matthey Fuel Cells. The ink was first dispersed by a homogenizer for up to one hour, followed by treatment using an ultrasonic horn at 20 kHz (Sonics VCX 750) for one hour. The ink deposition was carried out using a commercial ultrasonic coater (Sono-Tek Exactacoat™) as shown in Figure 2.2. A set of spraying parameters were determined through a trial-and-error process. The ink was atomized using ultrasonic 120 kHz spray head (AccuMist™ from Sono-Tek) and carried downward to the substrate via a low pressure air stream. The diameter of the ink plume is about 2.5 mm and a stand-off distance of 35 mm is maintained between the spray head and the substrate. The atomization frequency of 120 KHz at an ink feed rate of 0.2 ~0.4 mL/min was found to work well for the ink formulation. An X-Y-Z robot was programed to spray the ink in a raster pattern directly onto the Nafion membrane (NRE-212) held onto a horizontal heating platen heated to 100 ºC. Equal amount of ink was deposited on either side of the membrane. After spraying, the MEA was protonated in sulfuric acid, washed in DI water, dried, and hot pressed at 130 ºC at 300 N/m^2 pressure for 5 minutes.

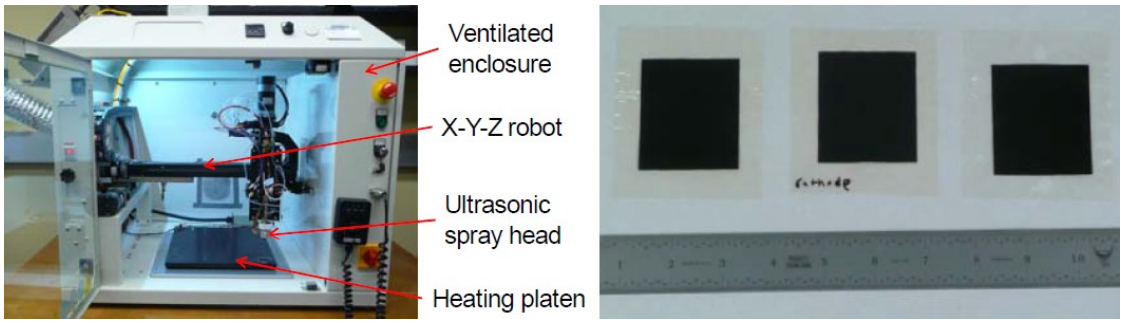

Figure 2.2 Ultrasonic spray deposition system (Sono-Tek Exactacoat) with labels and 25 cm^2 active area membrane electrode assemblies from templated fabrication

2.3.2. MEA Performance Testing and Post Analysis

After pressing and post-treatment, the MEA was assembled into 25 cm^2 fuel cell test hardware (Fuel Cell Technologies) for performance testing. Carbon paper with microporous layer (SGL 10BC) was used as the gas diffusion media. A graphite flow plate with single serpentine flow pattern was used for the anode side, and a graphite plate with triple serpentine flow field was used for the cathode side. The assembled fuel cell was connected to a fuel cell test station (Scribner Associate 840). Cell temperature was set at 75ºC, and the dew points (DP) of the fuel and oxidant were set at 75 and 73 ºC, respectively. A minimum flow rate of 300 sccm was set for both anode and cathode side reactants; when the flow rate needed exceeds 300 sccm, stoichiometric flow rates were applied. The cell was first hydrated with humidified nitrogen for one hour, and then held at 0.55 V with H_2/Air for 2+ hours to break in. Polarization curves were collected using H_2/Air and H_2/O_2, where the cell voltage was swept from open circuit voltage (OCV) to 0.4 V and back to OCV, with a 50mV increment. At each voltage step, the cell potential was held for 30 seconds. Short-term stability tests were also conducted; the cell was held at several constant voltage levels (0.8, 0.7, 0.6, 0.5 and 0.4 V) up to 2000 seconds to check the stability of cell

current and resistance.

For the estimation of platinum mass activity and specific activity, the cell was tested at 80 ºC in the kinetic-controlled potential range using fully humidified H_2 and O_2 at 150 kPa pressure; hydrogen cross-over test was also conducted by switching O_2 to N_2 while maintaining other test conditions the same, a Gamry Reference 3000 potentiostat was used to drive the cell voltage from 0 to 0.8 V at 2 mV/sec rate, the limiting current above 0.4 V was used as hydrogen cross-over current.

Cyclic voltammetry was conducted after cell performance testing. The cell was held at 35º C, humidified hydrogen and nitrogen (DP = 35º C, 300 sccm) were used for the reference and working electrode, respectively. A Gamry Reference 3000 potentiostat was used for the voltammetry scan with a scan rate 100mV/sec from 0 to 1.2 V; repeated scans (over 20 cycles) were conducted and the last scan was recorded and reported. The platinum loading of MEA was measured using X-Ray fluorescence (XRF) spectrometry (Fischer XDAL) under an absolute mode (without the need of calibration standard). For each MEA, the absolute Pt concentration (mg/cm^2) was measured at 16 points on the active area of the MEA. Since the Pt loading measured by XRF include both the anode and cathode side contribution. The average value of the 16 measurements divided by 2 was reported as the loading for each side the MEA.

2.4. Results and Discussion

2.4.1. MEA Performance

The polarization curves of an MEA with Nafion® NRE-212 membrane (from

DuPont, 50-microns thick, EW=1100) are shown in Figure 2.3; the corresponding IR-free polarization curves are shown in Figure 2.4. With hydrogen (Stoich = 3) and air (Stoich = 4) as reactants, without back pressure, the cell outputs over 1050 mA/cm^2 at 0.6 V; at 0.5 V, the cell outputs over 1500 mA/cm^2; a peak power density of 839 mV/cm^2 occurs at 0.4 V. When using hydrogen (Stoich = 1.5) and oxygen (Stoich = 2.0) as reactants, the cell outputs 2000 mA/cm^2 at 0.6V, and about 2750 mA/cm^2 at 0.5V; a peak power density of 1400 mW/cm^2 occurs at 0.5 V. Back pressurization of hydrogen and oxygen (200 kPa absolute) further improve cell performance.

Slight hysteresis was observed when the voltage is scanned from low level back to OCV, as shown in Figure 2.3. It was noticed that the returning portion of the I-V curve (cell voltage going from low to high) is located below the downward-scanning curve at high current density. The hysteresis of the corresponding IR-corrected I-V curves is much less pronounced, as shown in Figure 2.4. This indicates that the increased cell ohmic resistance after operation at high current density was likely responsible for the observed hysteresis in I-V curve.

Limiting current behavior was not observed even at very high current density. The slight downward bending trend of the I-V curve disappears after IR-correction. This indicates superb mass transport properties of the catalyst layer produced by the ultrasonic spray process. The electrode thickness was measured about ~10 μm on average. As such, with a thinner or a more conductive membrane, the cell performance can be further improved at high current density.

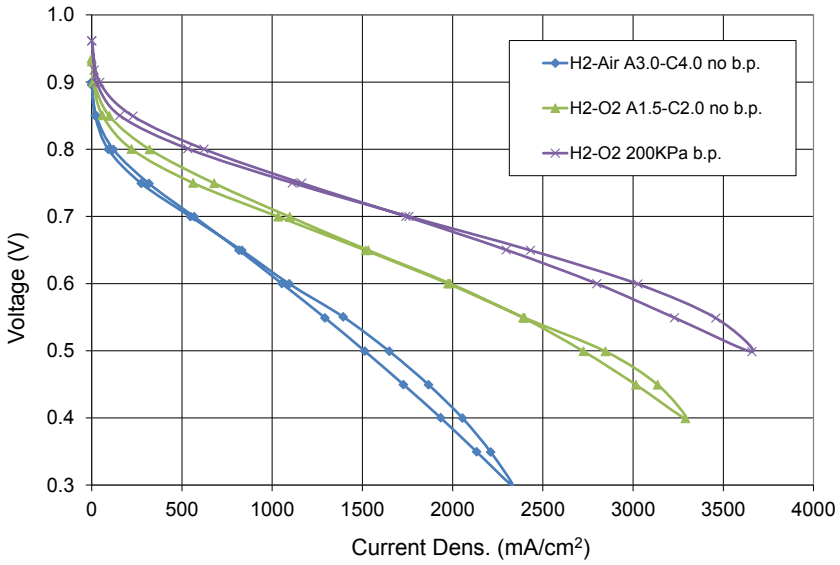

Figure 2.3 I-V performance curves of a 25 cm^2 MEA tested at different conditions; H_2-Air, H_2-O_2 at ambient pressure and H_2-O_2 with 200 kPa back pressure

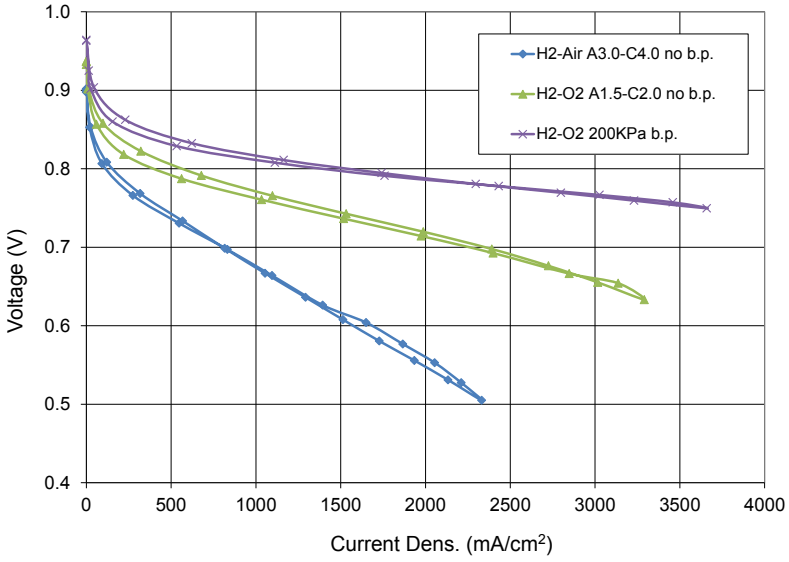

Figure 2.4 IR-free I-V performance curve tested at different conditions; H_2-Air, H_2-O_2 at ambient pressure and H_2-O_2 with 200 kPa pressure

2.4.2. Short-Term Stability Test

Constant voltage hold tests were conducted to check the cell operational stability and response during load transients (step-change). The tests were conducted using both

air and oxygen. The cell current density and the total ohmic resistance were recorded during the tests. The ohmic resistance was measured by a current interruption technique, a feature provided by the Scribner Associate 840 electronic load. At low current density (< 400 mA/cm^2), the current interruption technique is not reliable; hence the ohmic resistance for low current density was not reported.

The operational characteristic of the cell is not only related to the electrode layer but also affected by the nature of gas diffusion media, the electrolyte membrane, the flow pattern, the gas flow rates and humidification, cell operation temperature and pressure, cell cooling and heating mechanisms, etc. With the cell configuration and operation mode we used, the MEA was found to operate fairly stable at medium to low current density, as shown in

Figure 2.5 and

Figure 2.6. With the step-change of cell voltage, cell currents and ohmic resistance rapidly change and then stabilize. Since our single cell test fixture is not actively cooled; noticeable cell heating was observed at higher current. The rise of ohmic resistance is likely due to dehydration of the membrane. A better understanding of the asymmetric transient hydration behavior is depicted in poster presented in Appendix B. This is exemplified when the cell is operating at 0.4V using hydrogen and oxygen. At this condition, the cell outputs about 2500 mA/cm^2. At such a high current density, the cell temperature rises continuously. Membrane resistance is observed to rise with the cell temperature, and the accumulation of product water in the electrode and in the GDL at high current may also limit the reactant access to the electrode; as a result, the current density decreases over time.

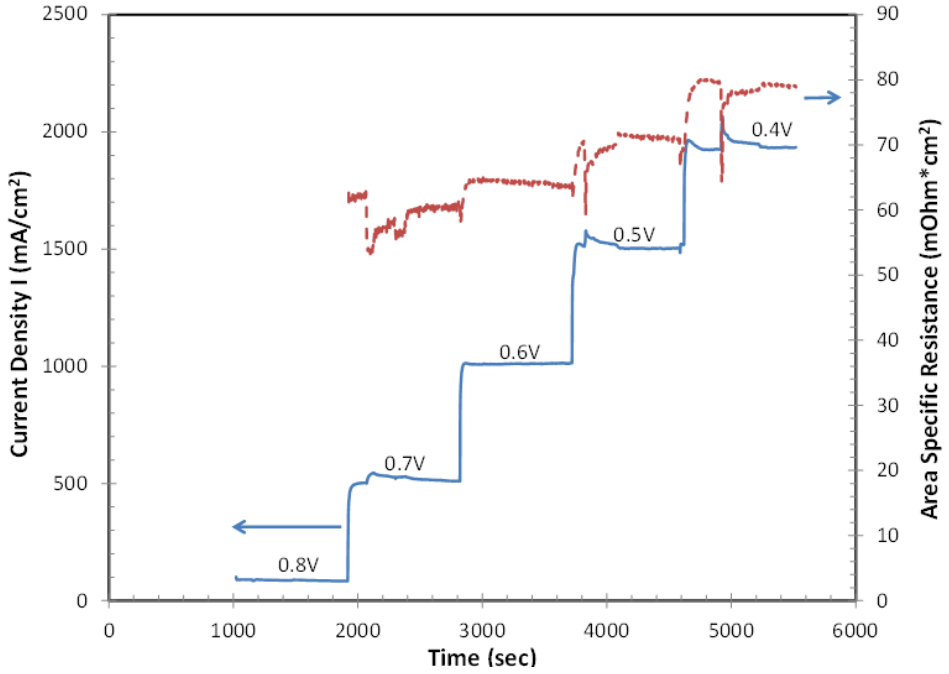

Figure 2.5 Cell current density and the area specific resistance (3/4) H_2 (Stoich = 3.0) and air (Stoich = 4.0) at 75ºC.

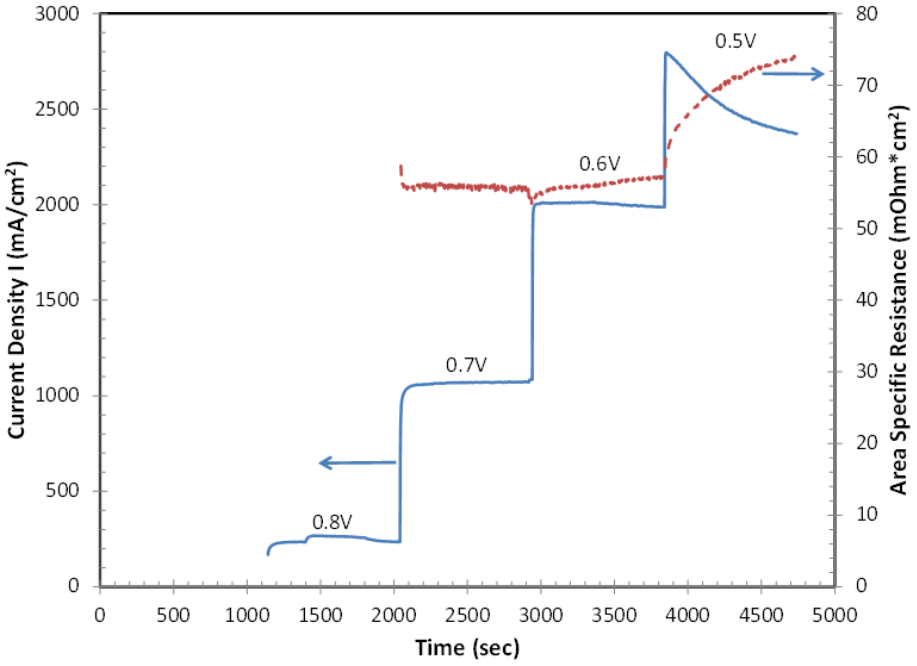

Figure 2.6 Cell current density and the area specific resistance (1.5/2) H_2 (Stoich=1.5) and O_2 (Stoich=2.0) at 75ºC.

2.4.3. Platinum Yield, Activity, and Utilization

The XRF analysis indicated Pt loading of 0.479 mg/cm^2 ($\sigma \pm 0.056$ mg/cm^2) by averaging 16 readings at different spots on the active area of the MEA. Based on the ink formulation, the platinum yield (percentage platinum transferred from the ink to the MEA) was found to be 89.4 %. This is a fairly high yield in a small-batch (3 MEAs) production considering the unavoidable losses of ink in the glass vials and plastic tubing during ink dispersion and transfer processes. Over-spray during ink deposition is also more prevalent with small geometric electrode areas. The soft spraying plume formed by the ultrasonic atomizer can greatly reduce the loss of ink by splashing and splattering from ricochet. Much lower Pt yield is typically observed when using an air-brush to spray ink onto the membrane, conversely. The cyclic voltammogram in

Figure 2.7 was analyzed to characterize the electrochemical surface area (ECSA) of the MEA. No significant change of cyclic voltammogram was observed during 20 potential cycles from 0 to 1.2 V at 100 mV/sec scan rate. After integration and baseline correction, the charge densities of the H- desorption and H- adsorption area was found to be 34 mC/cm^2 and 33.1 mC/cm^2, respectively. This translates to an ECSA of 33~34 m^2/g Pt. This represents the total surface area of platinum accessible to proton and electron.

The mass activity of the platinum catalyst was estimated to be 39 mA/mg$_{Pt}$ using the hydrogen cross-over (~3 mA/ cm^2) corrected current in the kinetic controlled region (~900 mV) of the IR-free curve. Based on the ECSA, the specific activity was estimated to be 243 μA/cm$^2_{Pt}$. The estimated catalyst activities are comparable to the activities

reported for carbon supported platinum catalysts [170]. While the measured ECA is relatively low as compared to typical values (60 to 90 m^2/g Pt) reported in literature, the good performance of the cell indicated exceptional productivity of the active sites in the electrode as well as low mass transport resistance. These results highlight the application of this ultrasonic spray deposition method for creating successful membrane electrode assemblies used in fuel cells and other related electrochemical cells.

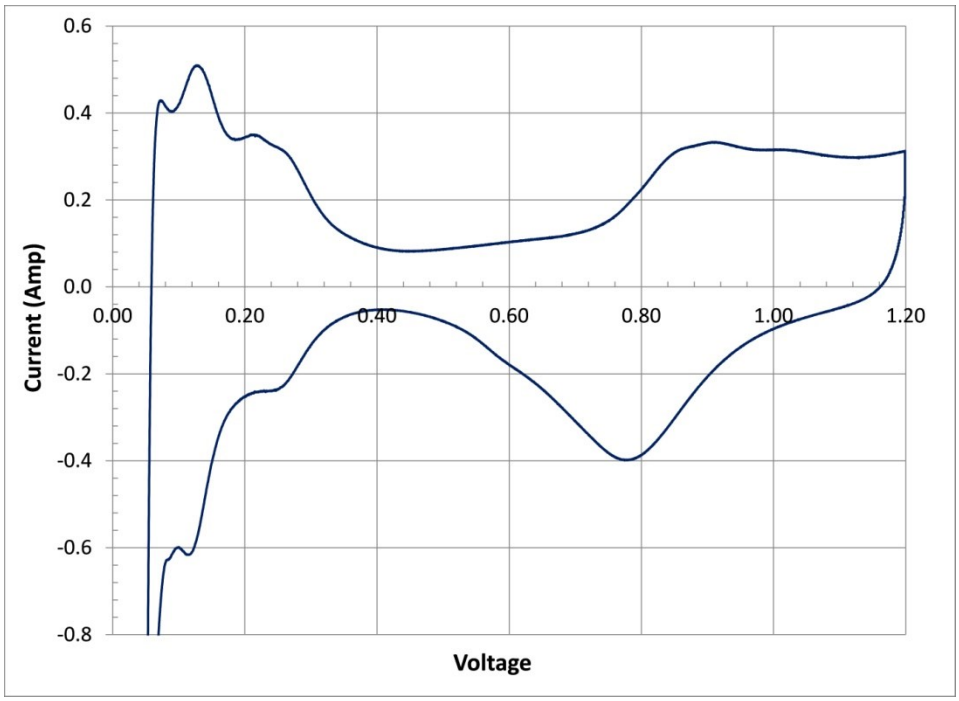

Figure 2.7 Cyclic voltammogram obtained at 35ºC

2.5. Conclusions

In summary, we have successfully developed a fabrication procedure of membrane electrode assemblies by using an ultrasonic atomization and spraying technique. The Pt/C based catalyst ink was coated directly onto the Nafion

membrane. The MEAs fabricated showed high performance and good stability. The Pt yield from the ultrasonic spraying process was found to be almost 90%, even in small-batch production. Performance from cell polarization revealed a high specific activity of available catalyst surfaces in the electrode and stable current output over a typical operating range.

2.6. Acknowledgements

This work was completed at the USC Horizon I facility. It was aided through the efforts of Jay K. Neutzler, Joshua J. Sightler, and Diana D. D. Larrabee. This work was written up for an ECS *Transaction* paper and presented by Dr. Xinyu Huang at the 220th ECS meeting in Boston, MA.

Chapter 3. Ultrasonic Spray Deposition of Unsupported Platinum Black Catalysts on Polymer Membranes for Fuel Cell Electrodes

3.1. Abstract

Proton exchange membrane (PEM) fuel cell systems were originally developed to enable NASA space exploration programs. The power producing element of a fuel cell system is the membrane electrode assembly (MEA). A process was developed to prepare MEAs for polymer electrolyte fuel cells using a direct ultrasonic spray deposition of platinum black catalyst suspensions. The ultrasonic spray head with frequency of 60 kHz is utilized for coating a thin and uniform electrode layer on the substrate. These electrodes are designed to run at high efficiency conditions when operated under pressurized H_2 and O_2 in order to meet NASA fuel cell system efficiency goal, current density of 200 mA/cm^2 with potential > 900 mV. For the electrode deposition, catalysts were suspended in a mixture of water and isopropanol solvents and an ink formulation was optimized. An improvement in the conductivity between the ion pathways can be realized by this direct deposition method on to the polymer. As a result, this electrode preparation process leads to a benefit in cell performance over conventional methods.

3.2. Introduction and Background

The goal of this work is to contribute to the operational goals outlined by NASA for a high efficiency PEM fuel cell. The design of the nanostructured noble platinum (Pt) catalyst in the cathode to optimize the oxygen reduction reaction is a goal of this work. A new construction method employing an ultrasonic sprayer was used to achieve the performance set as a NASA operating target. A composite electrode layer deposited directly on to the polymer membrane has been the key to achieving high efficiency operation. This is especially critical for this application because utilizing these fuel cells in space requires the maximum fuel utilization. Fuel storage is the main barrier in terms of mass and volume required. Therefore, the cost related to the development of the MEA should ensure that it has the best possible performance which can be maintained over the life of operation. Pt black was chosen as the catalyst for this application because it offers excellent combination of performance and durability. The progress and development in the research used to successfully complete this challenge is outlined in this report.

The main objective of this project has been to design an electrode for a PEM fuel cell which could run constantly at low current density with the maximum potential to give the greatest power density in this high efficiency region of polarization where the fuel losses are minimal. This is the most efficient region of operation for the fuel cell because the reaction kinetics are governed by current exchange density of available catalyst sites and fuel utilization is greater when other overpotential losses are minimized [[170]]. Minimizing wasted fuel, reduces the system requirements related fuel storage capacity. This electrode deposition can be applied for fuel cells and electrolyzers as well

as other related technologies. This project is part of the Electrochemical Technologies Group in Power and Sensor Systems at the Jet Propulsion Laboratory (JPL) and adds a new versatile capability to their group. A NASA goal was achieved in this project by surpassing the targeted performance above 900 mV at 200 mA/cm^2 in a hydrogen (H_2) and oxygen (O_2) fuel cell as outlined in the experimental methods section. The cathode was give special consideration for maximizing the Pt black catalyst performance, irrespective of the mass loading in the electrode.

Fuel cell systems for space operation are required to have low mass and volume so the fuel storage capacity is major limiting constraint from that regard. Therefore, the fuel cell should have the highest voltage efficiency possible [171, 172]. This requires the use of high loading content of nanostructured catalysts in electrode. The cost of the catalyst is not a concern for this project unlike most terrestrial applications. Although, alloyed Pt catalysts can exhibit better short-term catalytic activity, adding less-noble elements makes them more prone to corrosion reactions [173, 174]. The durability of the MEA is key to a long life of operation and cannot be compromised. A commercially available and stable Pt black catalyst was used for this study that focused primarily on the deposition strategy for the electrode design.

The ultrasonic spray technique can deposit a homogeneous layer of solid particles on a surface which have been delivered in solution to the nozzle head. This equipment can be purchased from an industrial vendor and used for many deposition applications. However, the research and development for this technique in the construction of fuel cell electrodes is a new and promising advancement. The frequency of the ultrasonic spray head determines the droplet size formed on the nozzle head as evidenced by equation (1)

where D is average diameter, γ (N m^{-1}) is the liquid's surface tension, ρ (kg m^{-3}) the solution density, and f (MHz) is the ultrasonic frequency [167]. At this high catalyst loading condition, the frequency had minimal effect on the electrode performance and did not cause significant variation in performance as evidenced by results in Appendix C. The droplets are then carried down to the substrate by pressurized gas in a plume formation. Many variables are considered including the flow rate, amplitude, head speed and position, gas pressure, substrate temperature, and more. The chemistry of the catalyst suspension and mixture with the other electrode ingredients including the ionomer is referred to as the ink and its preparation is also a science which is also critical to the result of the spray coating.

(1) $$D_{droplet} = 0.34\, x\, \left[\frac{8\pi\gamma}{\rho f^2}\right]^{1/3}$$

The preparation of the catalyst in the ink has been another area of the development important area of progress in this project. The electrode ink is made from a suspension of platinum catalysts and ionomer. Heavy platinum catalysts have a high mass density and can be difficult to keep in suspension. The ionomer is dispersed best in isopropanol and low molecular weight alcohols. However, Pt black cannot be suspended in alcohols directly because strong surface interactions in this solvent cause significant agglomeration and there is also a high probability of burning during solvent evaporation. Water prevents burning, and it is also better for inhibiting nanoparticle surface interactions when suspending the Pt black. The nanostructured Pt powder must be mixed with the ionomer in solution, but has the propensity to agglomerate and precipitate because of fast combination between the two ingredients. One way to prevent

agglomeration and improve dispersion quality is through addition of oxidized carbon nanotubes into the ink as demonstrated in Appendix D. They are first mixed with the ionomer in water and alcohol before being added to the Pt black suspension. It is proposed that protons in polar sulfonic acid groups in the electrolyte are complexed by hydroxyl groups on CNT that expose only the hydrophobic backbone which has less interaction with the catalyst surface and prevents entanglement [[175]]. Carbon could not be added to NASA electrodes though due to durability concerns. A strategy to control the preliminary ultrasonic mixing step under water controls the fast interaction between the ionomer and platinum. Isopropanol is not added until the final step when mixed in fixed proportion with water. Alcohol promotes the dissolution and strong interfacial contact between the PEM and the ionomer fused into the electrode layer during spray deposition. The mass transport to active surfaces is improved through minimizing the thickness of ionomer coverage on catalysts in the electrode. As a benefit, the resistance between the composite layers in MEA can be reduced. This is especially important for lowering the ionic resistance which dominates the cell resistance.

3.3. Experimental Procedures

A Prism 400 ultrasonic sprayer (USI) was used for this project with a spray head operated at 60 kHz. The ink was injected to the spray head by a syringe pump at 0.2 mL/min. The spray nozzle was adjusted 2.5 cm above the substrate and moved at 1 cm/sec in a raster pattern to form a spray line width of 0.25 cm until the total volume of the ink has been the templated substrate with targeted Pt catalyst loading ~ 5 mg/cm^2 .

The substrate was heated up to 90 °C to evaporate the solvents out of the PEM used, Nafion® NRE-212. This material has some of the most desirable properties for the fuel cell operation. The sprayed MEA was pressed under 250 N/cm^2 at 135 °C for 5 minutes. The MEAs were then soaked in 85 °C water and dried before cell build.

All fuel cell tests were conducted at the same conditions with same hardware and test station (Fuel Cell Technologies). The 25 cm^2 hardware had a single serpentine flow plate for the anode and a triple serpentine flow plate for the cathode. The cell was torqued at 9 N·m with 0.25 mm polytetrafluoroethylene gaskets and 10 BC (SGL) gas diffusion layers. The cell was heated to 70 °C and operated with H_2 and O_2 under absolute pressures of 1.5 or 3 atmospheres. Minimum flow rates of 100 mL/min were enforced as well as a reactant stoichiometric flow of 3 for both gases. Cell break-in was performed before all polarizations were collected in a cathodic sweep from 0 to 30 amps.

The preparation of catalyst ink was found to be critically important in the development in the successful spray deposition of a high performance electrode. The Pt black powder, Hi-Spec® 1000 (Johnson-Matthey), has a surface area of 27 m^2/g and the ionomer used was a 5% Nafion® solution, DE-521. The two ingredients were initially mixed separately in water. Two mass ratios of 1:10 and 2:10 of the Pt content were used. The Pt catalyst in water was slowly added to the ionomer by injection under constant stirring. The stirred mixture was then either introduced to SpeedMixer™ at 3000 rpm or dispersed under a 450 W Branson ultrasonic horn disruptor with fixed 20 kHz on pulsed medium amplitude setting for 5 minutes. During or following this step, isopropanol was added to the suspension to form either a 10% or 50% equivalent volume fraction with water. The optimized ink was found to maintain the catalyst suspension for improved

transfer yield, preventing spray congestion and particle agglomeration, as well as an improved ionomer distribution in the electrode.

3.4. Results and Discussion

Four successful MEAs were fabricated with the experimental method using the ultrasonic sprayer from Figure 3.1 and a representative sample is shown in Figure 3.2. Figure 3.1 is provided below to highlight the differences in ink preparation and the processing methods for preparing each MEA that was tested for performance.

1. 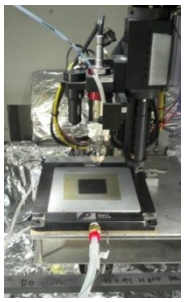

2. **a)** 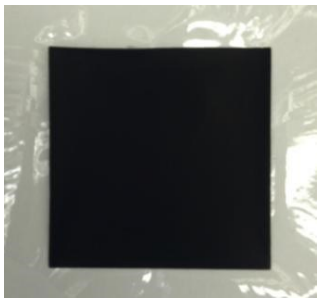

b) 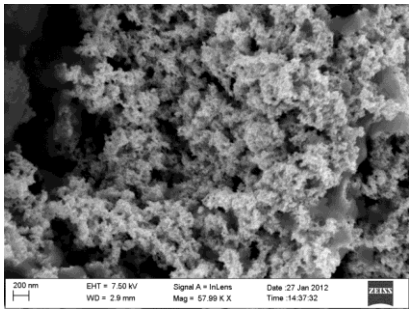

Figure 3.1 The ultrasonic spray head is shown above the heated polymer electrolyte

Figure 3.2 a) A catalyst coated membrane electrode assembly and b) is a field emission SEM image of the cathode structure with ionomer infused

Table 3.1 The summary of MEA preparation variables matrix

MEA	H_2O : IPA	Mixing	Nafion : Pt
1	10:90	speed mixer	2:10
2	50:50	speed mixer	2:10
3	50:50	ultrasonic horn	2:10
4	50:50	ultrasonic horn	1:10

The last MEA prepared by method 4 showed the best performance after adjusting the spray deposition procedure. Mixing under water before Nafion addition minimizes agglomeration and maximizes the added ionomer content. Thus, less ionomer was needed for binder. These electrodes did not require the use of PTFE for its water transport properties. The performance was the best on record for Pt black catalysts ever recorded in the Jet Propulsion Laboratory (JPL) at Caltech. The differences for the polarization between MEAs 1-4 at 1.5 and 3 atmospheres are shown in Figure 3.3. The previous best performance from a conventional spray method at JPL is shown for relative comparison purpose in Figure 3.4.

a)

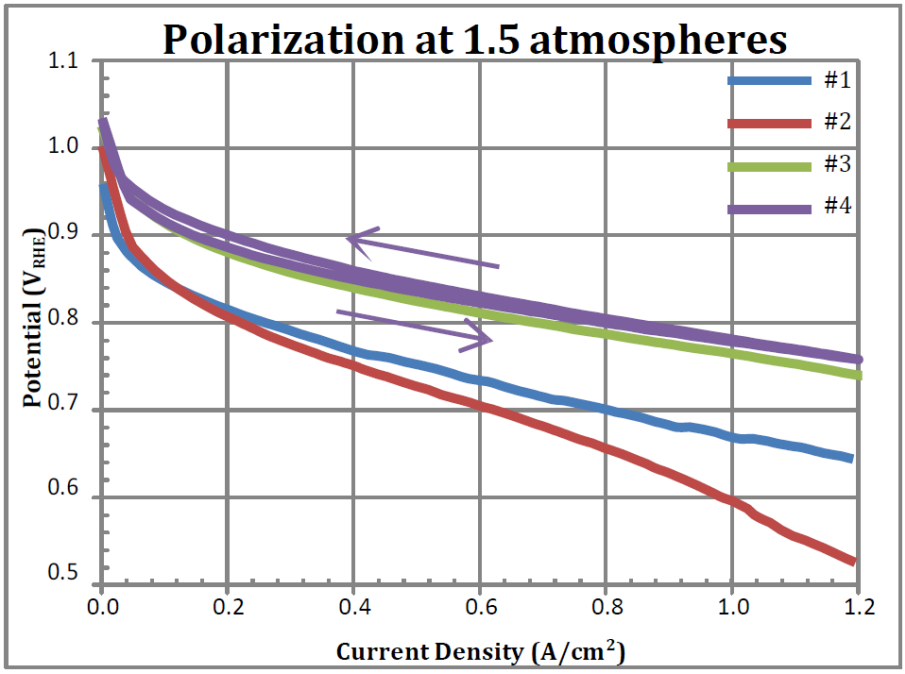

b)

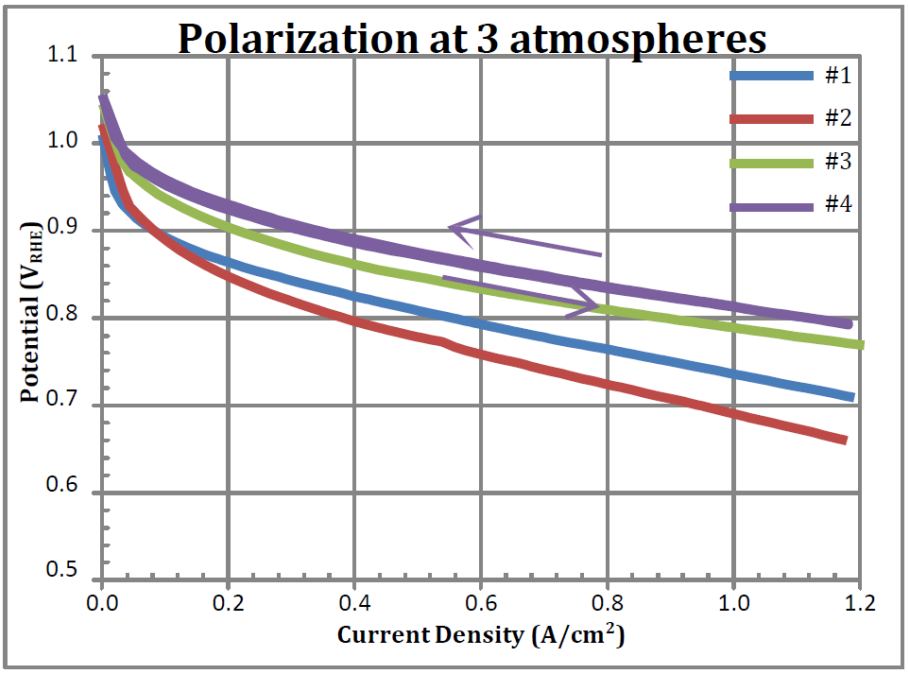

Figure 3.3 Polarization plots for fuel cell MEAs #1-4 under a) 1.5 and b) 3 atm b.p.

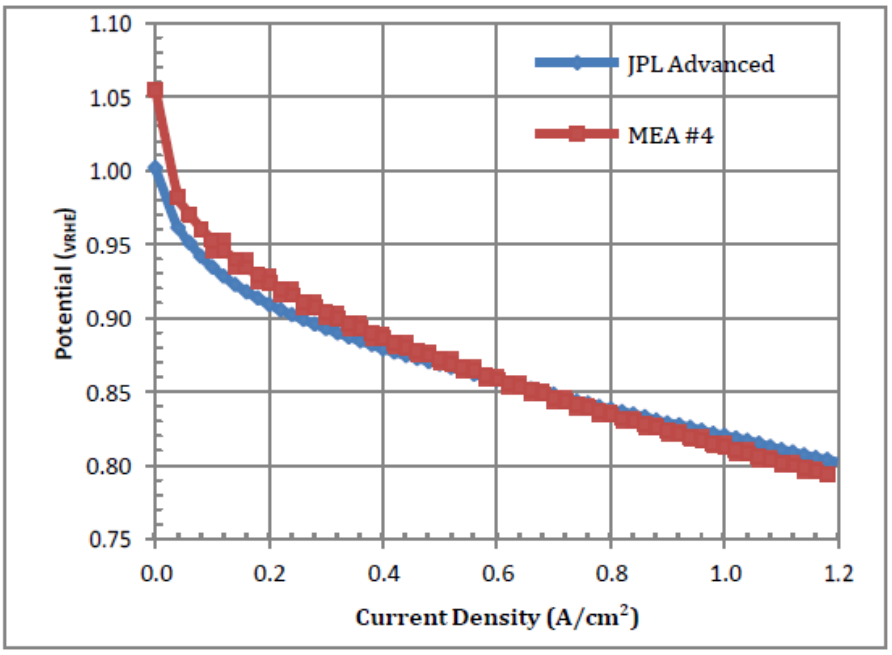

Figure 3.4 Relative comparison of the best MEA #4 to the best JPL performance

Advancements in the MEA development were made in each step from MEA #1-4. The first transition from the 10:90 to the 50:50 water:isopropanol (H_2O:IPA) solvent

increased the metal distribution in the suspension and within the ionomer. It is suspected that this resulted in a higher open circuit potential, but lower mass transport at high current due to over coverage of platinum surfaces with ionomer. The second variable used the same ink formulation, but added the ultrasonic mixing step which seemed to vastly improve the nanoparticle suspension in the ink. This was evidenced by decreased solid separation and improved transfer yield into a fine and homogeneous electrode on the polymer. Ultrasonic mixing had the single greatest contribution to the MEA performance over the speed mixer which combines rotational forces on different planes for fast mixing as seen in Figure 3.5 a and b. The polarization curve shows an increase of more than 50 mV at the 200 mA/cm^2 current density at 3 atm condition. The third step decreased the Nafion:Pt content from 2:10 to 1:10. This resulted in the highest measured value for MEA #4 which produced 200 mA/cm^2 well above 0.92 V, exceeding the NASA target performance. This polarization may very well be the highest ever recorded at this condition which is considered ideal for space operation. This equates to a voltage efficiency of > 75% and lead to reduction of fuel consumption for a fixed system output.

a) 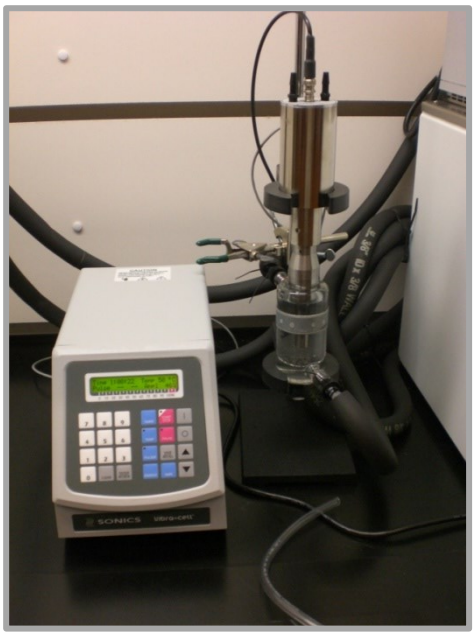 b) 

Figure 3.5 a) Ultrasonic horn disruptor shown with controller and b) SpeedMixer™

3.5. Conclusions

An ultrasonic spray deposition technique was optimized to produce MEAs for PEM fuel cells that meet critical NASA performance targets. Voltage efficiency of at least 72% was sought for performance under H_2 and O_2 at 3 stoichiometric flow, 3 atmosphere (absolute), and 70 °C operated at 0.2 A/cm^2 current density setting. Processing strategies from the suspension of commercial catalyst mixed with ionomer in solvents under ultrasonic agitation led to the best spray deposited electrode which had a voltage efficiency > 75% or 0.924 V_{Cell} during a cathodic polarization sweep at this condition. Electrode spraying on to the polymer by this highly automated and controlled process can improve the interfacial contact between the composite layers in the MEA. The direct deposition of Pt black catalyst on the PEM results in high performances that exceed critical NASA operation goals.

3.6. Acknowledgements

I appreciate the support of mentor, Dr. Thomas I. Valdez, and from other staff of Division 34 including Adam Kisor, Keith Billings, Dr. Gerald Voecks, and Dr. Shiao-Ping S. Yen. This project was completed under the Student Internship Program at Jet Propulsion Laboratory managed by California Institute of Technology and funded by the National Aeronautics and Space Administration. The collaboration was also facilitated by the partnership of my graduate education at University of South Carolina with support from the Graduate Research Assistantship received through the South Carolina Space Grant Consortium.

Chapter 4. Doped Strontium Titanate Catalyst Supports for Platinum in Proton Exchange Membrane Fuel Cell Cathodes

4.1. Abstract

Strontium titanate catalyst supports were tested for efficacy as catalyst supports for platinum in the cathode of PEMFC cathodes. A literature review on conductivity preempted the case study on synthesis of a high surface area perovskite oxide (ABO_3). Niobium donor dopant was added to substitute for titanium in the B-site of the oxide for added conductivity. A ceramic processing procedure was applied to prepare supports in the laboratory that were characterized and measured for stability and resistance. Platinum deposition by polyol reduction offered a composite electrocatalyst. Powders were mixed into an ink with carbon nanotubes and formed into an electrode by ultrasonic spray process. A cathode was tested for performance and durability. Accelerated stress tests provide a valuable insight into the mechanism of degradation that will be valuable in design of metal oxide catalyst supports.

4.2. Introduction and Background

A preliminary case study was conducted on strontium titanate with donor doped substitution of the B-site by niobium ($SrTi_{0.9}Nb_{0.1}O_{3-x}$) in perovskite ($ABO_3$) oxide structure as a catalyst support. Some metal oxide materials could be considered a possible alternative because they offer several advantages to carbon. They are used in many catalyst support applications, but are often not considered for fuel cell electrocatalysts because of the electronic conductivity obligation. Introducing dopants into the ceramic crystal structure is an effective way to create defect concentrations which can render the effective charge carrier concentration. This conductivity is found to be a function of the oxygen partial pressure at high temperatures. Defects can be locked in during quenching at these conditions to provide for some conductivity at low temperatures. The idea is to use metal oxide alternatives which show phase stability in the electrolyte environment of the fuel cell and also can serve as a conductive phase even though charge carriers don't have same mobility at typical operating temperatures.

The strontium titanate cubic perovskite has the potential to exhibit high electronic conductivity when donor atoms of higher oxidation state are substituted or doped into the A or B-sites of the ABO_3 coordination. Several reports have indicated that doping strontium titanate with donor niobium (V) on the titanium (IV) B-site in the perovskite can even induce an insulator to metal transition in the material by promoting electrons at defect states into conduction band. It is considered n-type conductivity when shallow Nb donors substitute Ti via reaction 1 for these Schottky defects in Kroger-Vink notation.

(1) $Nb_2O_5 \xrightarrow{2\,TiO_2} 2\,Nb_{Ti}^{\cdot} + 4\,O_O^X + \frac{1}{2}\,O_2 + 2\,e^-$

(2) $O_O^X \rightleftharpoons V_O^{\cdot\cdot} + 2\,e^- + \frac{1}{2}O_2$

When this is synthesized at low oxygen pressure, the positive niobium and oxygen vacancies formed via reaction 2 become charge balanced by excess electrons. These electrons are localized around the positive defect centers. It is reported that the conductivity can be several orders of magnitude higher than that of rutile titania in low oxygen pressures, $P(O_2)$. In this case, the conductivity is formed by quenching defects in the structure. It can be evidenced in the work, that p-type conductor which is typically prepared in higher $P(O_2)$ may be more suitable for future approaches in the cathode of low temperature fuel cells. Though, a dopant strategy can be employed to effectively improve electronic properties of support metal oxides with engineered defects.

This section includes reviews of defect chemistry in conductive oxides with detailed discussion on strontium titanate. Alternatives to traditional catalyst support materials in fuel cells are needed to lower their cost and improve the operative lifetime. Strontium titanate is one possible solution that offers unique conduction behavior over a range of temperatures and oxygen pressures. The material is widely used as dielectric in insulator and capacitor, but as charge carriers are introduced they can exhibit semiconductor and metallic conductivity which can even transition to superconductivity at very low temperatures. Donor-doped strontium titanate introduces mobile electron carriers into the structure which are compensated by positive donors and oxygen vacancies in the reduced condition. The electron conductivity which could be maintainable at low temperatures in these materials also makes them attractive for many other functions, including proton exchange membrane fuel cells (PEMFCs) as potential

electrocatalyst supports. Their use for catalyst supports has primarily been demonstrated at high temperature, but the application to low temperature electrodes may offer some significant improvements over conventional carbon materials; tolerance to impurities in the anode gas stream and resistance to catalyst poisoning, the strong metal-support interaction can resist corrosion by Pt dissolution, and the formation of high surface area nanostructured platinum crystallites with a preferred epitaxial orientation. These benefits all suggest that a further analysis of donor-doped strontium titanate is a worthy investigation.

Donor-doped strontium titanate ($SrTiO_3$) ceramics have found application in sensors, varistors, grain boundary layer capacitors, and catalysts. This wide range of applications is dependent on the defect chemistry of strontium titanate and customized properties by varying the processing parameters. The crystalline perovskite ABO_3 can be donor doped on the A or B site to introduce mobile electron carriers into the lattice compensated by oxygen vacancies and cation substitutions [97, 176]. A long history of research on the material has led to a well-developed understanding of the structure-property relationships and conduction mechanisms. It was predicted for the first time that a metal oxide, strontium titanate, could exhibit superconductivity at low temperatures near helium freezing point and a study of electronic energy bands later predicted this oxide could also display near metallic conductivity at higher temperatures [177, 98, 178]. The superconductivity transition was soon verified in 1967 and the low electronic resistivity at intermediate temperatures was considered "remarkable" [179]. An understanding of electron energy bands and more recent models developed by density functional theory explained how doping and reduction could introduce shallow donors

into the conduction band [180-182]. Many experiments have fine-tuned the processing parameters by high temperature calcinations and sintering to reach an optimal conductivity in ideal operational ranges. Much of the application focus and testing has been recorded at high temperatures. For example, it has generated some interest as an SOFC anode because of its satisfactory conductivity in reducing environments and added benefit of tolerance to catalyst poisoning by reactant impurities [183]. Only a few useful applications have arisen at room temperature including piezoresistivity and oxygen gas sensors. An attempt to use the material as a low temperature electrode and catalyst support is the motivation behind this review and the properties of the material in this application will be proposed. Metallic conductivity has been proven through several processing techniques that reveal an ideal performance for this application although very few papers have reported the material properties in this condition and nothing has been published on this potential possibility. An attempt to review the relevant literature and a proposal for the experimental work on the material is provided.

Donor-doped strontium titanate is commercially available at low cost and relatively simple to produce, but can offer some advantages to the limitations on carbon electrodes. The primary benefit is the strong metal-support interaction between Pt catalysts and titania supports as first described in 1978 by Tauster [89]. This effect is attributed in part to the intermetallic orbital overlap with Pt nanoparticles providing homogeneous distribution and high surface area. The well bonded material is less likely to disassociate, dissolve, and agglomerate. The strontium titanate supports also have proven some benefit in catalysis which increase tolerance and reduce poisoning susceptibility. In a heterogeneous catalysis application, it was found that nickel

supported on strontium titanate showed the highest coking tolerance of any perovskite [184]. The reduced metal donates an electron to the interface with platinum to form the strong-metal support interaction which can extend the catalyst surface to the support by creating a defect rich region that surrounds catalysts with hydroxylated surfaces as seen in. They presented a concept for the improved reactivity in oxidation reactions based upon a "spillover effect" of adsorbed hydrogen and carbon monoxide. Based on ab initio calculations and density functional theory, this model reflects adsorption energies on the surface of titania supported platinum. Titania can suppress Pt chemisorptive bonds impurities like CO to enhance oxidation reactions on the catalyst surfaces. This however would be more applicable to the anode of the fuel cell.

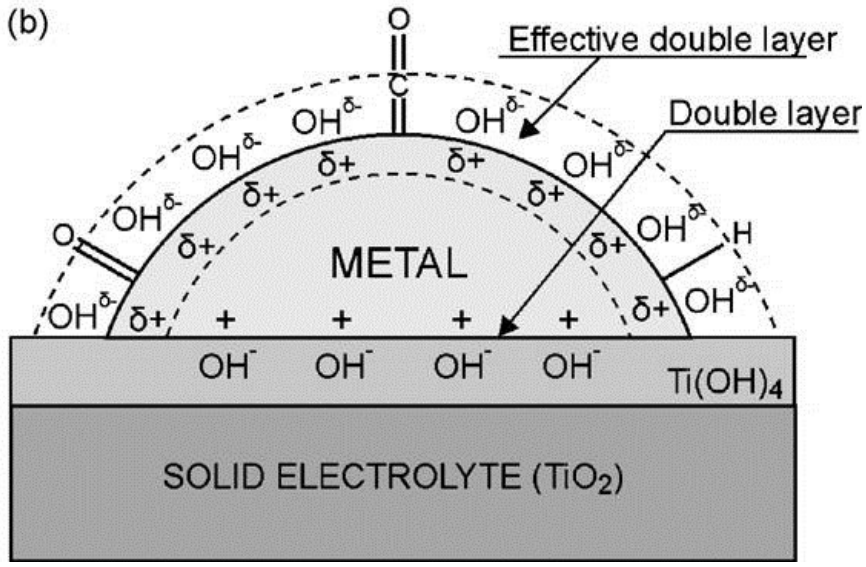

Figure 4.1 Titania can form reactive hydroxyls near the catalyst interface [185]

Since an article was published in 2002 detailing some advantages of doped titania as a conductive electrode for electrolyzer and fuel cell applications, many recent efforts have also sought the utilization of this catalyst support [82]. In the past decade and

especially in the past 3 years, several prominent groups have explored the use of oxide catalyst supports in low temperature fuel cells including the use of conductive niobium-doped titania [115]. A chemical engineering group at USC showed promising performance of a titania supported catalyst which held significant improvements in corrosion resistance over conventional carbon, but their performance was still limited by low electronic conduction and low surface area [117]. To circumvent the problem, a high Pt mass ratio was used to cover surfaces of the oxide support while conductive fillers were also added into the electrode in some cases. These titania supports have already been oxidized to some extent and thus can resist further corrosion. No publications could be found on the use of conductive perovskite oxides for this application even though they could possibly lead to much better electronic conductivity.

Oxide supported catalysts have been explored for their benefits in heterogeneous catalysis and photocatalytic reactions, although these reactions do not necessarily rely on high electronic conductivity. As a result, most of the publications have been focused on insulator or semi-conducting strontium titanate. Many significant advances have been made in the deposition of catalysts on titania supports for these applications while developing models for their strong interaction. As recent as March 2011, an intriguing paper discussed the effective distribution of ~ 2 nm Pt catalysts on high surface area strontium titanate nanocuboids. The paper by Enterkin et al. showed the favorable formation of oriented Pt (100) surfaces as shown in Figure 4.2 [186]. The Pt (100) family of planes has the highest measured catalytic activity for the oxygen reduction reaction in acidic environment [187]. Epitaxial orientation also piqued interest in possible application of conductive strontium titanate nanocuboids as high surface area electrocatalyst supports

for PEMFC applications. In this case, the Pt lattice can also be strained by small changes in crystals of the support oxide.

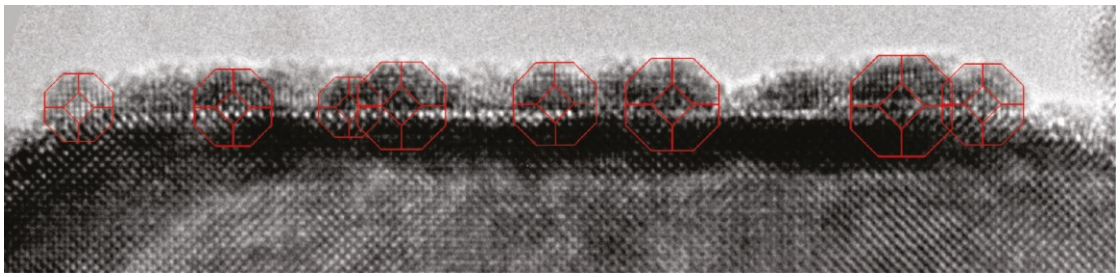

Figure 4.2 Epitaxially oriented catalytic Pt nanoparticles on {100} $SrTiO_3$ [186]

Strontium titanate maintains a cubic perovskite phase from about 110 K up to its melting temperature [177]. This ABO_3 configuration is comprised of the larger Sr^{2+} on the A-site at the center of the cube and the smaller Ti^{4+} on the B-site at the corner positions. Six oxygen ions O^{2-} are located at the cube edge centers thus forming TiO_6 octahedral units as shown in Figure 4.3 below. A near 1:1 stoichiometric ratio of A:B is required to maintain phase uniformity. The ferroelectric or magnetic property associated with the tetragonal phase is formed below the Curie temperature ~110 K, but will not be discussed in detail because the equilibrium at higher temperature involves only the perovskite structure. The un-doped crystal is an intrinsic wide-band gap insulator with $E_g \approx 3.2$ eV, but when reduced, it can become an n-type semiconductor [188]. Large STO single crystals have been used for insulators and capacitors because of its high dielectric constant [177]. Introduction of oxygen vacancies and donor substitutions are compensated by free electrons and change its conductivity behavior drastically as evidenced by Chan and Smyth [189]. Polycrystalline materials have also been created that can change conductivity by a grain-boundary mechanism that may account for some of the

discrepancies in early publications. The evolution of material understanding began in the 1960's and rapidly developed after the superconductivity of the material below 0.35 °K was demonstrated for the first time in a metal oxide [179].

An interesting progression from the theoretical predictions to real experimental results ensued. A theoretical examination of the energy bands by linear combination of atomic orbitals (LCAO) method was proposed by Kahn in 1964 [98]. In the same year at the National Bureau of Standards, experimental evidence showed that ferroelectric relationship and the phase transition temperature to tetragonal [177]. The prediction of energy bands and high electron mobility at low temperature was verified. Compared to the rutile crystal structure, the cubic perovskite showed lower electronic resistance due to lower phonon drag. A couple years later, the piezoresistance and the effect of increased carrier concentration *n*, was achieved by donor dopants like niobium [178, 190, 191]. The mechanism for this effect was related to ionized impurity scattering a low temperatures <10 °K, but the high electrical conductivity at the intermediate temperature ranges could not be explained by conventional theory and was thought to be a collision (ballistic) process contributing to electron scattering [83]. The Hall mobility, Seebeck coefficient, and resistivity were experimentally measured at low temperatures as well as the presence of several electron acceptor levels by optical absorption, but the understanding for the behavior would not come about until later [188, 192]. Advanced analytical techniques and evolution of DFT models would show the insulator to metal transition resulting from the presence of electron conduction bands near the valence band in the material.

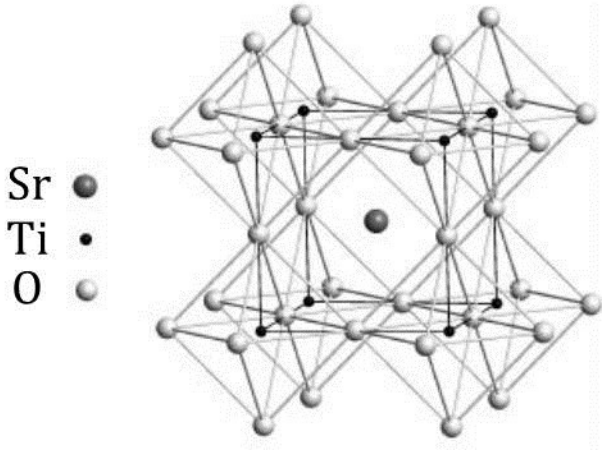

Figure 4.3 $SrTiO_3$ cubic perovskite crystal structure with lattice parameters a = 0.3905 nm, and ionic radii Ti^{4+} = 0.061 nm, and Sr^{2+} = 0.144 nm

Extrinsic defects such as aliovalent ions are often intentionally introduced as point defects (dopants). Donor dopants introduce cation substitutions on A or B sites with elements in higher oxidation state. The most important criterion for a possible substitution of A or B site ions by dopants is a comparable ionic radius of the dopant to maintain solubility. In the case of donor doped strontium titanate, a +3 cation on the Sr^{2+} and a +5 cation on the Ti^{4+} sites are substituted. Typically, La^{3+} and Nb^{5+} are used because their ionic radii, electronegativity, atomic size, and valence are most similar in accordance with the Hume-Rothery rules. The ionic radius of La^{3+} with coordination number of 12 is 0.136 nm and that of Nb^{5+} with coordination of 6 is 0.064 nm according the *CRC Handbook for Chemistry and Physics*. For this reason, these cations offer the best donor dopant solubility and are consequently the most comprehensively studied. However, other dopants have been investigated like dysprosium and gallium on the A-site; vanadium, tantalum, antimony, scandium and molybdenum on the B-site.

Donor dopants can be effectively substituted into the structure if their solubility is high. Phase uniformity proves their inclusion. Techniques like X-ray diffraction have

shown that doping does result in single phase material as seen in Figure 4.4. The distortion of the crystal lattice however may change with doping and defect concentration. It is generally predicted and observed that donor dopants increase the lattice as a result of relaxation of nearest O ions from reduced interaction between donor and Ti^{3+} centers [193]. The effect has been measured for many dopants and typically follows a linear relation with the dopant concentration. This correlation is plotted for niobium doped strontium titanate in Figure 4.5.

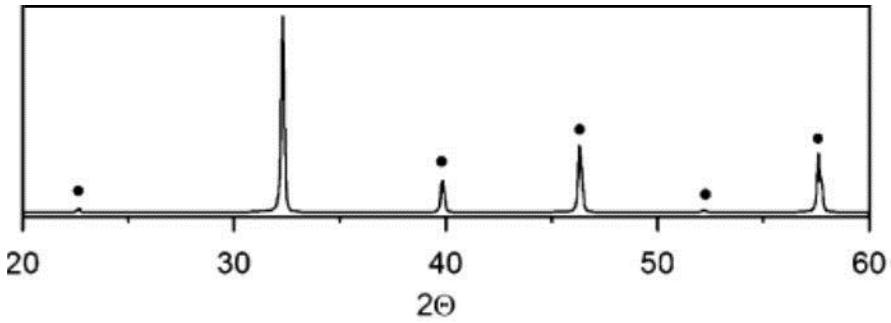

Figure 4.4 XRD crystalline peak peaks of $SrTiO_3$ perovskite structure [194]

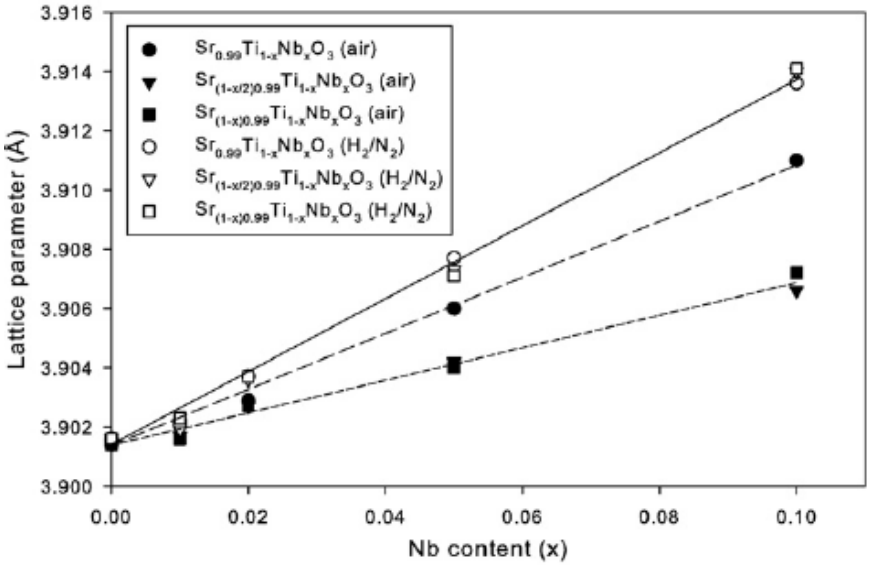

Figure 4.5 Lattice parameter plotted as function of Nb dopant [193]

The defect chemistry is related to Schottky type since interstitials are not favorable in the perovskite structure so the cation substitutions result in positively charged extrinsic defects [193]. Because of the overall charge neutrality condition in a crystal, the formation of charged defects is accompanied by the formation of oppositely charged defects. These processes can be considered in terms of defect-chemical reactions and must obey mass, site and charge balance. Defect concentrations are coupled via laws of mass action. The conduction band is made up of reducible Ti^{3+} 3d states and lies just above the valence band [182]. Therefore, the compensation of donor defects can be compensated by electrons in the conduction band.

A simple understanding of electronic conduction has not been easy to elucidate and many groups have attempted its explanation. The introduction of shallow donor dopants shifts the position of the Fermi energy level about 0.25 eV from below the conduction band gap around 3.3 eV [195]. The addition of Nb^{5+}, although reducible, was not observed to change oxidation state, but did enhance overlap of Ti 3d orbitals evidenced by X-ray absorption of near edge structures and these states of electronic compensation could become partially "frozen" in [196]. Electron doping of intrinsic crystals are not just simple 3d metal states, but hybridized Ti 3d and O 2p orbitals as found by angle-resolved photoemission spectroscopy [197]. The doping effect could not be described well within the rigid-band model, even at low doping concentrations [198]. This may be a result of the complexity of possible spatial configurations and complex chemical bonding [199].

The modeling efforts and analytical investigations have correlated with the experimental studies to explain the defect chemistries. In 1981, a comprehensive analysis

of the defect chemistry was attempted by Chan, Sharma, and Smyth [189]. This material and its properties, however, are notably one of the most difficult to understand [97]. The effect of defect concentration on conductivity has remained one of the most direct measurements. Although, it is speculated that some authors may have found different results based on processing procedures and the effect on grain size, grain boundaries, and separation of phases [200, 201]. The diffusion and segregation of phases evidenced at high temperatures does not change the fundamental chemistry of the doped perovskite [202]. Specifically, it was observed that Sr cations which compensate at intermediate $P(O_2)$ range can form SrO surface moieties [180, 189, 202-205]. Precisely controlling the Sr/Ti ratio to less than 1 could be used to avoid this effect in Nb-doped strontium titanate [206]. The conversion of insulating to metallic type strontium titanate was reported by several groups, but the equilibrium defect chemistry was best explained by Moos and Hardtl at high temperatures and described below.

The electrical conductivity is in direct relation to the defect concentration. The equilibrium defect concentration varies with environment conditions. Specifically, increases in temperature and pressure of oxygen return the donor-doped perovskite to its equilibrium configuration without vacancies or atomic substitutions. However, these defects can be energetically favorable under specific circumstance. When the material is synthesized, reducing conditions and low oxygen partial pressure create the greatest number of defects and compensating electrons in the structure [97]. A goal of this work is to understand the formation of donor substitutions and vacancies in the structure. These defects will be expressed in terms of Kröger-Vink notations and diagrams for the examples of La and Nb.

Because the reducing conditions are most relevant to the formation and operation of the conductive material in this instance, it will be discussed first and in the most detail. The relation to oxygen pressure is very critical and is the independent variable of the Kröger-Vink diagram. Several regions are observed in the diagram which relate to the ionic and electronic compensation for A and B site doping from Regime I-III pertaining to O_2 pressure low to high.

By doping the A site with La,

(3) $$La_2O_3 \xrightarrow{2\,SrO} 2\,La_{Sr}^{\cdot} + 2\,O_O^X + \frac{1}{2}\,O_2 + 2\,e^-$$

The equilibrium reaction for oxygen at low pressures is:

(4) $$O_O^X \rightleftharpoons V_O^{\cdot\cdot} + 2\,e^- + \frac{1}{2}O_2$$

The mass action law follows this expression for the equilibrium constant K for electrons

(5) $\frac{[V_O^{\cdot\cdot}]*[n]^2}{[O_2]^{1/2}} = K_n$ where $[O_2]$ = Partial pressure of O_2 or $P(O_2)$

At low $P(O_2)$, where e^- compensates for the oxygen vacancies $[n] \approx 2[V_O^{\cdot\cdot}]$

(6) $\frac{1}{2}[n] * [n]^2 = K_n * P(O_2)^{-\frac{1}{2}}$ therefore,

(7) $[n] = (2K_n)^{\frac{1}{3}} * P(O_2)^{-1/6}$

At intermediate $P(O_2)$, where [n] compensates for $[La_{Sr}^{\cdot}]$, the $[V_O^{\cdot\cdot}]$ becomes negligible [207]. Electron carrier concentration depends on donor content which does not vary with $P(O_2)$.

At the high $P(O_2)$ condition, the reaction takes the following form,

(8) $$\frac{1}{2}O_2 \rightleftharpoons O_O^X + V_{Sr}^{''} + 2\,h^{\cdot}$$

By substitution of the charge neutrality, $2[V_{Sr}^{''}] \approx [La_{Sr}^{\cdot}]$ into mass action equation

$$(9) \quad [V_{Sr}''] * [p]^2 = K_p * P(O_2)^{\frac{1}{2}} = \frac{1}{2}[La_{Sr}^{\cdot}] * [p]^2$$

$$(10) \quad [p] = (\frac{2\,K_p}{[La_{Sr}^{\cdot}]})^{1/2} * P(O_2)^{-\frac{1}{4}}$$

Since $K_I = np$, the intrinsic equilibrium constant then

$$(11) \quad [n] = {K_I}/{[p]} \text{ and}$$

$$(12) \quad [n] = \frac{K_I[La_{Sr}^{\cdot}]^{1/2}}{\sqrt{2\,K_p}} * P(O_2)^{-1/4}$$

The defect concentrations of electrons, oxygen vacancies, and strontium vacancies were calculated and explained in further detail by Meyer et al. in Figure 4.6.

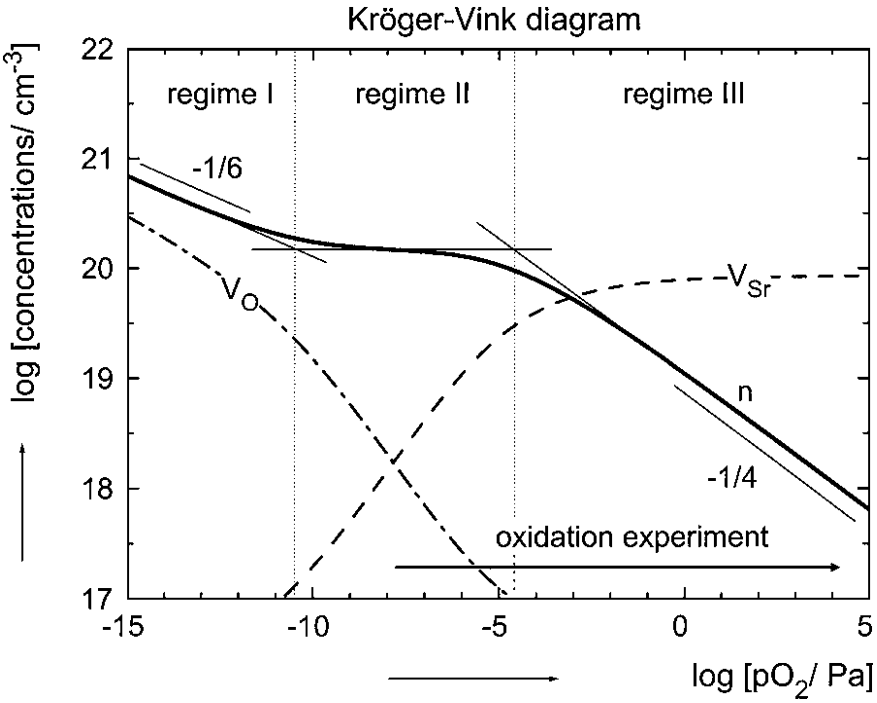

Figure 4.6 Kröger-Vink diagram for La-doped $SrTiO_3$ [206].

The defect chemistry for Nb doped titanium follows a similar relation…

By doping the B site with Nb,

(13) $Nb_2O_5 \xrightarrow{2\,TiO_2} 2\,Nb_{Ti}^{\cdot} + 4\,O_O^X + \frac{1}{2}\,O_2 + 2\,e^-$

The equilibrium reaction for oxygen at low pressures is:

(14) $O_O^X \rightleftharpoons V_O^{\cdot\cdot} + 2\,e^- + \frac{1}{2}O_2$

The mass action law follows this expression for the equilibrium constant K for electrons

(15) $\frac{[V_O^{\cdot\cdot}]*[n]^2}{[O_2]^{1/2}} = K_n$ where $[O_2]$ = Partial pressure of O_2 or $P(O_2)$

At low $P(O_2)$, where e^- compensates for the oxygen vacancies $[n] \approx 2[V_O^{\cdot\cdot}]$

(16) $\frac{1}{2}[n] * [n]^2 = K_n * P(O_2)^{-\frac{1}{2}}$ therefore,

(17) $[n] = (2K_n)^{\frac{1}{3}} * P(O_2)^{-1/6}$

At intermediate $P(O_2)$, where [n] compensates for $[La_{Sr}^{\cdot}]$, the $[V_O^{\cdot\cdot}]$ becomes negligible [207]. The electron concentration depends on the donor content which does not vary with $P(O_2)$.

At the high $P(O_2)$ condition, the reaction takes the following form,

(18) $\frac{1}{2}O_2 \rightleftharpoons O_O^X + V_{Sr}'' + 2\,h^{\cdot}$

By substitution of the charge neutrality, $4[V_{Ti}^{''''}] \approx [Nb_{Ti}^{\cdot}]$ into mass action equation

(19) $[V_{Ti}''''] * [p]^2 = K_p * P(O_2)^{\frac{1}{2}} = \frac{1}{4}[\,Nb_{Ti}^{\cdot}] * [p]^2$

(20) $[p] = (\frac{4\,K_p}{[Nb_{Ti}^{\cdot}]})^{1/2} * P(O_2)^{-\frac{1}{4}}$

Since $K_I = np$, the intrinsic equilibrium constant then

(21) $[n] = {K_I}/{[p]}$ and

(22) $[n] = \frac{K_I[\,Nb_{Ti}^{\cdot}]^{1/2}}{\sqrt{4\,K_p}} * P(O_2)^{-1/4}$

The ionic compensation at high $P(O_2)$ infers that hole conduction does not account for any electronic conductivity, and the strontium titanate material is an n-type conductor or semiconductor.

As mentioned, the conductivity of this material varies depending on the defect concentrations. The equilibrium defect concentrations can be frozen in during quenching from high temperature calcinations of the material. The kinetics of the re-oxidation will be discussed at the end of this section, but are relatively slow at low temperatures because of limited oxygen diffusion. The main contribution to conductivity in donor-doped strontium titanate is electron carriers. As electron compensation and carrier concentration increase, strontium titanate transitions from an insulator → semi-conductor → metallic conductor. The Fermi energy level is shifted closer to the conduction band and eventually overlaps when behaving as a metal [182].

Many reports on optimizing conductivity have focused on high temperature conduction because of the broad number of applications in this operational range including SOFC anodes. This mixed electronic and oxide conductivity is useful in solid oxide fuel cells although they were made into composite assemblies with yttria-stabilized zirconia electrolyte to improve oxygen ion conduction [183]. However, the low temperature electrical conductivity is even greater in correlation with the metallic type behavior of strontium titanate. Experimental conditions over a range of temperatures and oxygen pressures are used to confirm the defect chemistry models listed previously.

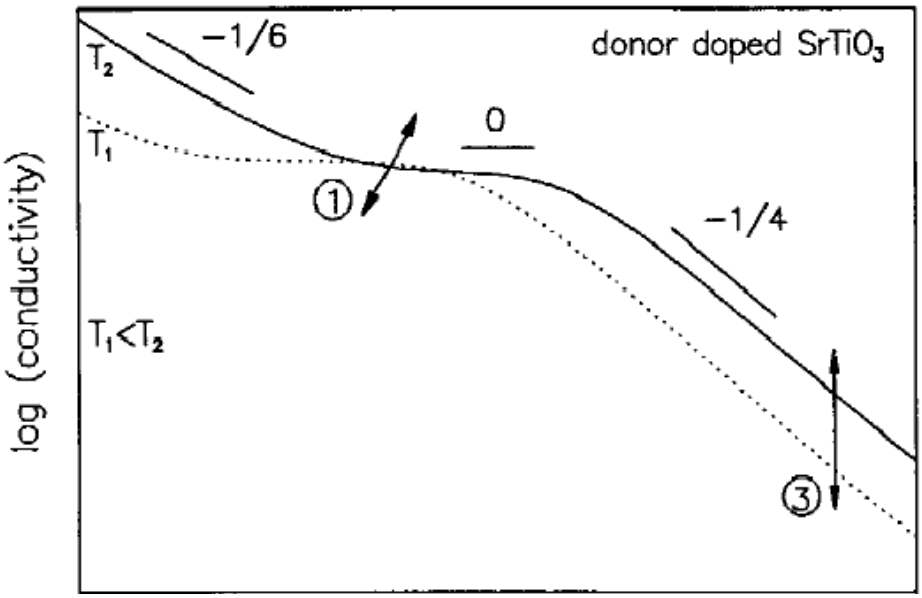

Figure 4.7 High temperature equilibrium conductivity for donor-doped STO [207]

The electronic conductivity is highest for the Nb-doped strontium titanate, followed by La-doped according to quantum calculations on the conductance channel [182. However, improvements in conductivity have also been shown for other donor dopants including dysprosium and gallium on the A-site, vanadium and tantalum on the B-site. These elements have similar valence and ionic radii, but Nb and La are the closest electron configurations and nearest neighbors in the periodic table with higher oxidation states. Some of the highest reported conductivities are a result of specialized processing techniques. The pulsed laser deposition or laser beam epitaxial growth for Nb-doped have provided the highest conductivities reported up to about 10^4 S/cm [181, 208]. Other groups have shown high conductivity that resulted from optimizing traditional ceramic processing techniques to minimize the grain boundary effects as shown in Figure 4.8 [209, 210]. They determined that undesired low conducting grain boundaries disappeared and the material acted like bulk single crystal after processing above 1100

°C. The carrier concentrations were considered frozen in below 400 °C and the measured electron concentration was as high as 6.7 x $10^{21}/cm^3$ [196]. There have been only limited reports of the material conductivity in standard temperatures and pressure, but commercially available samples from Shinkosha Co. Ltd. were measured at 10 S/cm. Other commercially available samples may also be purchased from National Lead Co., Commercial Crystal, Single Crystal Technology, amongst others. Although, producing highly tailored nanocuboids and other structures with high surface area likely requires application specific production necessitated by custom laboratory synthesis methods.

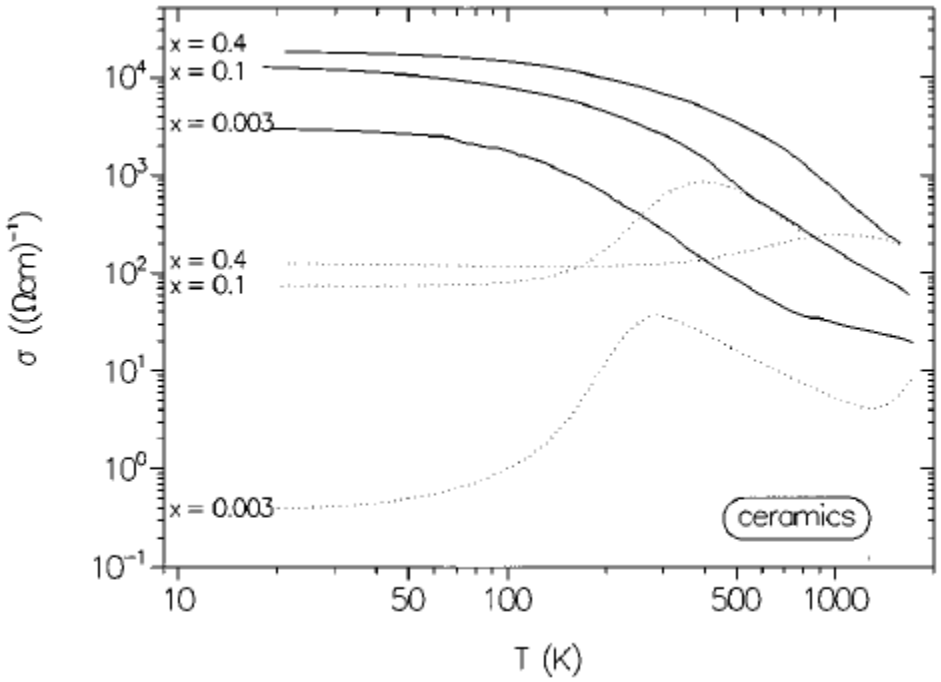

Figure 4.8 Conductivity of La doped STO in dry (···) and humidified H_2 (—) [196]

The effect of grain boundaries was not always unavoidable and was more pronounced in porous sample geometries [196, 211]. In fact, relying on the surface conduction is not ideal for the use in an electrode material which requires a high surface

area. Stable samples for SOFC anodes with ~30 % porosity were calcined in air then reduced and had conductivity of 55 S/cm in the targeted operating temperature range at 650 °C [212]. The samples with higher density that were co-doped with Nb and Dy had some of the best conductivity for conventional solid-state reaction preparations and followed a temperature dependent relationship of $T^{-1.5}$ above 200 °C as seen in Figure 4.9. A modified glycine-nitrate combustion preparation process which produces fine grain sizes ~100 nm and phase uniformity of Nb-doped strontium titanate may hold promise for the electrode preparation. These samples used 10% niobium substituted for titanium have the highest conductivity in the range targeted for PEMFC operation as shown in. Atomic modeling predicts a maximum in conductivity with 12.5% Nb doping according to the linear muffin tin orbital method with atomic sphere approximation [198]. At lower temperatures above 100 °C samples co-doped with La and Ga, showed fast reduction and a conductivity of about 170 S/cm for 60-70% volume density [176]. A novel liquid film migration technique determined that the reduction kinetics for Nb-doped samples could be quantified by determination of the chemical diffusion coefficient $D_{chem} = 4.6 \times 10^4$ [-(489±118 kJ)/RT] (cm^2/s) [180]. The re-oxidation kinetics of the material are slower for the doped sample than the purely reduced strontium titanate, however oxidation is not well studied especially at the low temperatures which would be suitable for PEMFC application.

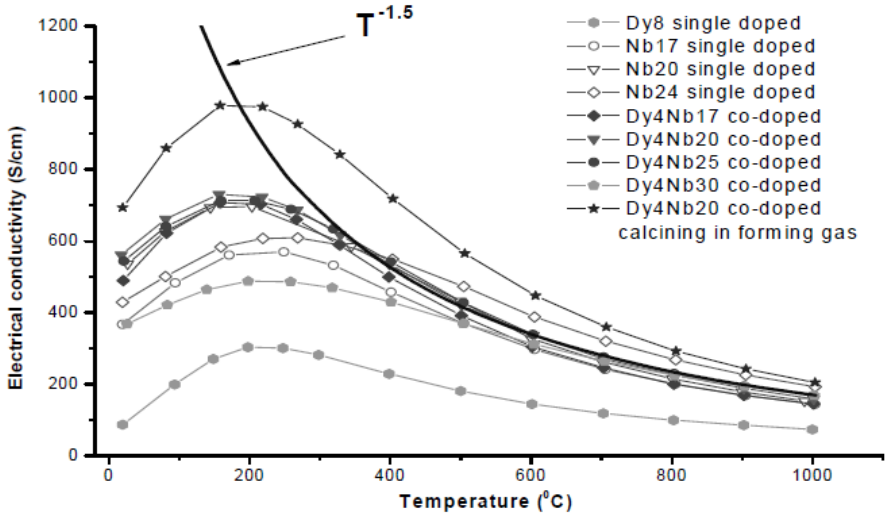

Figure 4.9 Samples tested from room temperature to 1000 °C [213]

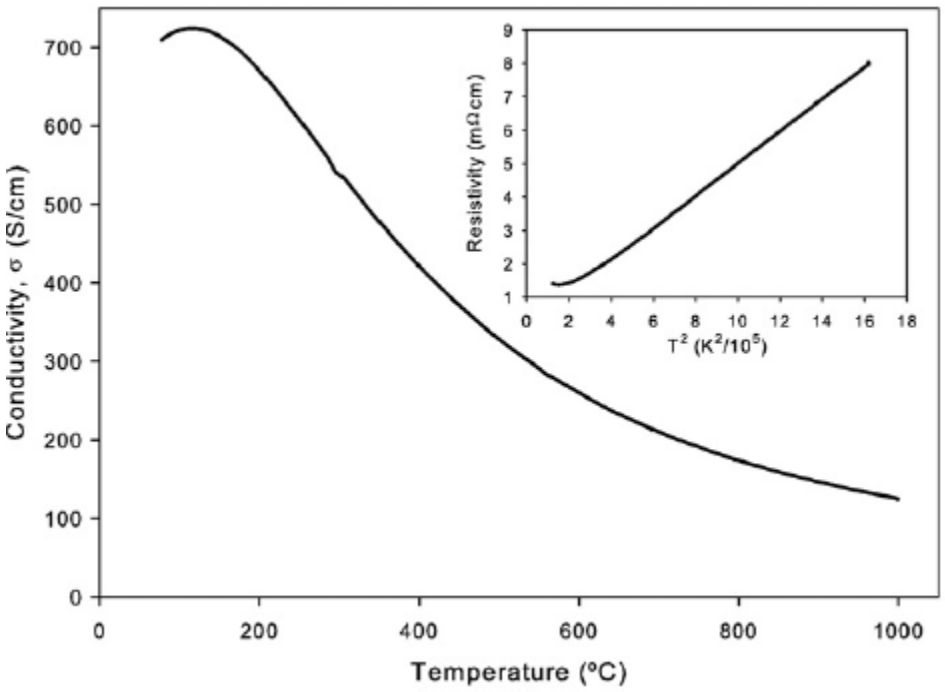

Figure 4.10 Nb-doped STO conductivity for $Sr_{0.94}Ti_{0.9}Nb_{0.1}O_3$ in dry H_2 [193]

Many models have been used to predict, confirm, and understand the conduction mechanism in the donor-doped strontium titanate. A brief history was provided and understanding of defect concentration is obviously critical. The material behavior has

been the subject of at least one hundred scholarly journals found by the author and is still not simply understood. The metallic type conductivity predicted by quantum physics DFT, has been shown to exist when the Fermi level enters the conduction band [[182]]. A number of other electronic properties have been investigated and reported by many authors like the Hall mobility, Seebeck coefficient, thermoelectric power, and others which won't be discussed in detail because they don't directly contribute to the scope of this review. For example, the mobile electron concentration has been shown to be much higher than those which contribute directly to conduction as a result of defect complexes and oxygen vacancy associations. The result may lead to single positively charged species of $V_O^{\cdot}$ after interaction with an electron for compensation below 400 °C [[192]].

However, the electronic conductivity still relies on the following equations;

(23) $\sigma_n = e\, n\, \mu_n$

(24) $where\ e = |z|F\ \ which\ converts\ concentration\ into\ Coulombs$

At low temperatures after oxygen diffusion into the perovskite and an equilibrium has been achieved in the oxygen sub-surface lattice, the electron concentration should be approximately [n] ≈ [$D^{\cdot}$]. When dopant concentrations are frozen in during fast cooling, the drift mobility of electrons is

(25) $\mu_n(T) = \frac{\sigma(T)}{e[D^{\cdot}]}$

Therefore, at low temperatures the constant charge carrier concentration follows results in a conductivity behavior which follows the temperature dependence of drift mobility derived from the Einstein relation.

(26) $\frac{D}{\mu} = \frac{kT}{e} = V_{(T)}\ which\ can\ be\ used\ to\ derive\ the\ following,$

(27) $\mu = \frac{|z|\,F\,D}{RT}$ *where D follows an Arrhenius − type behavior*

A function used to describe drift mobility at all dopant concentrations was calculated for La [207].

(28) $\mu_n(T) = \mu_{no}(\frac{T}{K})^{-M} \approx 3.95\ x\ 10^4\ cm^2 \cdot (V \cdot s)^{-1} \cdot (\frac{T}{K})^{-1.62}$

This data has been proven by experiment to temperatures as low as 600 °C, but the trend does not follow to lower temperatures [214]. The low temperature conductivity stability is not well studied and rarely measured in the 60 – 100 °C operational range of PEMFC. The conductivity at higher temperatures and oxygen pressures decreases following the Arrhenius relation of the mobility equation. The mobility of ions in the lattice at low temperatures becomes relatively slow, but their kinetics are not been examined in detail. However, nonbonding electrons added by donor dopants came still have some mobility at room temperature.

The experiment requires a specific synthesis of a conductive and high surface area support material. Many processing procedures have been detailed in the literature, but the structure of the cubic perovskite should first be verified by XRD characterization. Referenced procedures can be applied through mixing precursors powders with a pore former that undergoes appropriate annealing steps. The electronic conductivity of the material is critical to its success and thus should be quantified before further analysis. A high conductivity may not necessarily translate into an electrode material if does not satisfy stability testing. Determining the durability over exposure time to the real operating conditions found at the electrode would also be necessary. The material is expected to maintain its conductive properties in the humidified and acidic electrolyte of the anode. The uncertainty lies in its application to cathode conditions where it is

subjected to higher potentials and oxidizing conditions. Measuring stability under this atmosphere would determine whether it can resist the corrosion reaction which is the part of the motivation for this work. These tests would validate the capability of a catalyst support, but the material is hypothesized to offer several advantages over traditional carbon black, namely a strong support interaction. There are several methods to characterize the materials through microscopy, surface spectrometry, and electrochemistry. Measuring the kinetics of the oxygen reduction reaction, a rate-limiting step in activation, would suggest any benefit from the face-selective support. Finally, an electrocatalyst composite using the donor-doped STO electronic conductor should be applied to form a membrane electrode assembly and tested in real fuel cell conditions to realize the potential benefits it can offer.

A high electronic conductivity for a porous donor-doped strontium titanate seems to be an achievable task based on the literature review. Optimizing the defect chemistry and material properties through chemical processing techniques will be the necessary steps for demonstration. Depositing platinum nanocrystalline catalysts can form a strong interaction that leads to more active Pt catalyst surface atoms. An epitaxial catalyst arrangement may be able to benefit performance. However, thorough analysis of the material stability in the environment found for the operating range of the PEM fuel cell is a concern which needs to be addressed.

The goal of this research is to explore use of a metal oxide, strontium titanate, as catalyst supports for PEMFC. Improvements in its conductivity will be attempted by doping with niobium. Studies of the material property and support structure will be identified before Pt catalysts are reduced via a polyol process. Electrodes added CNT for

conductivity formed the cathode catalyst layer of a PEMFC prepared via an ultrasonic mixing and spray deposition. Tests for corrosion resistance through electrochemical methods and accelerated degradation in the cell were designed to target the catalyst support performance. This work demonstrates some possible benefits, weaknesses, and future concerns of using metal oxide catalyst supports from this case study

4.3. Experimental Procedures

The $SrTi_{0.9}Nb_{0.1}O_{3-x}$ nanocrystalline ceramic was prepared by a Pechini method using starting materials of strontium carbonate (Sigma-Aldrich 99+ %), titanium (IV) tetraisopropoxide (Sigma-Aldrich 98+ %), and niobium (V) ethoxide (Acros Organics 99.5%). The Nb doped sites theoretically substitute 10% molar concentration of the B-sites. A chelation reaction of metal precursors occurs in the sol-gel via mixing of a polymeric citric acid (CA) precursor in ethylene glycol (EG) under N_2 gas. The amount of solutions used to form the complex was from the molar ratio of 1:10:40 for (Ti/Nb:CA:EG) [215]. After forming a transparent solution with 3 hours stirring, the solution was heated on a hot plate to 300 °C to evaporate EG. The remaining black mass was heated in a furnace at 800 °C for 8 hours. Resulting white powders were then milled before being reduced at 1200 °C in 5% H_2/N_2 environment for 12 hour and transformed into a dark gray powder.

Platinum reduction on to the ceramic support was completed through a polyol reduction process. The solids were suspended in ethylene glycol by sonic horn before adding chloroplatinic acid. Then the pH was adjusted to 10 by a 1 M NaOH solution in

ethylene glycol. The suspension of STO and Pt precursors was deaerated with nitrogen gas and heated to 140 °C for 4 hours while stirring in 3-neck flask to promote nucleation and growth. Then the solids were separated by centrifuge before the material was washed and dried. These electrocatalysts had approximately 40% Pt loading as measured by weight.

In some cases, ceramic discs were formed for characterization purposes. When forming cylindrical discs, a 3 metric tons/cm^2 pressure was used for compaction before the last high temperature reduction in hydrogen was completed. The now dense ceramic discs were used for measuring the conductivity by a linear sweep voltammetry method. A potentiostat (Gamry Reference 300) was used to sweep from ±50 mV at 5 mV/second while measuring the current through the disc. A four electrode arrangement was attached with silver mesh and contact paint to minimize interfacial and lead resistance. Additionally, the corrosion studies in liquid H_2SO_4 (pH = 1) electrolyte also utilized these discs. A K0047 corrosion cell from Princeton Applied Research used a saturated calomel electrode to measure the response of the STO pellet in a specialized disc holder.

Several observations were made via spectroscopic methods. The grain size for the densified pellet was measured by a Leica optical microscope. The actual catalyst loaded powders were visualized by a Hitachi H-8000 TEM. A field emission scanning electron microscope Zeiss Ultra Plus FESEM imaged the composite catalyst layer. The X-ray diffraction pattern was recorded on Bruker with CuK_α 1.5418 A° wavelength. Absolute Pt concentrations in thin electrode layers were made by X-ray fluorescence on a Fischer XDAL spectrometer. A Thermo-Finnigan Element XR ICP-MS was also used to measure corrosion products from solution.

A catalyst ink composite suspension was created by mixing the Pt/ $SrTi_{0.9}Nb_{0.1}O_{3-x}$ with some Nafion® ionomer solution and functionalized carbon nanotubes for connectivity. Solids were mixed at a mass ratio of (electrocatalyst:ionomer:CNT) at (1:0.432:0.167) dispersed in isopropyl alcohol with aid of an ultrasonic horn (Sonics Vibra-Cell 750W) to aid the distribution of the nanoparticles. A starting mass of 0.24 g STO powder was used with about 40% Pt mass fraction. The ink was sprayed on to a Dupont™ NRE-212 polymer substrate heated to 100 °C to make the cathode shown in these PEMFC results. The membrane electrode assembly (MEA) was then hot pressed at 130 °C for 5 minutes at 300 N/m^2. Square 25 cm^2 cell hardware from Fuel Cell Technologies with triple serpentine flow channels was built with SGL 10 BC microporous gas diffusion layers. The cell was conditioned at 0.6 V potential hold for at least 3 hours before testing.

The performance of the fuel cell was monitored by Scribner 840 fuel cell test station or in-house test stand using the same software control. The hydrogen/oxygen were provided in a stoichiometric ratio $\lambda = 1.5/3$ for the high performance data, but a constant flow rate of 400/800 mL/min in durability testing on the anode/cathode, respectively. The saturator dew points were held at 75/73 °C while cell temperature was held at 77 °C corresponding to 92/84 % relative humidity (RH) also. The cyclic voltammetry, cross-over currents, and accelerated support degradation tests were conducted with Gamry Reference 3000 potentiostat.

The accelerated stress test was borrowed from the Department of Energy (DOE) protocol for the corrosion of the catalyst support suggested for automotive testing. The cathode potential is held at 1.2 V_{RHE} and the cathode is pressurized with fully humidified

N_2 gas streams at 80 °C. The anode is exposed to hydrogen for reference and the carbon oxidation can proceed via a simulated oxidation of the support.

4.4. Results and Discussion

This study aimed to explore the possibility of using $SrTi_{0.9}Nb_{0.1}O_{3-x}$ as a potential catalyst support used in making composite electrodes. Catalyst supports have a critical effect on catalyst performance and durability which is evident in these results. The structure of metal oxide supports is important to its properties in the electrode.

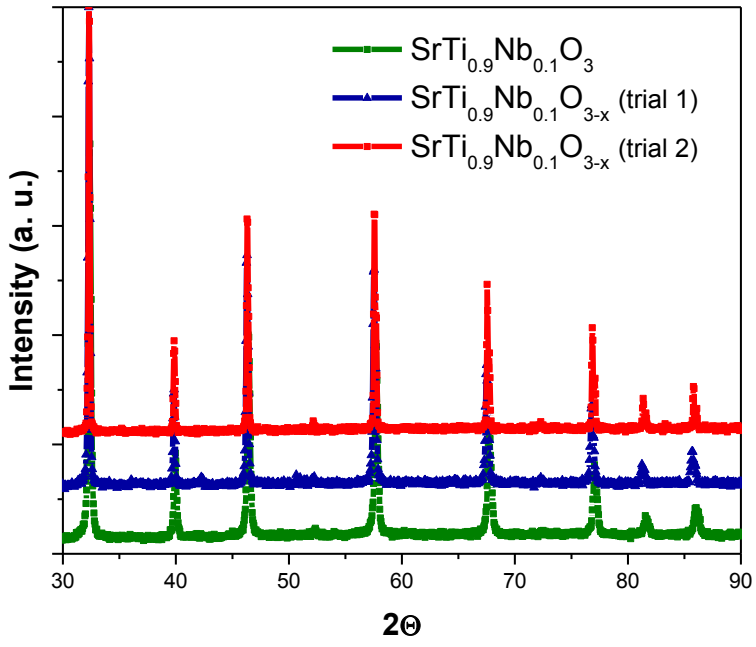

Figure 4.11 XRD of strontium titanate before and after reduction

First, preparation of the desired nanostructured perovskite is essential to the atomic arrangement that can provide higher conductivity than other phases. The

perovskite can be identified by the lattice diffraction peaks from XRD technique. It is apparent that even after high temperature reduction, the crystal structure is still preserved. Average crystallite size can be deduced from an individual peaks using the Scherrer equation which estimates an average 36 nm size of STO. Densified pellets had larger grains of about 1-2 micron diameter after annealing. The conductivity for these pellets measured at standard temperature and pressure is about 0.06 S/cm from a linear sweep. This is nearly equivalent to proton conductivity in the membrane at full humidification and 80 °C, but this value is at least two orders of magnitude lower than carbon black and much less than others have reported in the literature for larger crystals at higher temperature in low oxygen pressure. Typically, p-type or electron hole conductors are used in the cathodes of solid oxide fuel cells. It is hypothesized that a p-type conductor may also have better conductivity in higher oxygen partial pressures at low temperatures. In this case, positive holes can compensate for negative metal dopant centers.

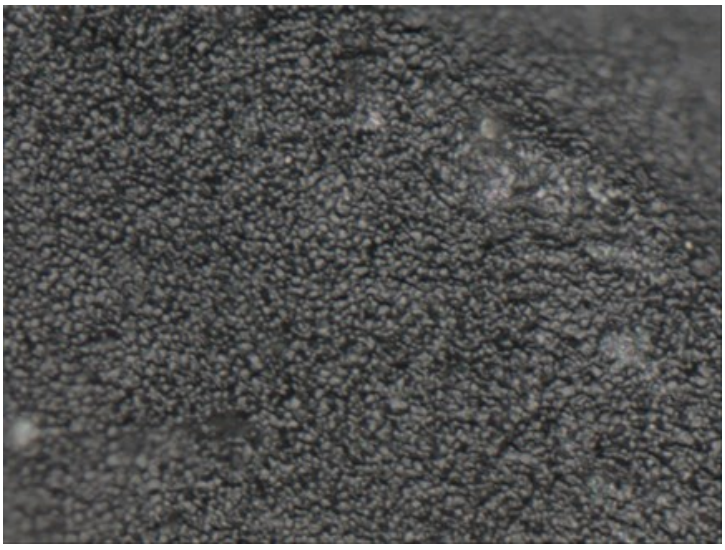

Figure 4.12 A dense STO pellet observed by light microscope

A modified Pechini method was chosen for its ease of implementation and intimate mixing which provided small crystallites with high surface area. However, future attempts could adopt other process such as the hydrothermal one used for creating the ideal nanocuboids with [100] surfaces for catalyst epitaxy. Details seen by TEM in Figure 4.13 TEM image of $SrTi_{0.9}Nb_{0.1}O_{3-x}$ with , show agglomerates of nanostructured ceramics which were grown by this method and distributed on to a copper grid.

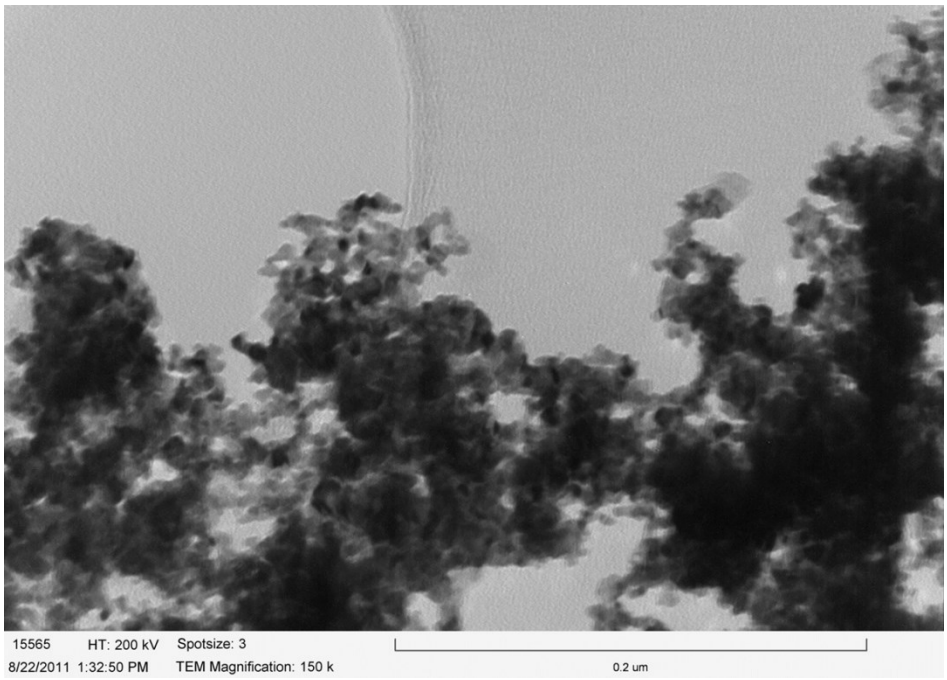

Figure 4.13 TEM image of $SrTi_{0.9}Nb_{0.1}O_{3-x}$ with supported Pt nanocrystals

The TEM picture shows the final electrocatalyst used in the actual composite electrode. The polyol process used yielded about a 40% Pt mass fraction of solids. The Pt particle size was estimated around 5 nm. Unfortunately, a high resolution TEM image was not possible for this sample to observe finer structural detail.

a) 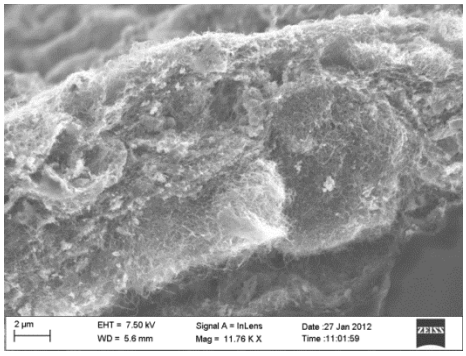

b) 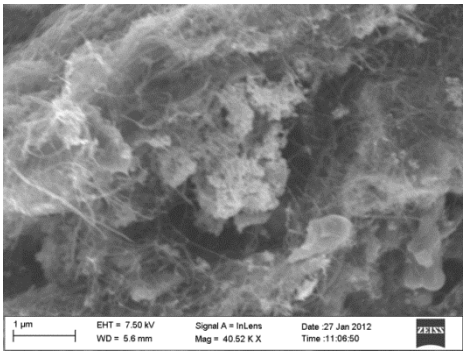

Figure 4.14 FESEM images of STO cathodes at a) low and b) high magnification

The MEA materials were freeze fractured before imaging the side profile morphology of the cathode layer. Figure 4.14 a) shows about 12 µm thick electrode layer and b) represents a higher magnification of the electrocatalyst interaction with the other solids in the composite. A catalyst ink suspension mixed in the ionomer suspension in alcohol solvents with an ultrasonic horn (20 kHz) before deposition on to the heated polymer substrate with an ultrasonic sprayer (120 kHz). Additionally, there was a small amount of graphitic multi-wall carbon nanotubes (8-15 nm O.D. and 1-5 x 10^4 nm) mixed in the ink as well. These have several beneficial properties which have a supposed contribution to mass transport and electron charge transfer in the layer. In addition, they could also help to stabilize ink suspensions as oxidized CNT can disperse well in polar solvents. CNT help to form electronic pathways between supported catalysts. Also, they are believed to help with water transport by formation of a hydrophobic ionomer skin that can help expel water and suggesting they can operate at higher current without lees concern for flooding [[216]]. This effect is not the subject of this work, but performance of a cathode made from single attempt is shown below for a fuel cell operated on oxygen.

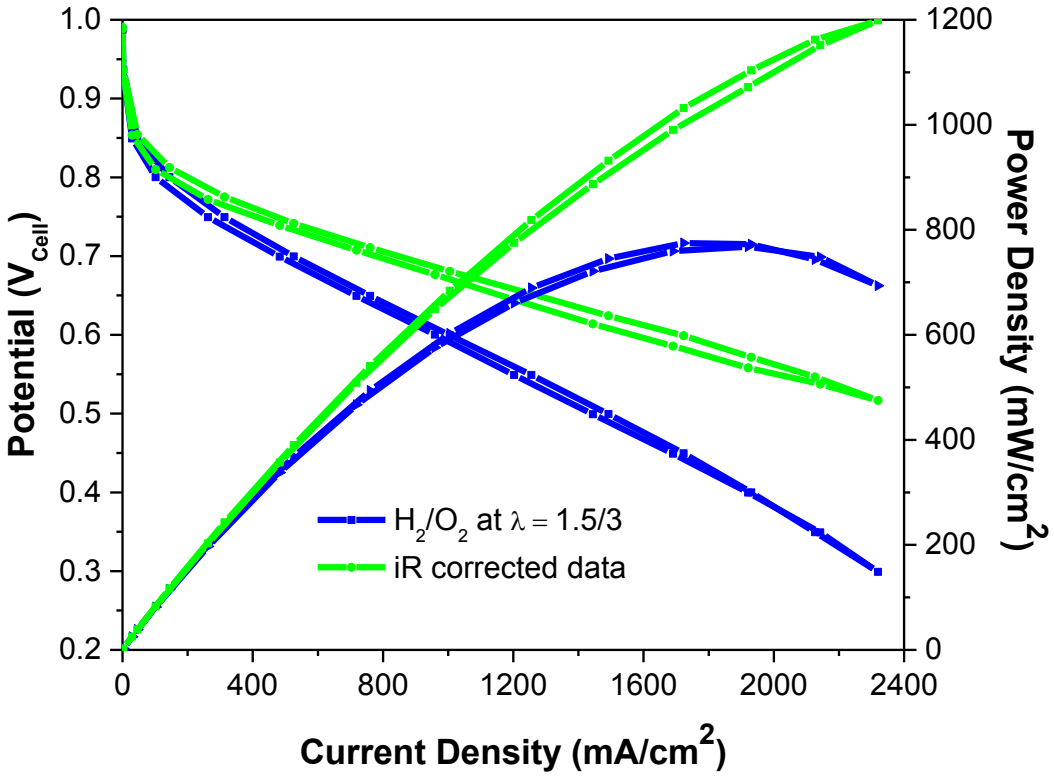

Figure 4.15 Polarization and power density of $Pt/SrTi_{0.9}Nb_{0.1}O_{3-x}$ cathode

The Pt content for this electrode layer was 0.36 mg Pt/cm^2 which is similar to commercial carbon supported loadings. Figure 4.15 represents initial cell performance and iR-corrected data corrects for purely resistive losses found in the membrane, electrode, and interfacial contacts. The electrode is very well behaved and appeared to suffer very minimally from transport losses at this condition. The Tafel plot in oxygen condition showed a slope ~71 mV/decade in the low current density regime. Electrochemical active surface area of 18 m^2/g was integrated from the CV and is considered low compared to many commercial carbon catalysts. This is probably a factor

in the low mass activity measured to ~0.02 A/mg_{Pt}; although, the specific activity ≈ 106 μA/cm^2_{Pt} was more comparable to conventional catalysts.

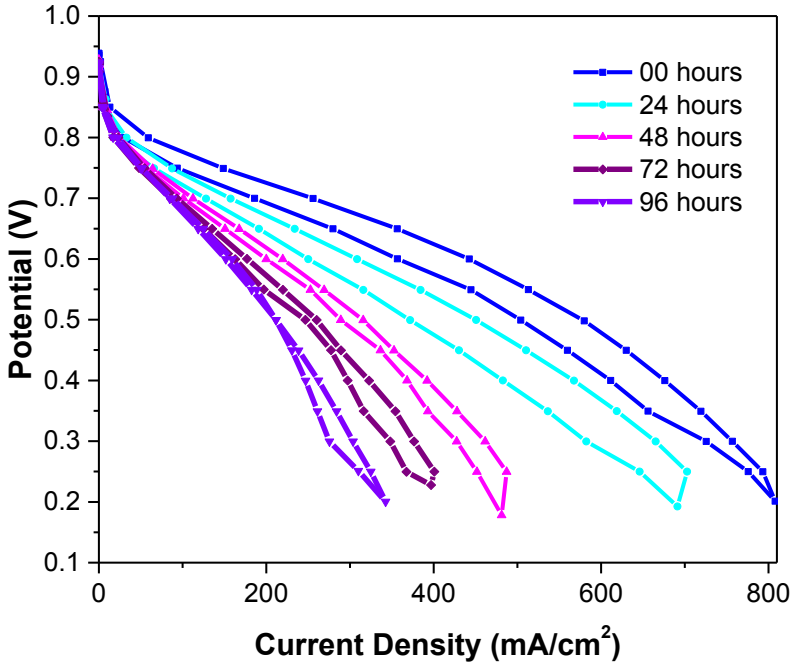

Figure 4.16 Polarization stability during V hold on Pt/STO electrode

The polarization performance on air was recorded using fixed flow rates and the cell was operated at 80 °C. Polarization was swept down (cathodic) and then back (anodic), to check for performance fluctuations. The accelerated stress test was interrupted every 24 hours to monitor the change in performance. The 1.2 V_{RHE} AST condition was set by DOE because it is known to be very aggressive specifically toward the supports. This specific material unfortunately did not meet the DOE USCAR targets for performance stability. The current density dropped by more than half during the first 4 days at this condition which is only about one quarter of the intended 400 hours test. However, it should be noted that most high surface area carbons also cannot pass this test

and often fail by this time. Future candidates should also pass the electrocatalyst stability test which cycles the potential and takes greater account of Pt catalyst effects. Durability test are important because to recognize any contribution of the SMSI and catalyst bonding to the oxide. In addition to monitoring performance, the electrochemical surface area was also estimated by integrating the hydrogen adsorption/desorption peaks after double layer subtraction of the cyclic voltammograms. A more promising result arises from this data.

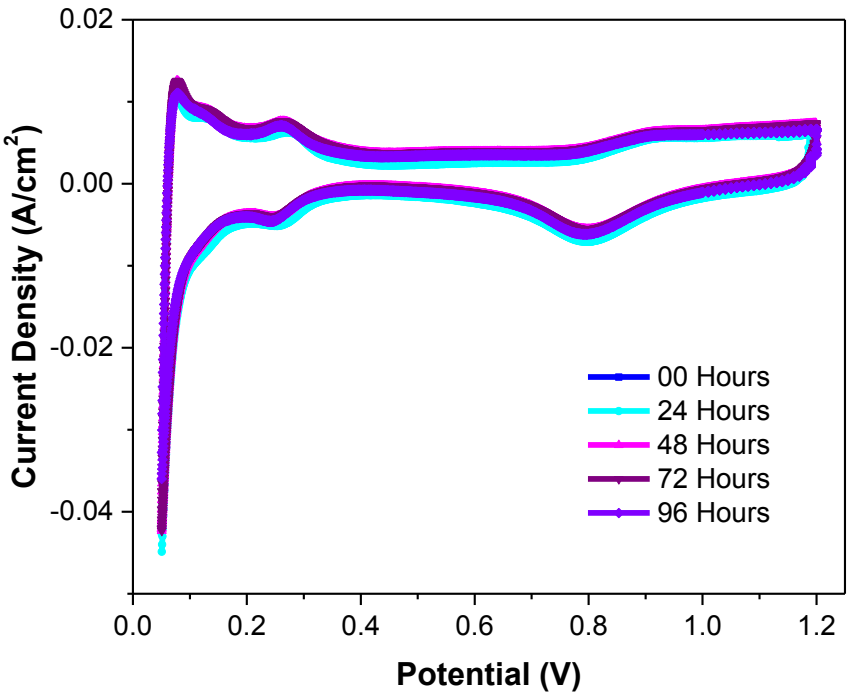

Figure 4.17 CVs of 25 cm^2 cathode through AST on catalyst support

Cyclic voltammetry of the cathode reveals the active area is experiencing only small changes even though polarization performance is degrading rapidly. It is likely that

more stable support phases have formed which can protect platinum against the corrosion reaction. Sacrificial oxidation of strontium at lower potential is probably acting to cathodically protect titanium. This would suggest that the strong bond between the platinum and titanium is also being preserved to minimize the losses in active catalyst area. However, when cations like Sr^{2+} become oxidized, they can easily become mobile in the ionomer. These cations diffuse into the electrolyte by an applied electrochemical driving force. Regrettably, these cations can block the proton path which would otherwise provide an access route to catalyst sites. The hydrogen pump test indicates this mass transport limitation in the ionomer.

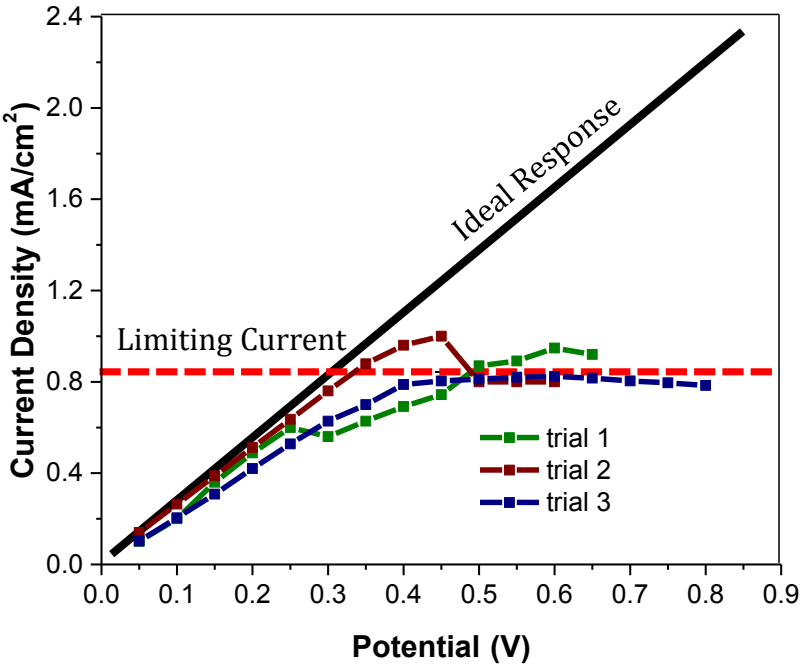

Figure 4.18 Hydrogen pump test shows a limiting current density

The H_2 pump test shown represents a means of identifying a limiting current density in the cathode as a result of transport resistance. An excess volume of hydrogen

is supplied to the anode for oxidation before it can be reduced back on the cathode in proportion to the applied potential. The half-reactions occur very quickly, so the main overpotential contributions come from the electrolyte and any transport issues. The limiting current above 0.8 mA/cm^2 shows deviation from ideal linear response. This added resistance is likely caused by the accumulation of metal cations like Sr in the electrolyte and catalyst interfaces. These results would indicate that the support is actually being irreversibly oxidized. After ion-exchanging the membrane, effluent water was analyzed by means of ICP-MS. The analysis showed qualitative presence of Sr, Nb, Ti, and Pt ions in the solution. Ion concentrations were not precisely quantified due to lack of accurate calibration standards, but Sr (II) had the highest signal intensity. This would suggest that Sr cations were being released into the electrolyte that eventually built up and blocked the catalysts sites. Another test to isolate the corrosion behavior in a simulated environment could be more insightful to these behaviors.

Table 4.1 ICP-MS results from ion-exchange with MEA after ADT

	Concentrations (ppm)		
Element	**Bckgrnd**	**Sample**	**Difference**
Ti	5.312	28.02	22.708
Sr	0.263	25.41	25.147
Nb	0	7.847	7.847
Pt	0	6.25	6.25

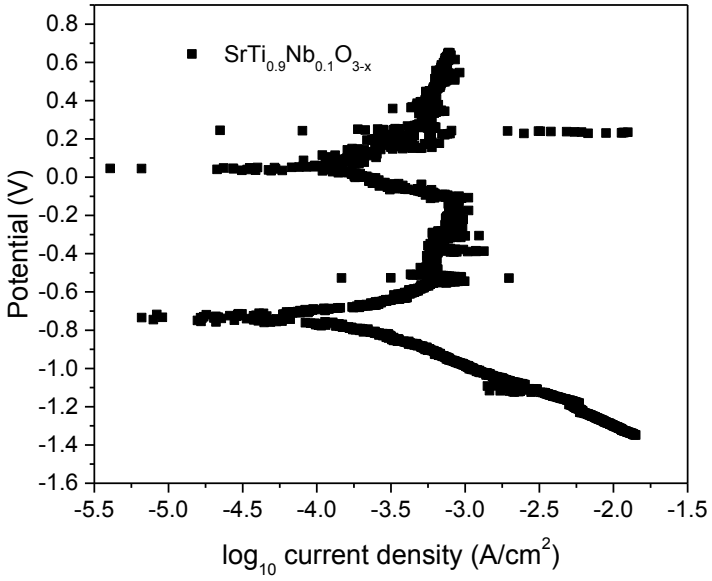

Figure 4.19 Ceramic STO disc in pH 1 H_2SO_4 of corrosion cell at 25 °C

The corrosion cell allows measurement of corrosion potential E_{corr} and corrosion current density i_{corr} in a simulated cathode environment for an STO pellete where pH is typical below 3 [2, 35, 49, 217, 218]. The intersection of Tafel slopes estimates lower E_{corr} is -0.73 V and i_{corr} is about $10^{-3.7}$ A/cm^2 for the lower potential which is assumed from the Sr^{2+} oxidation. The higher oxidation potential just above zero is assumed from the Ti^{4+} oxidation. The corrosion of strontium and current is roughly equivalent to carbon steel and not suitable as a catalyst support. A combination of low pH and high potential is very corrosive and seems to quickly alter the material chemistry. However, it is postulated that a more stable form may arise after passivation. Additional experimentation can be done to obtain insight on the change in material properties. An alternative stable metal oxide support may have not been made here in preliminary tests, but knowledge on the stability of this candidate is gained that can be applied to the future

construction of improved oxide support design. Also, expanded resources and processing experience will lend to further improvements. Choosing a more stable support material which does not include strontium will be necessary. Combining metal oxides with carbon in the support may also be able to provide some properties that can only be realized by forming a composite electrocatalyst.

4.5. Conclusions

A perovskite oxide, $SrTi_{0.9}Nb_{0.1}O_{3-x}$, was synthesized for its ability to act as a catalyst support for PEM fuel cell applications. Small crystalline ceramic powders were synthesized which were characterized before depositing Pt metals via polyol process to form the electrocatalyst. The results reveal a catalyst area of 18 m^2/g in a working electrode, but stability is still a concern before these materials can be suitable replacements for carbon. Air polarization performance showed a 2.75x drop in current output at 0.5 V after just 96 hours of accelerated testing. Despite a significant performance reduction, the electrochemical catalyst area is preserved during this time. This suggests a sacrificial oxidation of support oxides which act to protect Pt catalysts. The corrosion behavior in a simulated environment confirms a relatively low corrosion potential of metal oxides. Corrosion of strontium in the cathode and cation diffusion into the electrolyte seems to cause a significant problem related to blocking of the proton transport channels. This work reveals some weaknesses associated with metal oxide electrocatalysts, but it also demonstrates some potential benefits that can be built upon in future attempts.

4.6. Acknowledgements

I also appreciate the opportunity to pursue this research project provided by my advisor, Dr. Xinyu Huang. The literature review was developed for a class project that taught me valuable lessons in defect engineering principles taught by Dr. Kevin Huang and Dr. Kyle S. Brinkman. The work was carried out in the Solid Oxide Fuel Cell Center directed by Dr. Kenneth L. Reifsnider in Horizon I at USC. This work was aided by contributions from summer student Jungwoo Lee of Gyeonggi Science High School.

Chapter 5. Titania and CNT Catalyst Supports for Platinum in Durable Fuel Cell Cathodes

5.1. Abstract

The development of a dual phase catalyst support for the cathode of polymer electrolyte fuel cells with carbon and titanium oxide was tested for performance durability. Titania can form a strong bond with platinum catalysts and carbon nanotubes provide a conductive framework. The combination used for this catalyst support has been shown to offer some improvements in performance durability in comparison to a control without titania addition (Pt-CNT vs. Pt-Titania-CNT).

5.2. Introduction and Background

One problem plaguing fuel cell development is the durability of materials used to support platinum (Pt) catalysts. Supports are traditionally made from high surface area carbon black to connect the catalysts to electronic circuit. However, the carbon is susceptible to corrosion and especially at the interfaces where it is connected to the catalyst [2, 30, 35, 217, 218]. A dual phase catalyst support was synthesized through several

steps to design a more durable electrocatalyst. It was made as a proof of concept to demonstrate specific advantages for performance stability in the cathode of working polymer electrolyte fuel cells. In the dual phase support, the carbon nanotube (CNT) provides the framework for necessary electron conductivity. CNTs were used because long range ordered atomic structure contains fewer defects which act as initiation sites for its oxidation when compared to traditional carbon black. However, CNTs are still susceptible to corrosion and thus the introduction of second phase could provide additional advantages [68, 219]. The CNT were then coated with titania to offer several important benefits unavailable from carbon alone.

Titanium oxide, or simply titania, serves as an intermediate phase and it covers some of the CNT surface. This metal oxide can help anchor nanostructured Pt catalysts through a strong metal-support interaction if prepared be a method to prevent encapsulation [90]. Titania is also inherently more corrosion resistant in this environment because it can exist in a stable state of passivation [1]. When forming a strong metal-support interaction, the Ti^{4+} cations become reduced to Ti^{3+} when electrons are delocalized from oxygen vacancies created during reduction [93, 220]. This effect can result in a self-doped titania which introduces new mobility states [221, 222]. Through doping electronic conductivity of the material can be tuned by introduction of intermediate energy levels in the forbidden band gap [142, 144, 223-226]. Literature evidence suggests the platinum deposition is preferred at defects formed near the interface of phases and its presence can act to stabilized them [131, 227]. In titania, oxygen vacancies on the surface become nucleation sites for Pt catalysts [222, 228, 229]. Hence, the Pt can potentially be stabilized on the metal oxide to resist diffusion while maintaining an

electronic contact with the conductive phase in the dual support [157]. Although many groups have claimed a benefit to catalyst activity from this support, it was not necessarily a goal of this research [136, 138, 220, 230, 231]. One important objective was to demonstrate that metal oxide materials used in conjunction with graphitic carbon could be applied for practical use in low temperature polymer electrolyte fuel cell electrodes as others have also suggested from RDE and first principle simulations [135-137, 140, 232].

The fuel cell electrocatalysts were tested using an accelerated durability test (ADT) designed to rapidly degrade performance by potential cycling. Cycling tests can be very aggressive towards supported carbon supported platinum catalysts [35]. The test results were compared for electrocatalysts with and without titania addition to the CNT. The potential cycling protocol was adopted from a common procedure suggested by DOE USCAR Fuel Cell Tech Team using the same parameters including scan speed and potential limits, although specific deviations are listed in the experimental procedures. Electrochemical diagnostic tests were carried out to make a comparison between CNT supported Pt catalyst supports with and without the addition of titania.

5.3. Experimental Procedures

The multi-wall CNT (8-15 nm O.D. and 10-50 μm length) were purchased from Cheap Tubes, Inc. They were first pre-treated in nitric and hydrochloric acid (1:1 volume) at 140 °C for 4 hours to introduce functional groups on the surface and to remove impurities. The CNTs were filtered from the acids and rinsed extensively with de-ionized water. Then they were dispersed in isopropyl alcohol by an ultrasonic horn at

20 kHz (Sonics Vibra-Cell 750W). The dispersed CNT were added into a sol-gel solution prepared from titanium tetraisopropoxide (98+% Acros Organics). This alkoxide was added drop-wise under inert atmosphere into isopropyl alcohol (99.9% Fisher), nitric acid (69% Fisher), and de-ionized (D. I.) water. These were mixed in a molar ratio of 70:0.2:2.0 relative to the titanium precursor to form 100 mL of solution. The sol-gel contained 200 mg of CNTs and was heated at 80 °C for 3 hours under magnetic stirring. The solids were extracted by filtration (0.45 micron PTFE) to selectively separate the coated CNTs. The product was dried in a vacuum oven at 80 °C to evaporate remaining solvent and then heat treated at 330 °C for 2 hours in air. The resulting solids were ground by mortar and pestle into a powder. 80 mg of this titania/CNT powder was dispersed by ultrasonic horn in ethylene glycol (Acros Organics) solution before 1 g of choloroplatinic acid hexahydrate (8% wt. $H_2PtCl_6 \bullet 6\ H_2O$) from Sigma-Aldrich was added drop-wise. The pH was adjusted by 1N NaOH in ethylene glycol to above pH 9 measured with an Orion pH meter before the suspension was deaerated with N_2 and heated by 1100 W microwave oven at 60% power for 60 seconds to reach a temperature of 140 °C. After cooling, the electrocatalysts were separated again by filtration and rinsed with copious amounts of acetone and then D. I. water.

Ink formulated with these electrocatalysts was ultrasonic spray deposited (Sono•Tek Exactacoat) on Nafion® 212 to form membrane electrode assemblies. The ink was prepared by mixing the solid electrocatalysts in isopropyl alcohol with Nafion® DE 521 (Ion Power) that is 5% weight solution to provide for about 20% of the total mass in the cathode. The catalyst loading was confirmed by X-ray fluorescence technique using a Fischer XDAL instrument. The Pt loading was confirmed at 0.30 ± 0.02 mg Pt/cm^2 for

both cathodes. The anodes were prepared from a conventional high surface area carbon black with Pt from Tanaka K. K (TEC10E40E) with about 46% Pt by mass. An ultrasonic spray head (120 kHz Accumist) was used to deposit the ink on substrates heated at 100 °C to expedite the evaporation of solvents. After ink deposition, the coated membrane electrode assembly was hot pressed at 130 °C for 5 minutes under 3 kPa. The MEA was protonated in 0.5 M sulfuric acid at 80 °C (Fisher 98%) and then boiled in D. I. water. The MEA was assembled into cell hardware with 25 cm^2 active area using polytetrafluoroethylene gasket (0.010 inch thick), Sigracet® 10 BC gas diffusion layers, and torqued to 80 in·lbs with cell pinch about 35% before being connected to the test station.

The potential cycling and cyclic voltammetry tests were collected with use of a Gamry Reference 3000 potentiostat. The ADT cycled potential between 0.6 and 1.0 V at 50 mV/sec for 30,000 or more cycles. Fully humidified H_2/N_2 gases at 100 mL/min were fed to the anode/cathode side, respectively. The fuel cell was maintained at 80 °C for all tests. The electrochemical surface area and performance were checked periodically during ADT. The area was estimated from integration of the hydrogen under potential desorption region from cyclic voltammetry which were collected between 0.05 and 1.2 V with 100 mV/sec scan rate and 300 mL/min purge while other conditions were the same as during ADT.

The fuel cell performance on H_2 and air was measured by a Scribner Associates 840 fuel cell test station. The reactants were fed into the fuel cell at a minimum flow of 300 mL/min, and at higher current the stoichiometric ratio of 1.5/3 for the anode/cathode was used without back pressure. Dew points for anode and cathode were set at 78/76 °C

and the cell temperature was set at 80 °C. The fuel cell test hardware (Fuel Cell Technologies) had 25 cm^2 active area and triple serpentine flow pattern for the anode and pentuple serpentine cathode

Various material characterization methods were applied on the synthesized electrocatalyst. These include powder X-ray diffraction (XRD) by Rigaku Mini-Flex with CuKα radiation, high resolution SEM (STEM-Hitachi HD2000), FESEM (Zeiss Ultra Plus), and high resolution TEM (TEM 9500), and Raman spectroscopy (Horiba LabRam-HR system with a He-Ne laser 633nm).

5.4. Results and Discussion

The functionalization of CNTs to add defects to the surface is an important pre-treatment step. The strong acid can introduce functional groups onto the surfaces of the CNT, such as carboxylic acids and other anionic oxygen species. These negative charged groups will later act as nucleation sites for the metal cation reduction. The acid treatment also removes impurities like residual metals used for growing CNT and less stable amorphous carbon material. The acid treatment also served to improve the dispersion of CNTs in polar solvents and the sol-gel solution. The procedure for the sol-gel step was modified from the literature based on other successful strategies to coat crystalline anatase titanium dioxide on CNTs [126, 128]. The coating step was only performed once to prepare a thin coverage on CNT surfaces. Titania deposition was followed by a thermal treatment at 330 °C to induce the phase transformation to anatase without causing

excessive oxidation of CNT in air which becomes rapid at higher temperatures > 430 °C [122].

Platinum was deposited on the composite support by a microwave-assisted polyol reduction reaction. Choloroplatinic acid solution was added to supports in ethylene glycol which serves as a reducing agent when oxidized to glycolic acid. The glycolate anion stabilizes Pt colloids formed during the heating process while Cl^- can then be replaced by the negative surface species from functionalized nanotubes to bond with Pt^{2+} cations as the nucleation begins before crystallites grow. Platinum deposition on CNT and the resultant particle size and catalyst loading depends critically on the pH [233]. Adjusting the above 9 was found to give a catalyst loading of greater than 20% on support based on the mass differences from before and after the reaction. Microwave heating was used as a simple way to rapidly heat the mixture and the final temperature of the solution could be verified by a thermocouple probe. This temperature and pH were found by others to be near the optimal range to form small and stable crystallites used in the oxygen reduction reaction of the cathode [234].

A Raman spectroscopic analysis revealed the presence of surface bonding character. The Raman spectral scans show distinct peaks which match with reference data characteristic of the CNT and the anatase phase found in the composite [122, 235, 236]. Anatase vibrational modes are located below 750 cm^{-1} while the graphitic and disordered peaks from CNT are found at higher wavenumber. The main peak from anatase E_g mode is located 160.7 cm^{-1}. This value is higher than single crystal references and is a strong indicator of disorder induced in the crystal that is attributed to creation of oxygen vacancies [226].

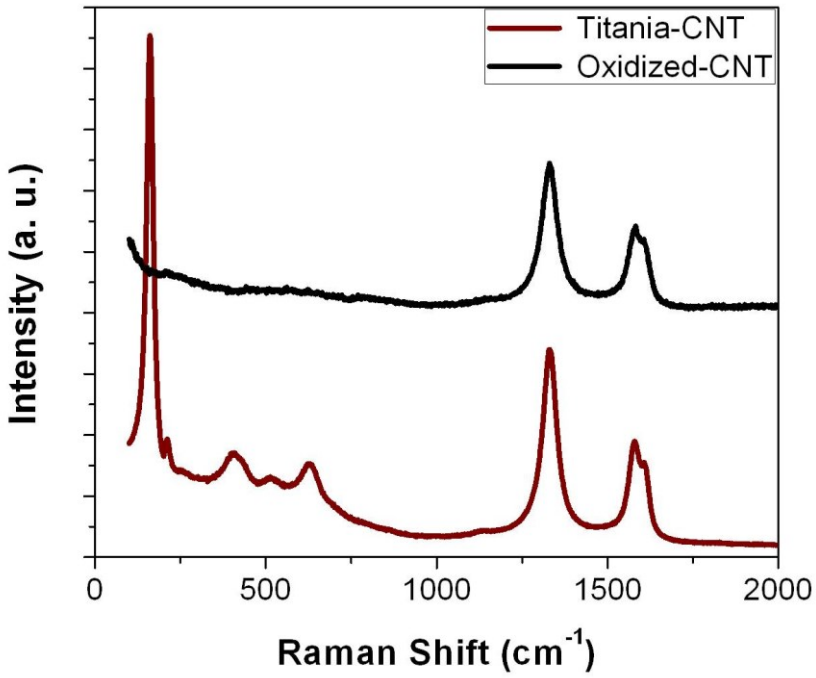

Figure 5.1 Raman spectra for oxidized CNT and titania functionalized CNT supports

XRD can reveal the crystalline nature of electrocatalysts. The spectrum does not clearly show the characteristic anatase phase in the support. Anatase peaks found near 25, 38, 48, 54, 63° may only be weakly exhibited for small, amorphous, and disordered crystallites which were difficult to differentiate from the predominant CNT features [237]. Supports were then coated with Pt from the polyol reduction method to form the electrocatalyst. Evidence of Pt peaks in the electrocatalyst becomes very clear in XRD shown by the black line of Figure 5.2 after deposition. Further analysis by electron microscopy can reveal further detail about the arrangement of metal atoms on CNT.

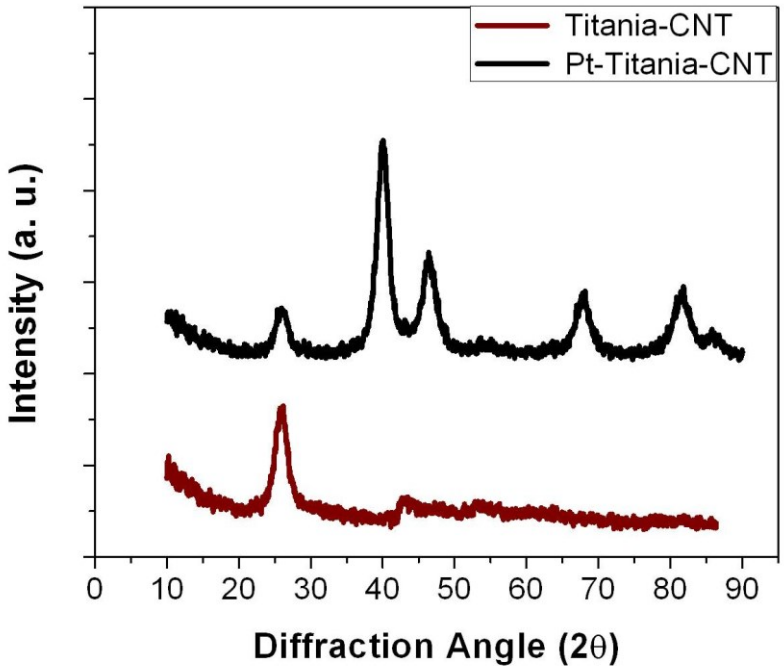

Figure 5.2 XRD spectra of composite support and electrocatalyst

Electron microscopy was used to observe the morphology of the electrocatalysts. The particle size distribution can be estimated from the SEM and TEM micrographs. The distribution of Pt nanoparticles was uniform on some dual phase supports, but in many other places concentrated clusters of Pt nanoparticles were observed. However, this phenomenon occurred in the control sample as well. Further optimization of material synthesis steps is needed to achieve a better Pt particle distribution, but formation of heterogeneous electrocatalysts was evident. The high resolution TEM (HRTEM) shows the result of material synthesis in Figure 5.3.

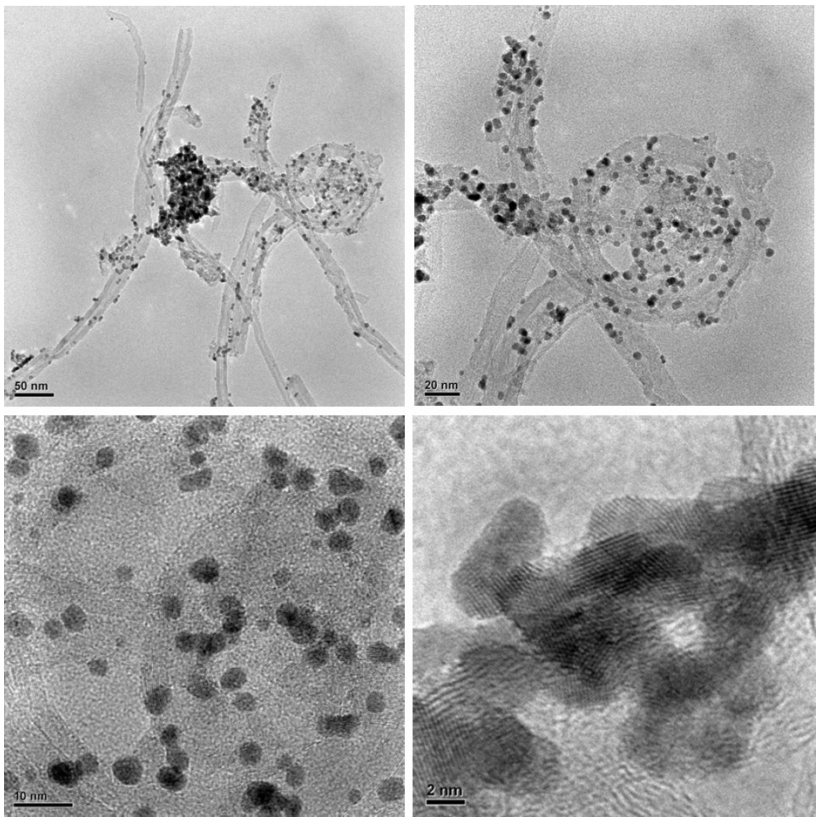

Figure 5.3 HRTEM images at increasing order of magnification

In high resolution STEM images of the Pt-Titania-CNT, the metal coverage can be seen as the brighter areas on the darker nanotubes. Pt catalysts are shown in brightest write and diffuse gray is from the titania phase wrapped around the surfaces of the CNT. At higher magnification in Figure 5.4 and in other images, it is consistently observed that Pt tends to locate in proximity to titania although some are also directly found on CNT. Clustering is also evident, especially in regions where dual phase support is present. In has been reported that Pt favorably nucleates at oxygen vacancies on titania and this likely leads to their preferred arrangement [[228, 238]].

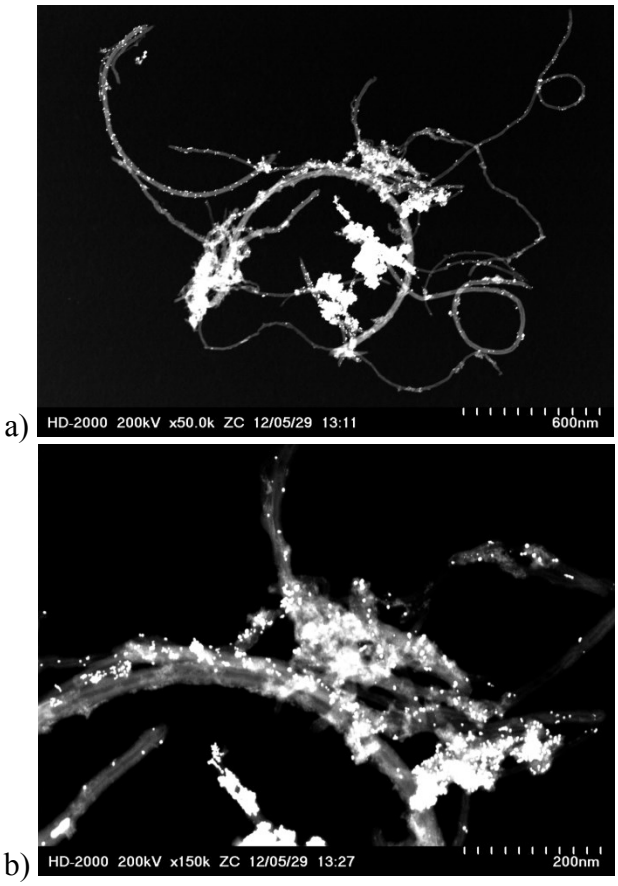

Figure 5.4 High resolution STEM images at a) low and b) high magnification

The location of metals is evident from the elemental distribution when STEM is coupled with atomic mapping by energy dispersive X-ray spectroscopy (EDX). In the ideal structure, Pt particles are located near interfaces of titania in the dual phase support while maintaining electronic contact with CNT network. Collocation of phases is apparent from STEM/EDX images in Figure 5.5. The EDX images (color) reveal the distribution of elements in the composite electrocatalyst structure. Pt bonding on titania phases becomes very evident in this picture where the atomic ratio is measured close to 1:1 and strong interaction with the oxide is probable.

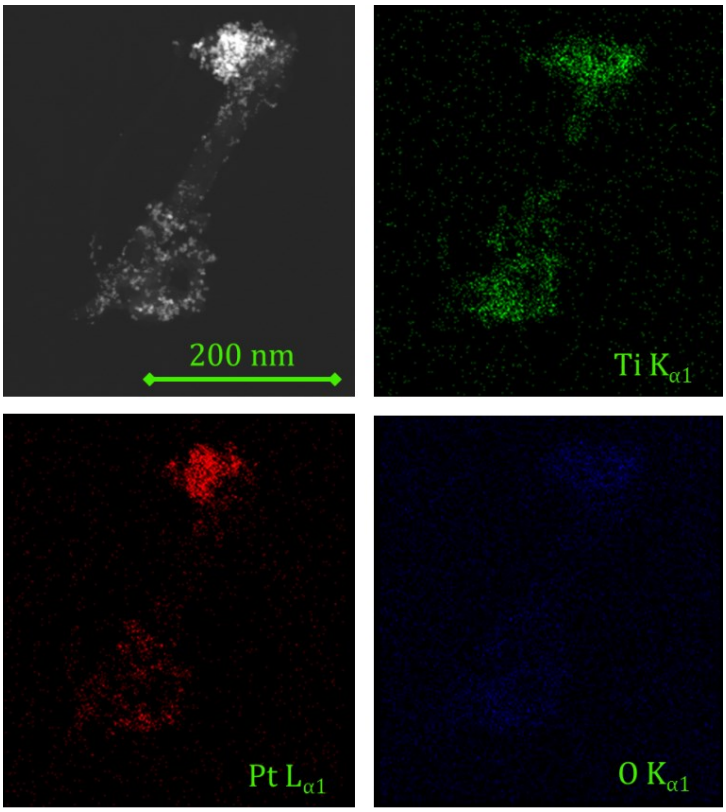

Figure 5.5 STEM/EDX with elemental mapping of the composite electrocatalyst

These electrocatalyst materials were then mixed into an ink suspension which was deposited on to polymer electrolyte membranes using an ultrasonic sprayer. Ionomer in the ink helped to suspend the solids to disperse the solids into an electrode which was also operated at 120 kHz frequency. This method is effective for fabricating thin homogeneous electrode layers for polymer fuel cells [[239]]. FESEM images from the side profile of the MEA after construction can be seen at increasing order of magnification in Figure 5.6. The catalyst coated membrane is then prepared and readied for electrochemical cell testing.

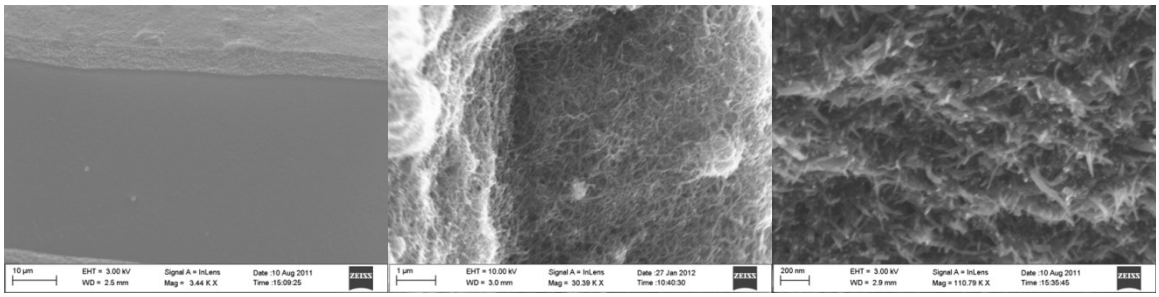

Figure 5.6 FESEM profile of Pt-Titania-CNT cathode at increasing magnifications

Figure 5.7 shows the hydrogen and oxygen performance at 3/3 stoichiometric flow rates. The following electrochemical data sets are meant to provide insight into the performance degradation behavior of the MEAs in accelerated testing and provide a relative comparison between Pt/Titania/CNT and Pt/CNT. Some of best electrocatalyst performance measured for ultrathin titania-CNT constructions have not been validated in working fuel cells [[137]]. Polarization performance suggests that most Pt catalysts are indeed in electronic contact with the conducting phase (i.e. CNT support).

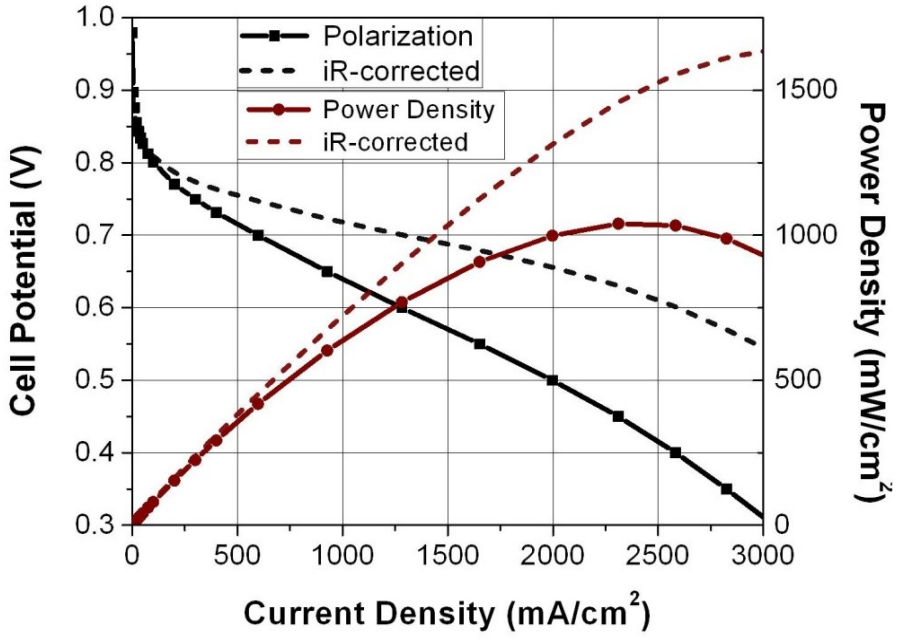

Figure 5.7 H_2/O_2 performance for the Pt-Titania-CNT cathode

The performance durability was also compared between the Pt/CNT and Pt/Titania/CNT electrocatalysts. The fuel cell performance measured with hydrogen and air was used to monitor behavior over the life of the cell and is shown here at three critical intervals during ADT. The accelerated cycling condition was designed to target the electrocatalyst by varying the potential with a triangular wave for 30,000+ cycles. The result on cell polarization in Figure 5.8 and the improvement in durability of the Pt/Titania/CNT can be contrasted with the Pt/CNT cathode.

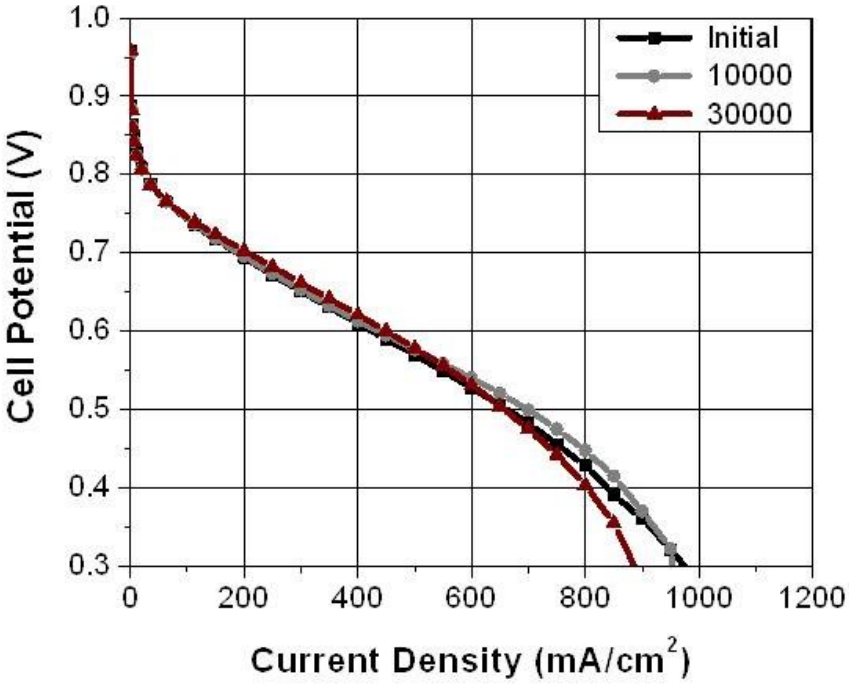

a)

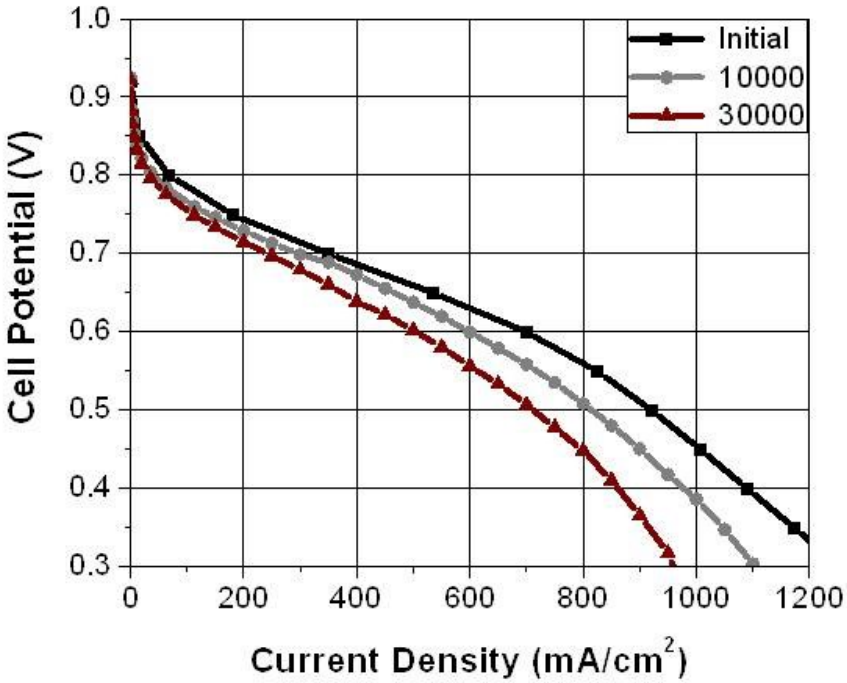

b)

Figure 5.8 Air polarization for a) Pt/Titania/CNT and b) Pt/CNT

The decrease in the potential at 800 mA/cm^2 current density for the Pt/Titania/CNT cell is from 0.429 to 0.404 V, or just 25 mV for this operating condition after the ADT. The Pt/CNT cell potential has dropped from 0.568 to 0.448 V, a loss of 120 mV. It is noted that the CNT cell had higher starting surface area and was part of the reason for better performance, initially. The activation region of polarization is shown in Figure 5.9. The Tafel plots also indicate the improved stability for in low current where overvoltage has only slight deviation from starting condition.

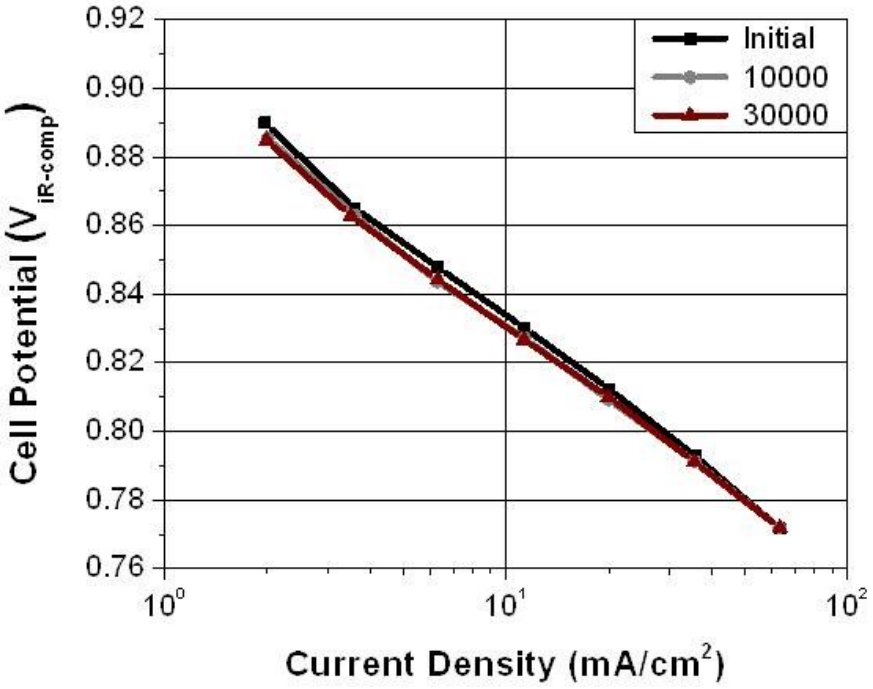

a)

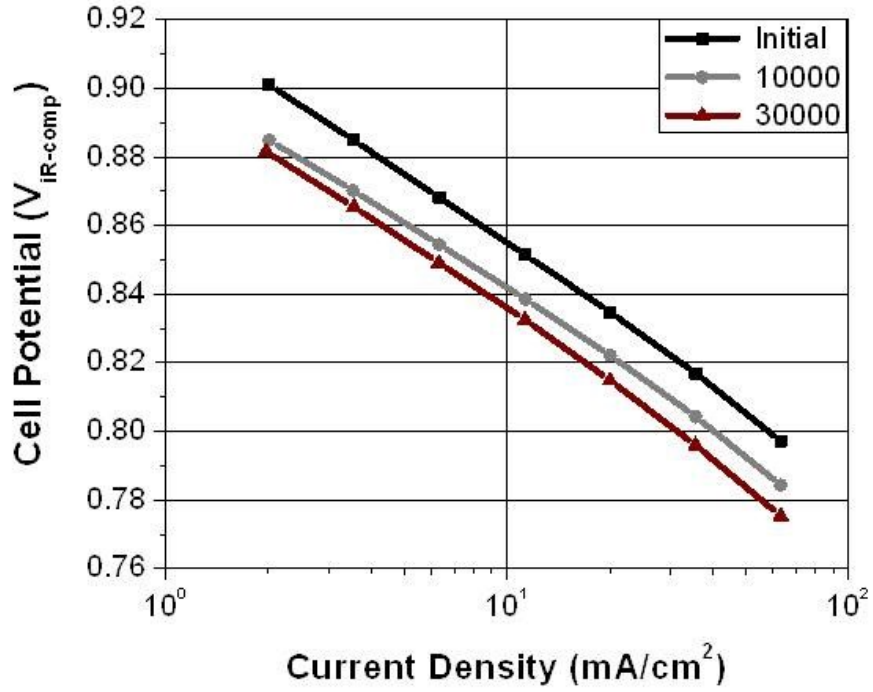

b)

Figure 5.9 Tafel plots in air of a) Pt/Titania/CNT and b) Pt/CNT

The cyclic voltammetry tests were conducted periodically to measure the change in available electrochemical surface area of the cathode. A smaller starting area for the Pt/Titania/CNT support is apparent, but it is also much more stable during potential cycling. The comparison of electrochemical surface area as function of potential cycles is plotted in Figure 5.11. The initial changes in surface area are similar for both cells which may have been a result of the growth of smaller particles in direct contact. After ADT, the Pt/Titania/CNT cathode had 60% of the surface area remaining compared to just 48% for the Pt/CNT. The Pt/Titania/CNT cathode started with 22.0 and ended with 13.1 m^2/g_{Pt} while the Pt/CNT cathode began with 36.2 and ended with 17.5 m^2/g_{Pt}.

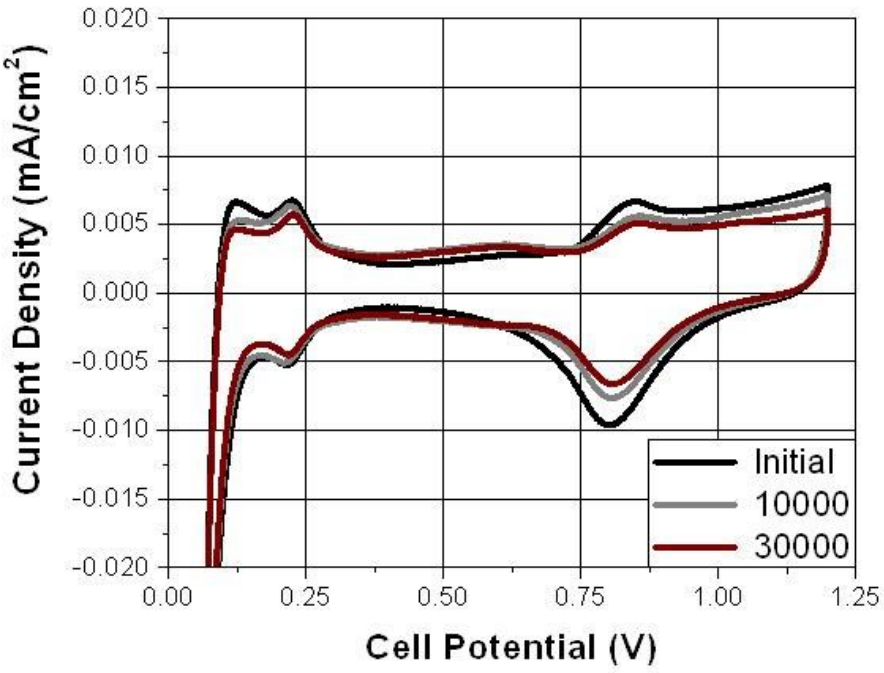

a)

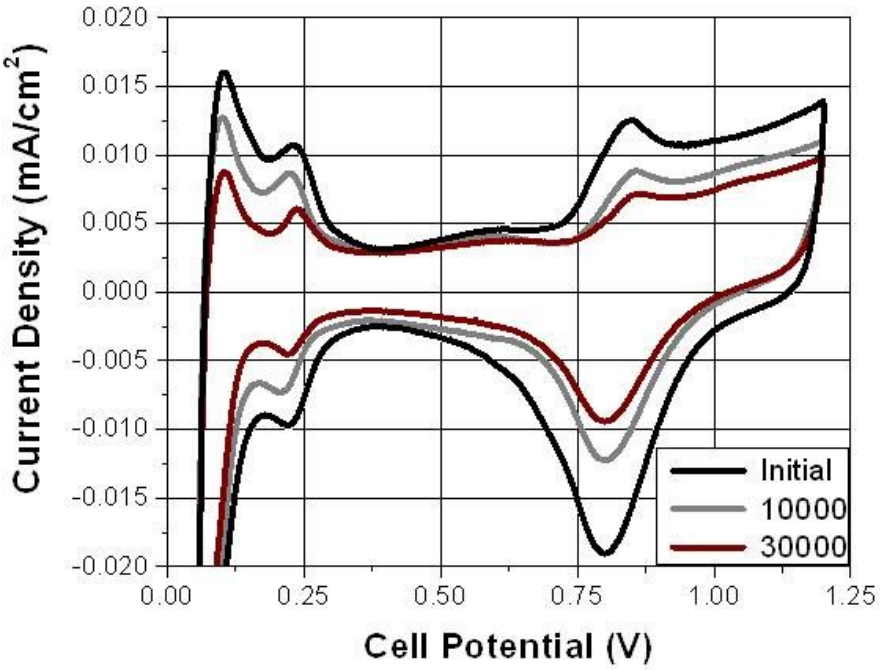

b)

Figure 5.10 Cyclic voltammetry of a) Pt/Titania/CNT b) Pt/CNT during ADT

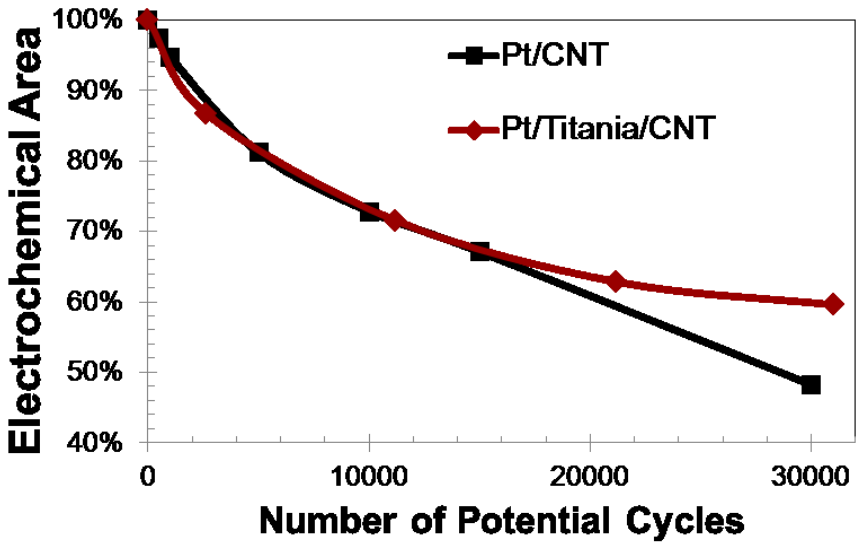

Figure 5.11 Relative ECSA change (normalized to starting condition)

The viability of a dual phase support including graphitic CNT and titania would appear to be possible from the evidence presented in this study. The durability of the support is critical to extending the life of the cell which has been improved over CNT only when compared by an accelerated degradation strategy. Quite possibly, some processing could be refined for further improvement in performance. Primarily, the distribution of titania and Pt particles and arrangement could be optimized during synthesis. Poorly distributed Pt in close proximity is probably more susceptible to ripening due to shortened diffusion pathways. In some highly concentrated regions, catalyst particle contact and oriented alignment of lattice atoms facilitates growth into larger crystals with less surface area for both electrocatalysts. Post-characterization would help to understand more about degradation mechanism. It is proposed that better functionalization of carbon and homogeneous addition of titania will also provide a more ideal platform. Regardless, the addition of a titania phase to the support had a significant effect of the electrocatalyst durability over 30,000 cycles. With additional or more aggressive cycling, the dual phase support may provide even greater advantage in the delayed loss of electrochemical performance. Mass activity from the catalyst seems to be almost completely preserved as evidenced by similar polarization and Tafel behavior through the test. If an optimum titania fraction is added to contribute only minimal resistance, even further developments could be possible. In any case, the design of catalyst supports is evidently very important to its performance.

5.5. Conclusions

The performance durability of Pt/Titania/CNT electrocatalyst has been improved over a Pt/CNT control when subject to accelerated degradation conditions in a polymer electrolyte membrane fuel cell cathode. The change in potential at 800 mA/cm^2 was only 25 mV as compared to 120 mV for the cathode without titania. The surface area remaining after an accelerated durability test was 60%, greater than the 48% left for the Pt/CNT cell. Despite a lower initial polarization for the composite electrocatalyst, the stability seems to be improved through the addition of a chemically bonded titania phase in the support. Material synthesis and structure optimization for the design of the electrode are under progress, but the preliminary results show a promising trend.

5.6. Acknowledgements

The authors thank the University of South Carolina and the Horizon I support staff. The Electron Microscopy Center at USC was used for FESEM pictures. HRTEM and STEM/EDX images were taken by Dr. Haijun Qian and Dr. JoAn Hudson at the Clemson University Electron Microscopy Facility. Undergraduate Magellan scholars, Diana D. D. Larrabee and Joshua J. Sightler, also participated in this research.

Chapter 6. Carbon Monoxide Tolerant Platinum Electrocatalysts on Niobium Doped Titania and Carbon Nanotube Composite Supports

6.1. Abstract

In the anode of electrochemical cells operating at low temperature, the hydrogen oxidation reaction is susceptible to poisoning from carbon monoxide (CO) which strongly adsorbs on platinum (Pt) catalysts and increases activation overpotential. Adsorbed CO is removed by oxidative processes such as electrochemical stripping, though cleaning can also cause corrosion. One approach to improve the tolerance of Pt is through alloying with less-noble metals, but the durability of alloy electrocatalysts has been an issue of concern. Without sacrificing stability, tolerance can be improved by careful design of the support composition using metal oxides. Promotion of the bifunctional mechanism occurs near junctions of the catalyst and metal oxides in the support. Stable metal oxides also form strong interactions with catalysts, as is the case for platinum on titania. In this study, niobium (Nb) serves as an electron donor dopant in titania (TiO_x). The transition metal oxides are joined to functionalized multi-wall carbon nanotube (CNT) supports to synthesize composite supports. Pt is then deposited to form electrocatalysts which are characterized before fabrication into anodes for tests as an

electrochemical hydrogen pump. Comparisons are made between the control from Pt-CNT to Pt-TiO_x-CNT and Pt-$Ti_{0.9}Nb_{0.1}O_x$-CNT in order to demonstrate advantages.

6.2. Introduction

Electrocatalysts are an essential part of many electrochemical cells which are often assembled in challenging ways in order to design the most effective electrodes. Unfortunately, catalysts such as platinum (Pt) are not cheap and often contribute substantially to the overall system cost. To reduce the amount needed, nanostructured Pt particles can be supported on conductive substrates that are intricately distributed into electrodes of polymer electrolyte cells. In the anode of a fuel cell, overpotential for oxidation of hydrogen (H_2) is relatively low when compared to the oxygen reduction reaction (ORR) in the cathode. However, presence of carbon monoxide (CO) in the hydrogen oxidation reaction (HOR) has a significant poisoning effect under typical operating conditions when active Pt sites become covered during exposure. At operation temperatures < 100 °C, even low concentrations about ≥ 10 ppm CO can severely impact cell performance in a short time [240-242]. Electrode poisoning from CO is one of the important challenges plaguing development of this technology. Therefore, a more resilient electrocatalyst in operations with CO can have very significant cost savings and deserves our attention [243].

Electrocatalyst properties of metals can depend on crystalline epitaxy, lattice strain, metal-ligand effects, and from their interfaces with adjoining compounds that could be a constituent phase of the support [244, 245]. Although it is possible to alter the

adsorption properties of CO on electrocatalysts by changing these parameters, the bifunctional mechanism has been well established for its removal once poisoned [246, 247]. In the case of adsorbed CO on the catalyst, most is converted to carbon dioxide (CO_2). This effect is promoted when dually adsorbed species are involved in its oxidation as shown in Langmuir-Hinshelwood type reaction of Equation 1. Metal oxide (MO_x) phases formed in proximity to catalysts can serve this purpose in analogous ways to alloys with Pt [244, 248]. Construction of a catalyst support with these materials could aid this property in addition to making it more durable.

(1) $MO_x{-}OH + Pt{-}CO_{ad} \rightarrow CO_2 + Pt + MO_x + H^+ + e^-$

Improving tolerance to CO has been extensively investigated through alloying Pt with less-noble elements to promote bifunctional effects, although alloys can be limited by their stability. Advances with Pt alloys containing promoters such as Ru, Sn, and Mo are considered a state-of-the-art for CO tolerance, but these metals can become irreversibly oxidized during operation [249-254]. From the perspective of stability, it is probably more rational to prepare those metals initially in a higher oxidation state to form junctions with Pt [255-257]. In any case, contamination from the fuel adsorbs on anode catalyst surfaces and to restore activity, oxygen pressure, temperature, and/or cell potential are generally adjusted to accomplish removal [258-260]. However, these processes can result in oxidation of the electrocatalyst as well. Unintended fuel starvation and fuel cell reversal can also lead to high anode potentials, low pH, and conditions that cause degradation of this electrode [35, 250, 261]. These events all result in

the loss of performance from electrocatalysts which can be corroded similarly to catalysts in the cathode of the fuel cell [253, 262]. Electrocatalyst losses may be measured by changes in reversible features from cyclic voltammetry which correlate with active sites [263]. In alloys with Pt, the more active metal tends to be sacrificed while passivation occurs on the surface and noble metal lattice strains are relieved [253, 262]. Catalyst activity is lost, but secondary symptoms originating from this issue may also persist. For example, dissolved cations from alloyed metals can diffuse into proton channels of the electrolyte and also plate out in the cathode after being reduced along with the fuel [250, 252]. Electrocatalyst degradation has a cumulative effect on performance which can eventually kill the cell; this paradox poses a challenge to the purpose of same materials which also make them work so well [26]. In the anode, tolerance to CO contamination should come without a big cost to stability for ideal electrocatalysts.

Electrocatalysts must be validated in electrodes with conditions similar to those found in real applications. Half-cells and rotating disk electrode (RDE) studies are essential in understanding fundamental behaviors to guide specific design, but results from full cell hardware are necessary in confirming the effectiveness of working electrodes. Though, fuel cell testing complicates understanding of the anode due to cathode effects and sluggish ORR. Electrochemical hydrogen pumps can provide more accurate characterization of the anode oxidation reactions, however. Protons formed in the anode are simply pumped across the membrane electrode assembly (MEA) and reduced at the cathode by applying potential. For the reference electrode, Pt black electrocatalysts dually serve as a cathode for the fast hydrogen evolution reaction. More sophisticated designs can also efficiently serve a critical role to purify diluted flows and

pressurize clean H_2 gas which is ideal for fuel cells. Other uses have found success in the form of sensors. Characterization of fuel cell cathodes by cyclic voltammetry is performed by a similar pumping procedure where fuel has been purged from working electrodes with inert gas. From a diagnostic perspective, losses in H_2 pump performance and overpotential can be relatively easy to separate and assign.

Transition metal oxides selected for this study were carefully chosen for stability and their interaction with Pt catalysts. The abundant element titanium (Ti) was picked as the major constituent with a minor addition of niobium (Nb) included as an electron donor in the oxide matrix. Both oxides have a wide passivation region overlapping the operating ranges used in the environment of related electrochemical cells, based on equilibrium Pourbaix (E_h-pH) diagrams [1, 145]. It is imperative that materials used in catalysts should at least be prepared near to their equilibrium state (e.g. TiO_2 or Nb_2O_5) or else they will eventually adopt it during operations, resulting in irreversible transformations and limited lifetimes. The metal oxides are intended to serve several functional roles in the support. Titania can provide a stronger interaction with catalysts than carbon, improving durability by limiting diffusional growth while also resulting in interfacial reduction of the metal oxidation state [264-267]. This can facilitate the dissociation of water to form hydroxyl groups (−OH) from extra nonbonding valence electrons made available by the metal in a reduced oxidation state and corresponding oxygen vacancy near the surface [185, 268-271]. Titanium dioxide has been used for numerous catalytic applications and the science of its surface chemistry has been the single most investigated transition metal system [272, 273]. In electrocatalysis, high conductivity is a necessary requirement and inadequate electronic conduction of metal

oxides has limited their use as support in related applications. Although, an extensive number of recent reports have emerged which indicate there can be a synergistic combination for benefits to activity and stability from metal oxides supported electrocatalysts. Solely using metal oxide phases alone in the support is perhaps not practical because long range order of larger doped crystals (e.g. rutile) is typically needed to effectively form conductive electronic pathways through them which comes with a sacrifice to available surfaces [146, 274, 275]. Nevertheless, using metal oxides in conjunction with carbon could still be an effective approach to maintain suitable conductivity in the electrode without requiring a high catalyst loading [131, 132, 137, 138, 232, 276-284]. Therefore, it is a goal to translate these conceivable developments into results that can be established in electrodes of low temperature cells.

The choice of doped metal oxides for this research is based on defect engineering principles that should be favored in the environment of the electrode. Defects are formed in host crystals by including irregular placement of ionized species in its lattice that add charge carriers, typically found in the gap state of oxides. Titanium (IV) dioxide has a wide gap, but can be reduced by extra electrons formed during loss of oxygen atoms in the compound and it is normally referred to as n-type semiconductor. Adding defects contribute to electron acceptor and donor properties, but are often skewed more toward one type. The selection of Nb as a donor dopant for Ti is based on its ionic radii, coordination number, and preferred valence state in the environment. Donor doping is ideal in reducing environments based on laws of mass action as suggested by the relationship of Equation 2 in Kröger-Vink notation [221, 285]. At low oxygen concentrations found in the anode, oxygen vacancies ($V_O^{\bullet\bullet}$) are compensated by electron

carriers as represented by reaction of Equation 3 and the laws of mass action. When Nb^{+5} is reduced to Nb^{+4}, a free electron on ($Nb_{Ti}^{\bullet}$) is formed as a shallow donor in titania [97, 286]. Solid oxide fuel cells rely on these defect relationships for conductivity, where defects are more mobile at high temperature. At lower temperatures, defects may become quenched in the lattice and considered as a quasi-equilibrium that can contribute to new mobility states in the gap [287-291]. There are only a few other stable elements with higher oxidation suggested as donors in titania; among these are Nb (V), Ta (VI), and W (VI) oxides found in high potentials ~ 1 Volt and at very low pH values often found in acidic electrolytes of electrochemical cells [1]. Importantly, the oxides of positive transition metals have a tendency to form oxygen vacancies and hydroxides at their surface when reduced through strong interactions with more electronegative metal clusters deposited on them [95]. Substitution limits for dopant cations depend on their ability to fit into the lattice of the host crystal. The observed coordination with oxygen in TiO_2 is 6 and ionic radius about 0.61 Å, where that of the closest possible donors are Nb^{+5}, Ta^{+5}, and W^{+6} with 0.64, 0.64, and 0.60 Å radii according to the *Handbook of Chemistry and Physics* [292]. These dopant cations can provide for the optimum replacement solubility while inducing only minimal strain in the crystalline lattice. In mesoporous titania films, it was shown that 20% of Ti can be replaced with Nb for very low electrical resistivity [114]. Furthermore, concentrations > 25% were successfully included in anatase titania that were stable during an insulator-to-metal transition [114]. Even low level doping in rutile of Nb < 1% replacement provided for substantial band gap narrowing and formation of intermediate energy states including shallow donors [110, 223]. Crystalline structure and processing conditions are clearly important to Nb inclusion

in the phases of titania and its electronic properties. A substitution of 10% Ti with Nb was decided upon for this study, but it has been suggested that the other oxides and dopant combinations could also be used as effective electrocatalysts [293-297].

(2) $$Nb_2O_5 \xrightarrow{2\,TiO_2} 2\,Nb_{Ti}^{\bullet} + 4\,O_O^X + \frac{1}{2}\,O_2 + 2\,e^-$$

(3) $$O_O^X \rightleftharpoons V_O^{\bullet\bullet} + 2\,e^- + \frac{1}{2}O_2$$

There are many descriptions of the interaction from Pt deposited on titania present in the literature, especially for catalysis. Tauster notoriously reported a loss of H_2 and CO chemisorption for these supported catalysts when heated in a vacuum or reducing atmosphere above ~ 300 °C due to the accumulation of electrons from TiO_2 at interfaces with Pt that can result in a rapid surface diffusion of Ti^{3+} cations around the noble metal islands [89, 298]. These encapsulated catalysts were rendered inactive after this conversion due to a dubbed strong metal-support interaction and loss of adsorption. Heating in low oxygen pressure results in a reorganization of electropositive transition metals from the left side of the series to encapsulate islands of electronegative metal clusters made of noble group elements on the oxide surface due to charge transfer and interfacial reactions that minimize surface energy through alignment of their Fermi levels [90, 95, 238, 299]. Without chemisorption of H_2 or CO reactants, catalysis is not practical. However, a beneficial catalytic property from the class of materials that demonstrate strong metal-support interactions can still be realized when prepared at ideal conditions that limit encapsulation [90]. Oxygen vacancies formed in the reduced metal oxide phase near interfaces with the catalyst can provide an important contribution to the bifunctional mechanism while acting as an extension of the active surface in oxidation of CO [300, 301].

Interaction of titania with supported Pt has been used in a number of other catalytic reactions (e.g. water-gas shift) where CO adsorption, vacancy formation energy, and electronic interactions have been modeled [222, 227, 302-304]. Interfaces formed with the metal are seemingly important and Schottky barriers are known to form in Pt @ titania where surface charges accumulate. Related phenomena have been referred to as catalytic nanodiodes and also used in CO oxidation [305, 306]. Electrocatalytic oxidation studies for 10% Nb doped anatase and lightly reduced versions of this titanium oxide phase (i.e. $TiO_{2-\delta}$) exemplified better performance and stability than its rutile, undoped, or Magnéli phase counterparts in electrochemical tests [82, 231, 307-309]. These results also have indicated effective alcohol oxidation in anode reactions where CO is formed as an intermediate in the mechanism. Although metallic support conduction is not necessarily required for electrocatalysis, use of dielectric oxides and resistive materials should be minimized. Addition of a carbon component is probably still imperative for improving conductivity and limiting the use of highly crystalline and wide gap oxides that can behave semiconductors.

Carbon is the most commonly used electrocatalyst support. Unfortunately, carbon can be corroded at low standard potentials. Although, the kinetics of oxidation are moderate until conditions become more severe such as those sometimes found in electrochemical cells [35]. The structure of carbon and its surface functionalization have important implications on its applicability in the electrode as well its corrosion resistance [310-312]. Graphitized forms of carbon in the support have been shown to be more stable in these applications than carbon blacks [51, 67, 68]. The Pt catalyst though poses another dilemma because it also facilitates carbon corrosion and bonds relatively weakly through

carbon surface functional groups [313]. CNTs have several attractive attributes which start with their strength, high surface to volume ratio, and relatively inexpensive production, making them a good candidate for graphitic carbon in the electrode as long as catalysts can be attached [313-316]. CNTs also have strong mechanical properties which can prevent electrode structure collapse, exhibit satisfactory electronic conductivity, and provide a percolating network along axial directions to provide diffusion paths with an open porosity [69, 317-319]. In CO tolerance, similar graphitized forms of carbon with oxygen functionality on their surface were shown to have a high activity and used as guides in our design [233, 314, 320]. The defect sites in carbon act as decoration centers for the metal oxide and catalyst [127, 137]. Multi-wall CNTs are known to also exhibit some semiconductor behaviors, but an inexpensive commercial version was chosen as a representative carbon platform in the foundation of composite supports for this research. It is purported that advancements made in this area will be reinforced by a simplified approach for material synthesis and electrode fabrication to demonstrate the support concept which may also serve as a case for further development in related electrocatalysts.

6.3. Experimental

6.3.1. Carbon nanotube composite supports

Multi-wall CNTs of 8-15 nm O. D. x 10-50 μm length (Cheap Tubes Inc.) were first oxidized in a mixture with equivalent volumes of concentrated nitric (70%) and sulfuric acid (96.5%) for 3 hours at 80 °C to functionalize their surfaces with oxygen

groups and remove impurities. Oxidized CNT solids were washed thoroughly with de-ionized water and separated with porous polytetrafluorethylene (PTFE) filters before drying. Functionalized CNT were ultrasonically dispersed in anhydrous isopropanol solvent before adding precursor amounts of titanium (IV) isopropoxide and in some cases niobium (V) ethoxide solutions (99+%) to reflux under N_2 purge gas at 80 °C for 3 hours in a modified sol-gel process [127]. De-ionized (DI) water was added slowly to promote hydrolysis, condensation, and growth of metal oxides on CNTs. Reflux was removed and evaporation of remaining solvents was necessary to collect resulting solids. All support powders were then calcined in N_2 at 450 °C for 2 hours to induce ordering and phase transformation. Two different loadings of titania were initially compared by varying ratio of CNTs to titanium isopropoxide with atomic proportions of [Ti:C] at [1:10] and [1:100]. The Nb doped titania target was 10% atomic substitution for Ti in the oxide. Three support formulations were prepared to form electrocatalysts: a carbon only control with oxidized CNT, a composite from TiO_x-CNT, and Nb doped titania $Ti_{0.9}Nb_{0.1}O_x$-CNT, where $x \approx 2$ [321]. For simplification, titania and Nb doped form are just denoted as TiO_x and $TiNbO_x$ in the remainder of the publication.

6.3.2. Electrocatalyst preparation

The deposition of Pt on composite supports was carried out by a microwave-assisted polyol reduction method. The catalyst supports were first ground into fine black powders that were dispersed by an ultrasonic probe (Sonics Vibra-Cell 750W) in ethylene glycol before choloroplatinic acid hexahydrate (8% wt. $H_2PtCl_6 \cdot 6\ H_2O$) was added to prepare electrocatalysts with projected yields of 20% Pt mass. The pH of solution was

then adjusted past the isoelectronic point and above pH 9 by adding 1N NaOH dissolved in ethylene glycol to promote Pt nucleation. After stirring, mixtures were rapidly heated in a 1100 W commercial microwave oven (GE) on 60% power setting for 60 seconds to reach a critical temperature of 140 °C where growth of Pt nanoparticles on the catalyst support is stimulated [322]. The resulting suspensions were again separated by vacuum filtration and the remaining black solids were washed with acetone and then DI water before drying and finally refining size of agglomerations with simple mortar and pestle technique. These composite materials were characterized and used as subjects of electrode testing. The three functionalized electrocatalysts are labeled Pt-CNT, Pt-TiO_x-CNT, and Pt-$TiNbO_x$-CNT.

6.3.3. Ultrasonic ink processing and electrode fabrication

The resulting electrocatalysts were dispersed into an ink with ionomer and solvents before deposition on polymer electrolyte membranes. After weighing the catalyst powders, a few drops of water saturate solids before they were submersed with isopropanol in 20 mL vials. A suspension of the ionic polymer, Nafion® DE-521, was added to equate 20% of solid mass formulation in the electrode. Electrocatalyst inks were then mixed by ultrasonic horn for at least 15 minutes before being loaded into a syringe used in the sprayer. An automated ultrasonic spray process (Sono-Tek Exactacoat system with an Accumist 180 kHz nozzle) was used to deposit inks directly on substrates, Nafion® NRE-212 membranes in this case [239]. Membranes were placed above platen heated to 100 °C to accelerate solvent evaporation. A raster pattern was used on template to obtain square MEAs with 25 cm^2 active area and 0.3 mg_{Pt} cm^{-2}

loading in the anode. The opposite side was coated with Pt black (Johnson-Matthey HiSPEC 1000) with 2 mg_{Pt} cm^{-2} loading by a highly specialized process and served as a pseudo-reference electrode [321].

6.3.4. Membrane electrode assembly and cell construction

MEAs were sprayed and then dried prior to pneumatic hot press at 130 °C for 5 minutes under 300 N/cm^2 force. The pressed MEAs were soaked in 0.5 M sulfuric acid for one hour at 80 °C to protonate ionomer electrolyte and then rinsed in hot DI water. Test cells were built with a set of SGL Carbon 10 BC gas diffusion layers (GDL) and 254 µm thick PTFE gaskets to impose a 33% pinch of GDL by applying 80 in•lbs torque to tie bolts in cell hardware (Fuel Cell Technologies, Inc.). Cells were assembled in graphite flow plates with triple serpentine flow channels, and connected to a fuel cell test station (Scribner 840) which feeds pure gas (H_2 and N_2) at controlled temperature and water saturation to the cell. An external humidifier and flow controller (MKS) were used to humidify and control H_2 mixed with 100 ppm CO (Praxair) fed into the cell. Experimental test set up is shown in Figure 6.1.

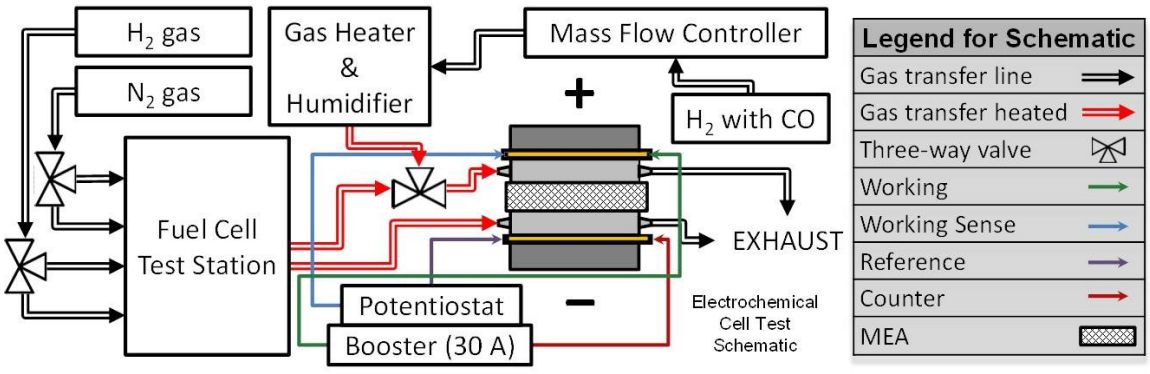

Figure 6.1 Experimental schematic for electrochemical cell to test working anodes

6.3.5. Electrochemical diagnostic tests

Several electrochemical experiments were carried out to compare performance of cells with different anode electrocatalysts. CO tolerance of the cell was measured by both chronopoteniometry and chronoamperometry experiments on cells operated in the hydrogen pump mode with contaminated fuel. The catalyst electrochemical area was measured by cyclic voltammetry (CV). The CO stripping voltammetry was used to compare CO oxidation peaks. Electrochemical impedance spectroscopy (EIS) techniques were used to measure cell impedance. Electrochemical tests were carried out with a potentiostat/galvanostat (Gamry Reference 3000) coupled to a power booster (Reference 30k). Flow rates for the fuel and purge gas were all set to 250 mL min^{-1}, unless otherwise noted. In hydrogen pumps, the Pt black cathode is supplied with clean H_2 and also serves as the reference electrode while anodes were exposed to flows of the contaminated H_2 to provide the source of protons. Cell temperature for all experiments was set at 75 °C with feed gases fully humidified to 100% relative humidity (RH).

Initially, potential cycling was applied to all electrodes from 0.05 to 1.2 V at 50 mV sec^{-1} for 500 cycles to accelerate aging during a break-in process. CO stripping was completed by the same potential cycle parameters. Working electrodes were under constant exposure to the 100 ppm CO in H_2 for at least 30 minutes. For accurate peak determinations, H_2 pump anodes were then purged with N_2 for another 15 minutes to remove excess CO and provide ample time for the open circuit voltage to stabilize in the cell. Chronopotentiometric tests with galvanostatic current density from 3.125, 6.25, 12.5, 25, 50, to 100 A m^{-2}_{Pt} were supplied throughout constant stoichiometric H_2 flow rate of 10 normalized to the Pt active surface area. Voltage measurements were collected

over a period of at least 2500 seconds and up to 1 hour at lowest current. Adsorbed CO in the electrode was cleaned up in between tests by stripping before repeating tests at the next highest current density setting. Chronoamperometric tests were applied at 25 mV potentiostatic for 10 minutes under constant flow rates normalized to the Pt surface area of catalysts. Current was recorded during this time which was sufficient to reach a CO saturated condition and stabilize cell performance during this span. EIS complemented the potentiostatic condition from the previous step using scans from 2500 to 2.5 Hz and 5 mV perturbations with successive spectra at exact intervals of 1 minute for the first 10 minutes of exposure to CO. The time dependent and steady state electrochemical behavior is presented in the results and discussion.

6.3.6. Materials characterization

The prepared materials were characterized by a suite of analytical techniques. The Raman spectra of the catalyst support were obtained by a Horiba LabRam-HR system with a He-Ne laser ($\lambda = 633$ nm). Powder X-ray diffraction (XRD) was collected by a Rigaku Mini-Flex instrument with CuK_{α} radiation and D/teX detector. Scanning transmission electron microscope coupled with energy dispersive X-ray spectroscopy (STEM/EDX) on a Hitachi S4800 and a high resolution transmission electron microscope (TEM) by a Hitachi H9500 were used to image the electrocatalysts. X-ray fluorescence (XRF) by Fischer XDAL instrument was used to analyze the Pt loading in the MEA. X-ray photoelectron spectroscopy (XPS) using a Kratos Axis Ultra DLD equipped with a monochromated Al K_{α} X-ray source and hemispherical analyzer can probe electronic

interactions. Binding energy was calibrated using an Ag foil with Ag $3d_{5/2}$ set at 368.21 ± 0.025 eV while the source was operated at 15 keV and 120 W.

6.4. Results and discussion

6.4.1. Material characterization of composite supports

The first characterization by XRD aimed to identify the structure of phases in composite supports. A spectrum from titania and CNT with an atomic ratio of Ti to C [1:10] showed peaks representing the formation for anatase phase from TiO_2 in well-defined structure on carbon supports at this concentration. The average anatase (A) crystal size was under 10 nm from Scherrer equation applied to A (200) and (204) peaks which have been labeled in Figure 6.2. When the ratio of titanium to carbon [Ti:C] was decreased by an order of magnitude for an estimated yield [1:100], the oxide structure was obscured due to reduced crystallinity with mass accounting for < 5% of total [128, 237]. This construction was prepared by the same procedure, but was more disordered with only partial coverage and resultant spectra dominated by the features of graphitized carbon (C) [106, 127, 135, 277]. A drastic improvement in performance from the [1:100] atomic ratio of oxide metal to C resulted in this parameter being held constant for supports used in electrochemical cell test results presented later in the publication.

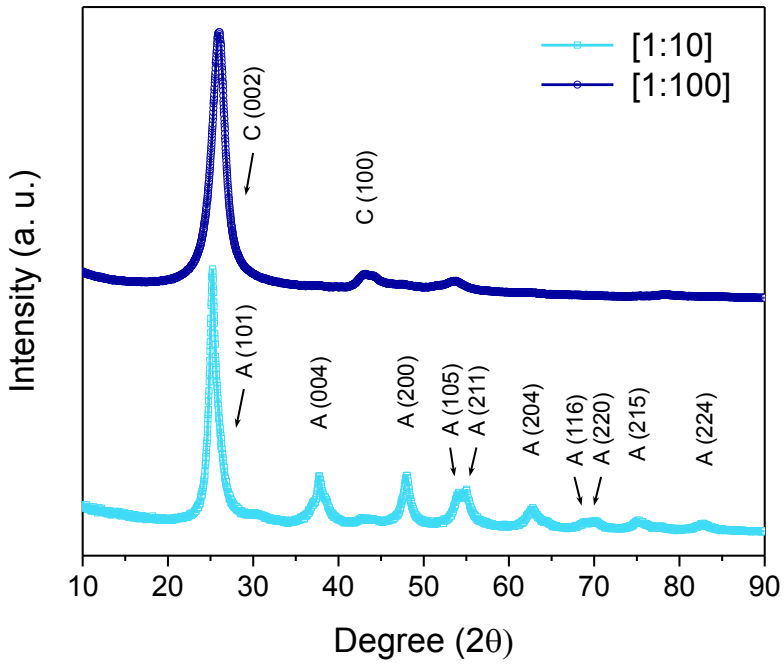

Figure 6.2 XRD of Titania-CNT composites

A confocal Raman spectroscopic investigation was used to probe the nature of metal oxides joined to CNT and confirm their presence. The six active vibrational modes of anatase titania are observed below 700 cm^{-1} from composite supports plotted in Figure 6.3 [235]. A decrease in all peak intensities is noticed for [1:100] ratio with lesser Ti content. The most intense peak is attributed to the lowest frequency for E_g mode and the reduced signal can be related to a lesser degree of crystallinity [323]. Moreover, this main peak has tendency to blue-shift and broaden asymmetrically towards higher wavenumber due to decrease of particle size, oxygen vacancy formation, interfacial surface vibrations, and photon confinement effects [226]. The resulting main E_g peaks have been identified at 159.4, 160.5, and 161.3 cm^{-1} with Nb doped titania showing the lowest intensity and largest Stokes shift. It has elsewhere been reported that additions of Nb in titanium

dioxide increase the temperature of phase transformations and retard its grain growth [112, 116, 324]. A decreased degree of order in the doped sample is the probable result. Presence of features in composites with peaks near 1350 cm^{-1} and 1600 cm^{-1} are associated with the graphitic and disordered carbon bonding vibrations of multi-wall CNTs [122].

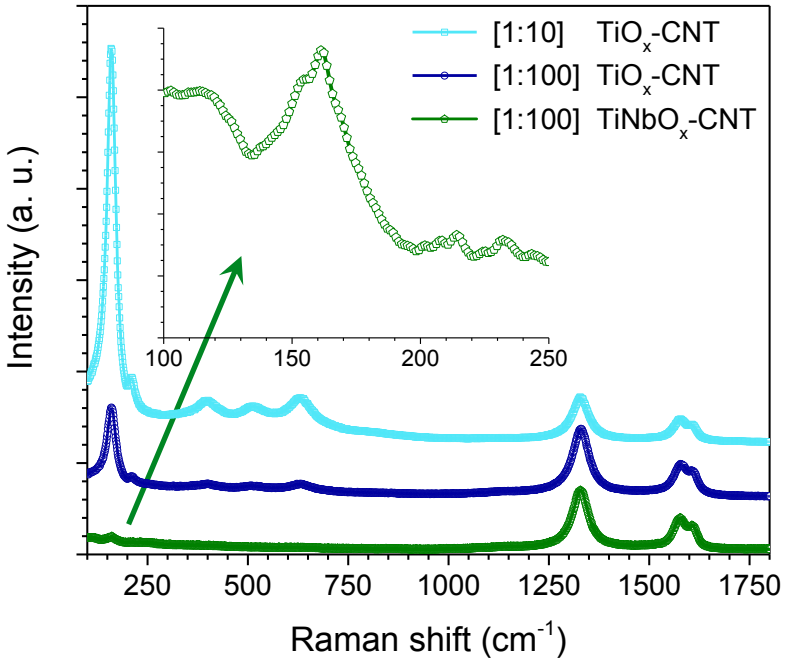

Figure 6.3 Raman spectra of composite supports

6.4.2. Material characterization of electrocatalysts

After polyol deposition of Pt on supports, XRD analysis was performed again to observe growth of Pt catalyst nanostructures. Similar crystalline peaks were observed in all three electrocatalysts, but there were differences in the average size of Pt on supports. From interpretation of Pt (220) facets, the average size of catalysts decreased from Pt-CNT > Pt-TiO_x-CNT > Pt-$TiNbO_x$-CNT at value of 8.15, 4.99, and 4.89 nm with peak centers identified at 2θ values of 67.62, 67.88, and 67.80, respectively. Composite

supports appear to improve distribution and limit the growth of catalysts to a much greater extent when synthesized under the same conditions [59, 135, 325, 326]. This may be attributed in part to the interaction between Pt and the electropositive transition metals used in the support. By this rationale, there could be some consideration of Pt size effects since the Pt-CNT grew to a larger diameter. Regardless, the order of size did not directly correlate with their performance, further suggesting support specific electrocatalyst effects.

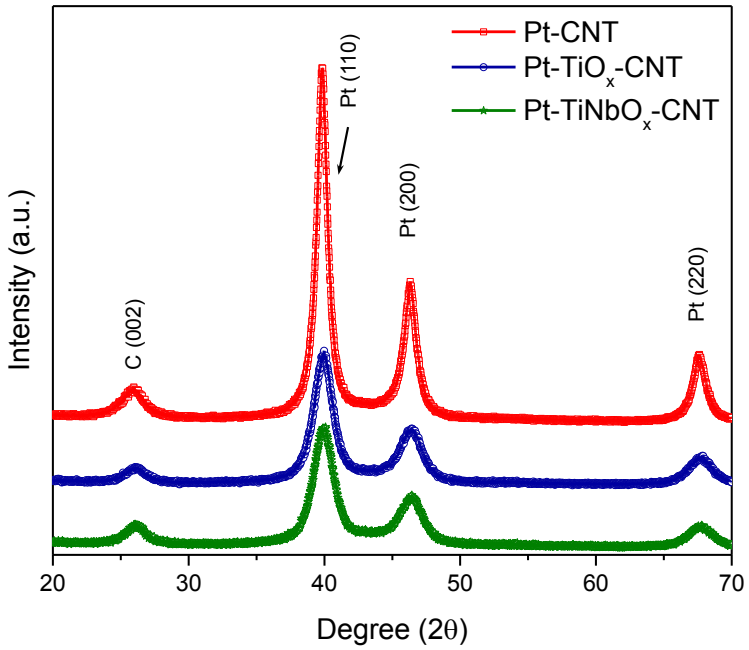

Figure 6.4 XRD of electrocatalysts after Pt deposition

XPS was used to verify the presence of transition metals and the effect on their core electrons after Pt deposition. Peak shoulders and shifts in the positive (oxidation) and negative (reduction) direction of the binding energy (BE) are observed. Deconvolutions are presented in Appendix E. The BE values have been referenced to fit

the main C 1s peak at BE of 284.6 eV due to various charging effects and all intensities have been overlaid for the sake of comparison purposes. As shown in Figure 6.5, a reduction shift in BE of core Ti 2p and Nb 3d orbitals for Pt electrocatalysts (—*—) is seen when compared to supports (——) only. Presence of reduced Ti (III) and Nb (IV) valence states in metal oxides are more apparent after Pt deposition by formation of shoulders and asymmetric artifacts extending to BE below support only values [110, 112]. The added signal noise in the plots with Pt is another indication that much of the oxide surface has been covered by catalysts. Interfaces formed with Pt seemingly increase the concentration of transition metal species in this instance. Defects in the native oxide form charge carriers residing in intermediate states of the mobility gap.

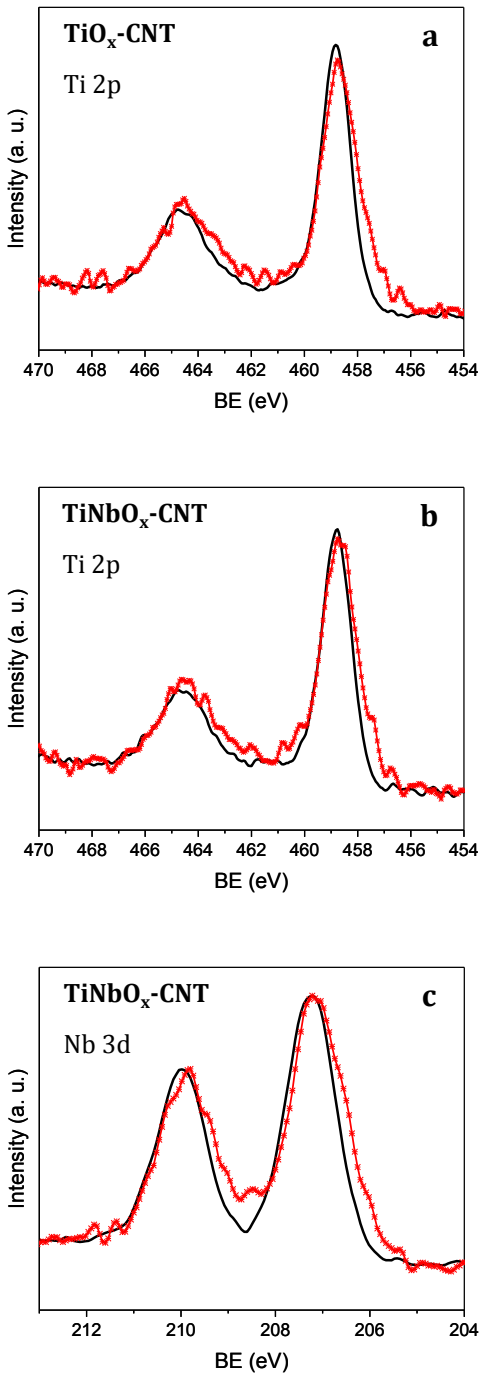

Figure 6.5 XPS analyses show the transition metal spectra in composites before (——) and after (—*—) Pt deposition

A cooperative interaction between Pt, the metal oxides, and multi-wall CNT may further be realized by examination of O 1s peaks. As shown in Figure 6.6, peaks

centered above 530 eV arise in composite supports shown in (**b**) and (**c**) which do not exist for the CNT control seen in (**a**). This peak with the highest binding intensity is attributed to the M−O bond. In composites with titania, it becomes considerably diminished after Pt deposition. This is a suspected result of the interaction between Pt and Ti or Nb along with the creation of critical oxygen vacancies. The surface oxygen vacancy has been found as a nucleation center for growth of Pt where charge transfer occurs providing for the strong interaction [229, 279, 325]. Addition of a donor dopant can assist in the creation of more oxygen vacancies that are facilitated by deposition of Pt. Oxygen vacancies or dangling bonds can be healed by dissociated hydroxyls near catalyst interfaces to form M-OH species in the oxide [152, 271]. Several reports have found this to be beneficial in ORR where a hole in the metal oxide could be assisting transfer of hydroxyl intermediates involved in the limiting step of that half-reaction [294, 296, 301, 327]. In the bifunctional mechanism for CO oxidation in the anode, the metal oxide would facilitate supply of hydroxyl groups to reaction sites.

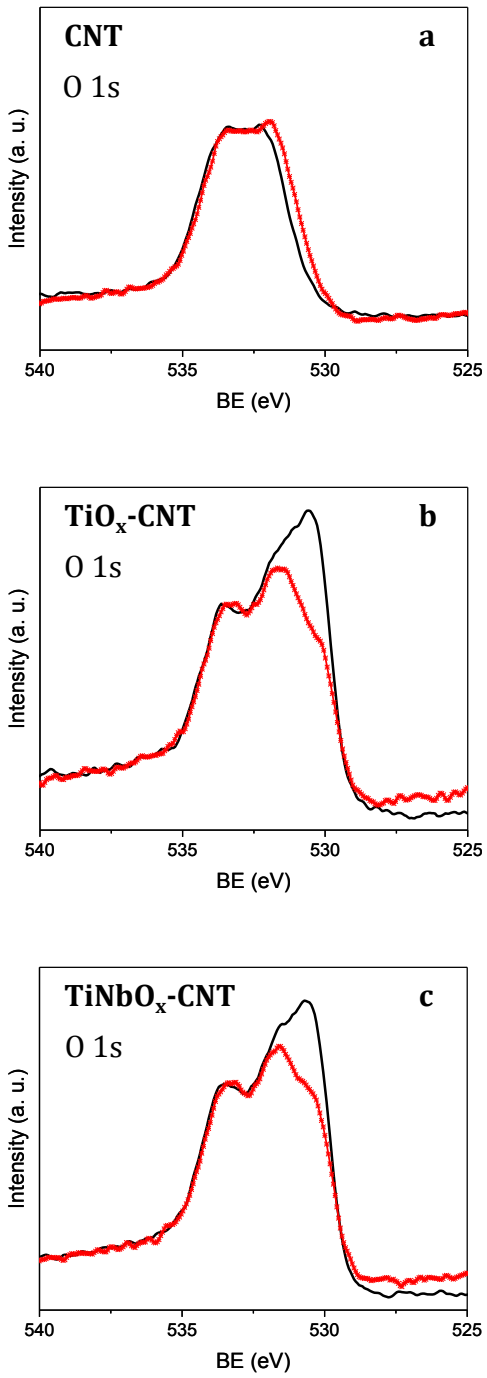

Figure 6.6 XPS of O 1s in (**a**) CNT, (**b**) TiO_x-CNT, and (**c**) $TiNbO_x$-CNT supports before (——) and after (—∗—) Pt

The Pt 4f peak from XPS also tells us important information about the properties of the electrocatalyst. Several XPS studies of Pt on titania catalysts prepared in a similar fashion to this paper that were also corrected to C 1s found BE values reduced by some extent when 4f plots were compared to a control where this was credited to the strong metal-support interaction [137, 294, 327-329]. In this study, titania electrocatalysts also revealed reductive shifts for Pt doublets when referenced to the C 1s peak. However, due to charging within varying functionalization of carbon surfaces and increased interfacial contact of Pt with metal oxides in composites, the 4f spectra were re-plotted with reference to valence band edges aligned at 0 eV and shown in Figure 6.7. In this comparison, a positive shift > 0.1 eV in BE was measured for Pt-$TiNbO_x$-CNT from the Pt-CNT control. Shallow Nb^{4+} donors in $TiNbO_x$ pin the Fermi level of the metal oxide from its valence band edge, allowing some nonbonding electrons to more easily enter the metal. These effects can be attributed to the formation of a Schottky junction which results from alignment of energy levels and the differing work functions in metal-metal oxide composites. Deeper defect states from Ti^{3+} are known to reside closer to the middle of the titania gap, producing a more mild Fermi level shift in Pt at the TiO_x-CNT junction. Several other strong-metal support electrocatalysts with similar composition also saw positive or only minor shift in BE when contrasted by this method to a Pt control [135, 232, 330]. In the anode, it seems a small shift in the Pt electron energy level probably does not significantly change CO adsorption properties. Advantages for CO tolerance may extend to the nature of its interface with support materials.

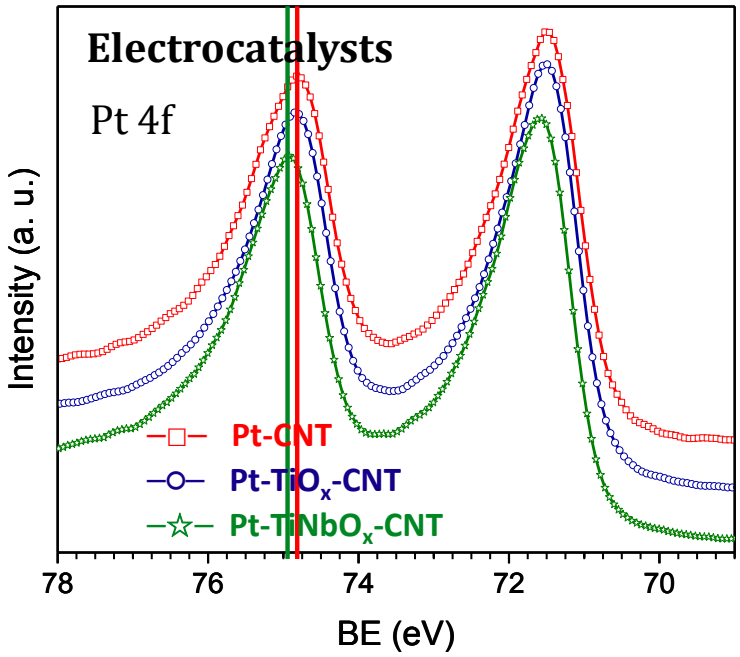

Figure 6.7 XPS spectra of Pt 4f peaks for all electrocatalysts

A sequence of TEM images show increasing magnification of a Pt-TiNbO$_x$-CNT electrocatalyst. Pt nanoparticles (dark) are supported on Nb doped titania and CNT presented in

Figure 6.8. The TEM images were zoomed in to a region where some catalysts are nicely distributed on the composite support, but others are not. The mean of Pt particles was confirmed under 5 nm from particle counting statistics. In comparison, Pt-CNT electrocatalysts demonstrated worse agglomeration of Pt and more irregular distribution of attachment. Evidence of the titania phases is not readily apparent in composites, another indication of their small size and more disordered nature. A high resolution TEM study found the metal oxide in hybrid support design with a disordered structure around Pt interfaces provided improvement to activity in methanol oxidation and CO tolerance

[327]. Other reduced metal oxides like ceria supported Pt electrocatalysts also found amorphous arrangements of defected oxide around catalyst interfaces with the best oxidation reactivity due to formation of reduced ceria cations [264, 331]. One recent report on doped titania supports proclaimed the origin of their ORR enhancement was derived from the resultant strain found in the Pt lattice [328]. However, several other examples of amorphous niobia in supports for Pt electrocatalysts found high activity and stability in both electrodes [139, 140, 332-335]. It seems that the low degree of crystallinity for metal oxides in this work and that found by many others would also suggest that the oxide effect extends beyond the Pt metal lattice by altering charge transfer reactions in the support.

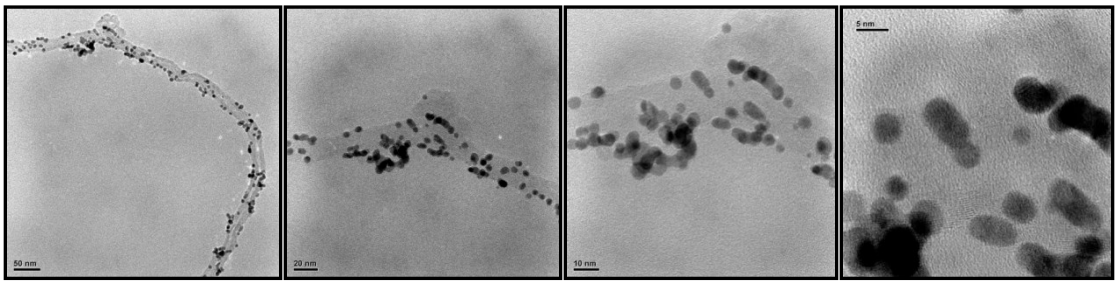

Figure 6.8 High resolution TEM at increasing magnification of Pt-$TiNbO_x$-CNT

STEM (upper left) coupled with energy dispersive X-ray (EDX) spectroscopy (in color) reveal presence of all the metals and their corresponding distributions in Figure 6.9. Metal oxides are evident in composite supports and it seems that the dopants were will mixed into the titania matrix. All of the supporting images consistently show that the Pt nanoparticles have a tendency to deposit on or near the metal oxide phase in the composite support, providing further evidence that noble metals are anchored by strong interfacial junctions [131, 336, 337]. Compositions of the metal oxide were more apparent

when coupled with EDX analysis than found with the high resolution TEM images alone. Niobium content was measured in this sample and several other images at concentrations ≥ 10% dopant fraction in titania. Additionally, in all samples the total atomic fraction of transition elements (Ti and Nb) was less than half the Pt atomic content. It is expected that these proportions could have been optimized for further improvements in electrochemical performance.

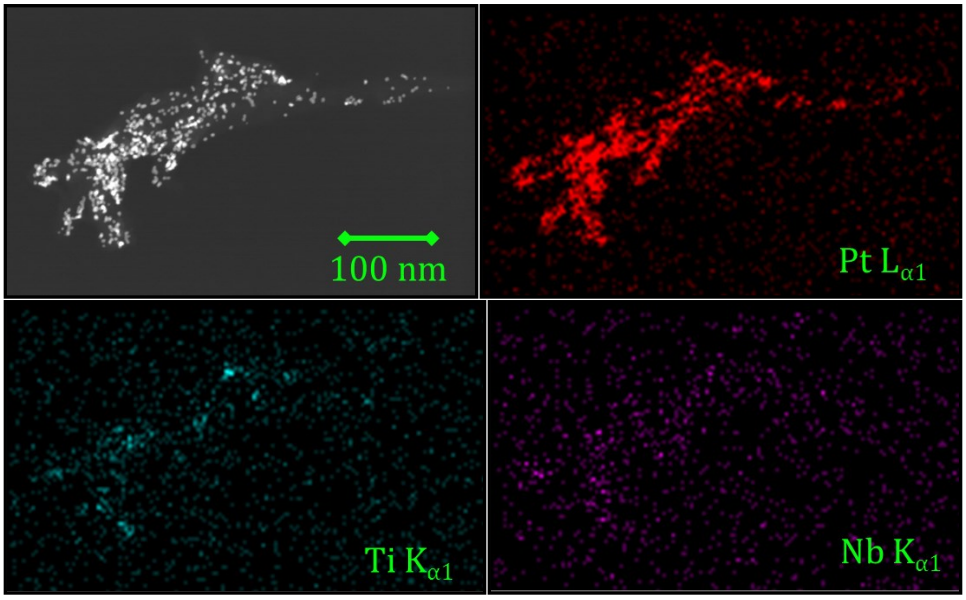

Figure 6.9 STEM/EDX of Pt-$TiNbO_x$-CNT

6.4.3. Electrochemical characterization of working electrodes

Initial electrochemical tests indicated that cell electrocatalyst area was evolving from the effects of potential cycling applied for CO stripping cycles. To stabilize electrodes and make consistent measurements, they were subjected to a series of 500 potential cycles up to 1.2 Volts before further tolerance testing. This process accelerated cell aging to break-in catalysts. After cycling, all three electrocatalysts demonstrated stable electrochemical performance. The CVs before and after the procedure are

compared in Figure 6.10. A clear trend in the order of active area preserved from this test shows Pt-$TiNbO_x$-CNT had the best stability after break-in cycling was completed to simulate stressors during aging. One Pt-$TiNbO_x$-CNT MEA were tested in an actual high pressure hydrogen pump under realistic cycling conditions through collaboration with Sustainable Innovations, LLC and presented in Appendix F. A more aggressive potential cycling was completed in a preliminary study which measured carbon corrosion resistance by monitoring CO_2 evolution from the electrodes that also followed same order of stability and is plotted in Appendix G. This would suggest the carbon corrosion of the support is closely tied to the preservation of active catalyst area. The hydrogen underpotential deposition (UPD) area from the reversible reaction before and after cell break-in are shown in Table 1; UPD features were integrated after subtracting double-layer capacitance to determine the total active electrocatalyst surfaces based on the area specific conversion of 210 $\mu C/cm^2$ [338, 339]. Notably, Pt-$TiNbO_x$-CNT had the widest double-layer of all three electrodes. Much better catalyst utilization from ultrasonic processing has been measured for commercial catalysts by this automated deposition procedure that provides for uniform, thin, and reproducible electrodes [239]. Based on areas remaining after break-in, stoichiometric flow rates and current densities were kept proportional to active Pt surfaces for comparison purposes.

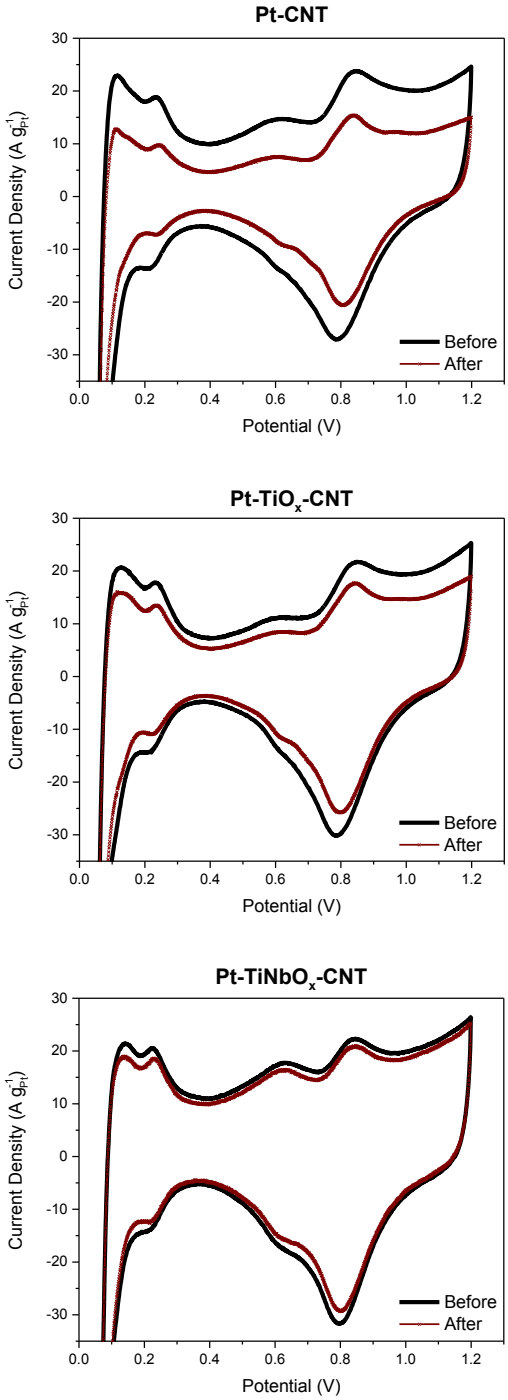

Figure 6.10 Cyclic voltammetry shown before and after break-in

Table 6.1 Summary of electrocatalyst utilization before and after break-in cycling

Pt Features	Pt-CNT	Pt-TiO_x-CNT	Pt-$TiNbO_x$-CNT
Utiliz. Before	18.5 $m^2 g^{-1}_{Pt}$	21.2 $m^2 g^{-1}_{Pt}$	15.3 $m^2 g^{-1}_{Pt}$
Utiliz. After	11.2 $m^2 g^{-1}_{Pt}$	16.9 $m^2 g^{-1}_{Pt}$	13.6 $m^2 g^{-1}_{Pt}$
Remaining	60.7 %	80.0 %	88.6 %

CO stripping peaks in Figure 6.11 were collected after extended exposure to the CO contaminated fuel. Peak maxima from anodic strips were measured at 591, 607, and 616 mV corresponding to the order of activation for the Pt-$TiNbO_x$-CNT, Pt-CNT, and Pt-TiO_x-CNT electrocatalysts, respectively. Interestingly, the CO tolerance and stripping behavior of Pt-CNT improved from the initial condition; specifically, the order of activity for the CNT only support surpassed that of the TiO_x composite [35, 320]. Although even higher temperatures would have improved tolerance, increasing to 75 °C offered satisfactory activity to make appropriate comparisons. Cell temperature can have impact on all the reactions, including corrosion. Faster degradation and loss of active Pt surfaces on CNT can lead to formation of carboxyl and hydroxyl groups in support corrosion which may also assist their tolerance [35, 320]. Furthermore, size effects and faceting of Pt can improve specific activity in oxidation reactions and could have become a factor [233, 322, 340-342]. Irrespectively, the order of catalyst size, utilization, and/or stability did not directly correlate with CO tolerance found in this study, suggesting support specific effects.

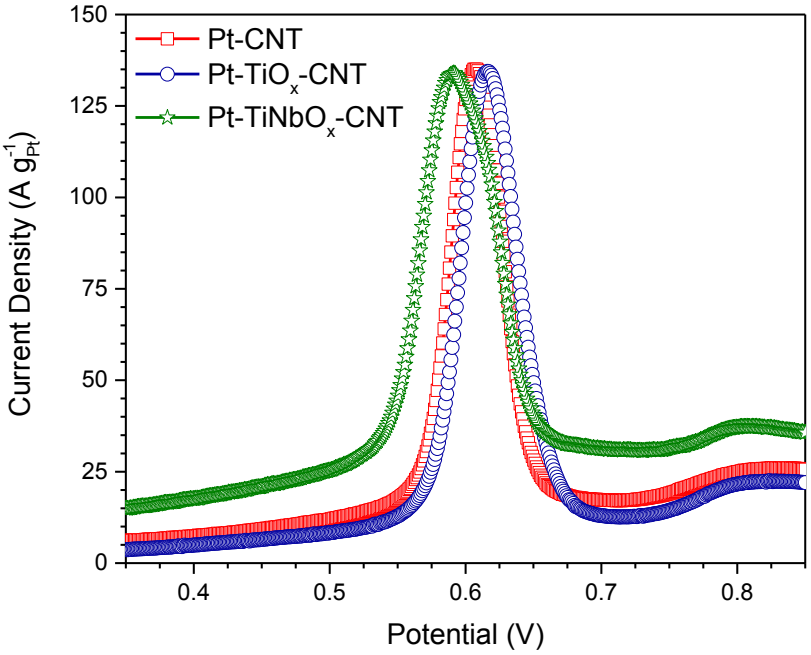

Figure 6.11 CO stripping behavior of electrocatalysts

At galvanostatic conditions, the potential can be measured over time (chronopotentiometry) while subject to a stoichiometric flow of contaminated H_2. This hydrogen pump mode is one of the best ways to test for CO tolerance of electrodes because the dynamic in working electrodes from increases in overpotential are easily observed and attributed to catalyst behavior. In clean H_2, the cells had identical polarization behavior in the pump. When CO is present, potential climbs gradually before a sharp transition is observed in each data series shown in Figure 6.12. After the transition, the cell potential plateaus as more stable performance is approached. At higher currents, the cell potential can undergo an oscillating behavior after the transition. In the Pt-CNT electrode for example, potential oscillations started during application of 100 A m^{-2}_{Pt} after about 1250 seconds. Oscillating behaviors were observed in all

electrodes although they did not begin in Pt-$TiNbO_x$-CNT until supplying higher current densities (> 100 mA/cm^2_{Pt}) and are marked in Figure 6.12 by transparent plots to prevent overlapping data sets. When the catalyst overpotential climbs above the CO oxidation peak, adsorbed CO on the catalyst surface will be oxidized, resulting in a rapid reduction of cell overpotential. However, unreacted CO diffusing into the electrode will re-adsorb onto active surfaces, leading to another rise in overpotential and then the cycle repeats as seen in magnified inset of Pt-TiO_x-CNT at 50 A m^{-2}_{Pt} current density. Similar oscillating phenomena are familiar to other types of heterogeneous catalysis and have also been reported in electrocatalysis [[343]]. Performance data recorded after the transitions when CO has covered active surfaces is most telling of electrocatalyst overpotential at semi-steady state.

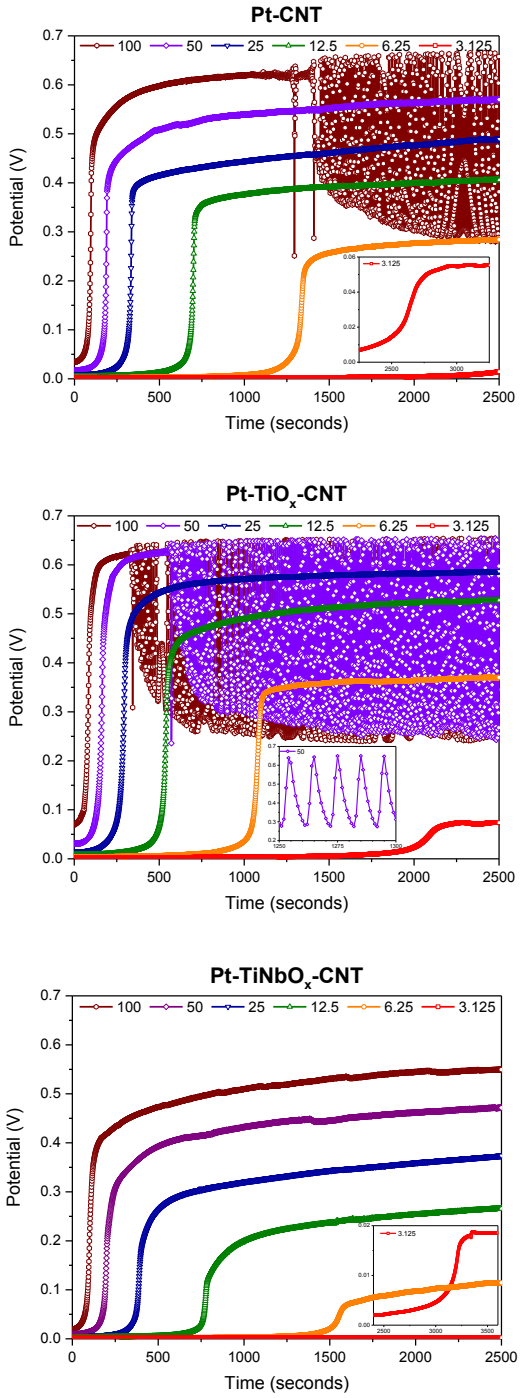

Figure 6.12 Galvanostatic responses to H_2 with CO (chronopotentiometry)

After surpassing the transition step, final values were recorded at each current density applied. Those points are plotted on a curve in Figure 6.13 for comparison

purposes and can correlate to differences in catalyst overpotential when CO is present at this fixed concentration with 10x stoichiometric flow of H_2. For galvanostatic current of 6.25 A m^{-2}_{Pt}, a reduction of 170 mV compared to Pt-CNT and 256 mV in case of Pt-TiO_x-CNT for Nb doped titania support. At 25 A m^{-2}_{Pt}, a savings of 117 mV was measured for Pt-$TiNbO_x$-CNT electrode from Pt-CNT electrode. Essentially, electrocatalysts made from Nb doped titania showed the best CO tolerance by large margins which narrowed at higher current density as cell potentials converged towards the CO stripping peak maxima.

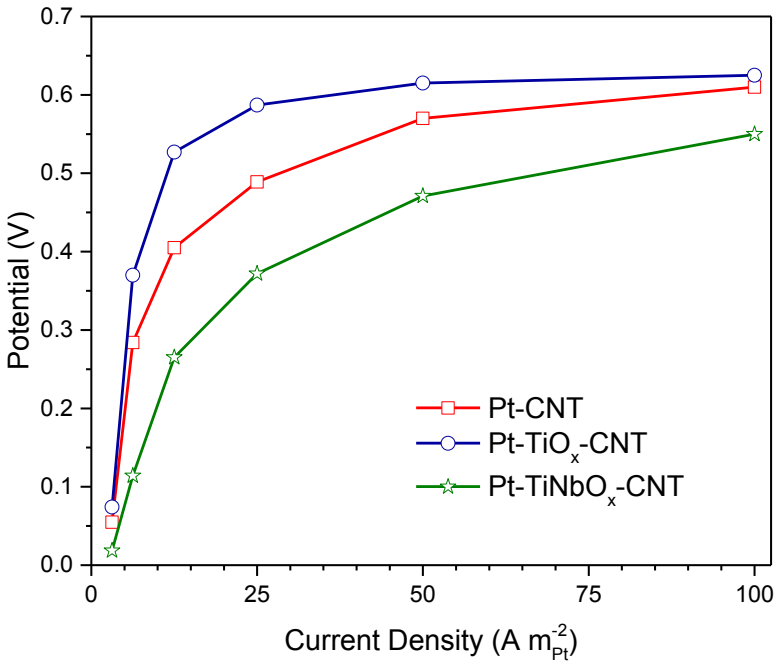

Figure 6.13 Cell potential due to activation overvoltage as function of current density

Several interesting trends were observed in the timing of transitional behavior encountered during chronopotentiometry experiments. The time of transitions was

compared by plotting the inflection point in curves Figure 6.14 (**a**) at each fixed current density. Inflections followed nearly perfect hyperbolic relationships. The inset in (**a**) shows the same relationship, but with the reciprocal of time coordinated to the X-axis. Interestingly, the order of the transition times also followed that of activity with an increasing delay in deactivation for Pt-$TiNbO_x$-CNT. Although electrodes can have variations in transport properties, it seems more than coincidental that this also followed the general trend of tolerance. In Figure 6.14 (**b**), the rate of the transition step is estimated by the slope (dE/dt) at the inflection. The rate is slower at lower current density for all electrodes. However, there are also variations in rates between different electrocatalysts where transitions grow fastest in Pt-CNT electrodes at higher current supply. An alteration of specific adsorption properties could affect the time it takes for CO to deactivate all catalyst sites, but it is expected that interfaces with the support play a role in charge transfer reactions that may increase active site availability due to hydroxyl formation in oxides in a mechanism that will be developed in further detail at the end of this discussion.

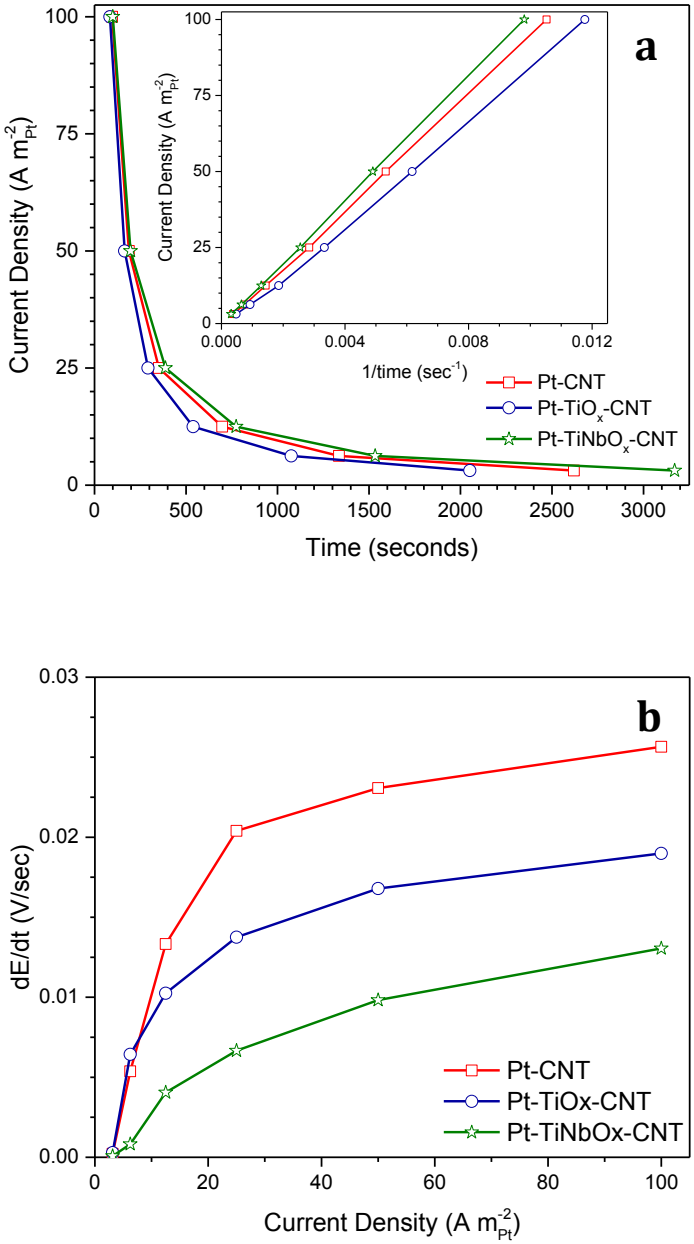

Figure 6.14 Transition behavior in chronopotentiometry
(**a**) inflection point in curve and (**b**) rate of transition vs. current density

During application of 25 mV constant potential, current responses were recorded over time (chronoamperometry). Currents were supplied from charged species generated in the anode while CO gradually diffused to catalyst surfaces. Flow rates were also

normal to UPD area and sufficient to provide limiting current at this low potential where adsorption is not significantly affected. During the initial decay of current density, it is perhaps not fair to compare performance due to different stoichiometric reaction values that cannot be controlled unless flow rates are continuously variable. However, after cell currents flatten out to semi-steady state, the response is more fairly compared in a direct relationship shown as the inset in top right of Figure 6.15. For 100 ppm CO in H_2, the cell with Nb doped titania support yields a current density about 3.5 versus 2.25 A m^{-2}_{Pt} for Pt-CNT, representing a 155% improvement. The same order of tolerance found in chronopotentiometry was also observed during this test.

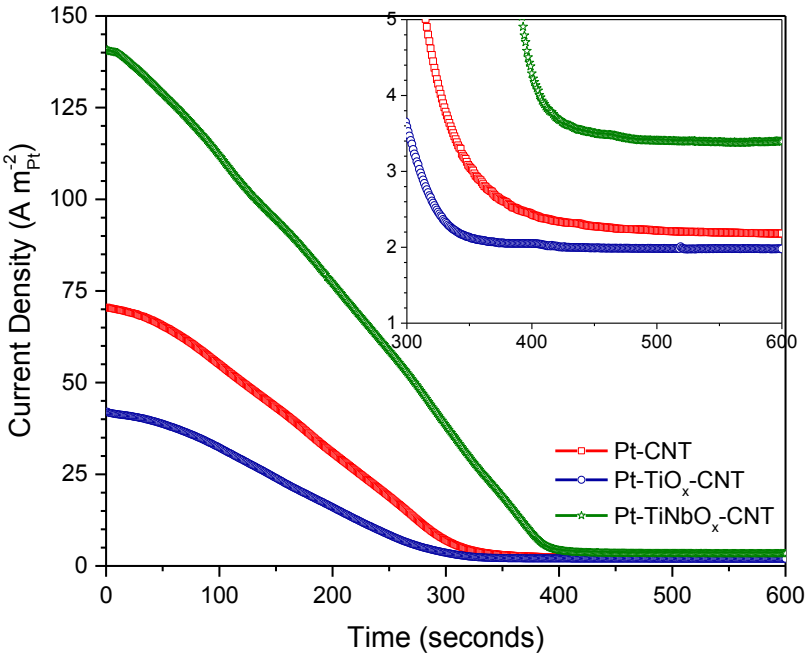

Figure 6.15 Potentiostatic condition at 25 mV reveals chronoamperometric response

To compare the time delayed poisoning response of electrodes during potentiostatic condition, an EIS technique was used to observe the loss in activity

dominated by charge transfer resistance that results in the growth of impedance arcs during poisoning [344]. With otherwise same test conditions described in chronoamperometry at 25 mV, EIS scans were collected at 1 minute intervals to show evolution of arcs in Nyquist plots during the cell deactivation by CO in Figure 6.16. Impedance plots are zoomed in to focus on earliest stages of development during first 5 minutes of operation with a high to low scan taken during each minute of this test. At 4 minutes, the impedance data is noted at the apex and reported as [ω (Hz), Z_{real} (mΩ)]. The highest impedance values were recorded from Pt-TiO_x-CNT [19.86, 7.62], [31.67, 5.94], to [49.87, 4.83] the lowest in Pt-$TiNbO_x$-CNT which was also recorded at the highest frequency. The doped composite support electrocatalyst exhibited the most prolonged rise in charge transfer resistance from the CO contamination effects at this condition.

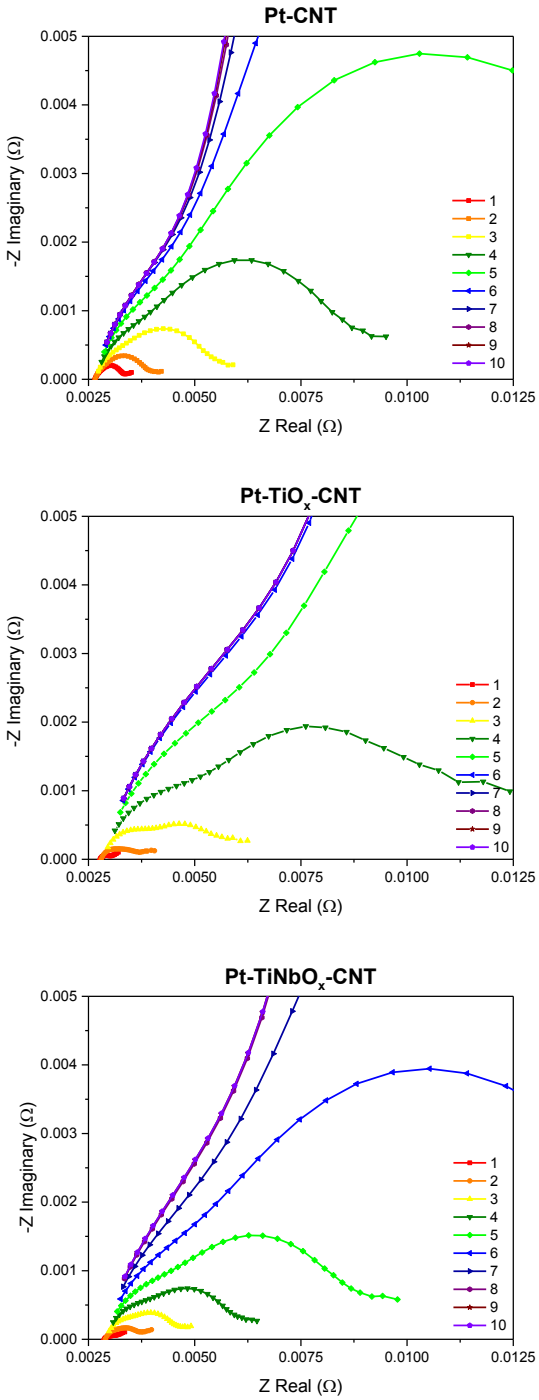

Figure 6.16 Evolution of EIS during CO exposure at 25 mV (1−10 minutes)

Very small addition of metal oxides to the catalyst support made for a marked contrast in electrode performance, warranting more detailed investigations. A probable

explanation for resulting reactivity differences may simply be attributed to interfaces with the active catalyst for the improvement in tolerance to CO provided by its design. Although there was not a direct measurement of interfacial areas with metal oxide phases, several characterizations could indicate this. Lower catalyst utilization measured from UPD in doped titania could in fact represent interfaces where bifunctional reactions are enhanced, but hydrogen redox gets limited by the metal oxide coverage. Oxygen vacancies formed in close contact to catalysts supply hydroxyl intermediates that maintain oxidation reactions and can extend active surfaces for CO oxidation. Strong chemical interactions between the metal and metal oxides result in changes of defect formation energy that can be galvanized by potential. Transition metals at the interface get reduced, and this may be more favorable for niobia according to the Gibbs free energy of reaction found in Ellingham diagrams. At higher concentrations, Nb is known to segregate to surfaces of titania during oxidative processes and possibly enrich defects there [[114, 324, 345]]. Niobia prefers a higher surface coordination with oxygen than titania cations as well. Nb substitution has also been reported to suppress encapsulation of Pt by Ti suboxides in addition to a having higher oxygen vacancy diffusion resulting from strong metal-support interactions [[153]]. These metal oxides may partially encapsulate catalysts when donating charge during the application of potential, which could also help to protect it from more severe oxidative corrosion. Nb_2O_5 is also known to have a wider band gap than TiO_2, though quantum size effects and interfaces with metals are known to change gap energies.

It is not exactly clear what lead to all the trends seen in tolerance, although it may be due in part to the semiconductor like properties of the support. The presence of metal

and semiconductor interfaces (i.e. metal oxide or CNT) result in sharp band bending and Schottky junctions or more ohmic like contacts. Heterojunctions found between phases of the electrocatalyst align Fermi levels and potentially shift their energy bands. Point defects from the reduction of titania contribute delocalized electrons and holes. Reduced Ti cations in substitutional or interstitial sites of titania induce deeper mobility states closer to middle of gap that cause it to act more like an ohmic contact when Pt is added [152, 153, 221, 303]. In the case of the Nb doped titania however, the Fermi level of the oxide at equilibrium should be pinned closer to the conduction band of this n-type conductor due to addition of shallow Nb^{4+} donor states that can create a useful Schottky barrier. When electrons are forced away and the work function of the metal is increased, more holes are left in the depletion region of the oxide forming a wider space charge layer (i.e. internal field). During forward bias, a lower activation for excited electrons in the conduction band of the oxide will allow them to cross the barrier into the metal, preventing recombination with a hole. Separated charges are more probable to participate in reactions like the formation of hydroxyls at holes or vacancy sites near the surface. Formation of Schottky junctions have elsewhere been reported for these metals and in our case, reduced transition metal states seen by XPS suggest they exist here as well. Evidence of band bending and Fermi level pinning can also be inferred from 4f spectra of Pt supported on $TiNbO_x$-CNT which falls further from the valence band edge due to greater accumulation of electrons at its interface with the oxide. For these reasons, strong metal-support interactions seen in electrocatalysts can also be treated from the perspective of semiconductor principles. Defects formed by Schottky type junctions can involve them in electrochemical reactions. However, it can become difficult to discuss

point defects and semiconductor behavior from nanostructured and amorphous oxides. Regardless, the role of charge carriers at junctions can be related to the separation of charge and could be imagined like the pictorial presented in Figure 6.17. A better comprehension of catalyst-support interplay and underlying electronic structure effects will be expected to help bridge energy barriers and tune gaps between phases that lead to further advances in electrochemistry.

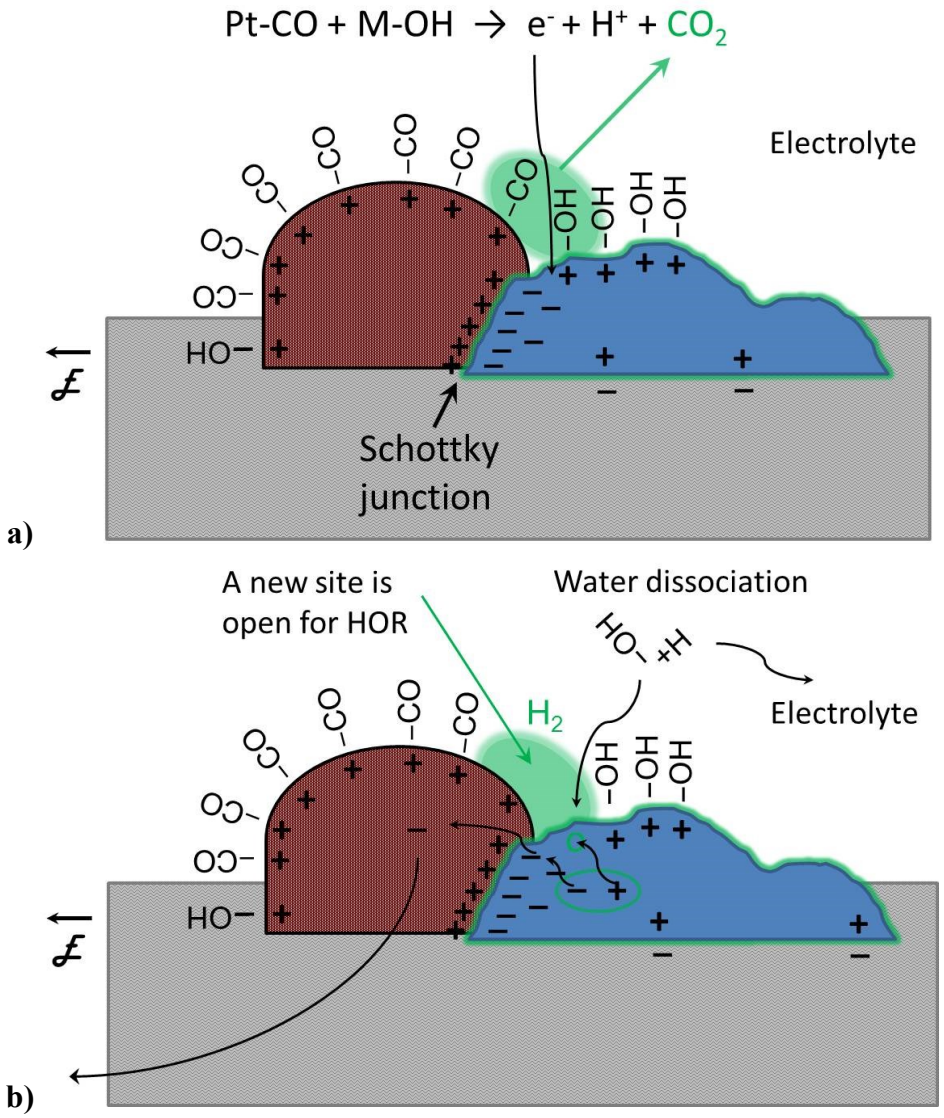

Figure 6.17 Schematic of (**a**) bifunctional mechanism for CO tolerance and (**b**) the creation of an electron-hole pair can separate an electron across Schottky barrier

There may also be several reasons why the composite supports with titania were more stable than the CNT counterparts. In general, the presence of catalysts on support chemistry and its effect on stabilizing defects is seemingly important. In widespread reports on electrocatalysts, strong interactions from catalysts on stable supports like titania have boosted their corrosion resistance. The immunity to break-in and operational conditioning from composite titania supports in these results may also be due to its Schottky junction. Excited electrons tunneling into the electrocatalyst from the oxide would protect electrocatalysts as the metal oxide passivates. In this case, titania could be acting like a gated interface to limit its corrosion once electron access gets cut off. Water dissociation on titania can also promote hydroxyl formation and facilitate oxygen coverage on catalysts during passivation. A wider space charge layer from the doped oxide is also proposed to have better buffering capacity. Titania bonds strongly to the catalyst through these interfaces, preventing its diffusion and detachment from the support while also limiting carbon corrosion in those regions. More systematic and exhaustive accelerated degradations tests would help elucidate specific advantages from metal oxides used in related electrocatalysts. There have been reports of non-Pt electrocatalysts such as those from heavily reduced Group IV-VI transition metal oxides (including titania) that provide high electrocatalytic reactivity, but their active sites are much further from equilibrium and subject to irreversible oxidation. Simply from the consideration of metal oxide defect equilibrium, acceptors are preferred at higher oxygen pressure while hydrogen and reducing gases used in the anode favor donor formation. Similar to tolerance though, there are many factors to consider in stability. Integrating

metal oxides into the support has a synergistic effect on electrocatalyst performance and durability, but further developments are needed in this area to derive the best arrangements and compositions.

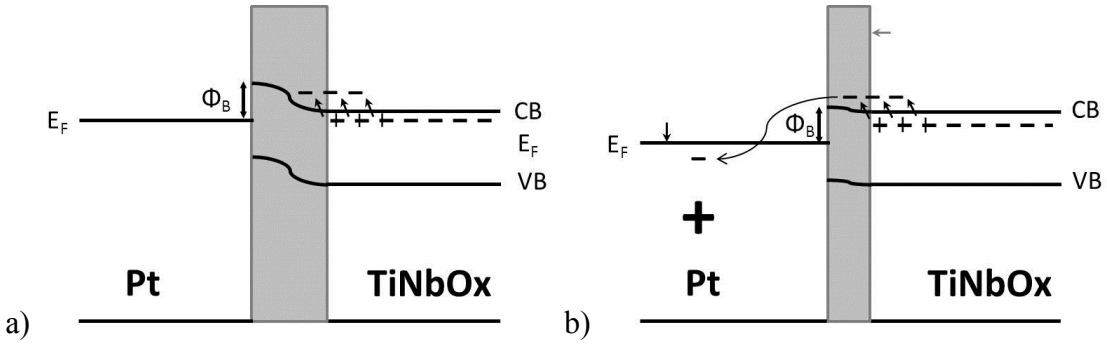

Figure 6.18 a) Schottky junction formed at Pt-$TiNbO_x$ and b) under forward bias

Relationships described in this set of materials result from their collective and varied properties. The complexity expected for composites is depicted in Figure 6.19 to help to visualize some of their interactions. The phases of titania are formed at defects on the surface of oxidized CNT supports to synthesize composites in the first step of the sequence. Blue patches represent fine anatase crystals and other disordered oxide arrangements with a higher concentration of defects near their (glowing) boundary. Although Pt catalysts can bond directly through defects in CNT, a stronger interaction with the metal oxide provides a favorable attachment point to form a secure bridge with the support. Triple junctions arise between the metal, oxide, and CNT framework. Titania composites grow smaller Pt crystals with a better distribution. Some of the Pt may become partially covered by the oxide in synthesis and also during operation, but this can have advantages including the extension of active bifunctional surfaces. The

coverage of Pt by the metal oxide and nature of their interfaces affect the oxide properties. In the case of doped titania, green borders represent surfaces where a greater concentration of donor species are expected from enrichment by Nb defects. It should be noted that the dimensions are not drawn to scale. Advantages from interfacial junctions can offer improved electrocatalysts, specifically in anode operations with CO present.

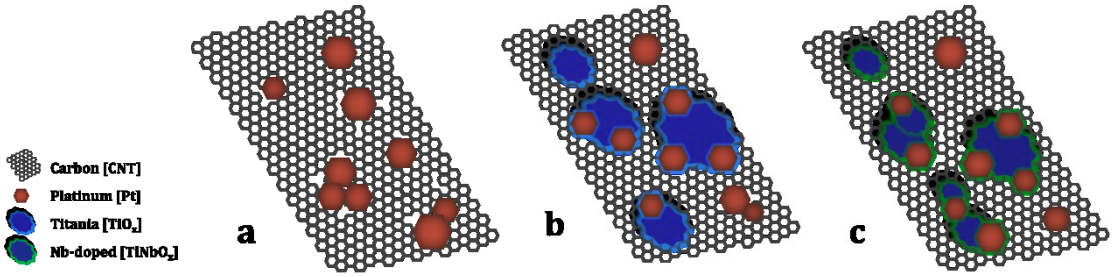

Figure 6.19 Representations of (a) Pt-CNT, (b) Pt-TiO_x-CNT, (c) Pt-$TiNbO_x$-CNT

Eventually, all active surfaces of the catalyst will get inundated by CO contamination at low temperatures. By selecting an optimum set of conditions to exercise greater productivity over longer intervals between periodic cleansing of electrodes at lower stripping potentials, a more resilient anode can be designed. Defect engineering and the interaction between material phases can improve activity and stability in its environment. In all cases, it is important to study catalysts in conditions similar to those found in real scenarios. The hydrogen pump serves as an excellent example for CO tolerance in the anode. Truly, a better set of controls is needed for deeper understanding on the influence of electrochemical potential in metal oxide defects used to form reactive electron-hole pairs. Additional materials characterization of electronic states, especially among metal oxide supports during operation and post-mortem would have been useful in developing this discussion further. Future study could

focus on other support compositions with respect to their acceptor and donor relationships. Some properties can be refined beyond geometry, crystal epitaxy, and strictly metallic considerations by starting with support interactions. These fundamental principles can be used to build electrocatalysts from the bottom up. It was not specifically the goal of this research to establish electronic interactions of electrocatalysts; rather, an example of a composite metal oxide supported catalyst is integrated into working electrodes to confirm and unify work completed by many others while also contributing insight to principles guiding the design of electrocatalysts for related applications.

6.5. Conclusions

The design of supports in the electrocatalyst is very important to their performance and durability in the electrode. In the anode of polymer electrolyte cells, there is a concern from the contamination of hydrogen fuel by carbon monoxide (CO). Bifunctional reactivity of platinum was improved by addition of select transition metal oxides (< 5% by mass) to the surfaces of multi-wall carbon nanotubes. Specifically, titania was donor doped with niobium to prepare stable electrocatalysts used in anodes with best tolerance to 100 ppm CO during hydrogen oxidation when compared to a set of controls with and without titania. The anodes were tested in electrochemical hydrogen pumps to characterize their performance and prove a synergistic relationship. Resilient behavior in working electrodes used for related applications can be recognized by

forming catalyst junctions with select metal oxide phases added to carbon composite supports.

6.6. Acknowledgements

This work was completed by the authors at the University of South Carolina in the Horizon I facility. It was supported by the USC – City of Columbia Fuel Cell Collaborative. Dr. Scott Greenway provided critical review and enabled our interactions with Sustainable Innovations, LLC. Special thanks to Diana Larrabee, undergraduate Magellan Scholar, for her assistance with experiments. TEM and STEM/EDX images were collected by Dr. Haijun Qian at the Clemson University Electron Microscopy Facility. Last but not least, XPS surveys were performed by Dr. Shuguo Ma in our College of Engineering and Computing. Thanks are also given to all the others who could not be referenced, but held important influence during the time of patient development for this research.

Chapter 7. Summary & Conclusions

The development of stable platinum electrocatalysts for durable electrode performance has been a goal of this research. Cost of these materials is a major barrier to commercialization of technology such as polymer electrolyte fuel cells. Catalysts need to be supported on inexpensive materials that use a minimal amount of platinum while maintaining a high activity over the life of the device. Carbon support corrosion is the origin of many problems plaguing electrocatalyst longevity. Instead of replacing carbon with a ceramic or another single phase material, this dissertation has explored a composite consisting of both carbon nanotubes and titania to support platinum catalysts. Graphitized carbons and stable metal oxides have become a popular material selection for catalyst supports in many recent publications, but their design lacks a fundamental understanding. High performance and durability have been reported, although successful application in working electrodes is necessary to validate these advantages. Titania-CNT supports for Pt were able to better preserve catalyst performance than a control without titania in the cathode. Choice of a niobium donor dopant in titania was used in an approach to modify the structure and electronic properties of the metal oxide phase when integrated into the anode. When included into electrocatalysts, semiconductor oxides

promote bifunctional mechanisms through junctions formed with the catalyst. Strong metal-support interactions enhanced catalyst bonding characteristics extended from the support. An ultrasonic spray deposition process was used to prepare membrane electrode assemblies from the synthesized electrocatalysts. A synergy between both performance and durability of electrodes can be realized by design of better composite supports used in fuel cells and potentially other related electrochemical devices.

Chapter 8. Future Considerations

In the future, we will need to investigate the mechanisms by which composite catalyst supports specifically benefit catalyst performance and durability. This will provide further insight into ideal electrocatalyst construction. The findings presented have already given many clues into a plan for implementing better control over material designs. Improvements in the corrosion resistance of nanostructured electrocatalysts can predict cost savings for long term operation. A composite support approach using metal oxides can explore a wider selection of materials and structures to maximize desirable properties. Better choice of controls and variables including defect concentrations, dopant type, and interfacial arrangements with catalyst are suggested, for example. Measuring the changes in electrocatalysts from before, during, and after accelerated testing will help to explain the science behind degradation mechanisms and quantify its impact on catalyst activity and stability.

The structure/property relationship is an essential aspect of materials science and engineering applied to maximize device performance. Preparing the ideal composite electrocatalyst requires engineering of most fundamental parameters that start on very small scales. Electronic interactions of electrocatalysts are essential to its design.

Ensuring the preferred phase and location of bonding between the phases is an important aspect of the concept for the composite. Arranging the material domains over these length scales rely on controlled synthesis and sequence in processing. Accurate control over material design provides for more uniform and desirable qualities. Nanostructured materials can take advantage of improvements in the distribution of phases in the heterogeneous electrode that serves a multitude of roles.

Improving the bonds between the selected materials can strengthen their interactions. Attachment of titania on CNT supports is enhanced through the chemical functionalization of carbon surfaces, for example. Titanium oxide additions were kept to a minimum and were often non-crystalline and discontinuous on carbon surfaces. There remains some uncertainty in the importance of titania content and crystallinity in the role of performance and durability. The band gap and defect states can alter electronic properties by these subtle variations. Every variation in the lattice requires balancing of charge to accommodate potential differences. If these energy states can be organized into domains that are linked by common wave functions then a charge transfer path can exist for carriers to become polarized. These charges can react or separate across barriers, allowing them to participate in the electrochemistry. Varying the nature of defects in titania has a very significant effect and defects can be created by the presence of catalyst at its interface. The interfacial bonds between Pt-Titania-CNT can be arranged to form ideal triple junctions that rely critically on each phase. Accurately predicting the trade-off in surface area and stability will suggest an optimal value for the metal oxide to catalyst proportion. Enhancing support interfaces in the composite can provide a valuable way to enhance stability. High temperature and potential can cause corrosion,

but this degradation can be mitigated. If we can understand how to design this contribution from the oxide dielectric behavior, better electrocatalysts can be realized in electrodes of low temperature electrochemical cells.

The properties of metal oxides processed under different conditions should be carefully characterized because even small variations in composition can result in a wide range of properties. This will provide a processing map for development of desirable traits that translate into performance. Some of the similar diagnostics which were previously applied would also be valuable to evaluate future progress in support design and with greater competence in the examination, more attention to detail at electronic level. Additional characterization techniques from after testing can give us a better idea of the dynamic between the catalyst and support. Advantages of strong metal-support interactions may generally be related to other metal-metal oxide heterogeneous catalyst systems if evaluated from perspective of defect engineering, semiconductor principles, and the relationship to junctions formed at their interfaces. Schottky junctions can be formed when platinum metals are chemically combined with semiconductor metal oxides, like titania. A more fundamental understanding from this perspective could lend to more accurate control over engineering this interface. The optimized junction arrangement would be ideal for creating the best electrocatalysts. Organization of energy levels in the composite can bridge electronic gaps which exist between different phases. Fermi levels align between the materials bonded in the composite and the electronic structures get shifted from their equilibrium to balance differences in charge. Knowledge of electronic structures is especially important in design when using semiconductors for low temperature electrocatalysts. Defect relationships and band diagrams can be used to

understand how they are involved in the separation of charges that can be useful for reactions. When surfaces get polarized, charges tend to migrate to surfaces and interfaces that may contribute through bifunctional mechanisms. A potential is created by relative differences in the speed of at least two complementary reactions in the transfer of energy. Variable density and distribution of charge states is expected at non-uniform fields near interfaces. Comprehension of these mechanisms has made significant contributions to so many important modern technology developments which includes the evolution of circuits in many other modern electronic technologies that depend on these junctions.

The proposed electrocatalyst developments for PEMFC may also be applied to other related applications such as fuel cells operated at higher temperatures, electrolyzers, catalytic converters, and sensors, for example. Solid acid electrolyte cells like polybenzimidazole polymers and others which operate at higher temperatures are more susceptible to carbon corrosion and platinum sintering; they are in even greater need of more stable catalysts and electrodes. Alkaline electrolyte cells should also be able to profit from an understanding of support and catalyst junctions that promote activity and stability. Electrocatalysts can be applied to electrochemical sensors for alcohol and CO that rely on low temperature oxidation of organics in the atmosphere. Catalytic converters and glucose sensors are a few other examples of catalysts that could be improved by resisting deactivation. A regenerative electrocatalyst can also be used in reversible cells that can synthesize chemicals when necessary. Hydrogen pumps are on cusp of commercialization for large scale gas purification that can deliver pressurized clean gas to the fuel cell. They can also be used for separation of diluted hydrogen from waste streams with inert purge gas, petroleum reformers, and metals refining, for

example. Providing reliable performance is critical to most applications that depend on related electrochemical cell technology.

More practically, questions still exist about the best way to harness energy available in our environment. Fundamentally, the storage of energy is the most challenging problem. Part of the answer to the energy storage problem is being able to efficiently convert it into useful forms and have it available when and where we need it. Being efficient also means minimizing waste whether it is directly related to the cost or indirectly related to the price our environment pays. Our future will be impacted by the choices we make with regard to these considerations of utilizing energy responsibly. Decisions on the best approaches for energy storage and conversion are important choices we have to make in order to sustain our harmonious existence with Earth.

References

1. M. Pourbaix: Atlas of Electrochemical Equilibria in Aqueous Solutions, 1974.

2. R. Borup and e. al.: Scientific Aspects of Polymer Electrolyte Fuel Cell Durability and Degradation, *ChemInform*, 2007, **38**(50), 1-48.

3. E. Antolini: Review: Formation, microstructural characteristics and stability of carbon supported platinum catalysts for low temperature fuel cells, *J. Mater. Sci.*, 2003, **38**, 2995-3005.

4. M. S. Wilson, F. H. Garzon, K. E. Sickafus, and S. Gottesfeld: Surface Area Loss of Supported Platinum in Polymer Electrolyte Fuel Cells, *J. Electrochem. Soc.*, 1993, **140**(10), 2872-2877.

5. M. S. Wilson and S. Gottesfeld: Thin-film catalyst layers for polymer electrolyte fuel cell electrodes, *J. Appl. Elecrtrochem.*, 1992, **22**(1), 1-7.

6. P. J. Ferreira, G. J. la O', Y. Shao-Horn, D. Morgan, R. Makharia, S. Kocha, and H. A. Gasteiger: Instability of Pt/C Electrocatalysts in Proton Exchange Membrane Fuel Cells, *J. Electrochem. Soc.*, 2005, **152**(11), A2256.

7. M. F. Mathias, R. Makharia, H. A. Gasteiger, J. J. Conley, T. J. Fuller, C. J. Gittleman, S. S. Kocha, D. P. Miller, C. K. Mittelsteadt, T. Xie, S. G. Yan, and P. T. Yu: Two Fuel Cell Cars In Every Garage?, *Interface*, 2005, **Fall**, 24-35.

8. R. S. Goeke: Model Electrode Structures for Studies of Electrocatalyst Degradation, Dissertation thesis, University of New Mexico, 2010.

9. X. Wang, R. Kumar, and D. J. Myers: Effect of Voltage on Platinum Dissolution, *Electrochem. Solid-State Lett.*, 2006, **9**(5), A225.

10. V. A. T. Dam and F. A. de Bruijn: The Stability of PEMFC Electrodes, *J. Electrochem. Soc.*, 2007, **154**(5), B494.

11. R. M. Darling and J. P. Meyers: Kinetic Model of Platinum Dissolution in PEMFCs, *J. Electrochem. Soc.*, 2003, **150**(11), A1523.

12. T. W. Patterson and R. M. Darling: Damage to the Cathode Catalyst of a PEM Fuel Cell Caused by Localized Fuel Starvation, *Electrochem. Solid-State Lett.*, 2006, **9**(4), A183.

13. R. M. Darling and J. P. Meyers: Mathematical Model of Platinum Movement in PEM Fuel Cells, *J. Electrochem. Soc.*, 2005, **152**(1), A242.

14. W. Gu, P. T. Yu, R. N. Carter, R. Makharia, and H. A. Gasteiger: Modeling of Membrane-Electrode-Assembly Degradation in Proton-Exchange-Membrane Fuel Cells - Local H2 Starvation and Start-Stop Indcued Carbon-Support Corrosion, *Mod. Aspects Electrochem.*, 2010, **Modeling and Diagnostics of Polymer Electrolyte Fuel Cells**(49), 45-87.

15. W. Bi and T. F. Fuller: Modeling of PEM fuel cell Pt/C catalyst degradation, *J. Power Sources*, 2008, **178**(1), 188-196.

16. P. Trogadas and T. F. Fuller: Role of Particle Size Distribution on Pt Stability, *ECS Trans.*, 2010, **33**(1), 115-124.

17. A. A. Franco and M. Gerard: Multiscale Model of Carbon Corrosion in a PEFC: Coupling with Electrocatalysis and Impact on Performance Degradation, *J. Electrochem. Soc.*, 2008, **155**(4), B367.

18. K. Yasuda, A. Taniguchi, T. Akita, T. Ioroi, and Z. Siroma: Platinum dissolution and deposition in the polymer electrolyte membrane of a PEM fuel cell as studied by potential cycling, *Phys. Chem. Chem. Phys.*, 2006, **8**(6), 746.

19. K. Kinoshita, J. T. Lundquist, and P. Stonehart: Potential cycling effects on platinum electrocatalyst surfaces, *J. Electroanal. Chem.*, 1973, **48**(2), 157-166.

20. T. Akita, A. Taniguchi, K. Maekawa, Z. Siroma, K. Tanaka, M. Kohyama, and K. Yasuda: Analytical TEM study of Pt particle deposition in the proton-exchange membrane of membrane-electrode-assembly, *J. Power Sources*, 2006, **159**(1), 461-467.

21. S. Mitsushima, S. Kawahara, K.-i. Ota, and N. Kamiya: Consumption Rate of Pt under Potential Cycling, *J. Electrochem. Soc.*, 2007, **154**(2), B153.

22. W. Bi, G. E. Gray, and T. F. Fuller: PEM Fuel Cell Pt/C Dissolution and Deposition in Nafion Electrolyte, *Electrochem. Solid-State Lett.*, 2007, **10**(5), B101-B104.

23. C. Zhou, M. A. Guerra, Z.-M. Qiu, T. A. Zawodzinski, and D. A. Schiraldi: Chemical Durability Studies of Perfluorinated Sulfonic Acid Polymers and Model Compounds under Mimic Fuel Cell Conditions, *Macromolecules*, 2007, **40**, 8695-8707.

24. K. Teranishi, K. Kawata, S. Tsushima, and S. Hirai: Degradation Mechanism of PEMFC under Open Circuit Operation, *Electrochem. Solid-State Lett.*, 2006, **9**(10), A475.

25. W. Yoon and X. Huang: Study of Polymer Electrolyte Membrane Degradation under OCV Hold Using Bilayer MEAs, *J. Electrochem. Soc.*, 2010, **157**(4), B599.

26. X. Huang and K. L. Reifsnider, eds.: *Durability of PEM Fuel Cell Membranes*, (ed. U. Pasogullari, et al.), Vol. 49, 1-43; 2010.

27. P. T. Yu, W. Gu, J. Zhang, R. Makharia, F. T. Wagner, and H. A. Gasteiger, eds.: *Carbon-Support Requirements for Highly Durable Fuel Cell Operation*, (ed. F. N. Buchi), 1-53; 2009.

28. W. Schmittinger and A. Vahidi: A review of the main parameters influencing long-term performance and durability of PEM fuel cells, *J. Power Sources*, 2008, **180**(1), 1-14.

29. W. Yoon and A. Z. Weber: Modeling Low-Platinum-Loading Effects in Fuel-Cell Catalyst Layers, *J. Electrochem. Soc.*, 2011, **158**(8), B1007-B1018.

30. S. Kreitmeier, A. Wokaun, and F. N. Buchi: Local Catalyst Support Degradation during Polymer Electrolyte Fuel Cell Start-Up and Shutdown, *J. Electrochem. Soc.*, 2012, **159**(11), F787-F793.

31. C. A. Reiser, L. Bregoli, T. W. Patterson, J. S. Yi, J. D. Yang, M. L. Perry, and T. D. Jarvi: A Reverse-Current Decay Mechanism for Fuel Cells, *Electrochem. Solid-State Lett.*, 2005, **8**(6), A273.

32. S. Zhang, X.-Z. Yuan, J. N. C. Hin, H. Wang, K. A. Friedrich, and M. Schulze: A review of platinum-based catalyst layer degradation in proton exchange membrane fuel cells, *J. Power Sources*, 2009, **194**(2), 588-600.

33. J. Wu, X. Z. Yuan, J. J. Martin, H. Wang, J. Zhang, J. Shen, S. Wu, and W. Merida: A review of PEM fuel cell durability: Degradation mechanisms and mitigation strategies, *J. Power Sources*, 2008, **184**(1), 104-119.

34. W. R. Baumgartner, E. Wallnöfer, T. Schaffer, J. O. Besenhard, V. Hacker, V. Peinecke, and P. Prenninger: Electrocatalytic Corrosion of Carbon Support at Fuel Starvation, *ECS Trans.*, 2006, **3**(1), 811-825.

35. S. Maass, F. Finsterwalder, G. Frank, R. Hartmann, and C. Merten: Carbon support oxidation in PEM fuel cell cathodes, *J. Power Sources*, 2008, **176**(2), 444-451.

36. G. Chen, H. Zhang, H. Ma, and H. Zhong: Electrochemical durability of gas diffusion layer under simulated proton exchange membrane fuel cell conditions, *International Journal of Hydrogen Energy*, 2009, **34**(19), 8185-8192.

37. P. Serp and L. L. Figuerido: Carbon Materials for Catalysis, *John Wiley & Sons*, 2009.

38. K. Kinoshita: Proceedings of the Workshop on the Electrochemistry of Carbon, Electrochemical Society, Pennington, NJ, 1984.

39. L. R. Radovic and F. Rodriguez-Reinoso: Chemistry and Physics of Carbon: A Series of Advances, *Carbon Materials in Catalysis*, 1998.

40. O. V. Cherstiouk, A. N. Simonov, N. S. Moseva, S. V. Cherepanova, P. A. Simonov, V. I. Zaikovskii, and E. R. Savinova: Microstructure effects on the electrochemical corrosion of carbon materials and carbon-supported Pt catalysts, *Electrochim. Acta*, 2010, **55**(28), 8453-8460.

41. R. L. Borup, J. R. Davey, F. H. Garzon, D. L. Wood, and M. A. Inbody: PEM fuel cell electrocatalyst durability measurements, *J. Power Sources*, 2006, **163**(1), 76-81.

42. J. P. Meyers and R. M. Darling: Model of Carbon Corrosion in PEM Fuel Cells, *J. Electrochem. Soc.*, 2006, **153**(8), A1432.

43. N. Takeuchi and T. F. Fuller: Modeling and Investigation of Design Factors and Their Impact on Carbon Corrosion of PEMFC Electrodes, *J. Electrochem. Soc.*, 2008, **155**(7), B770.

44. A. Panchenko, H. Dilger, J. Kerres, M. Hein, A. Ullrich, T. Kaz, and E. Roduner: In-situ spin trap electron paramagnetic resonance study of fuel cell processes, *Phys. Chem. Chem. Phys.*, 2004, **6**, 2891-2894.

45. C. F. Zinola, A. M. Castro Luna, W. E. Triaca, and A. J. Arvia: Electroreduction of molecular oxygen on Pt, *J. Appl. Elecrtrochem.*, 1994, **24**, 119-125.

46. I. Morcos and E. Yeager: Kinetics and study of the oxygen-peroxide couple on pyrolytic graphite, *Electrochim. Acta*, 1970, **15**(6), 1953-1975.

47. L. Franck-Lacaze, C. Bonnet, E. Choi, J. Moss, S. Pontvianne, H. Poirot, R. Datta, and F. Lapicque: Ageing of PEMFC's due to operation at low current density: Investigation of oxidative degradation, *International Journal of Hydrogen Energy*, 2010, **35**(19), 10472-10481.

48. Z. Y. Liu, B. K. Brady, R. N. Carter, B. Litteer, M. Budinski, J. K. Hyun, and D. A. Muller: Characterization of Carbon Corrosion-Induced Structural Damage of PEM Fuel Cell Cathode Electrodes Caused by Local Fuel Starvation, *J. Electrochem. Soc.*, 2008, **155**(10), B979.

49. R. O'Hayre, S.-W. Cha, W. Colella, and F. B. Prinz: Fuel Cell Fundamentals, 2006.

50. C. Prado-Burguete, A. Linares-Solano, F. Rodriguez-Reinoso, and C. Salinas-Martinez: The effect of oxygen surface groups on the transport on platinum dispersion in Pt/C catalysts, *Journal of Catalysis*, 1988, **115**(1), 98-106.

51. Y. Shao, G. Yin, Y. Gao, and P. Shi: Durability Study of Pt/C and Pt/CNTs Catalysts under Simulated PEM Fuel Cell Conditions, *J. Electrochem. Soc.*, 2006, **153**(6), A1093.

52. E. Antolini: Carbon supports for low-temperature fuel cell catalysts, *Appl. Catal., B*, 2009, **88**(1-2), 1-24.

53. R. S. Goeke, A. K. Datye, P. Atanassov, and J. St-Pierre: Model Electrode Structures for Studies of Electrocatalyst Degradation, *ECS Trans.*, 2010, **33**(1), 361-368.

54. L. M. Roen, C. H. Paik, and T. D. Jarvi: Electrocatalytic Corrosion of Carbon Support in PEMFC Cathodes, *Electrochem. Solid-State Lett.*, 2004, **7**(1), A19-A22.

55. X. Yu and S. Ye: Recent advances in activity and durability enhancement of Pt/C catalytic cathode in PEMFC, *J. Power Sources*, 2007, **172**(1), 145-154.

56. F. Coloma, A. Sepulveda-Scribano, and F. Rodriguez Reinoso: Heat-Treated Carbon-Black as Supports for Platinum Catalysts, *Journal of Catalysis*, 1995, **154**(2), 299-305.

57. A. Guerrero-Ruiz, A. Maroto-Valiente, M. Cerro-Alarcon, B. Bachiller-Baeza, and I. Rodriguez-Ramos: Surface properties of supported metallic clusters as determined by microcalorimetry of CO chemisorption, *Top. Catal.*, 2002, **19**(3-4), 303-311.

58. S. K. Roy: Use of Impedance Spectroscopy to Investigate Factors that Influence the performance and durability of PEMFC, Dissertation thesis, University of Florida, 2008.

59. L. Timperman, Y. J. Feng, W. Vogel, and N. Alonso-Vante: Substrate effect on oxygen reduction electrocatalysis, *Electrochim. Acta*, 2010, **55**(26), 7558-7563.

60. S. Suzuki, T. Onodera, J. Kawaji, T. Mizukami, and K. Yamaga: Effect of support materials on platinum lattice strain and its oxygen reduction activity, *Appl. Catal., A*, 2012, **427–428**(0), 92-97.

61. H. Tang, Z. Qi, M. Ramani, and J. F. Elter: PEM fuel cell cathode carbon corrosion due to the formation of air/fuel boundary at the anode, *J. Power Sources*, 2006, **158**(2), 1306-1312.

62. D. A. Stevens, M. T. Hicks, G. M. Haugen, and J. R. Dahn: Ex Situ and In Situ Stability Studies of PEMFC Catalysts, *J. Electrochem. Soc.*, 2005, **152**(12), A2309.

63. K. H. Kangasniemi, D. A. Condit, and T. D. Jarvi: Characterization of Vulcan Electrochemically Oxidized under Simulated PEM Fuel Cell Conditions, *J. Electrochem. Soc.*, 2004, **151**(4), E125.

64. B. Sompalli, B. A. Litteer, W. Gu, and H. A. Gasteiger: Membrane Degradation at Catalyst Layer Edges in PEMFC MEAs, *J. Electrochem. Soc.*, 2007, **154**(12), B1349.

65. B. Du, R. Pollard, M. Ramani, P. Graney, and J. F. Elter: Impact of Cold Start and Hot Stop on Performance and Durability of a Proton Exchange Membrane (PEM) Fuel Cell, *ECS Trans.*, 2007, **5**(1), 271-282.

66. O. V. Cherstiouk, V. L. Kuznetsov, A. N. Simonov, I. N. Mazov, K. V. Elumeeva, and N. S. Moseva: Electrocorrosion properties of multiwall carbon nanotubes, *physica status solidi (b)*, 2010, **247**(11-12), 2738-2742.

67. Z. Tang, H. Y. Ng, J. Lin, A. T. S. Wee, and D. H. C. Chua: Pt/CNT-Based Electrodes with High Electrochemical Activity and Stability for Proton Exchange Membrane Fuel Cells, *J. Electrochem. Soc.*, 2010, **157**(2), B245.

68. F. Hasché, M. Oezaslan, and P. Strasser: Activity, stability and degradation of multi walled carbon nanotube (MWCNT) supported Pt fuel cell electrocatalysts, *Phys. Chem. Chem. Phys.*, 2010, **12**(46), 15251.

69. X. Li, H. Wang, H. Yu, Z. Liu, and F. Peng: An opposite change rule in carbon nanotubes supported platinum catalyst for methanol oxidation and oxygen reduction reactions, *J. Power Sources*, 2014, **260**, 1-5.

70. R. K. Ahluwalia, S. Arisetty, X. Wang, R. Subbaraman, S. C. Ball, S. DeCrane, and D. J. Myers: Thermodynamics and Kinetics of Platinum Dissolution from Carbon-Supported Electrocatalysts in Aqueous Media under Potentiostatic and Potentiodynamic Conditions, *J. Electrochem. Soc.*, 2013, **160**(4), F447-F455.

71. J. A. Gilbert, N. N. Kariuki, R. Subbaraman, A. J. Kropf, M. C. Smith, E. F. Holby, D. Morgan, and D. J. Myers: In Situ Anomalous Small-Angle X-ray Scattering Studies of Platinum Nanoparticle Fuel Cell Electrocatalyst Degradation, *J. Am. Chem. Soc.*, 2012, **134**(36), 14823-14833.

72. K. Sasaki, F. Takasaki, Z. Noda, S. Hayashi, Y. Shiratori, and K. Ito: Alternative Electrocatalyst Support Materials for Polymer Electrolyte Fuel Cells, *ECS Trans.*, 2010, **33**(1), 473-482.

73. D. R. Gaskell: Introduction to the Thermodynamics of Materials, 5th Ed., 2008.

74. S. J. Smith, R. Stevens, S. Liu, G. Li, A. Navrotsky, J. Boerio-Goates, and B. F. Woodfield: Heat capacities and thermodynamic functions of TiO2 anatase and rutile: Analysis of phase stability, *American Mineralogist*, 2009, **94**(2-3), 236-243.

75. J. L. Murray and H. A. Wriedt: The O-Ti (Oxygen-Titanium) System, *Journal of Phase Equilibria*, 1987, **8**(2), 148-165.

76. J. E. Graves, D. Pletcher, R. L. Clarke, and F. C. Walsh: The electrochemistry of Magnéli phase titanium oxide ceramic electrodes Part I. The deposition and properties of metal coatings, *J. Appl. Elecrtrochem.*, 1991, **21**(10), 848-857.

77. K. M. Glassford and J. R. Chelikowsky: Structural and electronic properties of titanium dioxide, *Phys. Rev. B*, 1992, **46**(3), 1284-1298.

78. S.-D. Mo and W. Y. Ching: Electronic and optical properties of three phases of titanium dioxide: Rutile, anatase, and brookite, *Phys. Rev. B*, 1995, **51**(19), 13023-13032.

79. T. Ioroi, Z. Siroma, N. Fujiwara, S.-i. Yamazaki, and K. Yasuda: Sub-stoichiometric titanium oxide-supported platinum electrocatalyst for polymer electrolyte fuel cells, *Electrochemistry Communications*, 2005, **7**(2), 183-188.

80. J. R. Smith, F. C. Walsh, and R. L. Clarke: Electrodes based on Magneli phase titanium oxides: the properties and applications of Ebonex materials, *J. Appl. Elecrtrochem.*, 1998, **28**, 1021-1033.

81. J. M. Roller, M. J. Arellano-Jiménez, H. Yu, R. Jain, C. B. Carter, and R. Maric: Catalyst nanoscale assembly from the vapor phase on corrosion resistant supports, *Electrochim. Acta*, 2013, **107**, 632-655.

82. G. Chen, S. R. Bare, and T. E. Mallouk: Development of Supported Bifunctional Electrocatalysts for Unitized Regenerative Fuel Cells, *J. Electrochem. Soc.*, 2002, **149**(8), A1092-A1099.

83. F. A. Grant: Properties of Rutile (Titanium Dioxide), *Reviews of Modern Physics*, 1959, **31**(3).

84. R. G. Breckenridge and W. R. Hosler: Electrical Properties of Titanium Dioxide Semiconductors, *Phys. Rev.*, 1953, **91**(4), 793-802.

85. J. P. Shchaffer, A. Sexon, S. D. Antolovich, t. H. Snders Jr., and S. B. Warner: The Science and Design of Engineering Materials, 2nd Ed., *McGraw-Hill*, 1999.

86. S. A. Campbell, D. C. Gilmer, W. Xiao-Chuan, H. Ming-Ta, K. Hyeon-Seag, W. L. Gladfelter, and Y. Jinhua: MOSFET transistors fabricated with high permitivity TiO_2 dielectrics, *Electron Devices, IEEE Transactions on*, 1997, **44**(1), 104-109.

87. O. Carp, C. L. Huisman, and A. Reller: Photoinduced reactivity of titanium dioxide, *Progress in Solid State Chemistry*, 2004, **32**, 33-1777.

88. A. Fujishima and K. Honda: Electrochemical Evidence for the Mechanism of the Primary Stage of Photosynthesis, *Bulletin of the Chemical Society of Japan*, 1971, **44**, 1148-1150.

89. S. J. Tauster, S. C. Fung, and R. L. Garten: Strong Metal-Support Interactions. Group 8 Noble Metals on TiO2, *J. Am. Chem. Soc.*, 1978, **100**(1), 170-175.

90. S. Bonanni, K. Aït-Mansour, H. Brune, and W. Harbich: Overcoming the Strong Metal−Support Interaction State: CO Oxidation on TiO2(110)-Supported Pt Nanoclusters, *ACS Catal.*, 2011, **1**(4), 385-389.

91. S. Bonanni, K. Aït-Mansour, W. Harbich, and H. Brune: Effect of the TiO2 Reduction State on the Catalytic CO Oxidation on Deposited Size-Selected Pt Clusters, *J. Am. Chem. Soc.*, 2012, **134**(7), 3445-3450.

92. G. A. Somorjai: The catalytic nanodiode. Its role in catalytic reaction mechanisms in a historical perspective, *Catalysis Letters*, 2005, **101**(1-2), 1-3.

93. J. A. Horsley: A Molecular Orbital Study of SM-SI between Pt and TiO2, *J. Am. Chem. Soc.*, 1978, **101**(11), 2870-2874.

94. S. Neophytides, S. Zafeiratos, G. Papakonstantinou, J. Jaksic, F. Paloukis, and M. Jaksic: Extended Brewer hypo-hyper--interionic bonding theory II. Strong metal-support interaction grafting of composite electrocatalysts, *International Journal of Hydrogen Energy*, 2005, **30**(4), 393-410.

95. J. Robertson: Band alignment at metal-semiconductor and metal-oxide interfaces, *physica status solidi (a)*, 2010, **207**(2), 261-269.

96. S. J. Tauster: Strong Metal-Support Interactions, *Accounts of Chemical Research*, 1987, **20**(11), 389-394.

97. D. M. Smyth: The Defect Chemistry of Metal Oxides, 2000.

98. A. H. Kahn and A. J. Leyendecker: Electronic Energy Bands in SrTiO3, *Phys. Rev.*, 1964, **135**(5A), A1321-A1325.

99. D. Grosso, G. J. d. A. A. Soler-Illia, E. L. Crepaldi, F. Cagnol, C. Sinturel, A. Bourgeois, A. Brunet-Bruneau, H. Amenitsch, P. A. Albouy, and C. Sanchez: Highly Porous TiO2 Anatase Optical Thin Films with Cubic Mesostructure Stabilized at 700 °C, *Chem. Mat.*, 2003, **15**(24), 4562-4570.

100. W. Dong, H. J. Bongard, and F. Marlow: New Type of Inverse Opals: Titania With Skeleton Structure, *Chem. Mat.*, 2003, **15**(2), 568-574.

101. B. C. Beard and P. N. Ross: Characterization of a Titanium-Promoted Supported Electrocatalyst, *J. Electrochem. Soc.*, 1986, **133**(9), 1839-1845.

102. S. Shanmugan and A. Gedanken: Synthesis and Electrochemical Oxygen Reduction of Platinum Nanoparticles Supported on Mesoporous TiO2, *J. Phys. Chem. C*, 2009, **113**, 18707-18712.

103. N. Rajalakshmi, N. Lakshmi, and K. S. Dhathathreyan: Nano titanium oxide catalyst support for proton exchange membrane fuel cells, *International Journal of Hydrogen Energy*, 2008, **33**(24), 7521-7526.

104. X. Liu, J. Chen, G. Liu, L. Zhang, H. Zhang, and B. Yi: Enhanced long-term durability of proton exchange membrane fuel cell cathode by employing Pt/TiO2/C catalysts, *J. Power Sources*, 2010, **195**(13), 4098-4103.

105. S.-Y. Huang, P. Ganesan, S. Park, and B. N. Popov: Development of a Titanium Dioxide-Supported Platinum Catalyst with Ultrahigh Stability for Polymer Electrolyte Membrane Fuel Cell Applications, *J. Am. Chem. Soc. Comm.*, 2009, **131**, 13898–13899.

106. J. Shim, C.-R. Lee, H.-K. Lee, J.-S. Lee, and E. J. Cairns: Electrochemical characteristics of Pt-WO3-C and Pt-TiO2-C electrocatalysts in PEFC, *J. Power Sources*, 2001, **102**, 172-177.

107. S. Sambandam, V. Valluri, W. Chanmanee, N. R. De Tacconi, W. A. Wampler, W.-Y. Lin, T. F. Carlson, V. Ramani, and K. Rajeshwar: Platinum-carbon black-titanium dioxide nanocomposite electrocatalysts, *Journal of Chemical Sciences*, 2009, **120**(5), 655-664.

108. S. von Kraemer, K. Wikander, G. Lindbergh, A. Lundblad, and A. E. C. Palmqvist: Evaluation of TiO2 as catalyst support in Pt-TiO2/C composite cathodes for the proton exchange membrane fuel cell, *J. Power Sources*, 2008, **180**(1), 185-190.

109. T. Hitosugi, H. Kamisaka, K. Yamashita, H. Nogawa, Y. Furubayashi, S. Nakao, N. Yamada, A. Chikamatsu, H. Kumigashira, M. Oshima, Y. Hirose, T. Shimada, and T. Hasegawa: Electronic Band Structure of Transparent Conductor: Nb-Doped Anatase TiO2, *Applied Physics Express*, 2008, **1**, 111203.

110. D. Morris, Y. Dou, J. Rebane, C. E. J. Mitchell, R. G. Egdell, D. S. L. Law, A. Vittadini, and M. Casarin: Photoemission and STM study of the electronic structure of Nb-doped TiO2, *Phys. Rev. B*, 2000, **61**(20), 13445-13457.

111. N. G. Eror: Self-compensation in niobium-doped TiO2, *Journal of Solid State Chemistry*, 1981, **38**(13), 281-287.

112. Y. Liu, J. M. Szeifert, J. M. Feckl, B. Mandlmeier, J. Rathousky, O. Hayden, D. Fattakhova-Rohlfing, and T. Bein: Niobium-Doped Titania Nanoparticles:

Synthesis and Assembly into Mesoporous Films and Electrical Conductivity, *ACS Nano*, 2010, **4**(9), 5373-5381.

113. A. Ruiz, G. Dezanneau, J. Arbiol, A. Cornet, and J. R. Morante: Study of the influence of Nb content and sintering temperature on TiO2 sensing films, *Thin Solid Films*, 2003, **436**(1), 90-94.

114. J. Tao, H. Pan, L. M. Wong, T. I. Wong, J. W. Chai, J. Pan, and S. J. Wang: Mechanism of insulator-to-metal transition in heavily Nb doped anatase TiO2, *Materials Research Express*, 2014, **1**(1), 015911.

115. H. Chhina, S. Campbell, and O. Kesler: Ex Situ and In Situ Stability of Platinum Supported on Niobium-Doped Titania for PEMFCs, *J. Electrochem. Soc.*, 2009, **156**(10), B1232-B1237.

116. S. X. Zhang, D. C. Kundaliya, W. Yu, S. Dhar, S. Y. Young, L. G. Salamanca-Riba, S. B. Ogale, R. D. Vispute, and T. Venkatesan: Niobium doped TiO2: Intrinsic transparent metallic anatase versus highly resistive rutile phase, *J. Appl. Phys.*, 2007, **102**(1), 013701.

117. S.-Y. Huang, P. Ganesan, and B. N. Popov: Electrocatalytic activity and stability of niobium-doped titanium oxide supported platinum catalyst for polymer electrolyte membrane fuel cells, *Appl. Catal., B*, 2010, **96**(1-2), 224-231.

118. S.-H. Lee: Photocatalytic Nanocomposities Based On TiO_2 and Carbon Nanotubes, University of Florida, 2004.

119. H. Chang, S. H. Joo, and C. Pak: Synthesis and characterization of mesoporous carbon for fuel cell application, *J. Mater. Chem.*, 2007, **17**(214-230).

120. C. Largeot, C. Portet, J. Chmiola, P.-L. Taberna, Y. Gogotsi, and P. Simon: Relation between the Ion Size and Pore Size for an Electric Double-Layer Capacitor, *J. Am. Chem. Soc. Comm.*, 2008, **130**, 2730-2731.

121. Z. Wang, N. S. Ergang, M. A. Al-Daous, and A. Stein: Synthesis and Characterization of Three-Dimensionally Ordered Macroporous Carbon/Titania Nanoparticle Composites, *Chem. Mat.*, 2005, **17**(26), 6805-6813.

122. S. Osswald, M. Havel, and Y. Gogotsi: Monitoring oxidation of multiwalled carbon nanotubes by Raman spectroscopy, *J. Raman Spectrosc.*, 2007, **38**(6), 728-736.

123. P. Vincent, A. Brioude, C. Journet, S. Rabaste, S. T. Purcell, J. Le Brusq, and J. C. Plenet: Inclusion of carbon nanotubes in a TiO2 sol–gel matrix, *Journal of Non-Crystalline Solids*, 2002, **311**(2), 130-137.

124. B. G. Pollet: The use of ultrasound for the fabrication of fuel cell materials, *International Journal of Hydrogen Energy*, 2010, **35**(21), 11986-12004.

125. Y. Yu, J. C. Yu, J.-G. Yu, Y.-C. Kwok, Y.-K. Che, J.-C. Zhao, L. Ding, W.-K. Ge, and P.-K. Wong: Enhancement of photocatalytic activity of mesoporous TiO2 by using carbon nanotubes, *Appl. Catal., A*, 2005, **289**(2), 186-196.

126. B. Gao, G. Z. Chen, and G. Li Puma: Carbon nanotubes/titanium dioxide (CNTs/TiO2) nanocomposites prepared by conventional and novel surfactant wrapping sol–gel methods exhibiting enhanced photocatalytic activity, *Appl. Catal., B*, 2009, **89**(3-4), 503-509.

127. A. Jitianu, T. Cacciaguerra, M.-H. Berger, R. Benoit, F. Béguin, and S. Bonnamy: New carbon multiwall nanotubes – TiO2 nanocomposites obtained by the sol–gel method, *Journal of Non-Crystalline Solids*, 2004, **345-346**, 596-600.

128. A. Jitianu, T. Cacciaguerra, R. Benoit, S. Delpeux, F. Béguin, and S. Bonnamy: Synthesis and characterization of carbon nanotubes–TiO2 nanocomposites, *Carbon*, 2004, **42**(5-6), 1147-1151.

129. B. Liu and H. C. Zeng: Carbon Nanotubes Supported Mesoporous Mesocrystals of Anatase TiO2, *Chem. Mat.*, 2008, **20**(8), 2711-2718.

130. S. Orlanducci, V. Sessa, M. L. Terranova, G. A. Battiston, S. Battiston, and R. Gerbasi: Nanocrystalline TiO2 on single walled carbon nanotube arrays: Towards the assembly of organized C/TiO2 nanosystems, *Carbon*, 2006, **44**(13), 2839-2843.

131. R. Kou, Y. Shao, D. Mei, Z. Nie, D. Wang, C. Wang, V. V. Viswanathan, S. Park, I. A. Aksay, Y. Lin, Y. Wang, and J. Liu: Stabilization of Electrocatalytic Metal Nanoparticles at Metal−Metal Oxide−Graphene Triple Junction Points, *J. Am. Chem. Soc.*, 2011, **133**(8), 2541-2547.

132. N. Zhang, S. Zhang, C. Du, Z. Wang, Y. Shao, F. Kong, Y. Lin, and G. Yin: Pt/Tin Oxide/Carbon Nanocomposites as Promising Oxygen Reduction Electrocatalyst with Improved Stability and Activity, *Electrochim. Acta*, 2014, **117**, 413-419.

133. Y. Liu and W. E. Mustain: High Stability, High Activity Pt/ITO Oxygen Reduction Electrocatalysts, *J. Am. Chem. Soc.*, 2013, **135**(2), 530-533.

134. Z.-Z. Jiang, Z.-B. Wang, Y.-Y. Chu, D.-M. Gu, and G.-P. Yin: Ultrahigh stable carbon riveted Pt/TiO2–C catalyst prepared by in situ carbonized glucose for proton exchange membrane fuel cell, *Energy Environ. Sci.*, 2011, **4**(3), 728.

135. Z.-Z. Jiang, Z.-B. Wang, Y.-Y. Chu, D.-M. Gu, and G.-P. Yin: Carbon riveted microcapsule Pt/MWCNTs-TiO2 catalyst prepared by in situ carbonized glucose with ultrahigh stability for proton exchange membrane fuel cell, *Energy Environ. Sci.*, 2011, **4**(7), 2558.

136. B. Y. Xia, S. Ding, H. B. Wu, X. Wang, and X. Wen: Hierarchically structured Pt/CNT@TiO2 nanocatalysts with ultrahigh stability for low-temperature fuel cells, *RSC Adv.*, 2012, **2**(3), 792.

137. N. G. Akalework, C.-J. Pan, W.-N. Su, J. Rick, M.-C. Tsai, J.-F. Lee, J.-M. Lin, L.-D. Tsai, and B.-J. Hwang: Ultrathin TiO2-coated MWCNTs with excellent conductivity and SMSI nature as Pt catalyst support for oxygen reduction reaction in PEMFCs, *J. Mater. Chem.*, 2012, **22**(39), 20977-20985.

138. K. Huang, K. Sasaki, R. R. Adzic, and Y. Xing: Increasing Pt oxygen reduction reaction activity and durability with a carbon-doped TiO2 nanocoating catalyst support, *J. Mater. Chem.*, 2012, **22**(33), 16824.

139. K. Huang, Y. Li, L. Yan, and Y. Xing: Nanoscale conductive niobium oxides made through low temperature phase transformation for electrocatalyst support, *RSC Adv.*, 2014, **4**, 9701-9708.

140. L. Zhang, L. Wang, C. M. B. Holt, B. Zahiri, Z. Li, K. Malek, T. Navessin, M. H. Eikerling, and D. Mitlin: Highly corrosion resistant platinum–niobium oxide–carbon nanotube electrodes for the oxygen reduction in PEM fuel cells, *Energy Environ. Sci.*, 2012, **5**(3), 6156.

141. K. Sasaki, L. Zhang, and R. R. Adzic: Niobium oxide-supported platinum ultra-low amount electrocatalysts for oxygen reduction, *Phys. Chem. Chem. Phys.*, 2008, **10**(1), 159.

142. T. Ioroi, T. Akita, M. Asahi, S.-i. Yamazaki, Z. Siroma, N. Fujiwara, and K. Yasuda: Platinum–titanium alloy catalysts on a Magnéli-phase titanium oxide support for improved durability in Polymer Electrolyte Fuel Cells, *J. Power Sources*, 2013, **223**, 183-189.

143. S. G. Neophytides, K. Murase, S. Zafeiratos, G. Papakonstantinou, F. E. Paloukis, N. V. Krstajic, and M. M. Jaksic: Composite Hypo-Hyper-d-Intermetallic and Interionic Phases as Supported Interactive Electrocatalysts, *J. Phys. Chem. B*, 2006, **110**(7), 3030-3042.

144. K. Senevirathne, R. Hui, S. Campbell, S. Ye, and J. Zhang: Electrocatalytic activity and durability of Pt/NbO2 and Pt/Ti4O7 nanofibers for PEM fuel cell oxygen reduction reaction, *Electrochim. Acta*, 2012, **59**, 538-547.

145. E. Asselin, T. M. Ahmed, and A. Alfantazi: Corrosion of niobium in sulphuric and hydrochloric acid solutions at 75 and 95°C, *Corrosion Science*, 2007, **49**(2), 694-710.

146. A. Bauer, R. Hui, A. Ignaszak, J. Zhang, and D. J. Jones: Application of a composite structure of carbon nanoparticles and Nb–TiO2 nanofibers as electrocatalyst support for PEM fuel cells, *J. Power Sources*, 2012, **210**(0), 15-20.

147. L. Chevallier, A. Bauer, S. Cavaliere, R. Hui, J. Rozière, and D. J. Jones: Mesoporous Nanostructured Nb-Doped Titanium Dioxide Microsphere Catalyst Supports for PEM Fuel Cell Electrodes, *ACS Applied Materials & Interfaces*, 2012, **4**(3), 1752-1759.

148. A. Ignaszak, C. Song, W. Zhu, Y.-J. Wang, J. Zhang, A. Bauer, R. Baker, V. Neburchilov, S. Ye, and S. Campbell: Carbon–Nb0.07Ti0.93O2 composite supported Pt–Pd electrocatalysts for PEM fuel cell oxygen reduction reaction, *Electrochim. Acta*, 2012(0).

149. B. Avasarala, T. Murray, W. Li, and P. Haldar: Titanium nitride nanoparticles based electrocatalysts for proton exchange membrane fuel cells, *J. Mater. Chem.*, 2009, **19**(13), 1803.

150. B. Avasarala and P. Haldar: Electrochemical oxidation behavior of titanium nitride based electrocatalysts under PEM fuel cell conditions, *Electrochim. Acta*, 2010, **55**(28), 9024-9034.

151. B. Avasarala and P. Haldar: On the stability of TiN-based electrocatalysts for fuel cell applications, *International Journal of Hydrogen Energy*, 2011, **36**(6), 3965-3974.

152. S. A. Chambers, Y. Gao, Y. J. Kim, M. A. Henderson, S. Thevuthasan, S. Wen, and K. L. Merkle: Geometric and electronic structure of epitaxial NbTiO2 on TiO2, *Surf. Sci.*, 1996, **365**, 625-637.

153. Y. Gao, Y. Liang, and S. A. Chambers: Thermal stability and the role of oxygen vacancy defects in strong metal support interaction - Pt on Nb-doped TiO2(100), *Surf. Sci.*, 1996, **365**, 638-648.

154. T. B. Do, M. Cai, M. S. Ruthkosky, and T. E. Moylan: Niobium-doped titanium oxide for fuel cell application, *Electrochim. Acta*, 2010, **55**(27), 8013-8017.

155. J. H. Park, S. Kim, and A. J. Bard: Novel Carbon-Doped TiO2 Nanotube Arrays with High Aspect Ratios for Efficient Solar Water Splitting, *Nano Lett.*, 2005, **6**(1), 24-28.

156. C. Di Valentin, G. Pacchioni, and A. Selloni: Theory of Carbon Doping of Titanium Dioxide, *Chem. Mat.*, 2005, **17**, 6656-6665.

157. Z.-Z. Jiang, D.-M. Gu, Z.-B. Wang, W.-L. Qu, G.-P. Yin, and K.-J. Qian: Effects of anatase TiO2 with different particle sizes and contents on the stability of supported Pt catalysts, *J. Power Sources*, 2011, **196**(20), 8207-8215.

158. T. Sakai, S.-J. Kim, S. Kajitani, J.-i. Hamagami, H. Oda, M. Matsuka, T. Ishihara, and H. Matsumoto: Proton conduction properties of nano-titania modified by sulfuric acid impregnation, *Journal of Solid State Electrochemistry*, 2011, **16**(6), 2055-2059.

159. W. K. Chan, W. J. H. Borghols, and F. M. Mulder: Direct observation of space charge induced hydrogen ion insertion in nanoscale anatase TiO2, *Chemical Communications*, 2008(47), 6342.

160. S.-J. Kim, T. Sakai, H. Oda, Y. Okuyama, Y. Mizutani, J.-I. Hamagami, M. Matsuka, T. Ishihara, and H. Matsumoto: Long-term stability of sulfated hydrous titania-based electrolyte for water electrolysis, *Journal of Solid State Electrochemistry*, 2012, **16**(11), 3587-3592.

161. M. Gustavsson, H. Ekström, P. Hanarp, L. Eurenius, G. Lindbergh, E. Olsson, and B. Kasemo: Thin film Pt/TiO2 catalysts for the polymer electrolyte fuel cell, *J. Power Sources*, 2007, **163**(2), 671-678.

162. H. Ekström, B. Wickman, M. Gustavsson, P. Hanarp, L. Eurenius, E. Olsson, and G. Lindbergh: Nanometer-thick films of titanium oxide acting as electrolyte in the polymer electrolyte fuel cell, *Electrochim. Acta*, 2007, **52**(12), 4239-4245.

163. M. Watanabe, H. Uchida, Y. Seki, M. Emori, and P. Stonehart: Self-Humidifying Polymer Electrolyte Membrane for Fuel Cells, *J. Electrochem. Soc.*, 1996, **143**(12), 3847-3852.

164. Y. Garsany, A. Epshteyn, A. P. Purdy, K. L. More, and K. E. Swider-Lyons: High-Activity, Durable Oxygen Reduction Electrocatalyst: Nanoscale Composite of Platinum−Tantalum Oxyphosphate on Vulcan Carbon, *J. Phys. Chem. Lett.*, 2010, **1**(13), 1977-1981.

165. C. Yang: A comparison of physical properties and fuel cell performance of Nafion and zirconium phosphate/Nafion composite membranes, *Journal of Membrane Science*, 2004, **237**(1-2), 145-161.

166. G. Taylor: The Instability of Liquid Surfaces when Accelerated in a Direction Perpendicular to their Planes. I, *Proceedings of the Royal Society A*, 1950, **201**(1065), 192-196.

167. R. J. Lang: Ultrasonic Atomization of Liquids, *The Journal of the Acoustical Society of America*, 1962, **34**(6), 6-8.

168. M. N. Topp and P. Eisenklam: Industrial and medical uses of ultrasonic atomizers, *Ultrasonics*, 1972, **10**(3), 127-133.

169. B. Millington, V. Whipple, and B. G. Pollet: A novel method for preparing proton exchange membrane fuel cell electrodes by the ultrasonic-spray technique, *J. Power Sources*, 2011, **196**(20), 8500-8508.

170. H. A. Gasteiger, S. S. Kocha, B. Sompalli, and F. T. Wagner: Activity benchmarks and requirements for Pt, Pt-alloy, and non-Pt oxygen reduction catalysts for PEMFCs, *Appl. Catal., B*, 2005, **56**(1-2), 9-35.

171. S. R. Narayanan, T. I. Valdez, and S. Firdosy: Analysis of the Performance of Nafion-Based Hydrogen–Oxygen Fuel Cells, *J. Electrochem. Soc.*, 2009, **156**(1), B152.

172. M. A. Hoberecht: A Comparison of Flow-Through Versus Non-Flow-Through Proton Exchange Membrane Fuel Cell Systems for NASA's Exploration Missions, *NASA Technical Report*, 2010, **NASA/TM-2010-216107**.

173. N. M. Markovic, T. J. Schmidt, V. R. Stamenkovic, and P. N. Ross Jr: Oxygen Reduction Reaction on Pt and Pt Bimetallic Surfaces: A Selective Review, *Fuel Cells*, 2001, **1**(2), 105-116.

174. J. K. Norskov, J. Rossmeisl, A. Logadottir, L. Lindqvist, J. R. Kitchin, T. Bliggard, and H. Jonsson: Origin of Overpotential for Oxygen Reduction Reaction at a Fuel-Cell Cathode, *J. Phys. Chem. B*, 2004, **108**, 17886-17892.

175. C. Luo, X. Zuo, L. Wang, E. Wang, S. Song, J. Wang, J. Wang, C. Fan, and Y. Cao: Flexible Carbon Nanotube-Polymer Composite Films with High Conductivity and Superhydrophobicity Made by Solution Process, *Nano Lett.*, 2008, **8**(12), 4454-4458.

176. D. Neagu and J. T. S. Irvine: Enhancing Electronic Conductivity in Strontium Titanates through Correlated A and B-Site Doping, *Chem. Mat.*, 2011, 110211085543072.

177. H. P. R. Frederiske, W. R. Thurber, and W. R. Hosler: Electronic Transport in Strontium Titanate, *Phys. Rev.*, 1964, **134**(2A), A442-A445.

178. H. P. R. Frederiske and W. R. Hosler: Hall mobility in SrTiO3, *Phys. Rev.*, 1967, **161**(3), 822-827.

179. C. S. Koonce, M. L. Cohen, J. F. Schooley, W. R. Hosler, and E. R. Pfeiffer: Superconducting Transition Temperatures of Semiconducting SrTiO3, *Phys. Rev.*, 1967, **163**(2), 380-390.

180. S.-Y. Koo, G.-G. Lee, and S.-J. L. Kang: Measurement of reduction kinetics in Nb2O5-doped SrTiO3 by use of a new technique of liquid film migration, *Journal of Physics and Chemistry of Solids*, 2005, **66**(2-4), 498-503.

181. Z. Wang, S. Tsukimoto, M. Saito, and Y. Ikuhara: Quantum electron transport through SrTiO[sub 3]: Effects of dopants on conductance channel, *Appl. Phys. Lett.*, 2009, **94**(25), 252103.

182. C. Zhang, C. L. Wang, J. C. Li, K. Yang, Y. F. Zhang, and Q. Z. Wu: Substitutional position and insulator-to-metal transition in Nb-doped SrTiO3, *Materials Chemistry and Physics*, 2008, **107**(2-3), 215-219.

183. P. R. Slater, D. P. Fagg, and J. T. S. Irvine: Synthesis and electrical characterisation of doped perovskite titanates as potential anodes materials for solid oxide fuel cells, *J. Mater. Chem.*, 1997, **7**(12), 2495-2498.

184. K. Urasaki, Y. Sekine, S. Kawabe, E. Kikuchi, and M. Matsukata: Catalytic activities and coking resistance of Ni/perovskites in steam reforming of methane, *Appl. Catal., A*, 2005, **286**(1), 23-29.

185. J. M. Jaksic, N. V. Krstajic, L. M. Vracar, S. G. Neophytides, D. Labou, P. Falaras, and M. M. Jaksic: Spillover of primary oxides as a dynamic catalytic effect of interactive hypo-d-oxide supports, *Electrochim. Acta*, 2007, **53**(2), 349-361.

186. J. A. Enterkin, K. R. Poeppelmeier, and L. D. Marks: Oriented Catalytic Platinum Nanoparticles on High Surface Area Strontium Titanate Nanocuboids, *Nano Lett.*, 2011, **11**(3), 993-997.

187. N. N. Marković, H. A. Gasteiger, and P. N. Ross Jr: Oxygen Reduction on Platinum Low-Index Single-Crystal Surfaces in Sulfuric Acid Solution: Rotating Ring-Pt (hkl) Disk Studies, *J. Phys. Chem.*, 1995, **99**(113411-3415).

188. D. Parker and J. Yahia: ac Hall Measurements in Crystals of Strontium Titanate from 190 to 500 K: Dependence of Hall Mobility on Charge-Carrier Density, *Phys. Rev.*, 1968, **169**(3), 605-609.

189. N.-H. Chan, R. K. Sharma, and D. M. Smyth: Nonstoichiometry in SrTiO3, *J. Electrochem. Soc.*, 1981, **128**(8), 1762-1769.

190. O. N. Tufte and P. W. Chapman: Electron Mobility in Semiconducting Strontium Titanate, *Phys. Rev.*, 1967, **155**(3), 796-802.

191. O. N. Tufte and E. L. Stelzer: Piezoresistive Properties of Reduced Strontium Titanate, *Phys. Rev.*, 1966, **141**(3), 675-680.

192. C. Lee, J. Yahia, and J. L. Brebner: Electronic Conduction in Slightly Reduced Strontium Titanate at Low Temperatures, *Phys. Rev. B*, 1971, **3**(8), 2525-2533.

193. P. Blennow, A. Hagen, K. Hansen, L. Wallenberg, and M. Mogensen: Defect and electrical transport properties of Nb-doped SrTiO3, *Solid State Ionics*, 2008, **179**(35-36), 2047-2058.

194. P. Blennow, K. K. Hansen, L. R. Wallenberg, and M. Mogensen: Synthesis of Nb-doped SrTiO3 by a modified glycine-nitrate process, *Journal of the European Ceramic Society*, 2007, **27**(13-15), 3609-3612.

195. R. I. Eglitis and E. A. Kotomin: Ab initio calculations of Nb doped SrTiO3, *Physica B: Condensed Matter*, 2010, **405**(15), 3164-3166.

196. R. Moos and K. H. Hardtl: Electronic transport properties of SrLaTiO3, *J. Appl. Phys.*, 1996, **80**(1), 393-400.

197. M. Takizawa, K. Maekawa, H. Wadati, T. Yoshida, A. Fujimori, H. Kumigashira, and M. Oshima: Angle-resolved photoemission study of Nb-doped SrTiO3, *Phys. Rev. B*, 2009, **79**(11).

198. X. G. Guo, X. S. Chen, Y. L. Sun, L. Z. Sun, X. H. Zhou, and W. Lu: Electronic band structure of Nb doped SrTiO3 from first principles calculation, *Physics Letters A*, 2003, **317**(5-6), 501-506.

199. A. S. Hamid: Atomic and electronic structure of oxygen vacancies and Nb-impurity in SrTiO3, *Appl. Phys. A*, 2009, **97**(4), 829-833.

200. J. C. C. Abrantes, J. A. Labrincha, and J. R. Fade: Behavior strontium titanate ceramics in reducing conditions suggesting enhanced conductivity along grain contacts, *Journal of the European Ceramic Society*, 2002, **22**, 1683-1691.

201. S.-H. Kim, T.-H. Kim, J.-E. Park, and Y. Kim: I-V Characteristics and Impedance Spectroscopy of a Single Grain Boundary in Nb-Doped SrTiO3, *Materials Research Bulletin*, 1999, **34**(3), 415-423.

202. S.-Y. Chung and S.-J. L. Kang: Effect of Sintering Atmosphere on Grain Boundary Segregation and Grain Growth in Niobium-Doped SrTiO3, *J. Am. Ceram. Soc.*, 2002, **85**(11), 2805-2810.

203. S.-Y. Chung, B.-K. Lee, and S.-J. Kang: Core-Shell Structure Formation in Nb2O5-Doped SrTiO3 by Oxygen Partial Pressure Change, *J. Am. Ceram. Soc.*, 1998, **81**(11), 3016-3018.

204. C. Ohly, S. Hoffmann-Eiffert, K. Szot, and R. Waser: Electrical conductivity and segregation of doped SrTiO3 thin films, *Journal of the European Ceramic Society*, 2001, **21**, 1673-1676.

205. B. R. Kalkhoran: Microstructural Studies on the Reoxidation Behavior of Nb-doped SrTiO3 Ceramics, Max Planck Institute, 2003.

206. R. Meyer, R. Waser, J. Helmbold, and G. Brochardt: Cationic Surface Segregation in Donor-Doped SrTiO3 Under Oxidizing Conditions, *Journal of Electroceramics*, 2002, **9**, 101-110.

207. R. Moos and K. H. Hardtl: Defect Chemistry of Donor-Doped and Undoped Strontium Titanate Ceramics between 1000 and 1400 C, *J. Am. Ceram. Soc.*, 1997, **80**(10), 2549-2562.

208. T. Tomio, H. Miki, H. Tabata, T. Kawai, and S. Kawai: Control of electrical conductivity in laser deposited SrTiO3 thin films with Nb doping, *J. Appl. Phys.*, 1994, **76**(10), 5886-5890.

209. T. Zhao, H. Lu, F. Chen, S. Dai, G. Yang, and Z. Chen: Highly conductive Nb doped SrTiO3 epitaxial thin films grown by laser bean molecular epitaxy, *Journal of Crystal Growth*, 2000, **212**, 451-455.

210. K. Fukushima and S. Shibagaki: Niobium Doping Effect on Resistivity of Epitaxially Grown Nb-SrTiO3 Thin Films by Laser Ablation Method, *Journal of Electroceramics*, 1999, **4**(S1), 81-90.

211. J. C. C. Abrantes and J. A. F. Labrincha, J. R.: Evaluation of SrTiNbO3 materials for gas sensors, *Sensors and Actuators B*, 1999, **56**, 198-205.

212. J. Karczewski, B. Riegel, M. Gazda, P. Jasinski, and B. Kusz: Electrical and structural properties of Nb-doped SrTiO3 ceramics, *Journal of Electroceramics*, 2009, **24**(4), 326-330.

213. N. T. Tinh and T. Tsuji: Thermoelectric Properties of Heavily Doped Polycrystalline SrTiO3, *Physics and Engineering of New Materials*, 2009, **129**, 209-217.

214. P. Blennow, K. K. Hansen, L. R. Wallenberg, and M. Mogensen: Electrochemical characterization and redox behavior of Nb-doped SrTiO3, *Solid State Ionics*, 2009, **180**(1), 63-70.

215. P. R. Arya, P. Jha, and A. K. Ganguli: Synthesis, characterization and dielectric properties of nanometer-sized barium strontium titanates prepared by the polymeric citrate precursor method, *J. Mater. Chem.*, 2003, **13**(2), 415-423.

216. M. Arima, M. Kakihana, Y. Nakamura, M. Yashima, and M. Yoshimura: Polymerized Complex Route to Barium Titanate Powders Using Barium-Titanium Mixed-Metal Citric Acid Complex, *Journal of American Ceramic Society*, 1996, **79**(11), 2847-2856.

217. Y. Shao-Horn, W. C. Sheng, S. Chen, P. J. Ferreira, E. F. Holby, and D. Morgan: Instability of Supported Platinum Nanoparticles in Low-Temperature Fuel Cells, *Top. Catal.*, 2007, **46**(3-4), 285-305.

218. S. Park, Y. Shao, V. V. Viswanathan, J. Liu, and Y. Wang: Non-kinetic losses caused by electrochemical carbon corrosion in PEM fuel cells, *International Journal of Hydrogen Energy*, 2012, **37**(10), 8451-8458.

219. S. Park, Y. Shao, R. Kou, V. V. Viswanathan, S. A. Towne, P. C. Rieke, J. Liu, Y. Lin, and Y. Wang: Polarization Losses under Accelerated Stress Test Using Multiwalled Carbon Nanotube Supported Pt Catalyst in PEM Fuel Cells, *J. Electrochem. Soc.*, 2011, **158**(3), B297.

220. G. Sakai, T. Arai, T. Matsumoto, T. Ogawa, M. Yamada, K. Sekizawa, and T. Taniguchi: Electrochemical and ESR Study on Pt-TiOx/C Electrocatalysts with Enhanced Activity for ORR, *ChemElectroChem Comm.*, 2013, In Press.

221. J. Nowotny, T. Bak, M. K. Nowotny, and L. R. Sheppard: Defect Chemistry and Electrical Poperties of Titanium Dioxide. 1. Defect Diagrams, *J. Phys. Chem. C*, 2008, **112**, 590-601.

222. D.-e. Jiang, S. H. Overbury, and S. Dai: Structures and Energetics of Pt Clusters on TiO2: Interplay between Metal–Metal Bonds and Metal–Oxygen Bonds, *J. Phys. Chem. C*, 2012, **116**(41), 21880-21885.

223. M. K. Nowotny, L. R. Sheppard, T. Bak, and J. Nowotny: Defect Chemistry of Titanium Dioxide. Application of Defect Engineering in Processing of TiO2-Based Photocatalysts, *J. Phys. Chem. C*, 2008, **112**, 5275-5300.

224. C. Yao, F. Li, X. Li, and D. Xia: Fiber-like nanostructured Ti4O7 used as durable fuel cell catalyst support in oxygen reduction catalysis, *J. Mater. Chem.*, 2012, **22**(32), 16560.

225. R. Phillips, P. Hansen, and E. Eisenbraun: Atomic layer deposition fabricated substoichiometric TiOx nanorods as fuel cell catalyst supports, *Journal of Vacuum Science & Technology A: Vacuum, Surfaces, and Films*, 2012, **30**(1), 01A125.

226. A. Naldoni, M. Allieta, S. Santangelo, M. Marelli, F. Fabbri, S. Cappelli, C. L. Bianchi, R. Psaro, and V. Dal Santo: Effect of Nature and Location of Defects on Bandgap Narrowing in Black TiO2 Nanoparticles, *J. Am. Chem. Soc.*, 2012, **134**(18), 7600-7603.

227. S. C. Ammal and A. Heyden: Nature of Ptn/TiO2(110) Interface under Water-Gas Shift Reaction Conditions: A Constrained ab Initio Thermodynamics Study, *J. Phys. Chem. C*, 2011, **115**(39), 19246-19259.

228. D. Çakır and O. Gülseren: Adsorption of Pt and Bimetallic PtAu Clusters on the Partially Reduced Rutile (110) TiO2Surface: A First-Principles Study, *J. Phys. Chem. C*, 2012, **116**(9), 5735-5746.

229. U. Diebold, J.-M. Pan, and T. Madey: Ultrathin metal film growth on TiO2 (110): an overview, *Surf. Sci.*, 1995, **331-333**, 845-854.

230. K. Tiido, N. Alexeyeva, M. Couillard, C. Bock, B. R. MacDougall, and K. Tammeveski: Graphene–TiO2 composite supported Pt electrocatalyst for oxygen reduction reaction, *Electrochim. Acta*, 2013, **107**, 509-517.

231. F. Shi, L. R. Baker, A. Hervier, G. A. Somorjai, and K. Komvopoulos: Tuning the Electronic Structure of Titanium Oxide Support to Enhance the Electrochemical Activity of Platinum Nanoparticles, *Nano Lett.*, 2013, **13**, 4469−4474.

232. B. Y. Xia, B. Wang, H. B. Wu, Z. Liu, X. Wang, and X. W. Lou: Sandwich-structured TiO2–Pt–graphene ternary hybrid electrocatalysts with high efficiency and stability, *J. Mater. Chem.*, 2012, **22**(32), 16499-16505.

233. X. Li, W.-X. Chen, J. Zhao, W. Xing, and Z.-D. Xu: Microwave polyol synthesis of Pt/CNTs catalysts: Effects of pH on particle size and electrocatalytic activity for methanol electrooxidization, *Carbon*, 2005, **43**(10), 2168-2174.

234. S. Song, Y. Wang, and P. K. Shen: Pulse-microwave assisted polyol synthesis of highly dispersed high loading Pt/C electrocatalyst for oxygen reduction reaction, *J. Power Sources*, 2007, **170**(1), 46-49.

235. W. F. Zhang, Y. L. He, M. S. Zhang, Y. Zin, and Q. Chen: Raman scattering study on anatase TiO2 nanocrystals, *J. Appl. Phys. D*, 2000, **33**(8), 912-916.

236. S. Santangelo, G. Messina, G. Faggio, A. Donato, L. De Luca, N. Donato, A. Bonavita, and G. Neri: Micro-Raman analysis of titanium oxide/carbon nanotubes-based nanocomposites for hydrogen sensing applications, *Journal of Solid State Chemistry*, 2010, **183**(10), 2451-2455.

237. M. Chisaka, A. Ishihara, K.-i. Ota, and H. Muramoto: Synthesis of carbon-supported titanium oxynitride nanoparticles as cathode catalyst for polymer electrolyte fuel cells, *Electrochim. Acta*, 2013, **113**, 735-740.

238. O. Dulub, W. Hebenstreit, and U. Diebold: Imaging Cluster Surfaces with Atomic Resolution: The Strong Metal-Support Ineteraction State of Pt Supported on TiO2, *Phys. Rev. Lett.*, 2000, **84**(16), 3646-3649.

239. X. Huang, W. Rigdon, J. Neutzler, D. Larrabee, and J. Sightler: High Performance Membrane Electrode Assembly Fabricated by Ultrasonic Spray Technique, *ECS Trans.*, 2011, **41**(1), 901-907.

240. S. J. Lee, S. Mukerjee, E. A. Ticianelli, and J. McBreen: Electrocatalysis of CO tolerance in hydrogen oxidation reaction in PEM fuel cells, *Electrochim. Acta*, 1999, **44**(19), 3283-3293.

241. H. A. Gasteiger, N. M. Markovic, and P. N. Ross Jr.: H2 and CO Electrooxidation on Well-Characterized Pt, Ru, and Pt-Ru. 1. Rotating Disk Electrode Studies fo the Pure Gases Including Temperature Effects, *J. Phys. Chem.*, 1995, **99**, 8290-8301.

242. H. A. Gasteiger, N. M. Markovic, and P. N. Ross Jr.: H2 and CO Electrooxidation on Well-Characterized Pt, Ru, and Pt-Ru. 2. Rotating Disk Electrode Studies of CO/H2 Mixtures at 62 C, *J. Phys. Chem.*, 1995, **99**, 16757-16767.

243. J. E. Hu, J. B. Pearlman, G. S. Jackson, and C. J. Tesluk: Evaluating the impact of enhanced anode CO tolerance on performance of proton-exchange-membrane fuel cell systems fueled by liquid hydrocarbons, *J. Power Sources*, 2010, **195**(7), 1926-1935.

244. S. M. M. Ehteshami and S. H. Chan: A review of electrocatalysts with enhanced CO tolerance and stability for polymer electrolyte membarane fuel cells, *Electrochim. Acta*, 2013, **93**, 334-345.

245. Z. Peng and H. Yang: Designer platinum nanoparticles: Control of shape, composition in alloy, nanostructure and electrocatalytic property, *Nano Today*, 2009, **4**(2), 143-164.

246. S. M. M. Ehteshami, Q. Jia, A. Halder, S. H. Chan, and S. Mukerjee: The role of electronic properties of Pt and Pt alloys for enhanced reformate electro-oxidation in polymer electrolyte membrane fuel cells, *Electrochim. Acta*, 2013, **107**, 155-163.

247. S. Mukerjee and R. C. Urian: Bifunctionality in Pt alloy nanoncluster electrocatalysts for enhanced methanol oxidation and CO tolerance in PEM fuel cells, *Electrochim. Acta*, 2002, **47**, 3219-3231.

248. F. Micoud, F. Maillard, A. Bonnefont, N. Job, and M. Chatenet: The role of the support in COads monolayer electrooxidation on Pt nanoparticles: Pt/WOxvs. Pt/C, *Phys. Chem. Chem. Phys.*, 2010, **12**(5), 1182.

249. P. Strasser, Q. Fan, M. Devenney, and W. H. Weinberg: High Throughput Experimental and Theoretical Predictive Screening Materials - A Comparative Study of Search Strategies for New Fuel Cell Anode Catalysts, *J. Phys. Chem. B*, 2003, **107**, 11013-11021.

250. P. Piela, C. Eickes, E. Brosha, F. Garzon, and P. Zelenay: Ruthenium Crossover in Direct Methanol Fuel Cell with Pt-Ru Black Anode, *J. Electrochem. Soc.*, 2004, **151**(12), A2053.

251. G.-S. Park, C. Pak, Y.-S. Chung, J.-R. Kim, W. S. Jeon, Y.-H. Lee, K. Kim, H. Chang, and D. Seung: Decomposition of Pt–Ru anode catalysts in direct methanol fuel cells, *J. Power Sources*, 2008, **176**(2), 484-489.

252. J. E. Hu, Z. Liu, B. W. Eichhorn, and G. S. Jackson: CO tolerance of nano-architectured Pt–Mo anode electrocatalysts for PEM fuel cells, *International Journal of Hydrogen Energy*, 2012, **37**(15), 11268-11275.

253. Z. Liu, G. S. Jackson, and B. W. Eichhorn: PtSn Intermetallic, Core-Shell, and Alloy Nanoparticles as CO-Tolerant Electrocatalysts for H_2 Oxidation, *Angewandte Chemie International Edition*, 2010, **49**(18), 3173-3176.

254. F. J. Scott, S. Mukerjee, and D. E. Ramaker: Contrast in Metal-Ligand Effects on PtM Electrocatalysts with M Equal Ru vs Mo and Sn As Exhibited by in Situ XANES and EXAFS Measurements in Methanol, *J. Phys. Chem. C*, 2010, **114**, 442-453.

255. K. Kanda, Z. Noda, Y. Nagamatsu, T. Higashi, S. Taniguchi, S. M. Lyth, A. Hayashi, and K. Sasaki: Negligible Start-Stop-Cycle Degradation in a PEFC Utilizing Platinum-Decorated Tin Oxide Electrocatalyst Layers with Carbon Fiber Filler, *ECS Electrochemistry Letters*, 2014, **3**(4), F15-F18.

256. J. J. Pietron, M. B. Pomfret, C. N. Chervin, J. W. Long, and D. R. Rolison: Direct methanol oxidation at low overpotentials using Pt nanoparticles electrodeposited at ultrathin conductive RuO2 nanoskins, *J. Mater. Chem.*, 2012, **22**(11), 5197.

257. Z. Liu, J. E. Hu, Q. Wang, K. Gaskell, A. I. Frenkel, G. S. Jackson, and B. Eichorn: PtMo Alloy and MoOx@Pt Core-Shell Nanoparticles as Highly CO Tolerant Electrocatalysts, *J. Am. Chem. Soc. Comm.*, 2009, **131**, 6924-6925.

258. H. P. Dhar, L. G. Christner, A. K. Kush, and H. C. Maru: Performance Study of a Fuel Cell Pt-on-C Anode in Presence of CO and CO2, and Calculation of Adsorption Parameters for CO Poisoning, *J. Electrochem. Soc.*, 1986, **133**(8), 1574-1582.

259. S. A. Bilmes: The Multiplicity of Anodic Current Peaks Related to the Potentiodynamic Electro-oxidation of Carbon Monoxide on Polycrystalline Platinum, *J. Electrochem. Soc.*, 1980, **127**(10), 2184-2187.

260. S. Balasubramanian, C. E. Holland, and J. W. Weidner: Electrochemical Removal of Carbon Monoxide in Reformate Hydrogen for Fueling Proton Exchange Membrane Fuel Cells, *Electrochem. Solid-State Lett.*, 2010, **13**(2), B5.

261. A. Taniguchi, T. Akita, K. Yasuda, and Y. Miyazaki: Analysis of electrocatalyst degradation in PEMFC caused by cell reversal during fuel starvation, *J. Power Sources*, 2004, **130**(1–2), 42-49.

262. M. Oezaslan, F. Hasché, and P. Strasser: Pt-Based Core–Shell Catalyst Architectures for Oxygen Fuel Cell Electrodes, *J. Phys. Chem. Lett.*, 2013, **4**(19), 3273-3291.

263. S. Zhang, X. Yuan, H. Wang, W. Merida, H. Zhu, J. Shen, S. Wu, and J. Zhang: A review of accelerated stress tests of MEA durability in PEM fuel cells, *International Journal of Hydrogen Energy*, 2009, **34**(1), 388-404.

264. T. Mori, D. R. Ou, J. Zou, and J. Drennan: Present status and future prospect of design of Pt–cerium oxide electrodes for fuel cell applications, *Prog. Nat. Sci., Mater. Int.*, 2012, **22**(6), 561-571.

265. J. Masud, M. T. Alam, M. R. Miah, T. Okajima, and T. Ohsaka: Enhanced electrooxidation of formic acid at Ta2O5-modified Pt electrode, *Electrochemistry Communications*, 2011, **13**(1), 86-89.

266. Z. Awaludin, M. Suzuki, J. Masud, T. Okajima, and T. Ohsaka: Enhanced Electrocatalysis of Oxygen Reduction on Pt/TaOx/GC, *J. Phys. Chem. C*, 2011, **115**(51), 25557-25567.

267. N. R. de Tacconi, C. R. Chenthamarakshan, K. Rajeshwar, W.-Y. Lin, T. F. Carlson, L. Nikiel, W. A. Wampler, S. Sambandam, and V. Ramani: Photocatalytically Generated Pt/C–TiO2 Electrocatalysts with Enhanced Catalyst Dispersion for Improved Membrane Durability in Polymer Electrolyte Fuel Cells, *J. Electrochem. Soc.*, 2008, **155**(11), B1102-B1109.

268. S. Wendt, R. Schaub, J. Matthiesen, E. K. Vestergaard, E. Wahlström, M. D. Rasmussen, P. Thostrup, L. M. Molina, E. Lægsgaard, I. Stensgaard, B. Hammer, and F. Besenbacher: Oxygen vacancies on TiO2(110) and their interaction with H2O and O2: A combined high-resolution STM and DFT study, *Surf. Sci.*, 2005, **598**(1-3), 226-245.

269. J. Nowotny, T. Bak, M. K. Nowotny, and L. R. Sheppard: TiO2 Surface Acitve Sites for Water Splitting, *J. Phys. Chem. B*, 2006, **110**, 18492-18495.

270. J. M. Jaksic, D. Labou, C. M. Lacnjevac, A. Siokou, and M. M. Jaksic: Potentiodynamic estimation of key parametric criterions and interrelating reversible spillover effects for electrochemical promotion, *Appl. Catal., A*, 2010, **380**(1-2), 1-14.

271. O. Bikondoa, C. L. Pang, R. Ithnin, C. A. Muryn, H. Onishi, and G. Thornton: Direct visualization of defect-mediated dissociation of water on TiO2(110), *Nat. Mater.*, 2006, **5**(3), 189-192.

272. U. Diebold: The surface science of titanium dioxide, *Surface Science Reports*, 2003, **48**, 53-229.

273. X. Chen and S. S. Mao: Titanium Dioxide Nanomaterials: Synthesis, Properties, Modifications, and Applications, *Chem. Rev.*, 2007, **107**, 2891-2959.

274. S.-Y. Huang, P. Ganesan, and B. N. Popov: Titania supported platinum catalyst with high electrocatalytic activity and stability for polymer electrolyte membrane fuel cell, *Appl. Catal., B*, 2011, **102**(1-2), 71-77.

275. H. Chhina, D. Susac, S. Campbell, and O. Kesler: Transmission Electron Microscope Observation of Pt Deposited on Nb-Doped Titania, *Electrochem. Solid-State Lett.*, 2009, **12**(6), B97.

276. K. Y. Chen: Preparation and Characterization of High-Performance Pt-Ru/WO[sub 3]-C Anode Catalysts for the Oxidation of Impure Hydrogen, *Electrochem. Solid-State Lett.*, 1999, **3**(1), 10.

277. D.-J. Guo, X.-P. Qiu, L.-Q. Chen, and W.-T. Zhu: Multi-walled carbon nanotubes modified by sulfated TiO2 – A promising support for Pt catalyst in a direct ethanol fuel cell, *Carbon*, 2009, **47**(7), 1680-1685.

278. C. Ma, Y. Jin, M. Shi, Y. Chu, Y. Xu, W. Jia, Q. Yuan, J. Chen, D. Chen, and S. Chen: Study of Nano-WO3 Modified Carbon Nanotubes Supported Pt Electrocatalyst for Oxygen Reduction Reaction, *J. Electrochem. Soc.*, 2013, **161**(3), F246-F251.

279. G. Sakai, T. Arai, T. Matsumoto, T. Ogawa, M. Yamada, K. Sekizawa, and T. Taniguchi: Electrochemical and ESR Study on Pt-TiOx/C Electrocatalysts with Enhanced Activity for ORR, *ChemElectroChem*, 2014, **1**(2), 366-370.

280. J. Zhu, X. Zhao, M. Xiao, L. Liang, C. Liu, J. Liao, and W. Xing: The construction of nitrogen-doped graphitized carbon–TiO2 composite to improve the electrocatalyst for methanol oxidation, *Carbon*, 2014, **72**, 114-124.

281. J. Wang, J. Xi, Y. Bai, Y. Shen, J. Sun, L. Chen, W. Zhu, and X. Qiu: Structural designing of Pt-CeO2/CNTs for methanol electro-oxidation, *J. Power Sources*, 2007, **164**(2), 555-560.

282. D.-M. Gu, Y.-Y. Chu, Z.-B. Wang, Z.-Z. Jiang, G.-P. Yin, and Y. Liu: Methanol oxidation on Pt/CeO2–C electrocatalyst prepared by microwave-assisted ethylene glycol process, *Appl. Catal., B*, 2011, **102**(1-2), 9-18.

283. B. Ruiz Camacho, C. Morais, M. A. Valenzuela, and N. Alonso-Vante: Enhancing oxygen reduction reaction activity and stability of platinum via oxide-carbon composites, *Catal. Today*, 2013, **202**, 36-43.

284. P. Trogadas and V. Ramani: Pt/C–WO3 Electrocatalysts for Degradation Mitigation in Polymer Electrolyte Fuel Cells, *J. Electrochem. Soc.*, 2008, **155**(7), B696-B703.

285. J. Nowotny, T. Bak, M. K. Nowotny, and L. R. Sheppard: Defect Chemistry and Electrical Poperties of Titanium Dioxide. 2. Effect of Aliovalent ions, *J. Phys. Chem. C*, 2008, **112**, 602-610.

286. L. R. Sheppard, T. Bak, and J. Nowotny: Electrical Properties of Niobium-Doped Titanium Dioxide. 1. Defect Disorder, *J. Phys. Chem. B*, 2006, **110**, 22447-22454.

287. K. Sasaki and J. Maier: Low-temperature defect chemistry of oxides. I. General aspects and numerical calculations, *J. Appl. Phys.*, 1999, **86**(10), 5422-5433.

288. K. Sasaki and J. Maier: Low-temperature defect chemistry of oxides. II. Analytical relations, *J. Appl. Phys.*, 1999, **86**(10), 5434-5443.

289. L. R. Sheppard, T. Bak, and J. Nowotny: Electrical Properties of Niobium-Doped Titanium Dioxide. 2. Equilibration Kinetics, *J. Phys. Chem. B*, 2006, **110**, 22455-22461.

290. D. D. Mulmi, T. Sekiya, N. Kamiya, S. Kurita, Y. Murakami, and T. Kodaira: Optical and electric properties of Nb-doped anatase TiO2 single crystal, *Journal of Physics and Chemistry of Solids*, 2004, **65**(6), 1181-1185.

291. E. Comini, M. Ferroni, V. Guidi, A. Vomiero, P. G. Merli, V. Morandi, M. Sacerdoti, G. D. Mea, and G. Sberveglieri: Effects of Ta/Nb-doping on titania-based thin films for gas-sensing, *Sensors and Actuators B: Chemical*, 2005, **108**(1-2), 21-28.

292. W. M. Haynes, ed. *CRC Handbook of Chemistry and Physics*, Vol. 94th, 2013-2014.

293. D. Wang, C. V. Subban, H. Wang, E. Rus, F. J. DiSalvo, and H. D. Abruña: Highly Stable and CO-Tolerant Pt/Ti0.7W0.3O2 Electrocatalyst for Proton-Exchange Membrane Fuel Cells, *J. Am. Chem. Soc. Comm.*, 2010, **132**, 10218-10220.

294. A. Kumar and V. Ramani: Strong Metal–Support Interactions Enhance the Activity and Durability of Platinum Supported on Tantalum-Modified Titanium Dioxide Electrocatalysts, *ACS Catal.*, 2014, **4**(5), 1516-1525.

295. A. Kumar and V. Ramani: Ta0.3Ti0.7O2 Electrocatalyst Supports Exhibit Exceptional Electrochemical Stability, *J. Electrochem. Soc.*, 2013, **160**(11), F1207-F1215.

296. M. M. Jaksic, G. A. Botton, G. D. Papakonstantinou, F. Nan, and J. M. Jaksic: Primary Oxide Latent Storage and Spillover Enabling Electrocatalysts with Reversible Oxygen Electrode Properties and the Alterpolar Revertible (PEMFC versus WE) Cell, *J. Phys. Chem. C*, 2014, **118**(17), 8723-8746.

297. X. Liu, X. Wu, and K. Scott: Study of niobium and tantalum doped titania supported Pt electrocatalysts for methanol oxidation reaction and oxygen reduction reaction, *Catalysis Science & Technology*, 2014.

298. S. J. Tauster, S. C. Fung, R. T. K. Baker, and J. A. Horsley: Strong Interactions in Supported-Metal Catalysts, *Science*, 1981, **211**(4487), 1121-1125.

299. Y. Zhou, C. L. Muhich, B. T. Neltner, A. W. Weimer, and C. B. Musgrave: Growth of Pt Particles on the Anatase TiO2(101) Surface, *J. Phys. Chem. C*, 2012, **116**(22), 12114-12123.

300. S. G. Neophytides, S. H. Zafeiratos, and M. M. Jaksic: Selective Interactive Grafting of Composite Bifunctional Electrocatalysts for Simultaneous Anodic Hydrogen and CO Oxidation, *J. Electrochem. Soc.*, 2003, **150**(10), E512.

301. J. M. Jaksic, D. Labou, G. D. Papakonstantinou, A. Siokou, and M. M. Jaksic: Novel Spillover Interrelating Reversible Electrocatalysts for Oxygen and Hydrogen Electrode Reactions, *J. Phys. Chem. C*, 2010, **114**, 18298-18312.

302. L. R. Baker, A. Hervier, H. Seo, G. Kennedy, K. Komvopoulos, and G. A. Somorjai: Highly n-Type Titanium Oxide as an Electronically Active Support for Platinum in the Catalytic Oxidation of Carbon Monoxide, *J. Phys. Chem. C*, 2011, **115**(32), 16006-16011.

303. C. L. Muhich, Y. Zhou, A. M. Holder, A. W. Weimer, and C. B. Musgrave: Effect of Surface Deposited Pt on the Photoactivity of TiO2, *J. Phys. Chem. C*, 2012, **116**(18), 10138-10149.

304. Z. Jiang, Y. Yang, W. Shangguan, and Z. Jiang: Influence of Support and Metal Precursor on the State and CO Catalytic Oxidation Activity of Platinum Supported on TiO2, *J. Phys. Chem. C*, 2012, **116**(36), 19396-19404.

305. G. A. Hope and A. J. Bard: Platinum/Titanium Dioxide Interface. Formation of Ohmic and Rectifying Junctions, *J. Phys. Chem.*, 1983, **87**, 1979-1984.

306. J. Y. Park, J. R. Renzas, A. M. Contreras, and G. A. Somorjai: The genesis and importance of oxide–metal interface controlled heterogeneous catalysis; the catalytic nanodiode, *Top. Catal.*, 2007, **46**(1-2), 217-222.

307. R. E. Fuentes, B. L. García, and J. W. Weidner: Effect of Titanium Dioxide Supports on the Activity of Pt-Ru toward Electrochemical Oxidation of Methanol, *J. Electrochem. Soc.*, 2011, **158**(5), B461.

308. C.-S. Chen and F.-M. Pan: Electrocatalytic activity of Pt nanoparticles deposited on porous TiO2 supports toward methanol oxidation, *Appl. Catal., B*, 2009, **91**(3-4), 663-669.

309. X. Zhao, J. Zhu, L. Liang, J. Liao, C. Liu, and W. Xing: Enhanced activity of Pt nano-crystals supported on a novel TiO2@N-doped C nano-composite for methanol oxidation reaction, *J. Mater. Chem.*, 2012, **22**(37), 19718.

310. P. Stonehart and D. Wheeler: Phosphoric Acid Fuel Cells (PAFCs) for Utilities: Electrocatalyst Crystallite Design, Carbon Support, and Matrix Materials Challenges, *Mod. Aspects Electrochem.*, 2005, **38**, 373-424.

311. J. R. C. Salgado, R. G. Duarte, L. M. Ilharco, A. M. Botelho do Rego, A. M. Ferraria, and M. G. S. Ferreira: Effect of functionalized carbon as Pt electrocatalyst support on the methanol oxidation reaction, *Appl. Catal., B*, 2011, **102**(3-4), 496-504.

312. R. Escudero-Cid, A. S. Varela, P. Hernández-Fernández, E. Fatás, and P. Ocón: The effect of functionalised multi-walled carbon nanotubes in the hydrogen

electrooxidation reaction in reactive currents impurified with CO, *International Journal of Hydrogen Energy*, 2014, **39**(10), 5063-5073.

313. M. S. Saha and A. Kundu: Functionalizing carbon nanotubes for proton exchange membrane fuel cells electrode, *J. Power Sources*, 2010, **195**(19), 6255-6261.

314. A. O. Al-Youbi, J. L. Gómez de la Fuente, F. J. Pérez-Alonso, A. Y. Obaid, J. L. G. Fierro, M. A. Peña, M. Abdel Salam, and S. Rojas: Effects of multiwalled carbon nanotube morphology on the synthesis and electrocatalytic performance of Pt supported by multiwalled carbon nanotubes, *Appl. Catal., B*, 2014, **150-151**, 21-29.

315. A. K. Roy and C.-T. Hsieh: Pulse microwave-assisted synthesis of Pt nanoparticles onto carbon nanotubes as electrocatalysts for proton exchange membrane fuel cells, *Electrochim. Acta*, 2013, **87**, 63-72.

316. N.-Y. Hsu, C.-C. Chien, and K.-T. Jeng: Characterization and enhancement of carbon nanotube-supported PtRu electrocatalyst for direct methanol fuel cell applications, *Appl. Catal., B*, 2008, **84**(1-2), 196-203.

317. A. Guha, W. Lu, T. A. Zawodzinski, and D. A. Schiraldi: Surface-modified carbons as platinum catalyst support for PEM fuel cells, *Carbon*, 2007, **45**(7), 1506-1517.

318. K. Jukk, J. Kozlova, P. Ritslaid, V. Sammelselg, N. Alexeyeva, and K. Tammeveski: Sputter-deposited Pt nanoparticle/multi-walled carbon nanotube composite catalyst for oxygen reduction reaction, *J. Electroanal. Chem.*, 2013, **708**, 31-38.

319. F. Alcaide, G. Álvarez, O. Miguel, M. J. Lázaro, R. Moliner, A. López-Cudero, J. Solla-Gullón, E. Herrero, and A. Aldaz: Pt supported on carbon nanofibers as electrocatalyst for low temperature polymer electrolyte membrane fuel cells, *Electrochemistry Communications*, 2009, **11**(5), 1081-1084.

320. S. Sharma, A. Ganguly, P. Papakonstantinou, X. Miao, M. Li, J. L. Hutchinson, M. Delichatsios, and S. Ukleja: Rapid Microwave Synthesis of CO Tolerant Reduced Graphene Oxide-Supported Platinum Electrocatalysts for Oxidation of Methanol, *J. Phys. Chem. C*, 2010, **114**, 19459-19466.

321. W. A. Rigdon, X. Huang, and T. I. Valdez: High Performance Platinum Black Cathodes By Ultrasonic Spray Deposition, *ECS Meeting Abstracts*, 2013, **224**(15), 1507-1507.

322. Z. Q. Tian, S. P. Jiang, Y. M. Liang, and P. K. Shen: Synthesis and Characterization of Platinum Catalysts on Multiwalled Carbon Nanotubes by Intermittent Microwave Irradiation for Fuel Cell Applications, *J. Phys. Chem. B*, 2006, **110**(11), 5343-5350.

323. W. F. Zhang, M. S. Zhang, Z. Yin, and Q. Chen: Photoluminescence in anatase titanium dioxide nanocrystals, *Appl. Phys. B*, 2000, **70**, 261-265.

324. A. M. Ruiz, G. Dezanneau, J. Arbiol, A. Cornet, and J. R. Morante: Insights into the Structural and Chemical Modifications of Nb additive on TiO2 Nanoparticles, *Chem. Mat.*, 2004, **16**, 862-871.

325. Z. Awaludin, J. G. Sheng Moo, T. Okajima, and T. Ohsaka: TaOx-capped Pt nanoparticles as active and durable electrocatalysts for oxygen reduction, *Journal of Materials Chemistry A*, 2013, **1**(46), 14754-14765.

326. X. Guo, D.-J. Guo, X.-P. Qiu, L.-Q. Chen, and W.-T. Zhu: Excellent dispersion and electrocatalytic properties of Pt nanoparticles supported on novel porous anatase TiO2 nanorods, *J. Power Sources*, 2009, **194**(1), 281-285.

327. A. Lewera, L. Timperman, A. Roguska, and N. Alonso-Vante: Metal–Support Interactions between Nanosized Pt and Metal Oxides (WO3and TiO2) Studied Using X-ray Photoelectron Spectroscopy, *J. Phys. Chem. C*, 2011, **115**(41), 20153-20159.

328. J.-H. Kim, S. Chang, and Y.-T. Kim: Compressive strain as the main origin of enhanced oxygen reduction reaction activity for Pt electrocatalysts on chromium-doped titania support, *Appl. Catal., B*, 2014, **158-159**, 112-118.

329. X. Wang, J. C. Yu, H. Y. Yip, L. Wu, P. K. Wong, and S. Y. Lai: A Mesoporous Pt/TiO2 Nanoarchitecture with Catalytic and Photocatalytic Functions, *Chemistry - A European Journal*, 2005, **11**(10), 2997-3004.

330. L. Yan, K. Huang, Y. Chen, and Y. Xing: High Content Niobium in Rutile Titania as Catalyst Support to Promote Methanol Electro-Oxidation, *ECS Electrochemistry Letters*, 2014, **3**(5), F27-F29.

331. D. R. Ou, T. Mori, K. Fugane, H. Togasaki, F. Ye, and J. Drennan: Stability of Ceria Supports in Pt–CeOx/C Catalysts, *J. Phys. Chem. C*, 2011, **115**(39), 19239-19245.

332. C. Xu, P. Pietrasz, J. Yang, R. Soltis, K. Sun, M. Sulek, and R. Novak: Pt-based ORR Catalyst on Carbon-Supported Amorphous Niobium Oxide Support, *ECS Trans.*, 2013, **58**(1), 1779-1788.

333. B. B. Blizanac, S. Pylypenko, T. S. Olson, D. Konopka, and P. Atanassov: Functional DMFC Cathode Catalysts and Supports Based on Niobium Oxide Phase, *J. Electrochem. Soc.*, 2011, **158**(5), B485.

334. D. A. Konopka, M. Li, K. Artyushkova, N. Marinkovic, K. Sasaki, R. Adzic, T. L. Ward, and P. Atanassov: Platinum Supported on NbRuyOz as Electrocatalyst for Ethanol Oxidation in Acid and Alkaline Fuel Cells, *J. Phys. Chem. C*, 2011, **115**(7), 3043-3056.

335. D. Konopka, B. Kiefer, Y.-B. Jiang, T. Ward, and P. Atanassov: Electrochemical Studies and DFT Analysis of Pt Stability and Surface Passivation on NbRuyOz Support, *J. Electrochem. Soc.*, 2011, **158**(7), B804.

336. Y. Fan, Z. Yang, P. Huang, X. Zhang, and Y.-M. Liu: Pt/TiO2−C with hetero interfaces as enhanced catalyst for methanol electrooxidation, *Electrochim. Acta*, 2013, **105**, 157-161.

337. B. Ruiz-Camacho, H. H. R. Santoyo, J. M. Medina-Flores, and O. Álvarez-Martínez: Platinum deposited on TiO2-C and SnO2-C composites for methanol oxidation and oxygen reduction, *Electrochim. Acta*, 2014, **120**, 344-349.

338. K. R. Cooper, V. Ramani, J. M. Fenton, and H. R. Kunz: Experimental Methods and Data Analyses for Polymer Electrolyte Fuel Cells, 149; 2005, Southern Pines, NC, Scribner Associates, Inc.

339. K. Kinoshita and P. Stonehart: Preparation and Characterization of Highly Dispersed Electrocatalytic Materials, in 'Modern Aspects of Electrochemistry', (eds. J. O. M. Bockris, et al.), 183-266; 1977, Springer US.

340. Z. Xu, H. Zhang, H. Zhong, Q. Lu, Y. Wang, and D. Su: Effect of particle size on the activity and durability of the Pt/C electrocatalyst for proton exchange membrane fuel cells, *Appl. Catal., B*, 2012, **111-112**, 264-270.

341. G. Chen, Y. Tan, B. Wu, G. Fu, and N. Zheng: Carbon monoxide-controlled synthesis of surface-clean Pt nanocubes with high electrocatalytic activity, *Chemical Communications*, 2012, **48**(22), 2758.

342. N. Tian, Z. Y. Zhou, S. G. Sun, Y. Ding, and Z. L. Wang: Synthesis of Tetrahexahedral Platinum Nanocrystals with High-Index Facets and High Electro-Oxidation Activity, *Science*, 2007, **316**(5825), 732-735.

343. R. Imbihl and G. Ertl: Oscillatory Kinetics in Heterogeneous Catalysis, *Chem. Rev.*, 1995, **95**, 697-733.

344. N. Wagner and E. Gülzow: Change of electrochemical impedance spectra (EIS) with time during CO-poisoning of the Pt-anode in a membrane fuel cell, *J. Power Sources*, 2004, **127**(1-2), 341-347.

345. A. J. Atanacio, T. Bak, and J. Nowotny: Niobium Segregation in Niobium Doped Titanium Dioxide (Rutile), *J. Phys. Chem. C*, 2014, **118**(21), 11174-11185.

Appendix A: Carbon Support Corrosion Effects

INVESTIGATION OF CARBON CORROSION RESISTANCE OF CARBON NANOTUBE CONTAINING ELECTRODES

Diana D. D. Larrabee, William A. Rigdon, Eli B. McPherson, Joshua J. Sightler, James Z. Flynn, Xinyu Huang
University of South Carolina, College of Engineering and Computing Mechanical Engineering Department

Research Statement

Carbon is a common support material for platinum catalysts in low temperature fuel cells. Carbon bonding structure (sp, sp^2, and sp^3 hybridization) has an important role in relation to its oxidation resistance or corrosion properties. Carbon black (CB), the most commonly used catalyst support, is a complex mixture of amorphous and graphitic carbon with large amounts of oxygen-containing surface defect groups, which can serve as initiation sites for the decomposition of carbon. Carbon nanotubes (CNT) were integrated into the cathode of a hydrogen fuel cell as catalyst supports to contrast with more conventional CB support. The goal is to observe and characterize any benefits from the use of CNT as catalyst support and structural reinforcement of catalysts layer.

Objective

The objective is to create, compare, and test the performance and durability of electrodes in polymer electrolyte membrane fuel cells (PEMFCs) composed of the following:

1) **Pt/CB**: Platinum (Pt) catalysts supported by carbon black (CB)
2) **Pt/CNT**: Platinum (Pt) catalysts supported by multi-wall carbon nanotubes (Pt/CNT) and
3) **Pt/CNT+CB**: Hybrid electrode composed of 50% Pt/CB and 50% Pt/CNTs

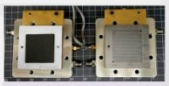

Figure 1. Fuel cell assembly for PEM fuel cell

Experimental Methods

Three different cathode constructions were created. All electrodes were prepared with a 0.5 mg-Pt/cm^2 loading deposited on 25 cm^2 area of Nafion® 212 membrane by an ultrasonic sprayer. Except for the materials, the electrode fabrication and sample preparation details are identical for control and comparison samples.

An accelerated durability test for the catalyst support outlined by the USCAR Fuel Cell Tech Team was applied to induce rapid corrosion of the carbon support structure. This condition was applied using the test setup shown in Figure 2. The cell was held at 1.2 V under humidified H_2 and N_2 on the anode and cathode at 150 kPa and 80 °C. Periodic diagnostic tests were conducted at 0, 12, 24, 36, 48, 72, 96, 120, and 144 hours to capture the evolution of the electrochemical surface area (ECSA), polarization behavior, catalyst activity, and cell resistance.

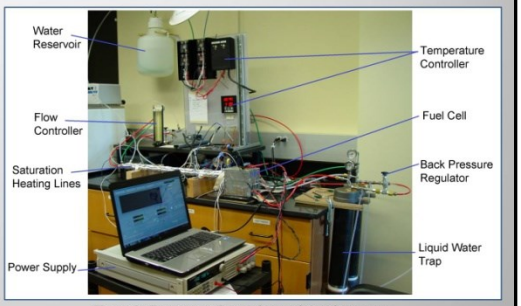

Figure 2. Experimental setup for accelerated aging test.

Results

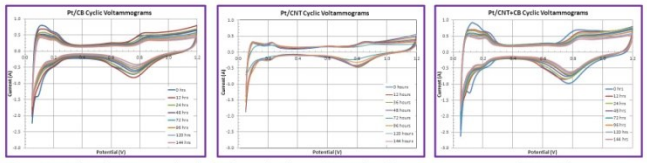

Figure 3. Cyclic voltammetry of cathode shows the electrochemical surface area at a scan rate of 100 mV/s.

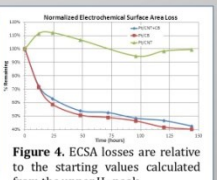

Figure 4. ECSA losses are relative to the starting values calculated from the upper H_2 peak

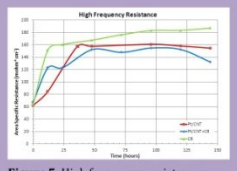

Figure 5. High frequency resistance increases measured by an AC impedance method of potentiostat at 0.2 V.

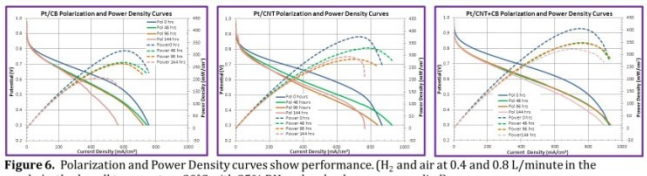

Figure 6. Polarization and Power Density curves show performance. (H_2 and air at 0.4 and 0.8 L/minute in the anode/cathode, cell temperature 80°C with 85% RH and no back pressure applied)

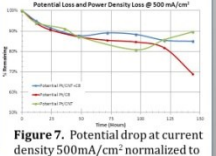

Figure 7. Potential drop at current density 500mA/cm^2 normalized to initial performance.

Figure 8. TEM image of Pt supported by a carbon nanotube

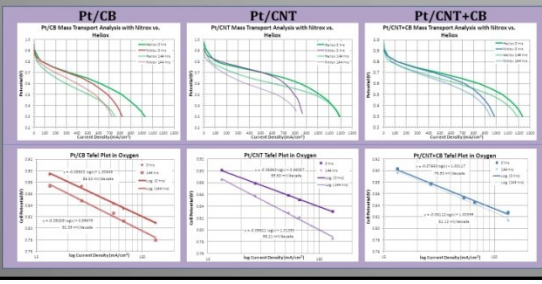

Figure 9. Cell behavior at mass-transport limited region. Diffusion properties were studied by varying the diluent gas for O_2 from N_2 to He to change the limiting current.

Figure 10. Tafel plots from H_2/O_2 polarization at low current in the catalyst activation show the difference in activity change for the catalyst.

Conclusion

The structure and bonding characteristics of carbon determine the durability of catalyst support in the corrosive environment of the polymer electrolyte membrane fuel cell (PEMFC) cathode. Bonding Pt nanocrystals to the surface of multi-wall CNT showed advantageous improvements over the more conventional CB supports when subjected to the aging process of these materials. The addition of CNT to the catalyst ink created a more structurally robust electrode by reinforcing the electrode layer to avoid and delay the collapse of the electrode structure, while keeping open pores for mass transport. This enhanced durability can be evidenced in the graphs presenting a greater resistance to change in properties from the initial condition. Further study to quantify reaction kinetics and dynamics specific to this corrosion mechanism will help reveal how to engineer a more stable cathodes in PEMFCs.

Acknowledgements

Thank you to the Mechanical Engineering Department at the University of South Carolina, to the USC Office of Undergraduate Research, and to the Magellan Scholar Program for supporting and funding this project.

Appendix B: Proton Conductivity during Transient Hydration

Proton Conductivity of Polymer Electrolyte Membranes during Transient Hydration

William A. Rigdon, Xinyu Huang
University of South Carolina

Daniel S. Hussey, David L. Jacobson
National Institute of Standards and Technology

Abstract

Most modeling work of the polymer electrolyte membrane (PEM) assumes that the correlation between proton conductivity and water content obtained under equilibrium condition is accurate even during transient hydration of the membrane. However, we present evidence that demonstrates significant deviation from the equilibrium proton conductivity/water content correlation. When dry Nafion is initially exposed to water vapor activity significantly greater than the equilibrium constant and is not diffusion limited at the interface, conductivity increases quickly as the as the sulfonic acid hydration reaction defines the rate limiting kinetic. Neutron imaging measured hydrogen absorbance in the solid membrane to correlate water content with absorption and desorption rates; these kinetics are nearly symmetric. During fast response, dry membranes initially gain conductivity much faster than the increase in water content, but the rate wet membranes lose conductivity during dehydration is about the same when cycled between (0~75% RH). The preserved conductivity during drying can possibly be attributed to a variable acid hydration kinetic which is also limited through the interface. This asymmetric behavior during non-equilibrium transient condition should be accounted for in new models.

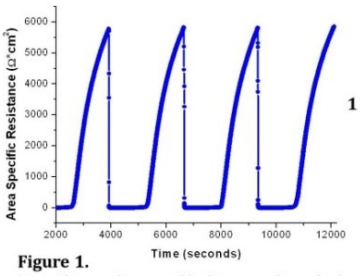

Figure 1.
Humidity cycling profile from working fuel cell measured by 1 kHz AC impedance method

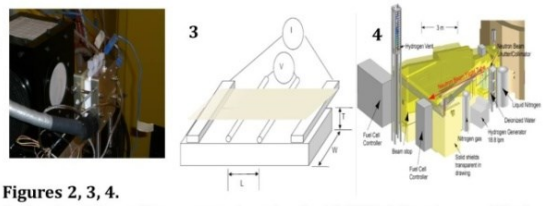

Figures 2, 3, 4.
2- Conductivity cell in neutron imaging by EMCCD following modified Beer-Lambert Law
3- Pt 4 electrode schematic with PEM sample N 117
4- NIST BT-2 Neutron Imaging at Center for Neutron Imaging

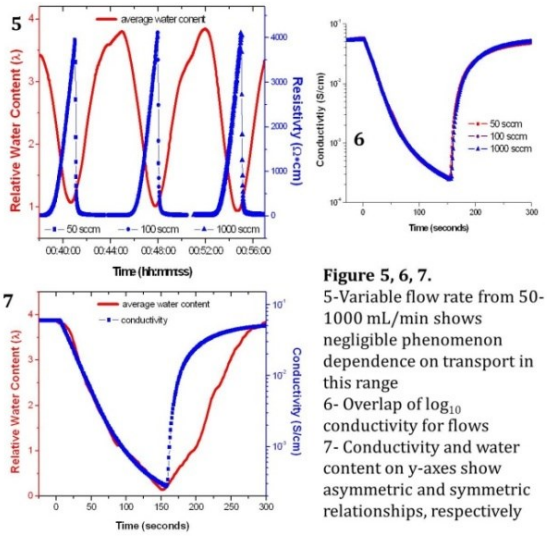

Figure 5, 6, 7.
5-Variable flow rate from 50-1000 mL/min shows negligible phenomenon dependence on transport in this range
6- Overlap of $\log_{10}$ conductivity for flows
7- Conductivity and water content on y-axes show asymmetric and symmetric relationships, respectively

Importance for PEMFC

- ✓Increased durability during dynamic loading
- ✓Reliable and fast start-up and shut-down
- ✓Economic operating protocol for stacks and systems
- ✓Water management and freezing prevention
- ✓Inhibition of flooding and cathode corrosion
- ✓Development of new membrane electrolyte materials

Conclusion

Experimental data shows membrane conductivity during transient hydration follows a non-equilibrium relationship on short time scales and can be a critical variable in operational performance of PEMFC. These factors suggest new models should account for the deviations from the linear equilibrium model. This test recognizes some advantages of Nafion significant to its transient operation.

Acknowledgements

National Science Foundation CBET Award 0829082
ECS Student Travel Grant tp Boston, MA for 221st Meeting

Appendix C: Ultrasonic Spray Frequency Effects

High Performance Platinum Black Cathodes by Ultrasonic Spray Deposition

William A. Rigdon, Ian A. W. Finch, and Xinyu Huang, Ph. D.
Department of Mechanical Engineering, University of South Carolina
Thomas I. Valdez, Ph. D.
Electrochemical Technologies, Jet Propulsion Laboratory at California Institute of Technology

Abstract and Introduction

Polymer electrolyte fuel cells rely on preparation of composite electrodes utilizing platinum (Pt) catalysts. Unsupported Pt black nanoparticles offer exceptional activity and stability for this purpose. However, they are difficult to prepare into a sprayable formula that can be distributed in a homogeneous layer directly on to the polymer membrane. An ultrasonic process to disperse and deposit the Pt suspension was optimized for high performance. Comparisons were made between ink formulations as well as the ultrasonic frequency used for spray deposition.

Experimental Procedures

A procedure was developed to suspend Pt black (Johnson-Matthey Hi-Spec® 1000) catalysts in solvent to prepare ink for ultrasonic spray deposition on to Nafion® polymers. An ExactaCoat system from Sono-Tek Corporation was used.

1. Pt black was mixed with D.I. water by a rotary speed mixer or ultrasonic horn
2. Nafion DE-521 suspension is separately diluted in D.I. water then mixed
3. Ionomer is added drop wise by syringe while under constant agitation
4. Water mixtures were then prepared at different concentrations with isopropyl alcohol
5. Alcohol must be added in the final step to avoid agglomerations of the ink
6. Ink is injected into the sprayer designed to spray a templated square electrode pattern
7. Flow rates and heated substrate control the evaporation of solvent from the electrode
8. Hot press of the membrane electrode assembly (MEA) at 250 N/m^2 for 5 min at 135 °C
9. MEAs installed in cell hardware with triple serpentine channels, GDL, 80 in•lbs torque
10. Variations in frequency of ultrasonic spray and test conditions were used for comparison

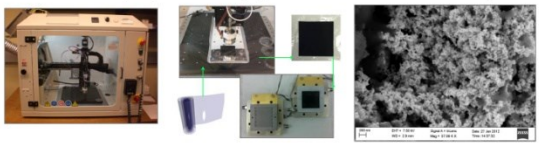

Results and Discussion

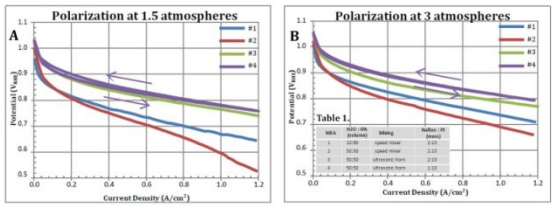

Figure 1. H_2 and O_2 polarization at 3/3 stoichiometric flow under A) 1.5 atm and B) 3 atm back pressure. The 25 cm^2 MEAs on NRE-212 with near 6 mg$_{Pt}$/cm^2 are fully humidified at 80 °C. MEA 4 performance at 3 atm exceeded a NASA target for i = 200 mA/cm^2 by operating above 0.92 Volts for maximum efficiency.

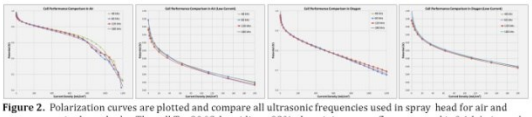

Figure 2. Polarization curves are plotted and compare all ultrasonic frequencies used in spray head for air and oxygen gases in the cathode. The cell T = 80 °C, humidity = 92%, the minimum gas flow rate used is 0.1 L/min, and the stoichiometric flow is based on 1.5/ 3 for anode/cathode where all tests performed without back pressure. The catalyst loading was 6 mg$_{Pt}$/cm^2 in the cathode with 10 cm^2 design on to Nafion XL membranes.

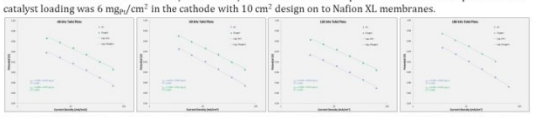

Figure 3. Tafel plots for each ultrasonic frequency used show polarization at low current. Cell T = 80 °C, humidity = 92%, gas flow rate used is 0.1 L/min, and tests were performed without back pressure.

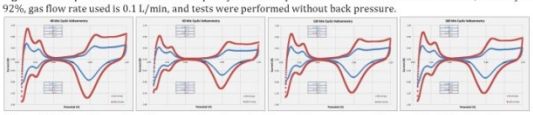

Figure 4. Cyclic voltammetry at two scan rates for each ultrasonic frequency used show catalyst behavior of cathode. The cell T = 80 °C, humidity = 92%, the gas flow rate used is 0.1 L/min with H_2/N_2 used on the A/C. The area is summarized in the tables in the plot and based on integration of hydrogen adsorption and desorption peaks.

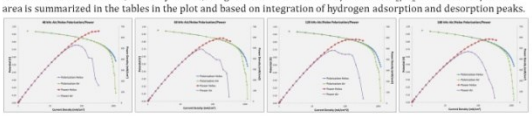

Figure 5. Polarization is compared for rates for air (oxygen in nitrogen) and helox (oxygen in helium). Each ultrasonic frequency used shows mass transport differences in cathode. The cell T = 80 °C, humidity = 92%, the gas flow rate used is 0.1 L/min with H_2/N_2 used on the A/C.

Summary and Conclusions

A procedure was developed for spray deposition of Pt black electrodes used in polymer electrolyte fuel cells. The suspension of catalysts is one of the most important factors in the preparation of high performance cathodes. A range of ultrasonic frequencies used for direct deposition on to the polymer had limited deviation in performance. At high catalyst loading small differences can be attributed to experimental variability. A performance goal at low current was achieved by using this loading to exceed a NASA goal for high efficiency.

Acknowledgements

The work summarized here has been sponsored by the South Carolina Space Grant Consortium through the Graduate Research Assistantship and the NASA EPSCOR Research Program. A part of this work was performed in JPL at Caltech through their Summer Internship Program.
Sono-Tek Corporation was very generous in the providing equipment and service for the project.

Appendix D: Platinum Cathodes with CNT Additives

Performance Optimization of Unsupported Platinum Black Cathodes in PEM Fuel Cells For High Efficiency Performance

William A. Rigdon[1*], Xinyu Huang[1], and Thomas I. Valdez[2]
[1]College of Engineering and Computing, University of South Carolina, Columbia
[2]Jet Propulsion Laboratory

Abstract and Introduction

The goal of this work is to contribute to the operational goals outlined by NASA for a high efficiency polymer electrolyte membrane (PEM) fuel cell. Progress has been made in processing and fabrication of noble platinum (Pt) cathodes for oxygen reduction utilizing an ultrasonic sprayer. The efficient operation will minimize fuel waste. A cathode was developed independently using alternative materials to the current technology which is subject to limitations. Required PTFE additive for mass transport does not contribute to charge transfer, while a CNT replacement can actually help to serve both functions.

Results and Discussion

A process for dispersion of the dense Pt metal catalysts in a liquid suspension which is sprayed on to the polymer substrate has been found critically important. Although difficult, the procedure prompted us to new strategies using ultrasonic mixing and spraying electrode layers with about 4 mg Pt/cm^2. The layer is finely dispersed and organized into a nanostructured network. The inclusion of the ionomer into the suspension has had the greatest effect on the utilization of active catalyst surfaces and the wrapped CNT has helped to distribute the electrolyte phase. The continuous percolating proton channels formed is not only known to be essential to performance, but it is also considered to be an important factor in durability.

Conclusions and Summary

A composite electrode layer deposited on to the polymer membrane has been the key to achieve the performance which rivals the materials produced by our collaborators at the Jet Propulsion Laboratory (JPL) Electrochemical Technologies Group. Quite possibly, it is the highest performance ever recorded in this high efficiency operational regime. The dispersion of the Pt catalyst for maximum utilization of active surfaces (> 75%) through improved charge transfer and mass transport with the use of new materials have been proven as effective performance benefits in the high efficiency realm of operation.

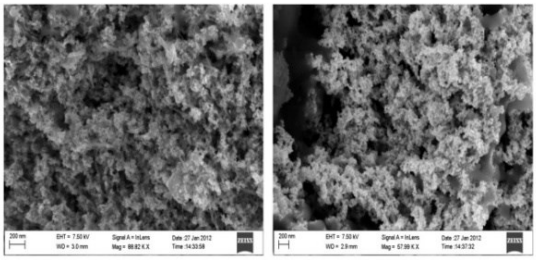

Figure 1 A and B.
FESEM images of Pt black cathode composites dispersed in Nafion® ionomer
A- Pt black with PTFE additive for beneficial product water removal properties
B- Ionomer has been predispersed in CNT solution under mixing and ultrasonic horn 20 kHz

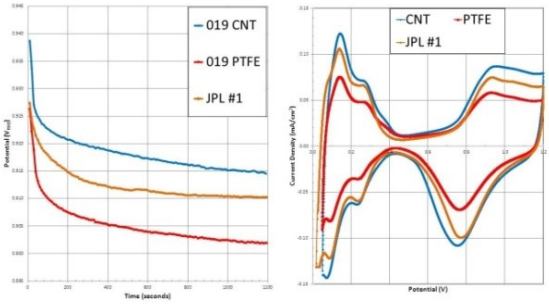

Figure 2 A and B.
Shows cathode performance and electrochemical characterization
A- Potential behavior at constant current density (200 mA/cm^2) in purified H_2 and O_2 fuel gases on anode/cathode at a 3/3 stoichiometric flows and 30 psig back pressure
B- Cyclic voltammetry (100 mV/sec) of the working cathode can be analyzed to interpret the reaction behavior, current crossover, and the active area. The surface area can be effectively increased for the same starting contents through improved dispersion and reduced use of inert PTFE insulator and replacement by functionalized CNT which can render ionomer to form a hydrophobic skin which has similar effect while still serving conduction purposes.

Acknowledgements The work summarized here has been sponsored by the South Carolina Space Grant Consortium through the Graduate Research Assistantship and the SC NASA EPSCOR Research Program

South Carolina Space Grant Consortium

Appendix E: XPS Deconvolutions

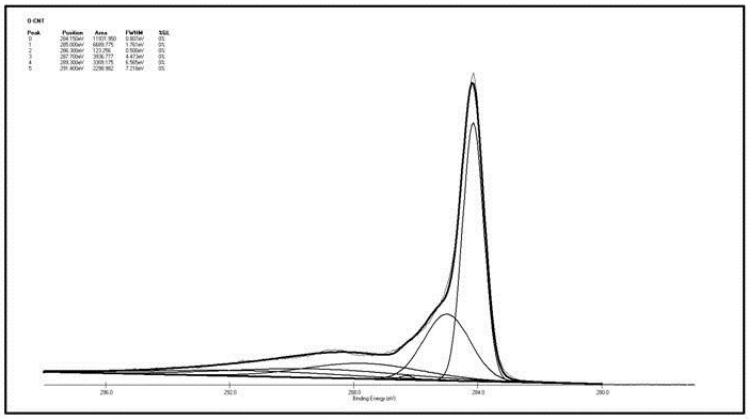

Figure E.1 O-CNT C 1 s

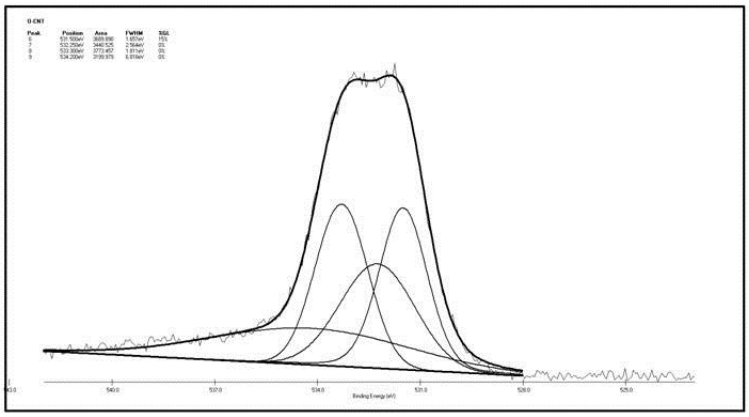

Figure E.2 O-CNT O 1s

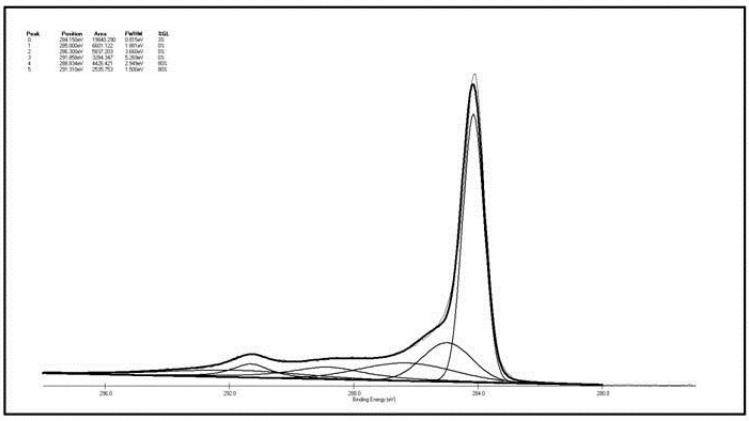

Figure E.3 Pt-CNT C 1s

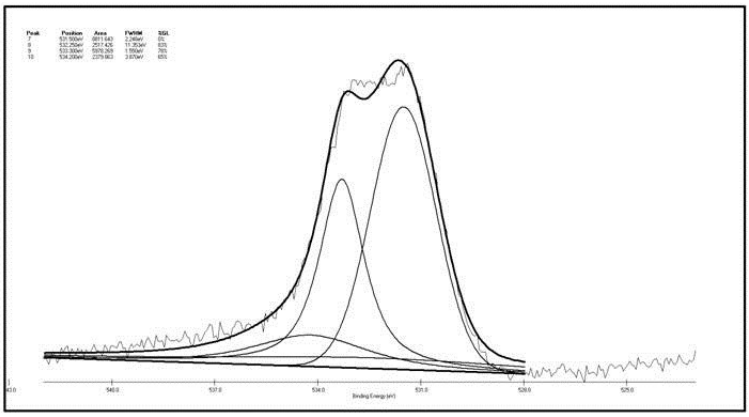

Figure E.4 Pt-CNT O 1s

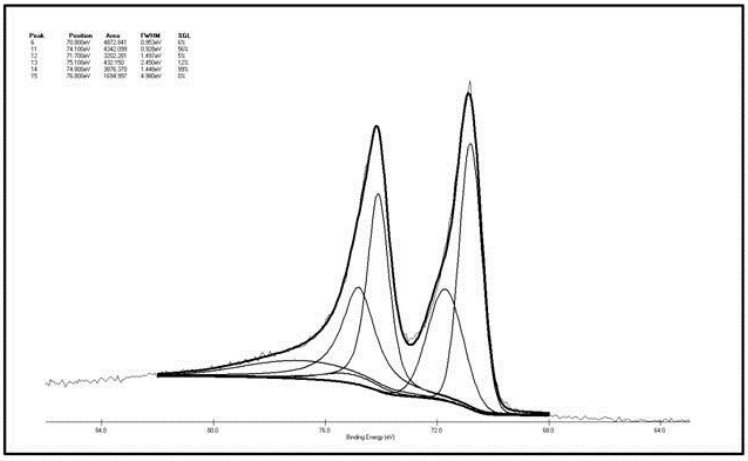

Figure E.5 Pt-CNT Pt 4f

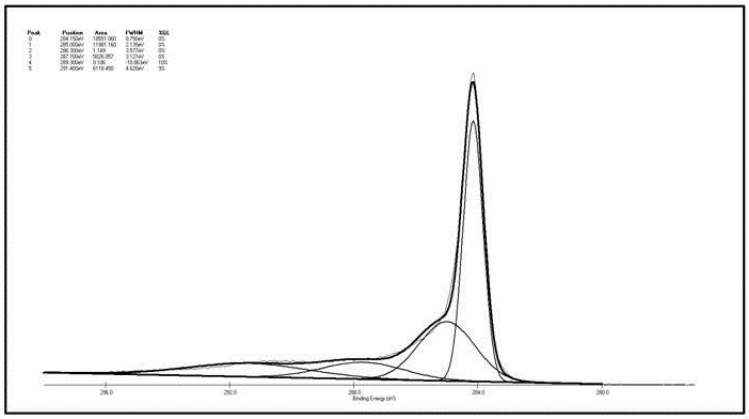

Figure E.6 TiO_x-CNT C 1s

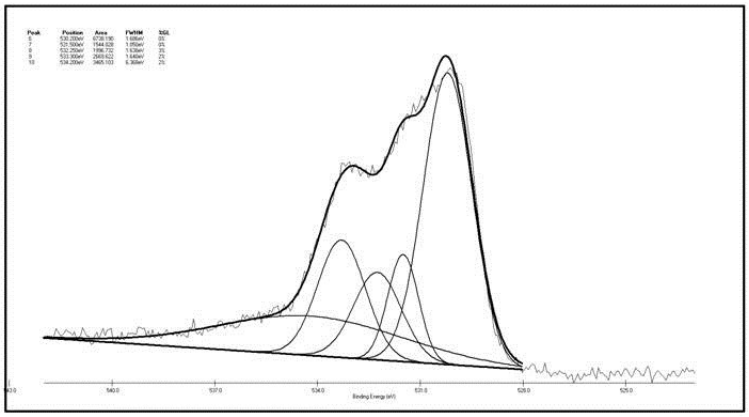

Figure E.7 TiO_x-CNT O 1s

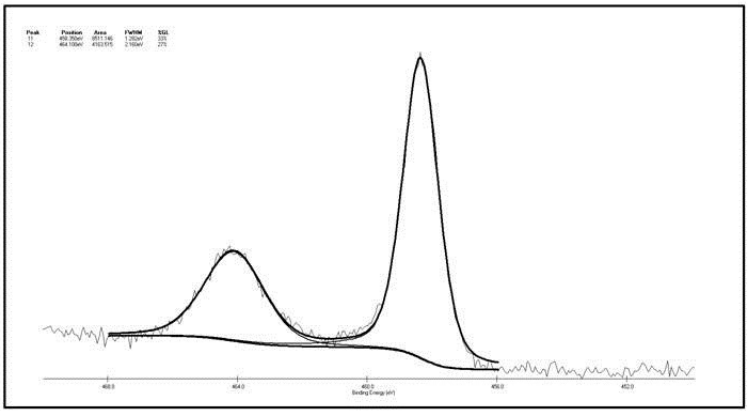

Figure E.8 TiOx-CNT Ti 2p

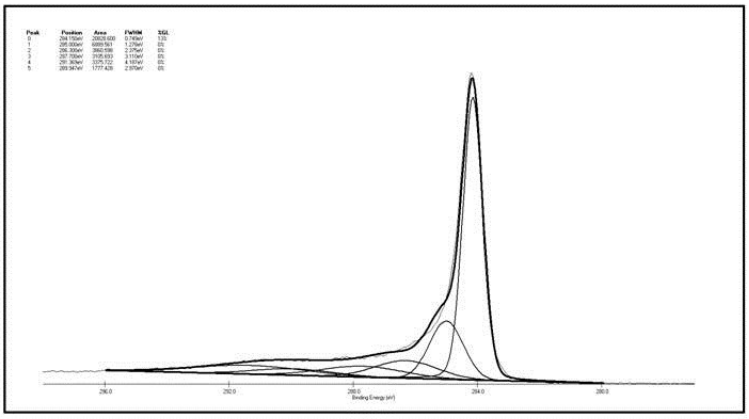

Figure E.9 Pt-TiO_x-CNT C 1s

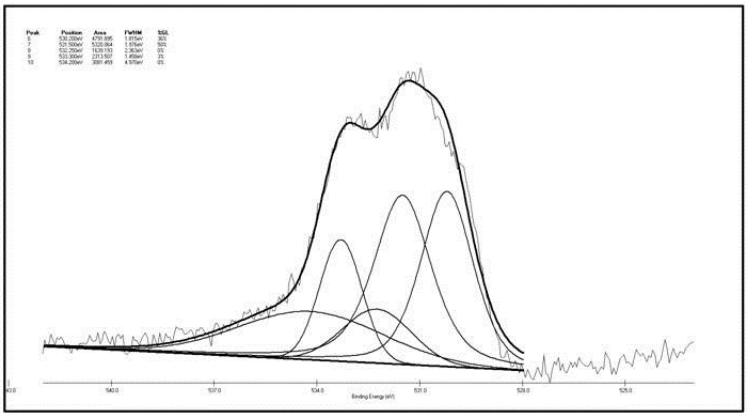

Figure E.10 Pt-TiO_x-CNT O 1s

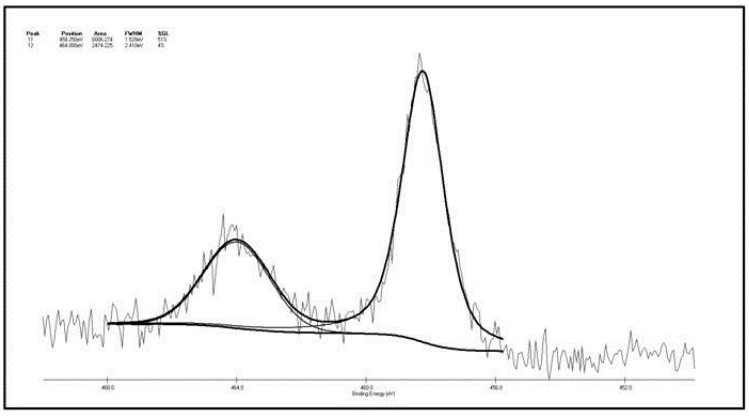

Figure E.11 Pt-TiO_x-CNT Ti 2p

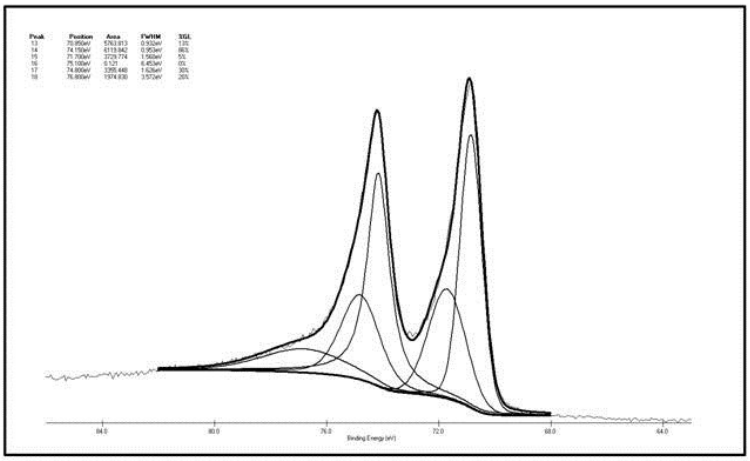

Figure E.12 Pt-TiO_x-CNT Pt 4f

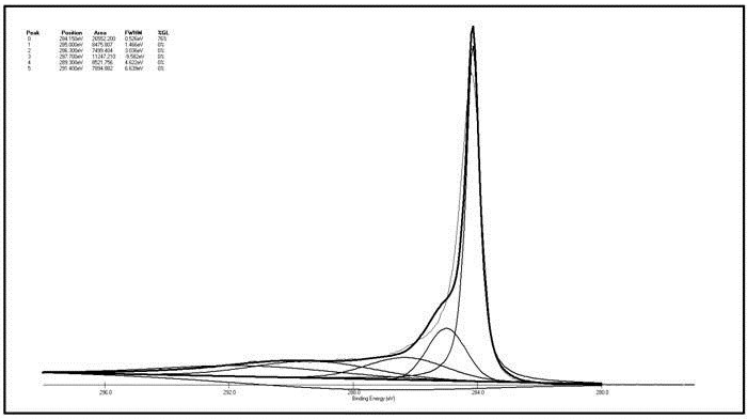

Figure E.13 $TiNbO_x$-CNT C 1s

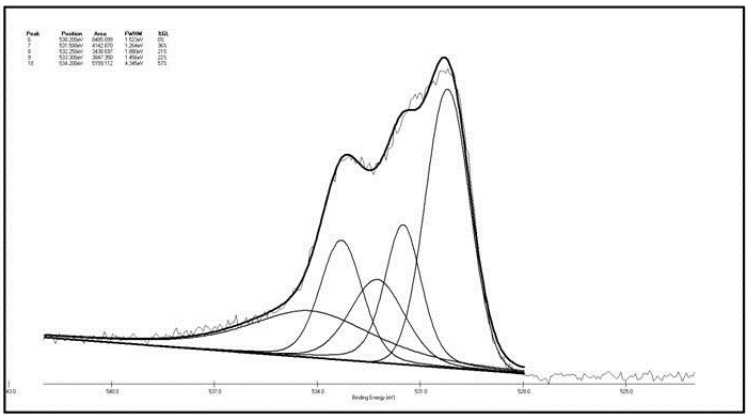

Figure E.14 $TiNbO_x$-CNT O 1s

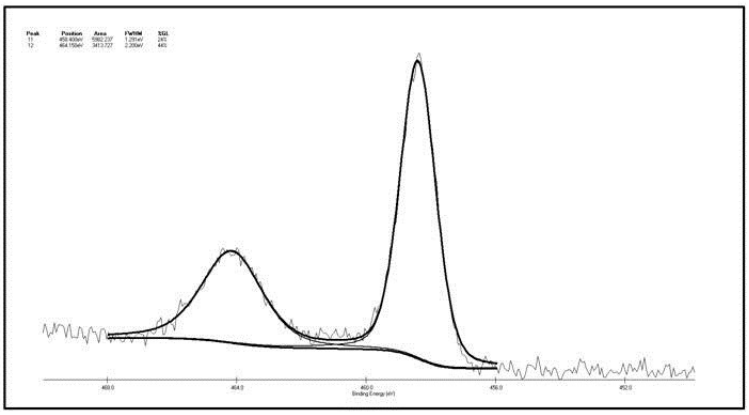

Figure E.15 $TiNbO_x$-CNT Ti 2p

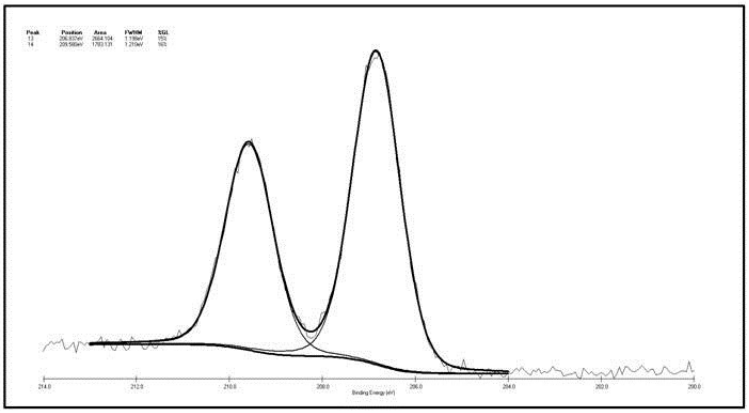

Figure E.16 $TiNbO_x$-CNT Nb 3d

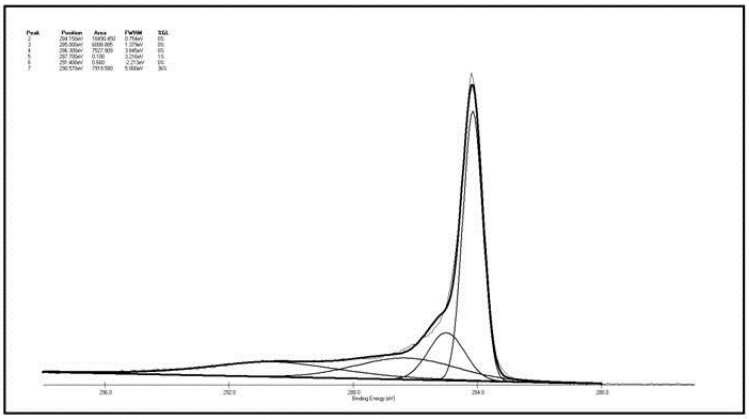

Figure E.17 Pt-$TiNbO_x$-CNT C 1s

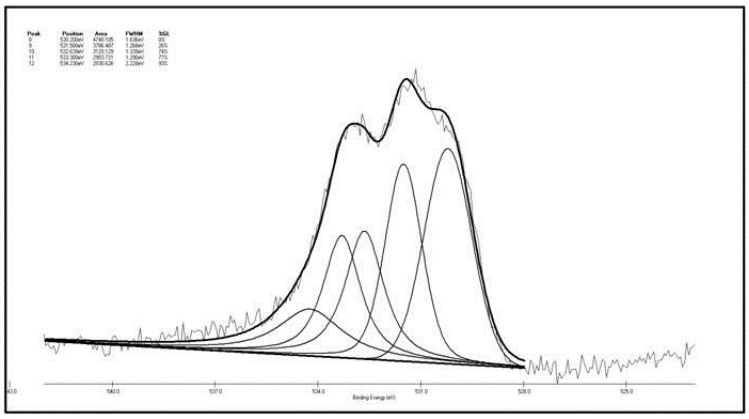

Figure E.18 Pt-TiNbO$_x$-CNT O 1s

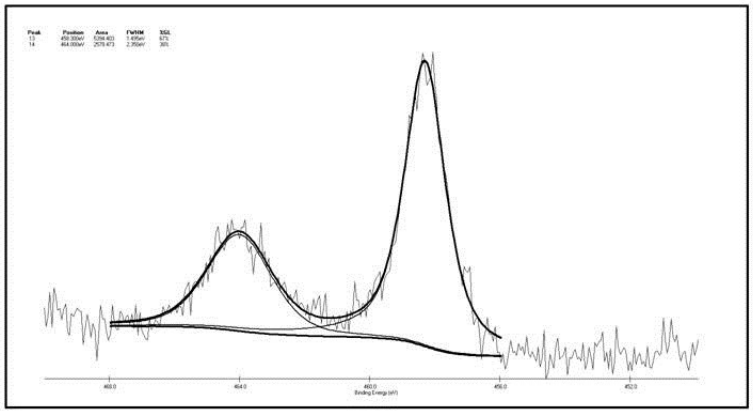

Figure E.19 Pt-TiNbO$_x$-CNT Ti 2p

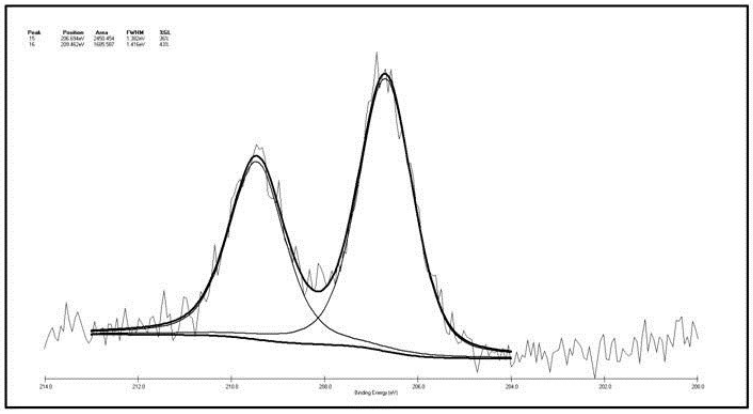

Figure E.20 Pt-TiNbO$_x$-CNT Nb 3d

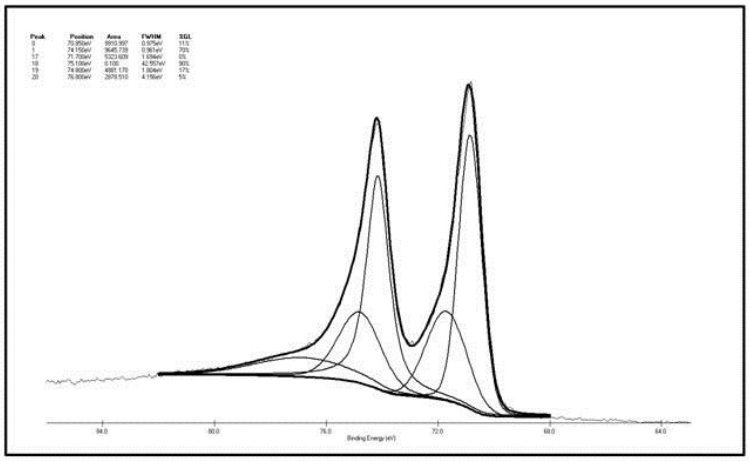

Figure E.21 Pt-TiNbO$_x$-CNT Pt 4f

XPS measurements were conducted using a Kratos AXIS Ultra DLD XPS system equipped with a monochromatic Al Kα source. The energy scale of the system is calibrated using a Au foil with Au4f scanned for the Al radiation and a Cu foil with Cu2p scanned for Mg radiation resulting in a difference of 1081.70 ± 0.025 eV between these two peaks. The binding energy is calibrated using an Ag foil with Ag $3d_{5/2}$ set at 368.21 ± 0.025 eV for the monochromatic Al X-ray source. The monochromatic Al Kα source was operated at 15 keV and 120 W. The pass energy was fixed at 40 eV for the detailed scans. A charge neutralizer (CN) was used to compensate for the surface charge. All peak deconvolutions were completed before any peaks were shifted to reference values. The peaks were plotted with XPSPEAK41 software. Backgrounds were subtracted from either linear or Shirley type baseline with 3 point averaging on end-points. Peak distributions were a combination of Gaussian-Lorentzian distributions. National Institute of Standards and Technology (NIST) reference values are listed in some cases.

Table E.1 Peak maximum binding energy B. E. (eV) location summary for all metals

Element	Ti	Ti	Nb	Nb	Pt	Pt	Pt	Pt
Electron Orbital	2p 3/2	2p 1/2	3d 5/2	3d 3/2	4f 7/2	4f 5/2	4d 5/2	4d 3/2
Pt-CNT	-	-	-	-	70.8	74.1	314.8	333
TiOx-CNT	458.35	464.15	-	-	-	-	-	-
Pt-TiOx-CNT	458.3	464.0	-	-	70.85	74.15	314.0	331.6
TiNbOx-CNT	458.4	464.15	206.84	209.58	-	-	-	-
Pt-TiNbOx-CNT	458.3	464.0	206.69	209.46	70.85	74.15	314.0	331.6

Table E.2 C 1s summary

280-298 eV								
C 1s	sp^2-C	sp^3-C	C-O	C=O	COO	π-π	Total	Actual
	284.15	285	286.3	287.7	289.3	291.4	Area	Area
O-CNT	11931.95	6689.78	123.26	3936.78	3309.18	2298.98	28289.93	28304.99
	42.18%	23.65%	0.44%	13.92%	11.70%	8.13%	100.00%	
Pt-CNT	19480.29	6601.12	5837.2	3284.35	4426.42	2535.75	42165.13	41982.78
	46.20%	15.66%	13.84%	7.79%	10.50%	6.01%	100.00%	
TiOx-CNT	18551.06	11981.16	1.15	5026.06	0.11	6118.45	41677.99	41747.51
	44.51%	28.75%	0.00%	12.06%	0.00%	14.68%	100.00%	
Pt-TiOx-CNT	20828.6	6889.56	3860.6	3105.69	3375.72	1777.43	39837.6	39755.32
	52.28%	17.29%	9.69%	7.80%	8.47%	4.46%	100.00%	
TiNbOx-CNT	26552.2	8475.81	7499.4	11247.21	8521.76	7894.88	70191.26	48392.76
	37.83%	12.08%	10.68%	16.02%	12.14%	11.25%	100.00%	
Pt-TiNbOx-CNT	18490.45	6008.89	7527.91	0.1	0.66	7919.58	39947.59	39345.05
	46.29%	15.04%	18.84%	0.00%	0.00%	19.82%	100.00%	

Table E.3 O 1s summary

542-525 eV							
O 1s	M-O	O-C=O	C-OH, C-OC	O-C=O	-COOH	Total	Actual
	530.2	531.5	532.25	533.3	534.2	Area	Area
O-CNT	0	3689.89	3440.53	3773.46	3199.98	14103.86	13995.09
	0.00%	26.16%	24.39%	26.75%	22.69%	100.00%	
Pt-CNT	0	8811.64	2517.43	5978.27	2379.86	19687.2	17984.48
	0.00%	44.76%	12.79%	30.37%	12.09%	100.00%	
TiOx-CNT	6738.19	1544.03	1996.73	2669.62	3465.1	16413.67	16427.51
	41.05%	9.41%	12.17%	16.26%	21.11%	100.00%	
Pt-TiOx-CNT	4791.9	5320.06	1639.19	2313.51	3081.46	17146.12	16521.33
	27.95%	31.03%	9.56%	13.49%	17.97%	100.00%	
TiNbOx-CNT	8485.1	4142.87	3438.7	3847.35	5159.11	25073.13	24055.82
	33.84%	16.52%	13.71%	15.34%	20.58%	100.00%	
Pt-TiNbOx-CNT	4740.11	3786.49	3120.13	2903.73	2030.63	16581.09	16145.65
	28.59%	22.84%	18.82%	17.51%	12.25%	100.00%	

Table E.4 Ti 2p summary

456-470 eV		NIST			NIST			
Ti 2p	**2p 3/2**	458.6		**2p 1/2**	464.7		**Total**	**Actual**
	Area	**Location**	**FWHM**	**Area**	**Location**	**FWHM**	**Area**	**Area**
TiOx-CNT	8511.14	458.35	1.28	4163.52	464.1	2.16	12674.66	12039.36
Pt-TiOx-CNT	6006.27	458.3	1.53	2474.23	464	2.41	8480.5	8032.74
differences	-38.3%	0.05			0.1	0.11		
TiNbOx-CNT	5982.24	458.4	1.29	3413.73	464.15	2.2	9395.97	8899.2
Pt-TiNbOx-CNT	5394.4	458.25	1.5	2578.47	464	2.35	7972.87	7278.81
differences	-34.0%	0.15			0.15	0.13876		

Table E.5 Nb 3d summary

204-213 eV		NIST			NIST			
Nb 3d	**3d 5/2**	207.6		**3d 3/2**	209.9		**Total**	**Actual**
	Area	**Location**	**FWHM**	**Area**	**Location**	**FWHM**	**Area**	**Area**
TiNbOx-CNT	2664.1	206.84	1.2	1783.13	209.58	1.21	4447.23	4324.59
Pt-TiNbOx-CNT	2450.45	206.69	1.38	1685.59	209.46	1.42	4136.04	3913.67
differences	4.0%	0.15			0.12			

Table E.6 Pt 4f summary

68-82 eV		NIST				NIST			
Pt 4f	**4f 7/2**	71.1	**4f 7/2**		**4f 5/2**	74.5			**Total**
	Area	**Location**	**Area**	**Location**	**Area**	**Location**	**Area**	**Location**	**Area**
Pt-CNT	4872.8	70.8	3202.3	71.7	4342.1	74.1	3876.4	74.8	16293.6
Pt-TiOx-CNT	5763.8	70.85	3729.8	71.7	6119.8	74.15	3355.5	74.8	18968.9
Pt-TiNbOx-CNT	9911	70.85	5323.6	71.7	9645.7	74.15	4881.2	74.8	29761.5

Appendix F: Hydrogen Pump Regeneration

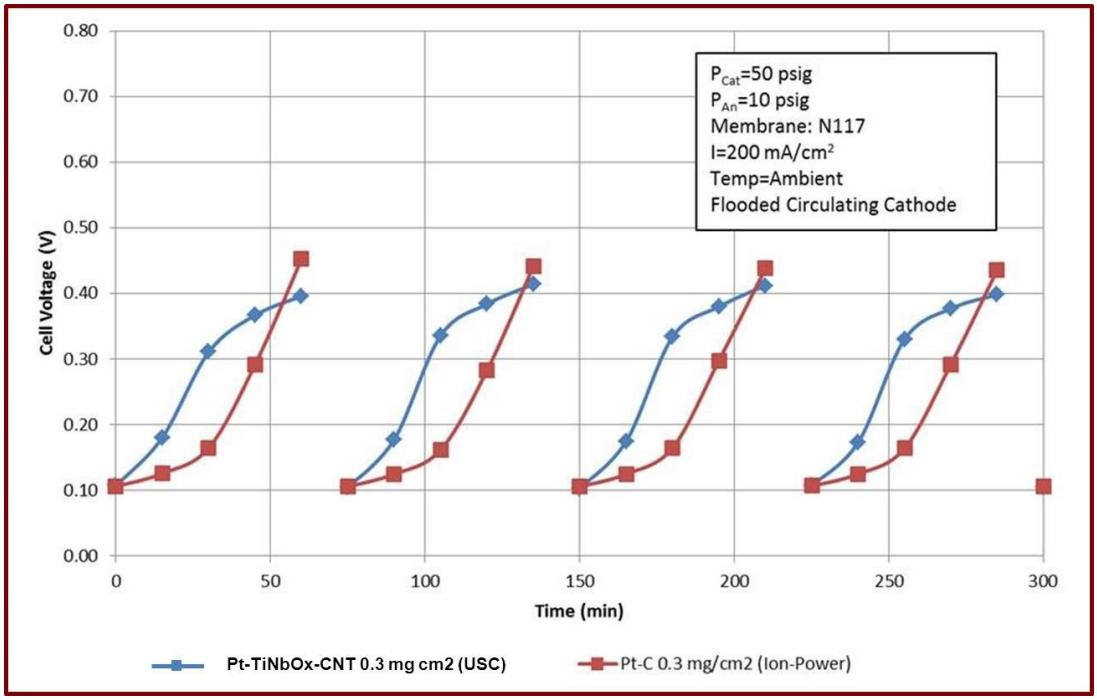

Figure F.1 Comparison of Pt-$TiNbO_x$-CNT versus commercial Pt-C in CO clean-up

Pt-$TiNbO_x$-CNT was compared against a commercial Pt-C electrocatalyst from Ion-Power, Inc in an electrochemical hydrogen pump during a simulated anode clean-up procedure. The test was performed by Joshua Preston at Sustainable Innovations, LLC to compare our laboratory material synthesis and ultrasonic spray deposition of circular 100 cm^2 MEA against a conventional design. Although, the composite electrocatalyst did not have the same mass activity, it showed an earlier onset for CO oxidation as evidenced by the change in slope > 0.3 V when tested at this set of conditions. This can indicate an enhanced longevity for this electrode construction when used in the anode.

Appendix G: CO_2 Evolution from CNT Supports

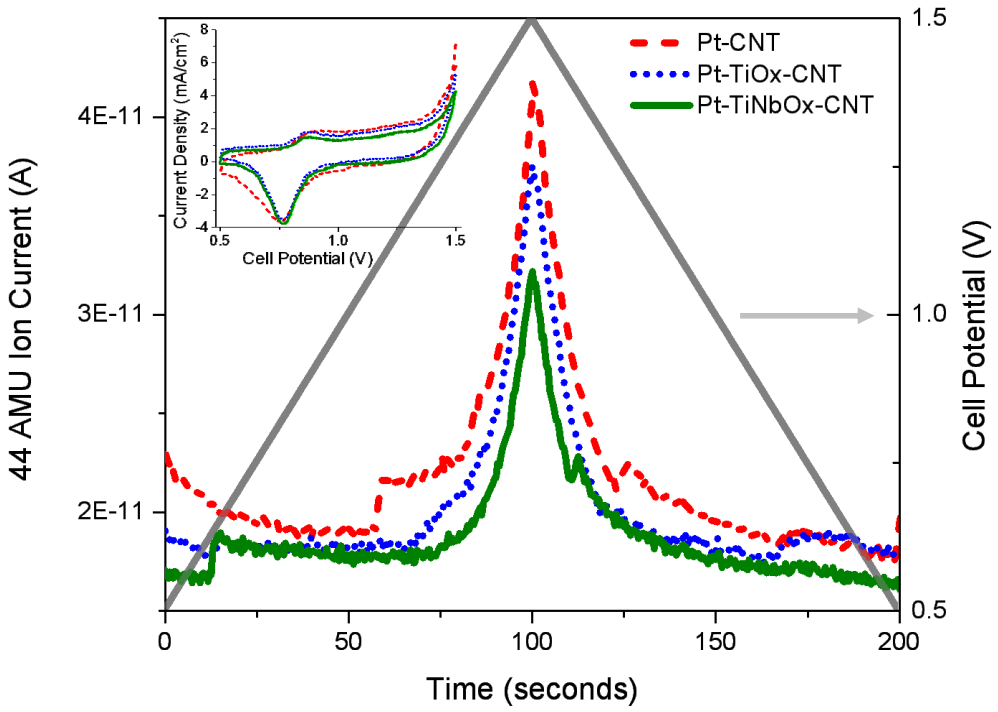

Figure G.1 Carbon support corrosion comparison by mass spectrometer

Mass spectrometer (Pfeiffer GSD 320) measured CO_2 ion current when cycling electrodes from 0.5 to 1.5 V at 10 mV/sec by an secondary electron multiplier detection after quadrupole. Exhaust from the cell was continuously monitored at ambient pressure with heated transfer line and cell temperature held at 80 °C. Humidity was lowered to 66% humidification in helium carrier gas to enhance signal-to-noise ratio of the response. A series of 10 cycles was carried out and the last is shown here for representative comparison. The carbon corrosion is reduced by the Pt-TiNbO_x-CNT composite electrocatalysts relative to other constructions, including Pt-CNT.